**Universidade de Lisboa**

**Faculdade de Ciências**

**Departamento de Química e Bioquímica**


# Re and $^{99m}$Tc Tricarbonyl Probes for Target-Specific Detection of Melanoma and Sentinel Lymph Node

Maurício da Silva Morais

**Doutoramento em Química**

**Especialidade de Química Inorgânica**

**2013**

**Universidade de Lisboa**

**Faculdade de Ciências**

**Departamento de Química e Bioquímica**


# Re and $^{99m}$Tc Tricarbonyl Probes for Target-Specific Detection of Melanoma and Sentinel Lymph Node

Maurício da Silva Morais

**Tese orientada por**:

Doutor João Domingos Galamba Correia

Doutora Isabel Rego dos Santos

Doutoramento em Química

Especialidade de Química Inorgânica

**2013**

The work described in this thesis was performed in the Radiopharmaceutical Sciences Group, Instituto Superior Técnico – Campus Tecnológico e Nuclear, Sacavém, Portugal, under the supervision of Doctor João D. G. Correia and Doctor Isabel Rego dos Santos.

NMR studies of the peptides and their derivatives were performed under the supervision of Prof. Dr. Maria Angeles Jiménez (Departamento de Química Física Biológica, Instituto de Química Física Rocasolano. CSIC. Madrid, Spain.)

Biological evaluation of the radioactive polymeric nanocompounds was performed in the groups of Prof. Dr. Grace Samuel (Radiopharmaceuticals Division, Bhabha Atomic Research Centre, Mumbai, India) and Prof. Dr. Yasushi Arano (Graduate School of Pharmaceutical Sciences, Chiba University, Chiba, Japan) as part of *Co-ordinated Research Project on the* "Development of $^{99m}$Tc Radiopharmaceutical for Cancer Diagnosis and Sentinel Node Detection", IAEA. Biological evaluation of a bimodal probe was performed under STSM of COST Action 1104 in the group of Prof. Dr. Tony Lahoutte and Prof. Dr. Vicky Caveliers (In Vivo Cellular and Molecular Imaging Laboratory, Free University of Brussels, Belgium).

The work was financially supported by Fundação para a Ciência e a Tecnologia through the PhD grant SFRH/BD/48066/2008. STSM was financially supported by COST Action 1104.

**Acknowledgements**

I am deeply indebted to my supervisor Prof. Dr. João Galamba Correia for his fundamental role in my doctoral work. I appreciate all his contributions of time, ideas, great guidance and patience to make my Ph.D. experience productive and stimulating.

I would like to express my deepest gratitude to Prof. Dr. Isabel Rego dos Santos for the opportunity to integrate and grow scientifically at the Radiopharmaceutcial Sciences group in Instituto Superior Técnico – Campus Tecnológico e Nuclear. I also would like to express my admiration for the thoroughness, enthusiasm and dedication with which she leads the research group.

My sincere appreciation is extended to Dr. Paula Raposinho for her valuable support, advice and effort to perform the *in vitro* and *in vivo* experiments.

I warmly thank Prof. Dr. Maria Angeles Jiménez for the opportunity to work with her in the conformational analysis of the peptides in solution. My heartfelt gratitude for the guidance, assistance, expertise and proof-reading during the preparation of publications.

I am very thankful to Dr. Célia Fernandes, Dr. Lurdes Gano and Dr Paula Campello for all their help, advice, good humor and encouragement.

I would like to thank Dr. Manuel Martins, Dr. Sérgio Pereira, Suresh Subramanian, Dr. Grace Samuel and Dr. Yasushi Arano for their time, suggestions and fruitful collaboration in the characterization and biological evaluation of polymeric compounds.

I would like to thank Prof. Dr. Tony Lahoutte and Prof. Dr.Vicky Caveliers for the opportunity to work in their group and all their team members for the valuable feedback. I also gratefully acknowledge Dr. Catarina Xavier who made me feel at home.

Dr. Joaquim Marçalo is acknowledged for the mass spectrometry analysis and his help in the discussion of the results.

My heartfelt gratitude to all my lab collegues for the great working environment, help and all the good times we spent together.

Aos meus amigos agradeço o estímulo, a paciência e a compreensão pela minha falta de disponibilidade.

À FáFá agradeço o apoio ao longo destes anos.

Por fim, um agradecimento muito especial aos meus pais.

**Resumo**

O melanoma é um tipo de cancro da pele que apesar de corresponder apenas a cerca de 4 a 5% dos casos, é responsável por mais de 75% das mortes associadas a este tipo de patologia. É um dos tumores malignos mais agressivos devido à elevada probabilidade de metastização, em particular para o sistema linfático, e consequente disseminação para diferentes órgãos e tecidos. O tratamento do melanoma em fases iniciais apresenta elevadas taxas de cura mas as terapias existentes para as fases mais avançadas são pouco eficazes.

Neste contexto, o aparecimento de novos radiofármacos específicos poderá contribuir para a detecção precoce e estadiamento desta patologia, bem como do processo de metastização permitindo definir o tipo de terapia a adoptar pelo clínico. Assim, o trabalho apresentado nesta tese tem como objectivo principal a concepção de novas sondas de $^{99m}$Tc(I) potencialmente úteis para a visualização *in vivo* de receptores da melanocortina do sub-tipo 1 (MC1R) sobreexpressos no melanoma e metástases, bem como dos receptores de manose (MR) expressos em macrófagos do sistema linfático e geralmente associados ao processo de metastização de tumores primários. O melanoma apresenta uma elevada probabilidade (cerca de 80%) de disseminação linfática sendo o primeiro gânglio linfático envolvido neste processo designado por gânglio sentinela. A sua detecção através do alvejamento dos MR e posterior excisão é importante não só para o seu estadiamento, como também para a definição da terapêutica.

Para alcançar os objectivos definidos, conceberam-se sondas radioactivas específicas contendo a unidade *fac*-[$^{99m}$Tc(CO)$_3$]$^+$ estabilizada por ligandos bifuncionais tridentados com a unidade quelante do tipo pirazolo-diamina (**L1**-**L3**, **L10**-**L12**), sendo a sua fórmula geral apresentada na **Figura 1**.

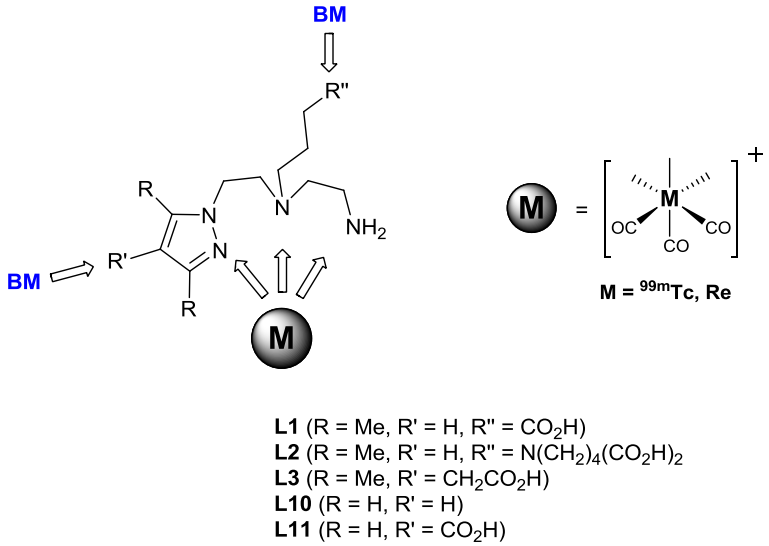


**Figura 1**: Ligandos bifuncionais com a unidade quelante pirazolo-diamina para coordenação ao metal e conjugação a biomoléculas (BM).

Esta unidade é adequada para a estabilização do fragmento organometálico *fac*-$[M(CO)_3]^+$ (M = $^{99m}$Tc, Re), enquanto a presença de grupos carboxilato pendentes permite a conjugação de biomoléculas capazes de reconhecer receptores específicos, nomeadamente o MC1R ou o MR.

Na tentativa de se obterem sondas radioactivas específicas para o MC1R com elevada acumulação no tumor e um perfil farmacocinético adequado, conceberam-se três estratégias que envolveram a preparação de análogos lineares e cíclicos da hormona de estimulação do crescimento dos melanócitos (α-MSH), péptido endógeno cuja principal função está relacionada com a estimulação da melanogénese através de interacção com o MC1R. Como análogo linear da α-MSH considerou-se o **NAPamide** (Ac-Nle-Asp-His-DPhe-Arg-Trp-Gly-Lys-$NH_2$) enquanto que **SNBA-MSH$_{hex}$** (c[S-$NO_2$-$C_6H_3$-CO-His-DPhe-Arg-Trp-Cys]-Lys-$NH_2$), **NNBA-MSH$_{hex}$** (c[NH-$NO_2$-$C_6H_3$-CO-His-DPhe-Arg-Trp-Lys]-Lys-$NH_2$) e o **βAlaNlecycMSH$_{hex}$** (βAla-Nle-c[Asp-His-DPhe-Arg-Trp-Lys]-$NH_2$) foram os análogos cíclicos sintetizados. Na primeira estratégia, descrita no capítulo 2 da tese, prepararam-se conjugados homobivalentes (**L5** e **L6**) e os correspondentes complexos organometálicos do tipo *fac*-$[M(CO)_3(\kappa^3$-**L**$)]^+$ (M = Re/$^{99m}$Tc; **Re5**/**Tc5**, L = **L5**; **Re6**/**Tc6**, L = **L6**) contendo duas unidades do péptido **NAPamide** separadas entre si por uma cadeia de nove (**L5**, **Tc5** e **Re5**) ou catorze atomos (**L6**, **Tc6** e **Re6**). A afinidade dos conjugados homobivalentes para o MC1R (**L5**: $IC_{50}$ = 0.04 ± 0.02 nM e **L6**: $IC_{50}$ = 0.16 ± 0.21 nM) é maior do que a observada

para o composto monovalente (**L4**: $IC_{50}$ = 0.66 ± 0.13 nM) e a sua coordenação à unidade *fac*-$[Re(CO)_3]^+$ não afectou substancialmente a capacidade de reconhecimento do alvo (**Re5**: $IC_{50}$ = 0.15 ± 0.08 nM e **Re6**: $IC_{50}$ = 1.14 ± 1.13 nM). Os radiopéptidos **Tc5** e **Tc6**, preparados por reacção dos conjugados **L5** e **L6** com o precursor *fac*-$[^{99m}Tc(CO)_3(H_2O)_3]^+$, foram caracterizados por comparação, em cromatografia líquida de alta eficiência (HPLC), com os congéneres de rénio **Re5** e **Re6**. Os radiopéptidos apresentaram uma rápida internalização mediada pelo MC1R em células de melanoma murino B16F1. Estudos de biodistribuição em ratinhos com melanoma induzido por células B16F1 revelaram baixa acumulação dos radiopéptidos no tumor (≤ 3.02 ± 0.27 % AI/g) com elevada fixação nos rins (≥ 33.2 ± 3.3 % AI/g), demonstrando que a aproximação bivalente para alvejar o MC1R *in vivo* não é superior à monovalente.

Na segunda estratégia, apresentada no capítulo 3 da tese, prepararam-se análogos da α-MSH ciclizados via ligação tioeter (**SNBA-MSH$_{hex}$**) ou amina (**NNBA-MSH$_{hex}$**) que por conjugação ao ligando bifuncional **L1** originaram os conjugados peptídicos **L7** e **L8**, respectivamente. A conjugação do complexo *fac*-$[Re(CO)_3(\kappa^3$-**L1**$)]^+$ (**Re1**), obtido por reacção de **L1** com *fac*-$[Re(CO)_3(H_2O)_3]^+$, a **SNBA-MSH$_{hex}$** e **NNBA-MSH$_{hex}$** originou os compostos **Re7** e **Re8**, respectivamente. A baixa afinidade demonstrada por estes compostos para o MC1R (**SNBA-MSH$_{hex}$**: $IC_{50}$ = 1800 ± 500 nM; **NNBA-MSH$_{hex}$**: $IC_{50}$ = 51 ± 12 nM; **L7**: $IC_{50}$ = 430 ± 0.1 nM; **L8**: $IC_{50}$ = 179 ± 39 nM; **Re7**: $IC_{50}$ = 690 ± 2.5 nM; **Re8**: $IC_{50}$ = 176 ± 5 nM) reflecte-se também na fraca acumulação no tumor (≤ 2.63 ± 0.5 % AI/g) observada para os radiopéptidos correspondentes **Tc7** e **Tc8** em ratinhos com melanoma induzido por células B16F1. Na tentativa de compreender quais as propriedades estruturais dos derivados peptídicos sintetizados que afectam a capacidade de reconhecimento do receptor, efectuou-se um estudo por espectroscopia de ressonância magnética nuclear (e.g. $^1H$-$^1H$ g-COSY, TCOSY, NOESY). Os resultados obtidos sugerem que a baixa afinidade dos compostos parece estar relacionada com o efeito anisotrópico, uma corrente electrónica que desprotege os protões da cadeia lateral da arginina, aminoácido essencial na interação com o receptor, que, provavelmente limita a interacção com o MC1R. Este efeito foi mais evidente para **SNBA-MSH$_{hex}$**, **L7** e **Re7**. O estudo revelou ainda que a conformação estrutural do péptido **SNBA-MSH$_{hex}$** em solução permanece intacta após conjugação ao quelato bifuncional e coordenação do conjugado resultante à unidade *fac*-$[Re(CO)_3]^+$.

Na terceira estratégia, discutida no capítulo 4, tentámos melhorar o perfil farmacocinético e aumentar a acumulação no melanoma do radiopéptido cíclico baseado no análogo **βAlaNlecycMSH$_{hex}$**. Numa primeira abordagem o péptido **βAlaNlecycMSH$_{hex}$** foi conjugado ao quelato bifuncional **L1** que contém grupos metilo no anel heteroaromático, originando **L9**. Por reacção de **L9** com *fac*-[$^{99m}$Tc(CO)$_3$(H$_2$O)$_3$]$^+$ obteve-se o radiopéptido do tipo *fac*-[$^{99m}$Tc(CO)$_3$($\kappa^3$-**L9**)]$^+$ (**Tc9**) cuja fixação tumoral e o perfil farmacocinético foram avaliado em ratinhos com melanoma induzido por células B16F1. **Tc9** apresentava elevada acumulação no tumor (11.31 ± 1.83 % AI/g) mas também nos orgãos de excreção (rins e fígado), conduzindo a uma relação tumor/orgãos não alvo desfavorável. Na tentativa de melhorar o seu perfil farmacocinético, o péptido **βAlaNlecycMSH$_{hex}$** foi conjugado ao ligando bifuncional com a unidade quelante pirazolo-diamina contendo grupos metilo nas posições 3/5 e um grupo carboxilato na posição 4 do anel heteroaromático (**L3**). O péptido foi ainda conjugado a ligandos do mesmo tipo sem grupos substituintes no anel (**L10**) ou com um grupo carboxilato na posição 4 do anel (**L11**). Os conjugados peptídicos resultantes, **L13 – L15**, apresentaram uma elevada afinidade para o MC1R (**L13**: IC$_{50}$ = 0.02 ± 0.01 nM; **L14**: IC$_{50}$ = 0.04 ± 0.01 nM; **L15**: IC$_{50}$ = 0.16 ± 0.10 nM), comparável à observada para o péptido não conjugado **βAlaNlecycMSH$_{hex}$**. Por reacção de **L13** – **L15** com *fac*-[$^{99m}$Tc(CO)$_3$(H$_2$O)$_3$]$^+$ obtiveram-se os radiopéptidos do tipo *fac*-[$^{99m}$Tc(CO)$_3$($\kappa^3$-**L**)]$^+$ (**Tc13**, L = **L13**; **Tc14**, L = **L14**; **Tc15**, L = **L15**). De salientar que a determinação do coeficiente de partilha num sistema octanol/tampão fosfato (pH 7,4) revelou que os compostos com grupo carboxilato na posição 4 do anel heteroaromático (**Tc14** e **Tc15**) apresentam uma natureza hidrofílica mais acentuada do que **Tc9** e **Tc13**.

Todos os radiopéptidos (**Tc13**-**Tc15**) apresentaram uma captação celular significativa em células de melanoma murino B16F1 (≥ 10.8 ± 0.3 % da actividade total), sendo a sua internalização específica e mediada pelo MC1R.

Estudos de biodistribuição em ratinhos com melanoma induzido por células B16F1 evidenciaram uma elevada acumulação no tumor para **Tc13** – **Tc15** (≥ 9.90 ± 1.10 AI/g, 1h p.i.). Destes radiopéptidos, os que possuem o grupo carboxilato no anel heteroaromático, **Tc14** e **Tc15**, apresentaram um perfil farmacocinético mais favorável pois foram rapidamente excretados, não se acumulando nos orgãos de excreção (rins e fígado). Este comportamento permitiu gerar imagens de grande contraste por tomografia

por emissão de fotão único (SPECT) para detecção do melanoma em ratinhos (**Figura 2**).

**Tc14** **Tc15**

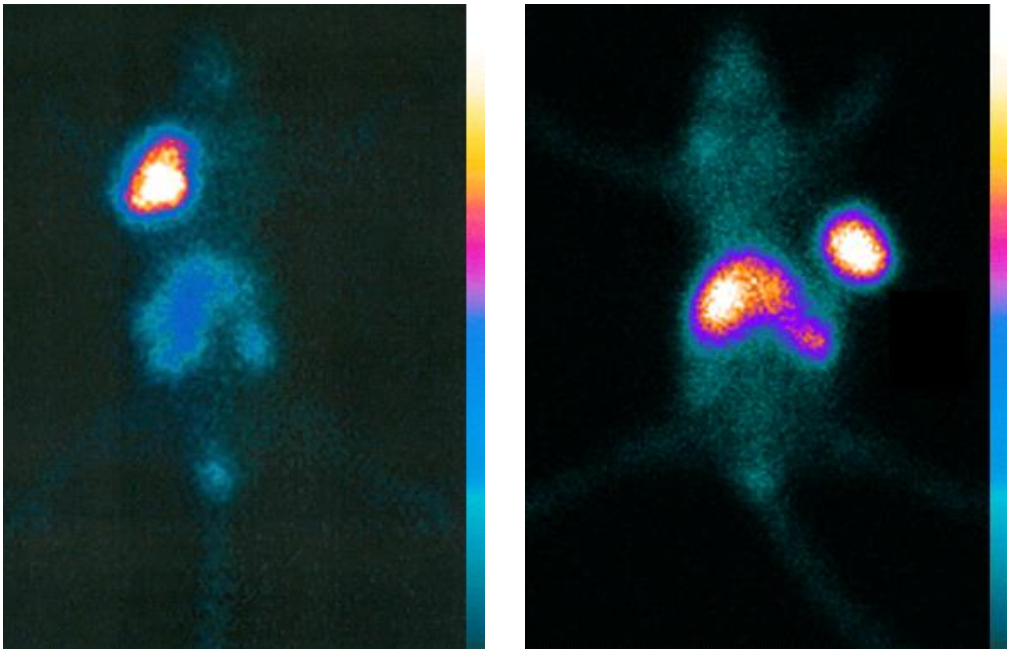

**Figura 2**: Imagens planares cintigráficas de ratinhos com melanoma induzido por células B16F1 injetados com **Tc14** e **Tc15**.

Em conclusão, das três estratégias apresentadas, esta última foi a que apresentou resultados mais promissores, sendo os compostos **Tc14** e **Tc15** potencialmente úteis para imagiologia do melanoma em humanos.

No capítulo 5 desta tese descreve-se a síntese e a caracterização de conjugados poliméricos de dextrano potencialmente úteis para a detecção de MR expressos em macrófagos no gânglio sentinela. Os conjugados **L18** e **L19** contêm, respectivamente, 4 e 8 unidades quelantes do tipo pirazolo-diamina/mol dextrano para estabilização do fragmento organometálico *fac*-$[M(CO)_3]^+$ (M = Re, $^{99m}$Tc), bem como 13 unidades manose/mol dextrano para detecção específica *in vivo* dos MR por SPECT. Preparou-se ainda o conjugado polimérico **L20** por conjugação de 3 ± 1 unidades de um fluoróforo a **L19**. O conjugado resultante foi utilizado para preparar uma sonda bimodal para detecção dos MR *in vivo* por SPECT e imagiologia óptica na região do infravermelho próximo.

Da reacção dos conjugados macromoleculares com os respectivos precursores organometálicos obtiveram-se compostos do tipo *fac*-$[M(CO)_3(\kappa^3\text{-}\mathbf{L})]^+$ (M = Re/$^{99m}$Tc;

**Re18**/**Tc18**, L = **L18**; **Re19**/**Tc19**, L = **L19**; **Re20**/**Tc20**, L = **L20**). A natureza isoestrutural destes compostos foi confirmada por comparação do perfil cromatográfico (HPLC) dos polímeros radioactivos com os respectivos congéneres de rénio. A caracterização física de **L18** – **L20** e **Re18** – **Re20** através da técnica de dispersão de luz dinâmica (DLS) revelou que o diâmetro hidrodinâmico dos compostos aumenta de acordo com a funcionalização do polímero, apresentando os conjugados **L18** – **L20** dimensões que variam entre 7,0 e 17,7 nm e os seus análogos metálicos **Re18** – **Re20** entre 8,4 e 22,5 nm.

As sondas radioactivas **Tc18** e **Tc19** apresentaram uma captação significativa no primeiro gânglio linfático (≥ 3.87 ± 0.63 % AI/orgão) com uma acumulação mínima nos tecidos não alvo (≤ 1.81 ± 0.46 % AI/orgão) em ratos Wistar. Estes compostos apresentaram igualmente uma retenção específica e prolongada no primeiro gânglio linfático, mediada pelo MR.

A sonda bimodal **Tc20** apresentou valores elevados para a extracção do primeiro gânglio linfático e semelhantes a **Tc19** em ratos Wistar, permitindo a visualização do gânglio sentinela por SPECT e imagiologia óptica (**Figura 3**).

**A** **B**

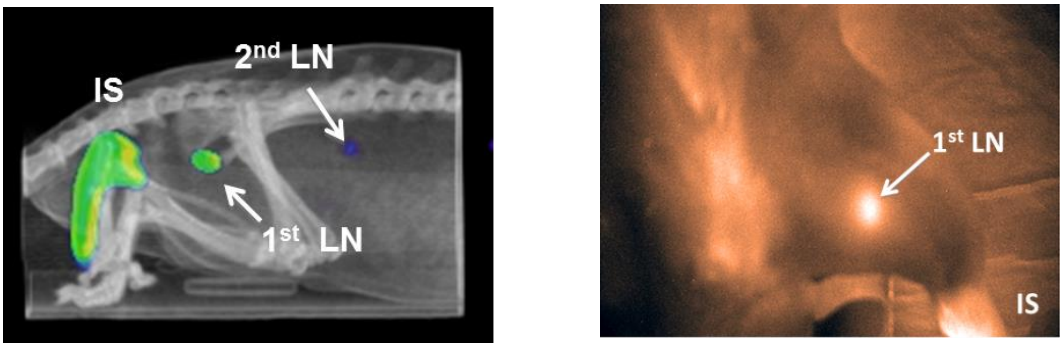


**Figura 3**: Imagens obtidas após injecção de **Tc20** em rato Wistar; A) Fusão de imagem de SPECT com tomografia computorizada; B) imagem de fluorescência na região do infravermelho próximo. IS, local de injeção; 1st LN, gânglio linfático poplíteo; 2nd LN, gânglio linfático inguinal.

Em conclusão, o desenvolvimento de nanopartículas radioactivas contendo unidades manose apresentam resultados promissores para a detecção do gânglio sentinela por SPECT e/ ou imagiologia óptica, sendo os compostos **Tc19** e **Tc20** promissores para futura avaliação biológica em humanos.

**Abstract**

The work described in this thesis aimed at the development of M(I) (M = $^{99m}$Tc, Re) specific probes for the detection of malignant melanoma and sentinel lymph node (SLN) through the *in vivo* targeting of membrane receptors. In the former case we have designed $M(CO)_3$-complexes stabilized by tridentate chelators containing a pyrazolyl-diamine chelating unit (*N*,*N*,*N* donor atom set) and pendant α-melanocyte-stimulating hormone (α-MSH) derivatives for targeting the melanocortin receptor 1 (MC1R), which is overexpressed in melanotic and amelanotic human melanoma cells. Among the various strategies described herein to improve both the MC1R targeting properties and the biological profile of $^{99m}$Tc-labeled α-MSH analogs, the **chapter 2** of this thesis focus on the design of homobivalent constructs containing two copies of a linear α-MSH analog (**NAPamide**) separated by linkers of different nature (**L5**, *symmetric* alkyl chain; **L6**, *asymmetric semirigid* spacer) and length (**L5**, 9 atoms; **L6**, 14 atoms). The MC1R-binding affinity of both peptide conjugates is significantly higher than that of the monovalent conjugate **L4**. Metallation of **L4 - L6** yielded complexes of the type *fac*-$[M(CO)_3(\kappa^3\text{-}\mathbf{L})]^+$ (M = $^{99m}$Tc/Re; **Tc4**/**Re4**, L = **L4**; **Tc5**/**Re5**, L = **L5**; **Tc6**/**Re6**, L = **L6**), with the rhenium compounds presenting $IC_{50}$ values in the sub- and nanomolar range, which are still better than or comparable to the $IC_{50}$ values of the non-conjugated **NAPamide**. The MC1R-mediated internalization of **Tc5** and **Tc6** in B16F1 melanoma cells is higher than that of **Tc4**. However, biodistribution studies in melanoma-bearing mice have shown low tumor uptake and significant accumulation of radioactivity in kidneys. Moreover, no correlation between tumor uptake and valency was found.

**Chapter 3** describes novel peptide conjugates (**L7** and **L8**), which contain a thioether (**SNBA-MSH$_{hex}$**) or amine (**NNBA-MSH$_{hex}$**) bridge-cyclized α-MSH analog, respectively, and a pyrazolyl-diamine chelating unit. Metallation of **L7** and **L8** gave complexes of the type *fac*-$[M(CO)_3(\kappa^3\text{-}\mathbf{L})]^+$ (M = $^{99m}$Tc/Re; **Tc7**/**Re7**, L = **L7**; **Tc8**/**Re8**, L = **L8**). Competitive binding affinity assays demonstrated that the compounds containing the alkylamine bridge-cyclized peptide moiety present lower $IC_{50}$ values than the one cyclized via the alkylthioaryl bridge. NMR structural analysis suggested that such difference could be ascribed to an anisotropic effect arising from the interaction between the Arg side chain and the surrounding aromatic residues in the pharmacophore sequence (His-DPhe-Arg-Trp) of **SNBA-MSH$_{hex}$**, hampering a favorable interaction of the peptide with the MC1R. NMR studies have also shown that the three-dimensional

structural features of the peptide moiety were conserved upon conjugation to the chelator and, most importantly, after metallation.

The **chapter 4** of this thesis reports the impact of pyrazolyl-diamine chelators with different azolyl-ring substitution patterns (carboxylate at the 4-position and methyl groups at the 3,5 positions, **L3**; no substituent groups, **L10**; carboxylate at the 4-position, **L11**) on the MC1R-targeting properties and pharmacokinetic profile of a $^{99m}Tc(CO)_3$-labeled lactam bridge-cyclized α-MSH analog (**βAlaNleCycMSH$_{hex}$**). Conjugation of those bifunctional chelators to **βAlaNleCycMSH$_{hex}$** yielded the peptide conjugates **L13** – **L15**, which upon reaction with *fac*-$[^{99m}Tc(CO)_3(H_2O)_3]^+$ gave the (radio)metallated compounds **Tc13 – Tc15**. Biodistribution studies in murine melanoma-bearing mice have shown that all radiopeptides (**Tc13** – **Tc15**) presented a good melanoma uptake (≥ 9.90 ± 1.10 % IA/g). The introduction of a carboxylate group in the azolyl-ring lead to a remarkable reduction of kidney (> 89 %) and liver (> 91 %) uptake for **Tc14** and **Tc15**, respectively, when compared to the lead radiopeptide **Tc9**, which has methyl groups at the 3,5 positions of the azolyl-ring. The remarkable tumor uptake and favorable tumor/non-target organs ratios of **Tc14** and **Tc15** highlights the potential of both compounds as melanoma imaging agents.

**Chapter 5** reports the design, characterization and biological evaluation of mannosylated dextran derivatives with pyrazolyl-diamine chelating units for sentinel lymph node detection (SLND) through mannose receptor (MR) targeting. The mannosylated dextran derivatives **L18** and **L19** contain, respectively, 4 and 8 chelating units per mol of dextran to stabilize the *fac*-$[M(CO)_3]^+$ moiety (M = Re, $^{99m}Tc$), as well as 13 mannose units per mol of dextran for MR targeting. A bimodal probe for SLND by SPECT and optical imaging in the near infrared (NIR) field is also reported in chapter 5. **L20** was prepared by conjugation of 3 to 4 fluorophore units to **L19**. Metallation of **L18 – L20** gave polymeric complexes of the type *fac*-$[M(CO)_3(\kappa^3\text{-}\mathbf{L})]^+$ (M = $^{99m}$Tc/Re; **Tc18**/**Re18**, L = **L18**; **Tc19**/**Re19**, L = **L19**; **Tc20**/**Re20**, L = **L20**). Physical characterization of the mannosylated dextran derivatives has shown that the hydrodynamic diameter and the zeta potencial of the nanoparticles were affected by chemical modification. Indeed, the hydrodynamic diameter of **L18** – **L20** are within the range of 7.0 to 17.7 nm while the diameter of the respective metallated compounds (**Re18** – **Re20**) is slightly higher, within the range 8.4 to 22.5 nm.

Biological evaluation of the polymeric radiotracers in Wistar rats has shown a good accumulation in the popliteal (sentinel) node at 1 h p.i. (6.71 ± 2.35 % IA/organ,

**Tc18**; and 7.53 ± 0.69 % IA/organ, **Tc19**), with significant retention up to 3 h, which is mediated by MR. The high popliteal extraction value of **Tc19** (94.47 ± 2.45 % at 1 h p.i.) highlights its potential as a very promising radiotracer to be further explored as SLN imaging agent in humans. The biological evalution of **Tc20** has shown that the incorporation of a fluorophore into the nanoparticle did not not alter the pharmacokinetic properties of the bimodal probe as compared to the radiotracer **Tc19**. In fact, **Tc20** and **Tc19** presented high popliteal extraction value (89.66 ± 0.03 % and 87.81 ± 3.75 %, respectively) at 3 h p.i. Furthermore, the biological evaluation of **Tc20** demonstrated a perfect coregistration of the two signals, allowing nuclear and optical imaging techniques to complement each other in the detection and excision of the popliteal lymph node.

**Palavras-Chave**

Re/$^{99m}$Tc-tricarbonilo
Receptor da Melanocortina do Sub-tipo 1 (MC1R)
Detecção Gânglio Sentinela
Tomografia por Emissão de Fotão Único (SPECT)
Imagiologia Óptica

**Keywords**

Re/$^{99m}$Tc-tricarbonyl
Melanocortin-1 Receptor (MC1R)
Sentinel Lymph Node Detection (SLND)
Single Photon Emission Computed Tomography (SPECT)
Optical Imaging

**Table of Contents**

**Figures**

**Tables**

**Schemes**

## Abbreviations

**A**

AAT = Amino acid transporter

Ac = Acetyl

$Ac_2O$ = Acetic anhydride

ACTH = Adrenocorticotropic hormone

AFM = Atomic Force Microscopy

Arg or R = Arginine

Asp or D = Aspartic acid

AuNP = Gold nanoparticle

ATC = Anatomical Therapeutic Chemical classification system

ALND = Axillary-lymph-node dissection

**B**

BFC = Bifunctional chelator

Boc = *Tert*-butoxycarbonyl

BP = Bisphosphonate

Bq = Becquerel

br = Broad

BM = Biomolecule

BBB = Blood brain barrier

**C**

ca. = circa

cAMP = Cyclic Adenosine Monophosphate

CBTE2A = 4,11-bis(carboxymethyl)-1,4,8,11-tetraazabicyclo[6.6.2]hexadecane

CCD = Charge-Coupled-Device

CXCR4 = Chemokine (C-X-C motif) receptor 4

Ci = Curie (1 Ci = $3.7 \times 10^{10}$ Bq)

Cys or C = Cysteine

COSY = Correlation Spectroscopy

CT = Computed Tomography

CTN = Campus Tecnológico e Nuclear

Cpm = Counts per minutes

**D**

d = Doublet

dd = Doublet of doublets

DPhe or f = D-Phenylalanine

D3R = Dopamine D3 receptor

DCM = Dichloromethane

DIPEA = *N*,*N*-Diisopropylethylamine

DLS = Dynamic Light Scattering

DMF = *N*,*N*-Dimethylformamide

Dmab = 4-(N-[1-(4,4-dimethyl-2,6-dioxocyclohexylidene)-3-methylbutyl]amino)benzyl

DMSA = Dimercaptosuccinic acid

DMSO = Dimethylsulfoxide

DOPA = Dihydroxyphenylalanine

DOTA = 1,4,7,10-tetraazacyclo-dodecane-1,4,7,10-tetraacetic acid

DTPA = Diethylenetriaminepentaacetic acid

DMEM = Dulbecco's Modified Eagle's Medium

DSS = Sodium 2,2-dimethyl-2-silapentane-5-sulfonate

**E**

e.g. = exempli gratia

EL = extracellular loop

EMA = European Medicines Agency

ESI = Electrospray ionization

EtOH = Ethanol

ECD = Ethylenecysteine diester

**F**

FBZA = Fluorobenzamide

f = D-Phenylalanine

FDA = Food and Drug Administration

FDG = Fluorodeoxyglucose

FLT = Fluorodeoxy-L-thymidine

FMISO = Fluoromisonidazole

*fac* = Facial

**G**

GalNAc = Acetylgalactosamine

Glu or E = Glutamic acid

GLUT = Glucose transporter

Gly or G = Glycine

GPCR = G protein-coupled receptor

**H**

h = Hour

HATU = 2-(7-Aza-1H-benzotriazole-1-yl)-1,1,3,3-tetramethyluronium hexafluorophosphate

His or H = Histidine

HBTU = O-Benzotriazole-N,N,N′,N′-tetramethyl uroniumhexafluoro phosphate

HPLC = High-performance liquid chromatography

HMPAO = Hexamethyl-propylene-amine oxime

HMW-MAA or HMP = high molecular weight melanoma associated antigen

HYNIC = 6-Hydrazinopyridine-3-carboxylic acid

HSA = Human Serum Albumin

HSQC = Heteronuclear Single Quantum Coherence Spectra

**I**

IME-thiomannose = 2-imino-2-methoxethyl-1-thio-β-D-mannoside

ivDde = 1-(4,4-Dimethyl-2,6-dioxocyclohex-1-ylidene)-3-methylbutyl

IA = Injected Activity

IL = Intracellular loop

ICG = Indocyanine green

IR = Infrared

IST = Instituto Superior Técnico

ITLC = Instant Thin-Layer Chromatography

**K**

keV = kilo-electronvolt

kg = kilogram

**L**

Lys or K = Lysine

LET = Linear energy transfer

$P_{o/w}$ = Partition coefficient Octanol/water

LDV = Laser Doppler Velocimetry

**M**

m (IR spectroscopy) = Medium

m (NMR spectroscopy) = Multiplet

$MAG_2$ = 2-Mercaptoacetylglycylglycyl

$MAG_3$ = Mercaptoacetyl-triglycine

MCR = Melanocortin receptor

MC1-5R = Melanocortin 1-5 receptor

MDP = Methylenediphosphonate

Me = Methyl

MeV = Mega-electronvolt

MR = Mannose receptor

min = Minute

MS = Mass spectrometry

MSA = Mannosylated human serum albumin

MRI = Magnetic Resonance Imaging

Mtt = 4-methyltrityl

$^{99}Mo$ = Molibdenium-99

M.W. = Molecular Weight

**N**

n.c.a. = non carrier added

nd = not determined

nm = nanometer

NIR = Near-infrared

NOE = Nuclear Overhauser effect

NOESY = Nuclear Overhauser Effect Spectroscopy

NOTA = Triazacyclononane-1,4,7-triacetic acid

NMR = Nuclear Magnetic Resonance

NMP = *N*-methylpyrrolidone

NMDAR = N-methyl-D-aspartate receptor

**P**

$pNO_2$-BenzAcid = 2-fluoro-5-nitrobenzoic acid

Pbf = pentamethyl-2,3-dihydrobenzofuran-5-sulfonyl

PBS = Phosphate buffered saline

PET = Positron Emission Tomography

Phe or F = L-Phenylalanine

p.i. = Post injection

POMC = Pro-opiomelanocortin

ppm = Part per million

Pz = Pyrazolyl-diamine chelating unit

**Q**

q = Quartet

**R**

RC = Random Coil

RGD = Arginine-Glycine-Aspartic acid

RP = Reversed phase

rpm = rotation per minute

ROE = Rotating Frame Overhause Effect

ROESY = Rotating-frame Nuclear Overhauser Effect Correlation Spectroscopy

r.t. = room temperature

**S**

s (IR spectroscopy) = strong

s (NMR spectroscopy) = singlet

SC = sulfur colloid

SLN = Sentinel lymph node

SLNB = Sentinel lymph node biopsy

SLND = Sentinel lymph node detection

SPECT = Single Photon Emission Computed Tomography

SPPS = Solid Phase Peptide Synthesis

S.D. = Standard deviation

**T**

t = Triplet

$t_{1/2}$ = Half-life

*t*-Bu = *tert*-butyl

TCOSY = Total Correlated Spectroscopy

TFA = Trifluoroacetic acid

THF = Tetrahydrofuran

TIS = Triisopropylsilane

$t_R$ = Retention time

Trt = trityl

TM = transmembrane

TMS = Tetramethylsilane

Trp or W = Tryptophan

TLC = Thin-Layer chromatography

**U**

US - Ultrasound

U.V. - Ultraviolet

**V**

vs = Very strong

**W**

w = Weak

**Y**

y = Year

Å = angstrom

α-MSH = α-Melanocyte-Stimulating Hormone

α = Alpha

β = Beta

$\beta^+$ = Positron

γ = Gamma

κ = Denticity

δ = Chemical shift

ν = Frequency

## Scope and Aim

Henri Becquerel discovered the natural radioactivity in potassium uranyl sulphate in 1896. Almost fourty years later, Irene Curie and Frederic Joliot were the first to report artificial radioactivity, identifying positron-emitting elements from the bombardement of aluminum, boron, and magnesium targets with alpha particles from polonium.

In the advent of these discoveries, George de Hevesy developed the fundamental principles for the use of radioactive tracers to study physiological and chemical processes.[1] However, only after major scientific and technological advances in radioisotope production, imaging instrumentation and biology, those principles were extended to the visualization of biological functions associated with a wide range of pathologies, namely neurological disorders, cardiovascular diseases and cancer.

Positron Emission Tomography (PET) and Single Photon Emission Computed Tomography (SPECT) are nowdays the embodiment of this concept, allowing quantitative tracing of biochemical processes *in vivo*. This is only possible because radioactive probes can be synthesized at high specific activity, enabling the use of tracer concentrations to detect small-capacity molecular systems *in vivo* (e.g. cell surface receptors, transporters, etc.) without interfering with the processes under study.[2]

Despite remarkable advances, the design of specific probes for targeted imaging or therapy remains still a great challenge and a demanding task within the field of radiopharmaceutical sciences. This is a multidisciplinary research area, which profits from the input of chemists, radiochemists, radiopharmacists and clinicians. One of the major challenges facing nuclear molecular imaging is the early detection and quantification of biochemical and metabolic changes at the molecular and cellular level that precede morphological changes, allowing early diagnosis of diseases. To achieve this goal, the design of new radioactive probes with high specificity and molecular affinity for recognition of particular targets associated to certain disease states is mandatory.

Within this framework, the goal of this thesis is to contribute for the design of $^{99m}Tc(CO)_3$-based probes for imaging of membrane receptors, namely the overexpressed melanocortin receptor 1 (MC1R) in malignant melanoma, and the mannose receptor (MR) expressed by macrophages in the lymph nodes. Whereas in the former case, new tracers would allow early detection of a particularly aggressive type of

skin cancer and associated metastasis, in the latter case it would allow the detection of sentinel lymph node (SLN), which is a relevant procedure in medicine.

The thesis is organized in seven chapters. A general introduction to imaging in oncology and radiopharmaceuticals, as well as on melanoma-targeting probes and sentinel lymph node detection (SLND) is presented in the **first chapter**. **Chapters 2 – 4** are dedicated to the design and biological evaluation of $^{99m}Tc(CO)_3$-labeled α-melanocyte-stimulating hormone (α-MSH) analogs for MC1R targeting. In an attempt to improve melanona imaging, homobivalent contructs containing two copies of a linear α-MSH analog (**NAPamide**) are described in **chapter 2**. The **third chapter** reports on the synthesis of novel cyclic α-MSH analogs. Moreover, a study by nuclear magnetic resonance (NMR) spectroscopy is performed to establish a preliminary correlation between the receptor-targeting properties of the peptide derivatives and their structural features in solution. **Chapter 4** describes the improvement of the overall biological profile of a $^{99m}Tc(CO)_3$-labeled lactam bridge-cyclized α-MSH analog (**βAlaNleCycMSH$_{hex}$**) as a function of the structural modifications in the ring substitution pattern of the pyrazolyl-diamine chelating unit. **Chapter 5** is dedicated to the design, macroscopic characterization and biological evaluation of $^{99m}Tc(CO)_3$-labeled mannosylated dextran-based nanoparticles for MR-targeting in SLND. Furthermore, a bimodal probe was also synthesized for SLND by SPECT and optical imaging in the near infrared (NIR) field. Concluding remarks and future work are presented in **chapter 6**. Finally, in **chapter7** it is described the experimental details of the work presented in **chapters 2 – 5**.

# 1

# INTRODUCTION

# 1. Introduction

## 1.1. Imaging in Oncology

Imaging, one of the main pillars of comprehensive cancer, allows screening and provides significant information during all phases of disease management.[3] Indeed, the use of imaging techniques enables cancer screening programs with improved outcome in cancer detection among population. Moreover, cancer patients undergo a number of different imaging studies throught the course of their disease. The role of imaging in cancer management is shown in **Figure 1.1**.

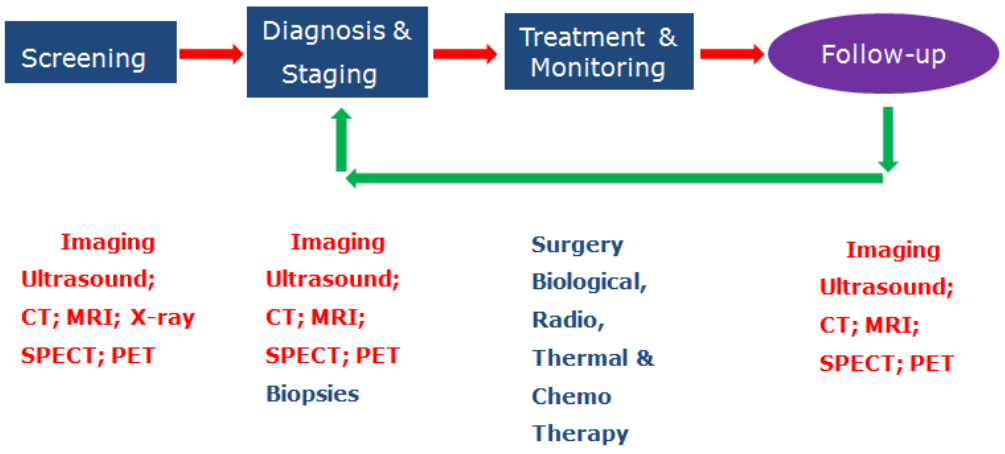


**Figure 1.1**: Current role of cancer imaging in cancer management.[3]

Clinical decision-making is based on the information of multiple non-invasive imaging modalities such as the nuclear techniques Single Photon Emission Computed Tomography (SPECT) and Positron Emission Tomography (PET), X-ray, Magnetic Resonance Imaging (MRI), Computed Tomography (CT) and Ultrasound (US).[4]

These imaging modalities can be included into two large categories: structural and functional imaging. Structural imaging techniques such as X-ray, CT and MRI provide anatomical details on tumor location, size, morphology, and structural changes to adjacent tissues.[4a] Functional imaging, rather than anatomical, aims at the visualization and characterization of biochemical pathways, molecular interactions, drug pharmacokinetic and pharmacodynamics. SPECT and PET are currently accepted as the most important functional imaging techniques. Examples of images obtained with all the imaging techniques referred above are shown in **Figure 1.2**.[2, 4]

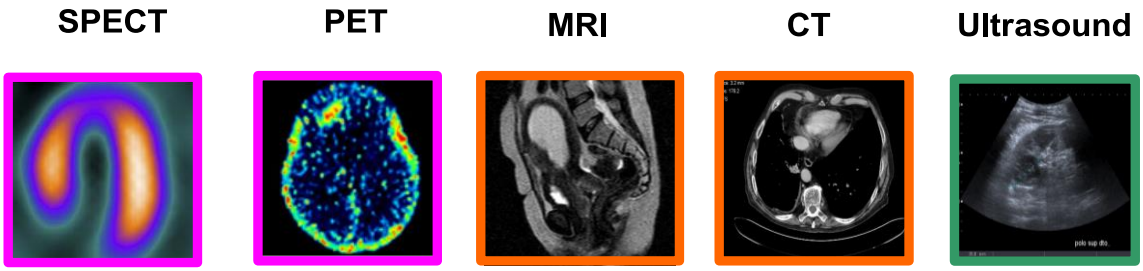


**Figure 1.2**: Examples of images obtained with SPECT, PET, MRI, CT and US techniques, adapted from Weissleder et al.[2]

Despite unlimited depth penetration and exquisite sensitivity due to the ability to image tissues with micro- to picomolar concentrations of a radioactive tracer, nuclear imaging techniques present low spatial resolution and inability to provide anatomical detail.[4a, 5] These issues were addressed by the introduction of dual modality imaging techniques, mainly nuclear-computed tomography fusion systems (PET/CT and SPECT/CT), that maximized their separate strengths and provide anatomical localization of biochemical processes with detailed visualization of the tumor structure. **Table 1.1** summarizes the most relevant characteristics of the imaging modalities mentioned above, including the major strenghts and weaknesses.

**Table 1.1:** Relevant characteristics of the imaging modalities used in the clinical set.[5a]

| Technique | Spatial Resolution | Amount of probe used | Main use | Advantages | Disadvantages |
|---|---|---|---|---|---|
| SPECT | 1-2 mm | ng | Metabolic | High sensitivity, quick, easy, low cost, relative high throughput | Low spatial resolution |
| PET | 1-2 mm | | | High sensitivity, isotopes can substitute naturally occurring atoms | Cyclotron needed and low spatial resolution |
| MRI | 10-100 µm | mg-µg | Anatomical, physiological, metabolic | High spatial resolution, combines morphological and functional imaging | Low sensitivity, amount of probe |
| CT | 50 µm | Not applicable | Anatomical, physiological | Bone and tumor imaging, anatomical imaging | Limited soft tissue resolution |
| US | 50–500 µm | mg-µg | Morphological | Easy-to-use and less expensive than other imaging methods | Limited spatial resolution |

The advances in imaging instrumentation changed the paradigm of oncological imaging from lesion measurement to lesion characterization and target quantification. Another contribution to this revolution is based on the decoding of the human genome and

developments in proteomics, which enabled the identification of a new spectrum of targets (e.g. cell membrane receptors, enzymes, genes, etc.) linked to various oncological pathologies. The possibility to visualize biomolecules or biochemical processes associated to oncological pathologies, through the interaction of a target molecule with a molecular probe will improve the ability to non-invasively detect and characterize disease processes, select the correct treatment (personalized medicine) and follow therapeutical responses.

Taken together, the technical and scientific advances prompt the design of novel radiopharmaceuticals that might enable the developement and optimization of new therapeutics as well as an early detection of cancer, which is most likely the major contribution of nuclear molecular imaging techniques to reduce the mortality of certain cancers.[3, 6]

## 1.2. Nuclear Medicine and Radiopharmaceuticals

Nuclear medicine is a medical specialty that uses radiopharmaceuticals for diagnosis and treatment of diseases.

Radiopharmaceuticals are drugs containing a radionuclide in its composition and must comply with all quality requirements applied to medicines in order to be routinely used for the diagnostic (ATC code V09) or therapy (ATC code V10) of various diseases.[7] These medicines are used in tracer quantities ($10^{-6}$ – $10^{-8}$ M), and are not intended to have any pharmacological action in the classical sense. Almost all radiopharmaceuticals are administered via intravenous injection but they can also be administered orally (e.g. $Na^{131}I$ capsules) or by inhalation (pulmonary ventilation).[8]

From the chemical point of view, radiopharmaceuticals can be inorganic salts (e.g. $Na^{131}I$ and $Na^{18}F$), small organic molecules (e.g. $^{18}FDG$), and inorganic or organometallic complexes, which may contain or not a biologically active molecule for targeting. The latter can be a monoclonal antibody, a small peptide, and inhibitors or substrates of enzymes, among others. Currently, the majority of radiopharmaceuticals in the clinical set are still based on radiometals, with $^{99m}Tc$ accounting for more than 90 % of all nuclear medicine procedures worldwide.[9]

These imaging agents are roughly divided into two main categories: perfusion and target-specific agents. The pharmacokinetic profile of the perfusion radiopharmaceuticals, namely of those based on metals (**Figure 1.3 A**), is determined

mainly by their chemical and physical properties (e.g. molecular weight, charge and lipophilicity). In the case of the target-specific agents, the biodistribution is influenced not only by the physicochemical properties, but also by the nature of the bioactive pendant molecule, which must interact specifically with the desired target. In general, metal-based target-specific radiopharmaceuticals comprise a radiometal stabilized by a bifunctional chelator (BFC), a spacer, and a targeting biomolecule (**Figure 1.3 B**).

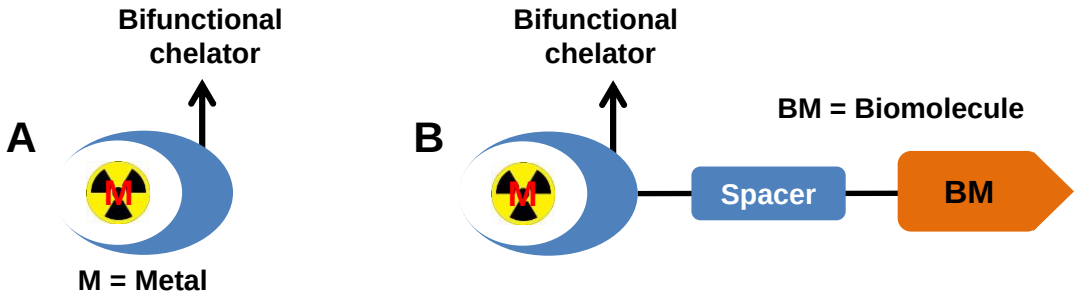


**Figure 1.3**: Schematic representation of a perfusion (A) and targeted (B) specific metal-based radiopharmaceutical.[10]

### 1.2.1. Diagnosis *versus* Therapy

The radionuclide present in a radiopharmaceutical is an unstable nuclide, which undergoes a radioactive decay emitting gamma rays (γ) and/ or subatomic particles (α, $\beta^-$, $\beta^+$, and Auger electrons).[7] Depending on the medical application, diagnosis or therapy, different physical properties are required for the radionuclide. Among these properties, the type and energy of the emitted radiation as well as the half-life ($t_{1/2}$) of the nuclide are the most important for selection of a suitable radionuclide to the desired medical application. Thus, a radiopharmaceutical for diagnosis contains a positron- ($\beta^+$) or gamma- (γ) emitting radionuclide of sufficiently high energy (> 50 keV) in their composition, which after administration and distribution accumulates in the target organ or tissue.[7] The physicochemical and biological properties of the radiopharmaceutical determine its differential uptake and clearance between normal and diseased tissues whereas external detection of the radiation allows the construction of an image.[11] Such detection and image construction can be attained by the nuclear imaging techniques SPECT and PET. Whereas SPECT scanners detect γ rays emitted by radiopharmaceuticals containing γ-emitting radionuclides, PET scanners detect two high

energy (511 keV) antiparallel photons that result from the annihilation of a $\beta^+$ emitted by the radiopharmaceutical with an electron.[12]

As mentioned earlier, the clinical availability of bimodal imaging by SPECT/CT and PET/CT enhanced both sensitivity and specificity of this non-invasive diagnostic approach to patients with various disorders. Thus, SPECT or PET and, simultaneously, X-ray CT images are acquired together providing functional/molecular information along with anatomical information.[11, 13] **Figure 1.4** displays examples of images obtained by SPECT/CT.

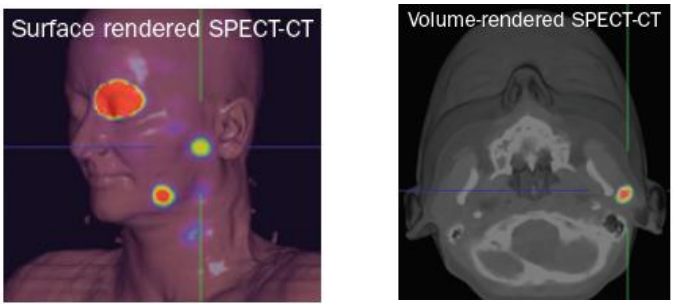


**Figure 1.4**: Example of $^{99m}$Tc-colloids SPECT/CT images for sentinel lymph node detection.[14]

Although SPECT imaging has lower detector sensitivity and less quantitative accuracy than PET, it has broader clinical applications.[14] Unlike PET, the radioisotopes used in SPECT have longer half-life and therefore can be produced away from the site of administration and transported whenever required.[14] Moreover, the detection period can be widened, allowing the observation of biological processes *in vivo* over several hours or days after the administration of the radioactive probe.[15]

The γ-emitting radionuclides with the most suited characteristics for SPECT imaging are $^{99m}$Tc ($t_{1/2}$ = 6.02 h, Eγ(max) = 140 keV), $^{123}$I ($t_{1/2}$ = 13.20 h, Eγ(max) = 159 keV), $^{67}$Ga ($t_{1/2}$ = 78.26 h, Eγ(max) = 296 keV), $^{201}$Tl ($t_{1/2}$ = 72 h, Eγ(max) = 167 keV) and $^{111}$In ($t_{1/2}$ = 67.9 h, Eγ(max) = 245 keV).

The $\beta^+$-emitting radioisotopes used in PET imaging are in general short-lived non-metallic isotopes, such as $^{18}$F ($t_{1/2}$ = 109.8 min, $E_{\beta^+}$ (max) = 202 keV), $^{11}$C ($t_{1/2}$ = 20.4 min, $E_{\beta^+}$(max) = 326 keV), $^{15}$O ($t_{1/2}$ = 2.03 min, $E_{\beta^+}$(max) = 650 keV), and $^{13}$N ($t_{1/2}$ = 9.98 min, $E_{\beta^+}$(max) = 432 keV). These radioactive elements can replace the natural

elements in biologically active molecules, without disturbing significantly their activity and function. Fluorine has been explored as a suitable bioisostere for hydrogen because both elements display similar atomic radius. As an example, [$^{18}$F] 2-fluoro-2-deoxy-D-glucose ([$^{18}$F]-FDG) is the most widely used positron-emitting radiopharmaceutical for PET imaging, making $^{18}$F the most used radionuclide in this nuclear imaging technique. [$^{18}$F]-FDG has also shown clinical usefulness in cardiology and neurology but is used mainly in oncology, in the diagnosis, staging and post-therapy evaluation.[16]

Most PET radionuclides have the disadvantage of requiring costly technology, namely cyclotrons for their production and sophisticated automated methods for the radiosynthesis of the radiopharmaceuticals. Owing to the short half-life of most $\beta^+$-emitting radioisotopes, the production and synthesis must occur close to the administration site. A few $\beta^+$-emitting radiometals such as $^{64}$Cu ($t_{1/2}$ = 12.7 h, $E_{\beta}^{+}$(max) = 660 keV) and $^{68}$Ga ($t_{1/2}$ = 1.1 h, $E_{\beta}^{+}$(max) = 1899 keV) are also of great interest for developing new PET radiopharmaceuticals, due to their physicochemical properties, and the latter radiometal deserves special attention because of its availability from a long-lived $^{68}$Ge/$^{68}$Ga generator system.[8, 10-11, 17]

Radiopharmaceuticals for systemic radiotherapy have in their composition a radionuclide that emits ionizing radiation with a high linear energy transfer (LET) to destroy selectively cells or tissues.[10] The most used radionuclides are $\beta^-$ emitters, but intense research involving α- and Auger electron emitters is also underway. These particles have different ranges in the tissues and can be described by the amount of transfered kinetic energy as a function of distance.

The selection of a radionuclide for therapy depends not only on the type, energy, half-life and range of emitted particles, but also on the size of the tumor or tissue to irradiate and treat. Since the penetration depth range of $\beta^-$ particles in biological tissues is relatively long (0.1 – 10 mm), radiopharmaceuticals containing $\beta^-$-emitting radionuclides can be used for the treatment of large solid tumors.[18] Among $\beta^-$-emitting radionuclides with potential application, $^{131}$I ($t_{1/2}$ = 8.0 d, $E_{\beta}^{-}$(max) = 0.81 MeV, $E_{\gamma}$(max) = 0.364 MeV), $^{153}$Sm ($t_{1/2}$ = 1.9 d, $E_{\beta}^{-}$(max) = 0.8 MeV, Eγ(max) = 0.103 MeV), $^{90}$Y ($t_{1/2}$ = 2.7 d, $E_{\beta}^{-}$(max) = 2.27 MeV), $^{186}$Re ($t_{1/2}$ = 3.8 d, $E_{\beta}^{-}$(max) = 1.07 MeV, Eγ(max) = 0.137 MeV), and, more recently, $^{188}$Re ($t_{1/2}$ = 0.7 d, $E_{\beta}^{-}$(max) = 2.10 MeV, Eγ(max) = 0.155 MeV), are used in the clinical set for the treatment of different tumor types. Moreover, $^{177}$Lu ($t_{1/2}$ = 6.7 d, $E_{\beta}^{-}$(max) = 0.497 MeV, Eγ(max) = 0.208 MeV) and

$^{166}$Ho ($t_{1/2}$ = 1.1 d, $E_{\beta^-}$(max) = 1.86 MeV, Eγ(max) = 0.081 MeV) have been fully explored both at the preclinical and clinical levels as bone palliative agents and for peptide receptor radionuclide therapy in the case of $^{177}$Lu-labeled somatostatin analogs.[18b, 19]

The α particles are heavy and charged helium nuclei with high LET. These particles "travel" only short distances and cause the most ionizing damage over a small distance (30 – 80 μm). Hence, α-emitting radionuclides are appropriate for the treatment of small tumors and/or metastasis.[18a]

Most of the α-emitters have a half-life that is too long to be compatible with in vivo applications. As a result, only a few of these radioisotopes have received serious attention for radiotherapeutic applications, namely, $^{211}$At ($t_{1/2}$ = 7.2 h, $E_\alpha$(avg) = 6.8 MeV), $^{212}$Bi ($t_{1/2}$ = 1 h, $E_\alpha$(avg) = 7.8 MeV) and $^{223}$Ra ($t_{1/2}$ = 11.4 d, $E_\alpha$(avg) = 5.65 MeV).[18b, 19a, 20] As an example, $^{223}RaCl_2$ (Alpharadin®) is currently under clinical evaluation for the treatment of bone metastases resulting from prostate cancer.[21]

The Auger electrons are less energetic particles with a very short range of penetration (< 1 μm), having a LET similar to that of α particles, which makes them potentially interesting for therapy. Unlike α and $\beta^-$ particles, treatment based on Auger electron-emitters requires the targeting of individual cells, specifically the DNA in the nucleus. Among the available Auger electrons-emitting radionuclides, $^{125}$I ($t_{1/2}$ = 57 d, 24 electrons/decay), $^{111}$In ($t_{1/2}$ = 67 h , 14 electrons/decay), $^{67}$Ga ($t_{1/2}$ = 78 h, 4 electrons/decay) and $^{99m}$Tc ($t_{1/2}$ = 6.02 h, 4 electrons/decay) are the most interesting for potential clinical applications.[18a, 22]

### 1.3. Coordination Chemistry of Technetium and Rhenium

Technetium (Tc) and rhenium (Re) are group 7 transition metals, belonging respectively to the 2nd and 3rd transition series, with atomic numbers 43 and 75 and electronic configurations $[Kr]4d^5 5s^2$ and $[Xe]4f^{14}5d^5 6s^2$, respectively. Tc complexes can have the metal in the oxidation sates -I ($d^8$) to +VII ($d^0$), whereas for Re complexes the metal presents oxidation states -III ($d^{10}$) to +VII ($d^0$). These metals present very similar atomic radii (Tc, 1.36 Å; Re, 1.37 Å), forming structurally analog complexes. However, there are differences between both metals that must be taken into consideration in the

preparation of Tc and Re complexes. The most striking difference is related with the higher kinetic inertness and easier oxidation associated to Re complexes.[10, 23]

### 1.3.1. The Radiochemistry of Technetium

The growth and wide application of diagnostic nuclear medicine have been mainly driven by the coordination chemistry and unique features of technetium, first isolated by Segré and Perrier in 1937.[24]

Currently, there are 21 known artificial isotopes with masses ranging from $^{90}$Tc to $^{110}$Tc and 7 of these species are metastable. Among them, technetium-99m ($^{99m}$Tc) is the most useful radioisotope in nuclear medicine, as it displays almost ideal characteristics:

- half-life ($t_{1/2}$) of 6.02 h is optimal for diagnostic, which is long enough to examine metabolic processes and yet short enough to minimize the radiation dose to the patient;
- γ-emitter (140 keV) with energy sufficiently high to penetrate easily the human body and to be detected externally by a gamma camera, and sufficiently low to minimize the dose to the patient;
- available at reduced prices from a commercial $^{99}$Mo/$^{99m}$Tc generator, being one of the greatest advantages of this radionuclide;
- diverse coordination chemistry, which enables the preparation of a wide variety of complexes with different physicochemical and biological properties.

The prominence achieved by $^{99m}$Tc as a useful radioisotope in nuclear medicine is directly related to the design and development of a $^{99}$Mo/$^{99m}$Tc generator in the late 1950s.[25] Molybdenum-99 ($^{99}$Mo), with a half-life of 66 h, undergoes a radioactive decay emitting $\beta^-$ particles in which 87% of the $^{99}$Mo atoms are converted directly into the metastable state $^{99m}$Tc, whereas 13% pass directly to the fundamental state $^{99}$Tc (**Scheme 1.1**).

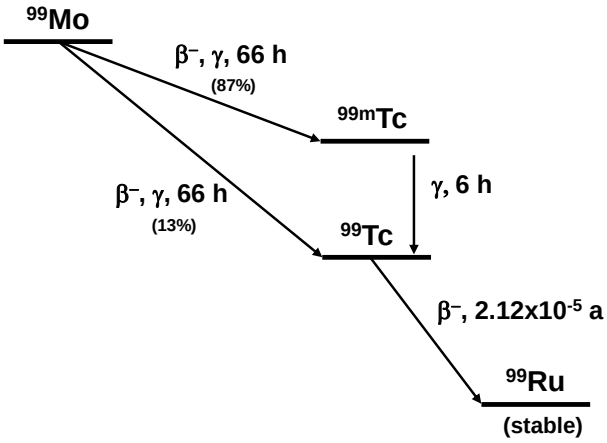


**Scheme 1.1**: Schematic representation of the radionuclides decay in a $^{99}Mo/^{99m}Tc$ generator.[26]

The commonly available generators contain $[^{99}MoO_4]^{2-}$ adsorbed onto an alumina column that decays to $^{99m}Tc$ (**Scheme 1.1** and **Figure 1.5**). The latter isotope is eluted from the generator in the form of sodium pertechnetate – $[^{99m}TcO_4]Na$ – using a saline solution (NaCl 0.9%).

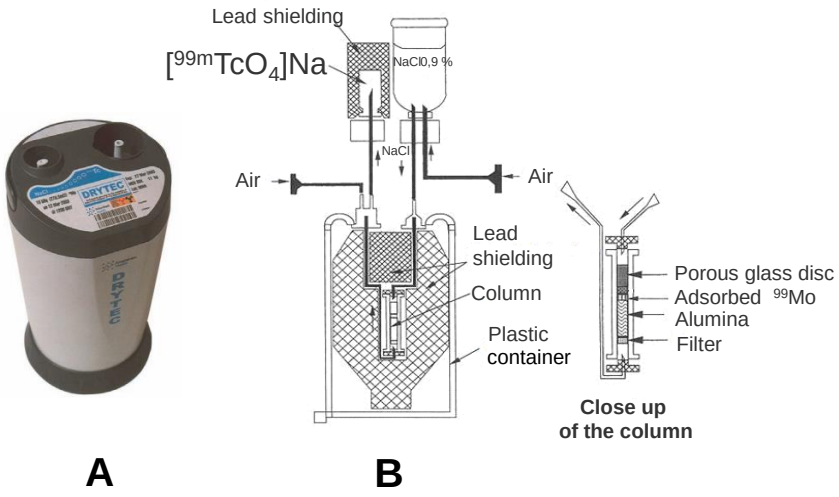


**Figure 1.5**: A - $^{99}Mo/^{99m}Tc$ generator. B - Conceptual view of the generator.

Sodium pertechnetate is an easily accessible precursor in the synthesis of all $^{99m}Tc$-based complexes for imaging application, however, it is the most stable form of technetium (oxidation state +VII) in aqueous solution. Several reducing agents such as tin salts ($SnCl_2$, tin citrate, tin tartrate) or sodium borohydride, as well as different reaction conditions (pH, temperature, concentration) are used to reduce $[TcO_4]^-$ in

aqueous solution, yielding a technetium core in a lower oxidation state that is stabilized by a suitable chelator. [8a, 10]

Owing to the low concentration ($10^{-8}$ – $10^{-10}$ M) of $[^{99m}TcO_4]^-$ in the saline solution, it is impossible to characterize the resulting $^{99m}$Tc complexes by the normal methods used in chemistry. Therefore, such complexes are often characterized by the synthesis of the surrogate complexes with the long-lived isotope $^{99}$Tc ($t_{1/2}$ = 2.12 x $10^5$ years, $\beta^-$ emitter, $E_{max}$ = 0.3 MeV), which is available in milligram amounts, or with natural rhenium ("cold metal"), which present similar coordination chemistry.[27]

Besides its importance as surrogate of technetium, rhenium has two important radioisotopes with great importance in therapeutic nuclear medicine, namely $^{186}$Re and $^{188}$Re. $^{186}$Re, produced in nuclear reactors, is simultaneously a $\beta^-$- and a $\gamma$-emitter allowing imaging during systemic radiotherapy. $^{188}$Re is a $\beta^-$-emitter obtained from a $^{188}$W/$^{188}$Re generator. The availability of this generator makes $^{188}$Re one of the most promising candidates for the development of novel radiopharmaceuticals for use in systemic radiotherapy.[28]

### 1.3.2. $^{99m}$Tc Radiopharmaceuticals

The $^{99m}$Tc-based perfusion agents, which are well established in routine nuclear medicine, follow a non-specific biological pathway after *in vivo* administration, accumulating in distinct tissues or organs according to their physicochemical properties (e.g. size, charge and lipophilicity). Examples of such commercially available compounds and respective clinical application are presented in **Figure 1.6**.[8b, 10, 29]

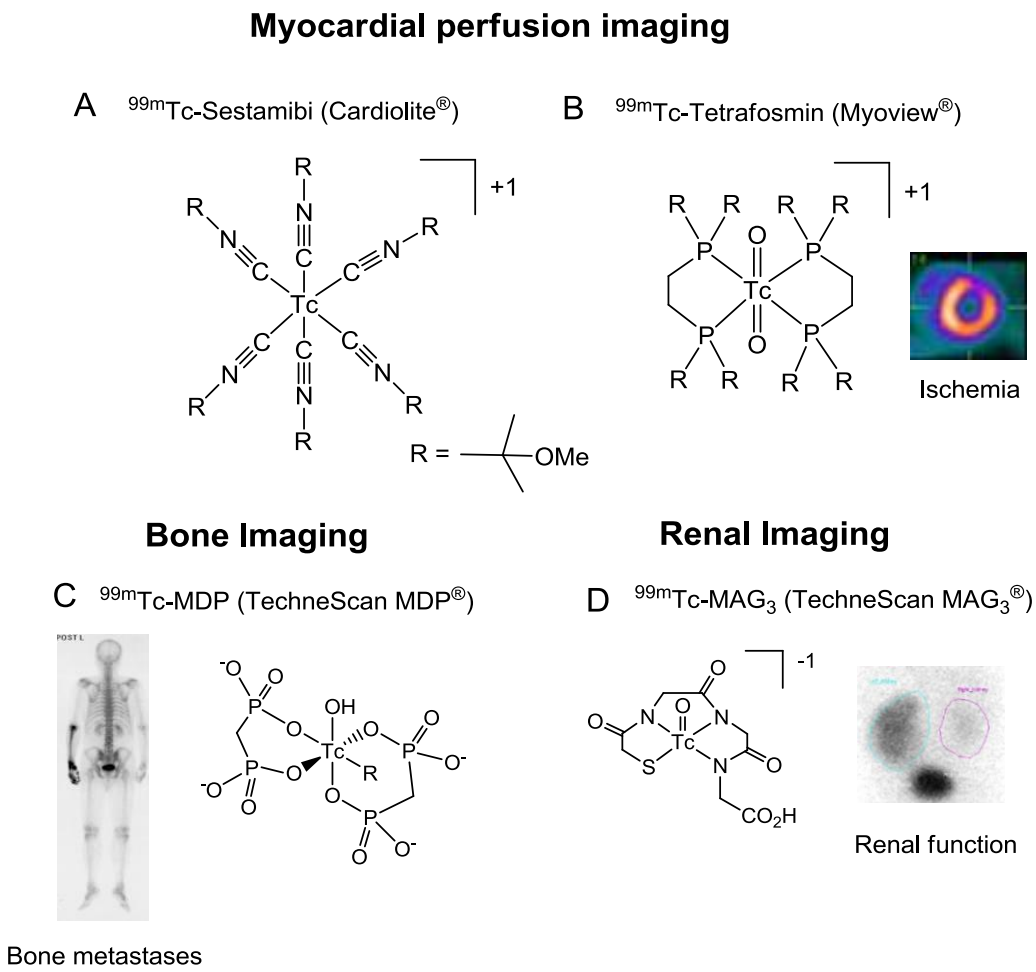


**Figure 1.6**: $^{99m}$Tc-based radiopharmaceuticals for diagnosis in clinical use.[8b] (MDP = methylenediphosphonate, $MAG_3$ = mercaptoacetyl-triglycine).

One of the most widely used SPECT perfusion imaging agents, the organometallic complex $^{99m}$Tc-Sestamibi (**Figure 1.6A**), originally developed as a myocardial perfusion agent is nowadays successfully applied in tumor imaging and detection of multidrug resistance.[30] The myocardial uptake is mediated by a metabolic process that involves its diffusion across the membrane, while its retention in the myocytes is provided by partial enzymatic cleavage of the ether functionalities.[27] The cationic complex $^{99m}$Tc-Tetrafosmin (**Figure 1.6B**) enters rapidly into the myocardial cells due to its lipophilic properties, being the proposed uptake mechanism similar to that of $^{99m}$Tc-Sestamibi.[24, 27]

Complexes of $^{99m}$Tc with bisphosphonate (BP) ligands (e.g. $^{99m}$Tc-MDP, $^{99m}$Tc-HMDP) are examples of imaging agents widely used for diagnostic of metastatic disease in bone (**Figure 1.6C**). Although the exact composition and structure of the $^{99m}$Tc-BP´s is

unknown, these compounds are well-established as diagnostic agents. In the case of $^{99m}$Tc-MDP, the oxidation state of the metal at the macroscopic level could not be unambiguously assigned in a X-ray diffraction analysis of a polymeric structure.[31] The mechanism of specific uptake in bone is believed to be via coordination of the free phosphoryl oxygens to the calcium of the hydroxyapatite bone surface.[32]

The anionic complex $[^{99m}Tc(MAG_3)]^-$ ($MAG_3$ = Mercaptoacetyl-triglycine) is widely used for functional kidney imaging and the free carboxylic acid group is essential for an efficient renal excretion (**Figure 1.6D**).[33] Moreover, complexes such as $^{99m}$Tc-DMSA (DMSA = dimercaptosuccinic acid) and $^{99m}$Tc-DTPA (DTPA = diethylenetriaminepentaacetic acid) are also used for renal imaging.

As mentioned before, the targeting ability of specific radiopharmaceuticals rely on the capacity of the pendant biologically active molecule in the metal complex to recognize its target *in vivo* (e.g. membrane receptor, antigen or enzyme).[2, 34] The most relevant examples of specific $^{99m}$Tc-based radiopharmaceuticals approved for SPECT imaging are radiolabeled peptides. Illustrative examples of such type of compounds are shown in **Figure 1.7**.

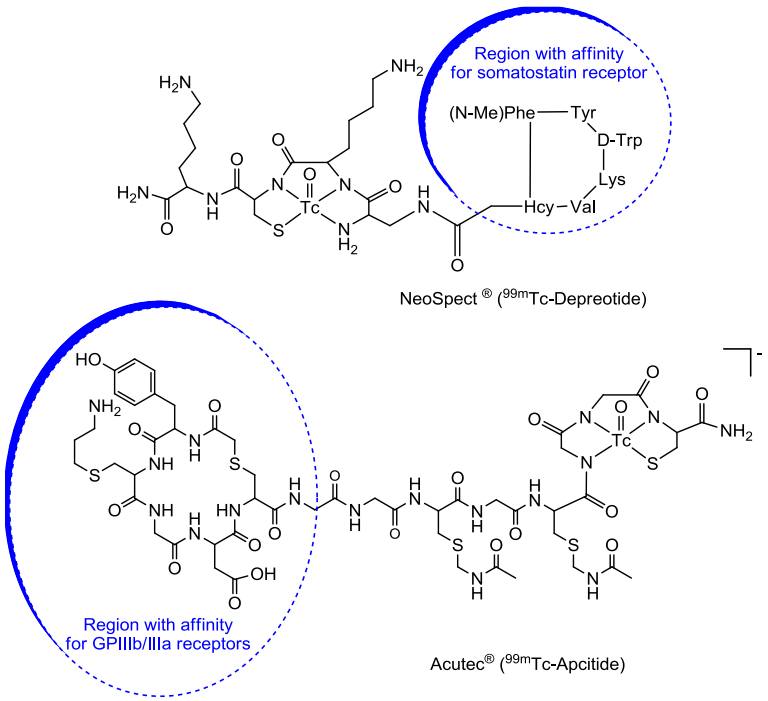


**Figure 1.7**: Examples of $^{99m}$Tc-based target-specific radiopharmaceuticals.

The complex $^{99m}$Tc-Depreotide (NeoSpect®) was the first receptor-targeted radiopharmaceutical that entered in clinical use as imaging agent for lung tumors.[35] It contains a synthetic somatostatin analog, which has high affinity for somatostatin receptor subtypes 2 (SSTR2), 3 (SSTR3), and 5 (SSTR5).

$^{99m}$Tc-Apcitide (Acutec®) is a target specific radiopharmaceutical with affinity for the GPIIb/IIIa receptors overexpressed on the surface of activated platelets, and is indicated for scintigraphic imaging of acute venous thrombosis.[36]

Besides the targeting moiety, also the spacer/linker between the metal and the biomolecule has a decisive influence in the overall biological properties of the radiopharmaceutical.[27]

The modulation of the metal coordination environment with different chelators is also another parameter that opens great opportunities towards the design of innovative target specific radiopharmaceuticals with improved biological properties. Indeed, the design and selection of the most appropriate BFC is the corner stone for the development of clinically relevant imaging agents. **Figure 1.8** shows selected Tc cores, which have been used for labeling different type of biomolecules (BM) with $^{99m}$Tc.

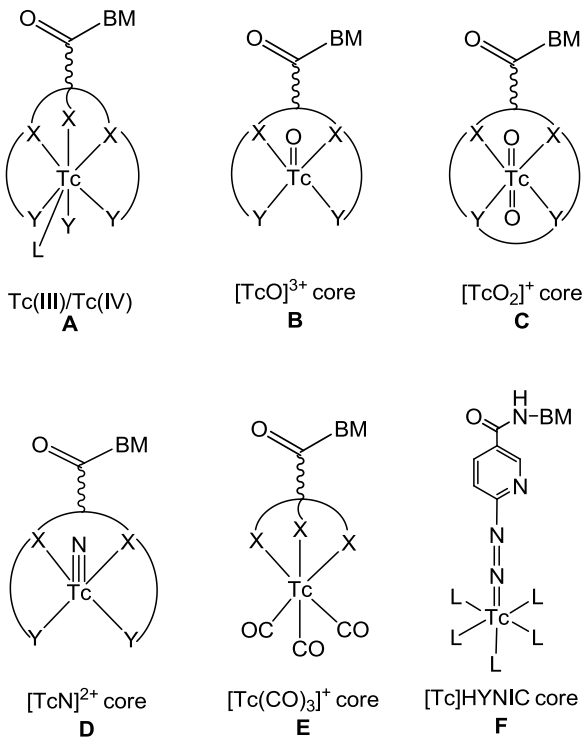


**Figure 1.8**: Technetium cores useful for labeling biomolecules.

In these compounds, nitrogen, oxygen, phosphorus and sulfur containing chelating systems of various denticities were used for metal stabilization. The oxidation state +V and, more recently, +I, have been the most studied towards biomedical applications (**Figure 1.8**).

The chemistry of Tc(V) is mainly dominated by the formation of oxo-complexes with the $[Tc=O]^{3+}$ or trans-$[O=Tc=O]^{+}$ moieties (**Figure 1.8B** and **C**). In fact, the coordination chemistry of $[Tc=O]^{3+}$ has been optimized in the last three decades. However, the formation of stereoisomers with distinct physicochemical properties is the major drawback, limiting the efficacy of specific oxo-complexes of Tc(V) due to the presence of species with different biological behavior.[37]

To overcome this limitation, new metallic fragments and methodologies were introduced in radiopharmaceutical chemistry. Among the novel approaches, the lower oxidation states Tc(I) and Tc(III) have been the most explored and further advances rely mainly in the development of novel bifunctional chelating systems. The *fac*-$[Tc(CO)_3]^{+}$ core is being adopted more widely as a preferred moiety for labeling biomolecules and investigation of different types of bifunctional chelators for linking this fragment to biomolecules is underway.

### 1.3.3. The *fac*-$[M(CO)_3]^{+}$ Core (M = Tc, Re)

The octahedral metal center in *fac*-$[Tc(CO)_3]^{+}$ is facially arranged with three carbonyls and three vacant coordination sides. The +I oxidation state on the metal allows for coordination of a broad variety of donor and acceptor atoms.

Alberto and co-workers were the first to report the one step synthesis of the precursor *fac*-$[^{99m}Tc(CO)_3(H_2O)_3]^{+}$ by direct reduction of $Na[^{99m}TcO_4]$ with sodium borohydride in aqueous solution in the presence of carbon monoxide. This synthetic procedure, although being suitable for research, was not adequate for the nuclear medicine centers due to the use of carbon monoxide. Thus, a more attractive method was further developed, which involved the use of boranocarbonate ($K_2[H_3BCO_2]$) to produce CO *in situ* and, simultaneously, reduce Tc(VII) to Tc(I).[38] Currently, the synthesis of *fac*-$[^{99m}Tc(CO)_3(H_2O)_3]^{+}$ is done using a kit formulation (IsoLink®, Covidien, former Mallinckrodt BV). As shown in **Scheme 1.2**, upon addition of $[^{99m}TcO_4]^{-}$ to the

IsoLink® kit, the precursor complex *fac*-[$^{99m}$Tc(CO)$_3$(H$_2$O)$_3$]$^+$ is obtained in quantitative yield.

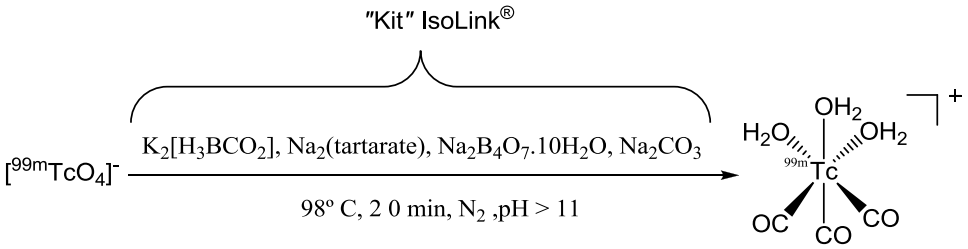


**Scheme 1.2**: Synthesis of *fac*-[$^{99m}$Tc(CO)$_3$(H$_2$O)$_3$]$^+$ with IsoLink® Kit.

The *fac*-[M(CO)$_3$]$^+$ core (M = $^{99m}$Tc, Re) has been one of the most explored metallic fragments in the past few years for the labeling of biomolecules due to a set of recognized superior features. Indeed, it exhibits a significantly reduced size when compared to Tc and Re complexes in the +V oxidation state. (**Figure 1.9**).[39] Owing to this feature, it was hypothesized that the metal core would have minor impact on the biological activity of the targeting agent, enabling the design of novel specific $^{99m}$Tc(I)-based radiopharmaceuticals.

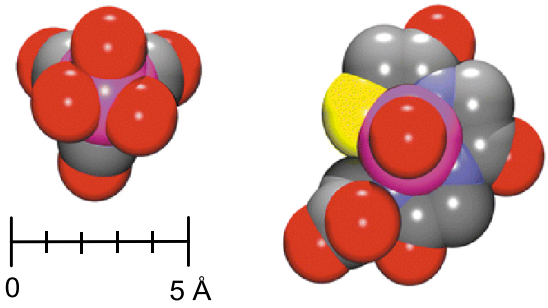


**Figure 1.9**: Qualitative size comparison of the organometallic precursor *fac*-[Tc(CO)$_3$(H$_2$O)$_3$]$^+$ (left) and Tc-MAG$_3$ (right) based on X-ray analyses. Purple = technetium, red = oxygen, grey = carbon, blue = nitrogen, yellow = sulphur. Hydrogen atoms are omitted.[39]

A second feature of this type of organometallic complexes is linked to the compact nature of the octahedral coordination sphere with an appropriate ligand system, becoming the metal center quite compact in an almost spherical shape. Unlike the open square pyramidal structures of Tc(V) oxocomplexes anchored by tetradentate chelators that can be characterized as unprotected metal centers and prone to further ligand

attacks and protonation, the metal center of the tricarbonyl moiety gives kinetically inert complexes and, thus, protected against ligand attacks or re-oxidation.[39]

The three water molecules in the precursor *fac*-$[^{99m}Tc(CO)_3(H_2O)_3]^+$ are labile with respect to substitution, and the precursor can interact with potential coordination sites in proteins in human serum (e.g. histidine and cysteine residues). Therefore, the precursor itself is not suitable for diagnostic purposes displaying a very unfavorable biological profile as demonstrated by biodistribution studies in mice.[40]

Hence, to develop suitable radiopharmaceuticals based on this core, it is necessary to replace the water molecules by mono, bi, or tridentate ligands to form stable complexes. A wide variety of organometallic complexes have already been described, with those stabilized by tridentate chelating systems displaying the highest stability both *in vitro* and *vivo*.[41] Histidine, pyridine, pyrazole, thioimidazole, 2,3-diamino propionic acid and cysteine bearing chelators, together with pure aliphatic or mixed aromatic aliphatic triamines, among others, are quite efficient tridentate bifunctional chelators, suitable for the labeling of relevant biomolecules. In **Figure 1.10** are represented selected complexes, stabilized by tridentate bifunctional chelators, bearing or not pendant targeting moieties.

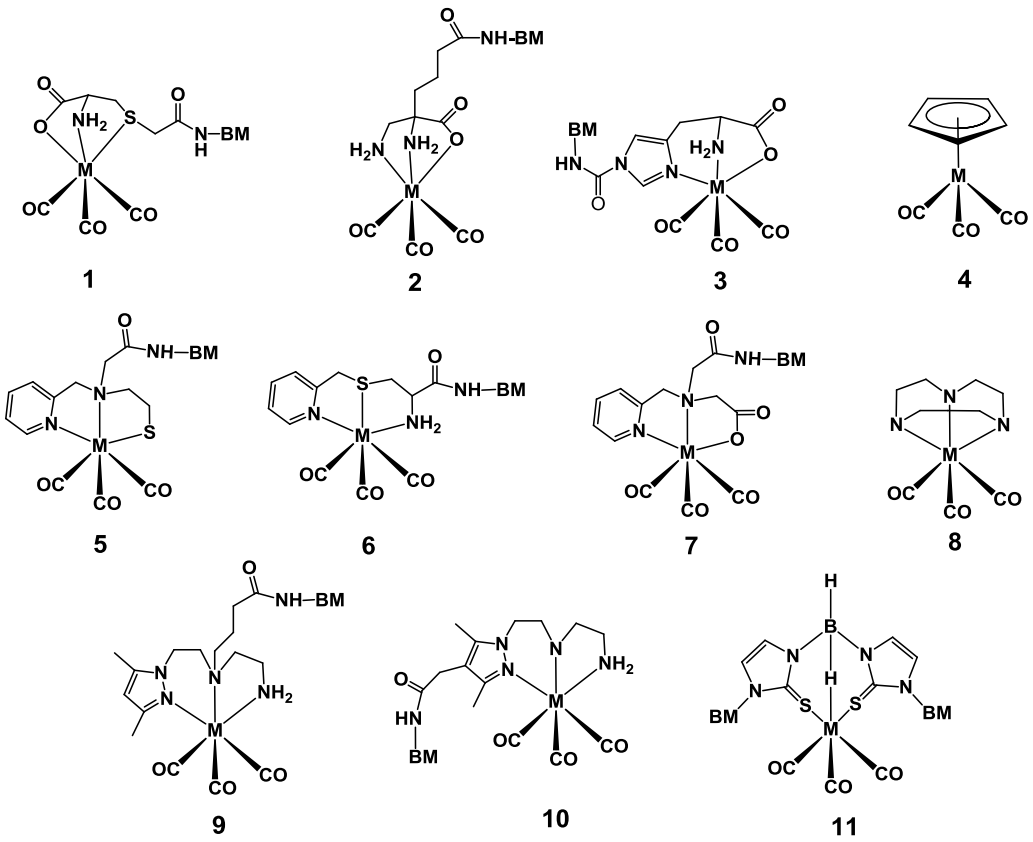


**Figure 1.10**: Examples of $M(CO)_3$-complexes stabilized by various types of chelating agents (BM = biomolecule; M = Re/$^{99m}$Tc). 1 - Functionalized cysteine;[42] 2 - Funcionalized 2,3-diamino propionic acid derivatives;[43] 3 Functionalized histidine derivatives;[44] 4 - Cyclopentadienyl;[45] 5, 6 and 7 - Functionalized picolinic acid derivatives;[46] 8 Triazacyclononane;[47] 9 and 10 Functionalized pyrazolyl-diamine containing ligands;[48] 11 - Functionalized bis(mercaptoimidazolyl)borates.[49]

Over the last few years the radiopharmaceutical sciences group of the CTN/IST has introduced a large family of tridentate bifunctional ligands, some of them sharing a common pyrazolyl chelating unit. Those chelators have a great ability to stabilize the organometallic unit *fac*-$[M(CO)_3]^+$ (M = $^{99m}$Tc, Re) (**Figure 1.10**, **9** and **10**).[50] In this way it has been possible to label a wide range of biomolecules such as peptides, small molecules, and antibodies, just to mention a few examples, in high radiochemical and purity yield, and high specific activity.[32, 48a, 48e, 51]

## 1.4. Detection of Melanoma and Sentinel Lymph Node

### 1.4.1. Melanoma

Malignant melanoma is the most serious type of skin cancer. Although melanoma represents only 10% of all skin-cancers, at least 65% of deaths linked to skin cancer are attributed to melanoma. It is not only the most common malignancy among young adults but the fastest growing cancer worldwide.[52]

Unless detected at an early stage, melanoma has poor prognosis due to the enormous metastatic potential.[52b, 52d, 53] In fact, at its earliest invasive stage (i.e., stage IA), the prognosis is favorable, with 5-year and 10-year survival estimates of 97% and 93%, respectively. In contrast, the prognosis for a patient with distant metastasis (stage IV melanoma) is poor; 1-year and 5-year overall survival rates are 45% and 12%, respectively.[54] Metastasis tends to occur first to regional lymph nodes and subsequently to various secondary sites.[54-55] This type of cancer arises from melanocytes, melanin-producing cells derived from the neural crest, that are found at the dermal–epidermal junction of the skin.[52b, c, 53-54, 56] Tyrosinase in melanocytes mediate melanin production, however, this process is upregulated in malignant melanoma.[52c, 57]

The most effective therapy for melanoma is surgery, however, this procedure only improves patient survival if the tumor is detected in an early stage. For metastic melanoma, excision is not applicable and the only goal is to relieve symptoms and prolong life. Moreover, there is no standard therapy for disseminated melanoma in today's clinical practice. Several strategies have been evaluated, namely mono-chemotherapy, poly-chemotherapy, combined therapies with cytokines, or even complex schemes with up to five different drugs but, because malignant melanoma is resistant to current cytotoxic agents, real improvement of the patients survival could not be achieved.[58] Recently, Food and Drug Administration (FDA) and the European Medicines Agency (EMA) approved vemurafenib as a monotherapeutic drug for the treatment of metastatic melanoma in adult patients. This compound inhibits the mitogen-activated protein kinase (MAPK/BRAF) signaling pathway, leading to programmed cell death in melanoma cell lines, however, two mechanisms of resistance have already been reported.[59]

Therefore, improvement of patient survival relies mostly on an early diagnosis of both the primary tumor and initial metastasis, in combination with an accurate

staging of disease extension and excision.[52d] $^{18}$F-FDG is the only PET radiotracer routinely used for melanoma imaging.[60] This compound is transported into cells through the up-regulated glucose transporters and then phosphorylated by hexokinase, remaining trapped inside the cells. However, $^{18}$F-FDG can not be considered a specific molecular probe for melanoma detection because it targets glucose metabolism non-specifically. Furthermore, $^{18}$F-FDG also failed to identify metastatic lesions smaller than 1 cm in diameter located mainly in common sites for melanoma metastases such as the lungs, liver, or brain.[52c, 60]

In an attempt to efficiently visualize melanoma, several non-specific and target-specific radiotracers have been reported. The non-specific agents aim at probing cellular processes such as tumor metabolism, apoptosis, hypoxia, angiogenesis and sigma receptors that are also up-regulated in a variety of tumors. Target-specific radiotracers for melanoma aim at specific targets associated with the pathology, namely, melanin, antigen expression, melanocortin 1 receptor (MC1R), among others. The main specific and non-specific targets as well as the respective PET/SPECT imaging probes for malignant melanoma visualization are depicted in **Figure 1.11**.

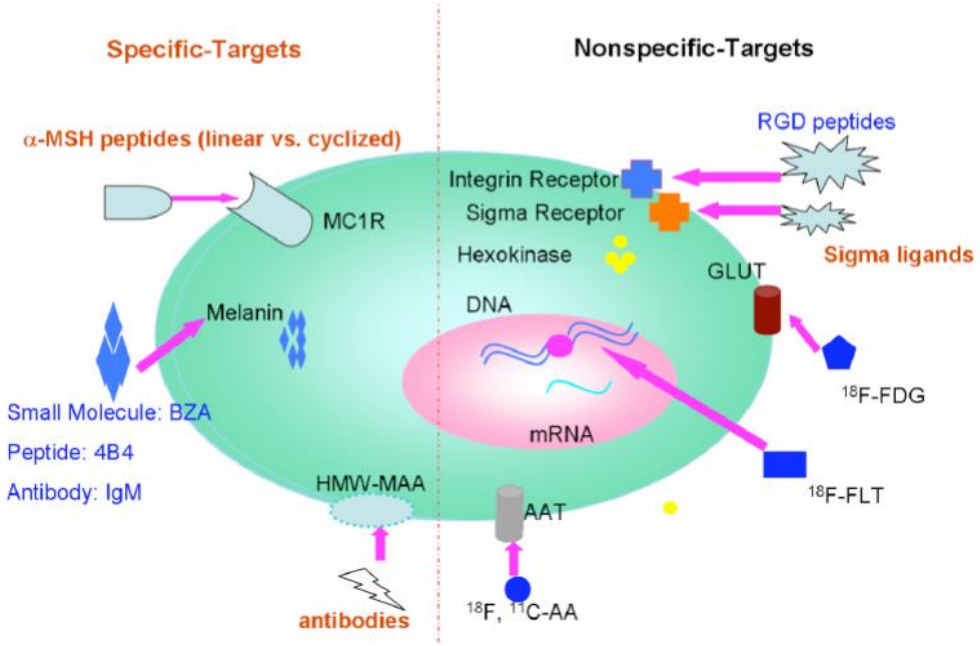


**Figure 1.11**: Molecular targets (melanoma specific *versus* nonspecific) and probes for PET/SPECT imaging of malignant melanoma. Melanocortin 1 receptor (MC1R); high molecular weight melanoma associated antigen (HMW-MAA); benzamide analog (BZA); amino acid transporter (AAT); glucose transporter (GLUT); $^{18}$F-fluorodeoxyglucose ($^{18}$F-FDG); 3'-$^{18}$F-fluoro-3'-deoxy-L-thymidine ($^{18}$F-FLT); arginine-glycine-aspartic acid (RGD).[52c]

Among the non-specific probes, $^{18}$F-fluoro-3'-deoxy-3'-L-fluorothymidine ($^{18}$F-FLT) was developed to monitor tumor metabolism, however, preliminary results in humans have shown lower sensitivity and specificity than $^{18}$F-FDG in metastatic melanoma patients.[52c, 61] Moreover, high liver uptake caused by glucuronidation of $^{18}$F-FLT also limited its usefulness for detection of liver metastatic melanomas. The $^{11}$C-labeled natural amino acid L-[methyl-$^{11}$C]methionine ($^{11}$C-methionine) used to target tumor metabolism in humans proved to be a viable approach for melanoma imaging. However, probes that target tumor metabolism share a common disadvantage that is the lack of specificity for malignant melanoma.

Reports on the evaluation of $^{18}$F-Fluoromisonidazole ($^{18}$F-FMISO) for hypoxia targeting and $^{99m}$Tc-annexin-V for tumor apoptosis allowed a clear-cut visualization of the tumor in melanoma bearing mice. The probes $^{18}$F-galactco-arginine-glycine-aspartic acid (RGD) for imaging tumor angiogenis and $^{123}$I-N-(2-diethyl aminoethyl) 4-Iodobenzamide ($^{123}$I-IDAB) for sigma receptor targeting also enabled tumor visualization in humans with melanoma.[52c, 62] Despite their potential, the lack of specificity of these compounds may lead to false positives. Furthermore, some of these tracers, particularly the ones evaluated in murine model, present lower tumor uptake when compared to melanoma specific probes. Further studies also suggest that the compounds reported above display ''extremely low'' overall detection rate for occult metastatic lesions.

Profiting from the unique physiological process of melanin synthesis and overproduction in melanotic melanoma, PET imaging probes that target the melanin biosynthesis pathway such as $^{18}$F-L-dihydroxyphenylalanine ($^{18}$F-DOPA) present higher tumor uptake when compared with non-melanotic tumors and may be usefull to identify melanoma metastases in patients with negative $^{18}$F-FDG scans.[52c]

Benzamide analogs show specific and high affinity to melanin and have been extensively explored in the development of SPECT imaging agents for melanoma detection over the past two decades.

Several radioiodinated benzamide derivatives, including N-(2-diethylaminoethy1)-4-$^{125}$I-iodobenzamide ($^{125}$I-BZA), $^{123}$I-BZA, N-(2-diethylaminoethyl)-2-$^{123}$I-iodobenzamide ($^{123}$I-BZA$_2$), and $^{123}$I-2-hydroxy-3-iodo-6-methoxy-N-[(1-ethyl-2-pyrrolidinyl) methyl]benzamide ($^{123}$I-IBZM) exhibit excellent *in vivo* tumor targeting profiles in murine melanoma. Among them, $^{125}$I-BZA presented the most promising result in C57BL6 mice bearing B16F1 melanoma.[52c, 63] Good melanoma

uptake values were also found for the radiofluorinated benzamide analog N-[2-(diethylamino)ethyl]-4-18F-fluorobenzamide ($^{18}$F-FBZA) in melanotic melanoma bearing mice, however, this compound displays unfavorable pharmacokinetics.[62] Similar results were also found for some $^{99m}$Tc(V)-labeled benzamide analogs for murine melanoma SPECT imaging.[52c, 64] In the case of $^{99m}$Tc(CO)$_3$-benzamide complexes, low tumour uptake was found in B16F1 melanoma bearing mice.[51c, 65]

Besides small molecules, peptides and antibodies have also been explored to target melanin but high kidney uptake/toxicity, poor tissue penetration and short biological half-life hindered the use of both approaches. Despite the advances on the design of specific melanin-targeting probes, this pigment is not produced in amelanotic melanoma and therefore can not be considered an ideal target.

As an alternative to melanin targeting probes, monoclonal antibodies were used to target high molecular weight melanoma-associated antigen (HMW-MAA or HMP), that is expressed in 80% of human melanoma cells, for both melanoma imaging and radioimmunotherapy studies. Therapeutic effect was achieved with either intact or fragments of monoclonal antibodies. Tumor uptake was observed in the majority of the patients, however, high uptake in normal tissues, including excretory organs such as liver, spleen and intestine, limited their use in the clinical set.[66]

Several ligand-binding studies demonstrated that the melanocortin 1 receptor (MC1R) isoform is expressed in melanocytes and melanoma cells.[67] Further studies confirmed the overexpression of MC1R (~400 to 22 000 receptors/cell) in both murine and human melanoma compared to normal melanocytes.[67c, 68] Moreover, this receptor is overexpressed in melanotic and amelanotic murine and human melanoma cells.[46b, 50, 67b, c, 68a, 69] These findings present MC1R as an attractive target for primary and metastatic melanoma imaging. Thus, the following sections will briefly describe the function, localization, structure and native ligand of this receptor as well as the design of MC1R targeting probes.

#### 1.4.1.1. α-MSH/MC1R System

The human gene coding MC1R was first cloned in 1992.[70] Since then, genetic analysis, phenotypic association and structure function studies opened new perspectives for the assignment of its function as a key regulator of skin biological events. The receptor is involved in the regulation of skin pigmentation, animal coat coloration, and melanocyte

function.[71] Polymorphisms in the receptor gene have been attributed to the red hair phenotype, melanoma and non-melanoma skin cancer.[71a, 72]

The MC1R belongs to a five-member subfamily of G protein-coupled receptors (GPCR), the melanocortin receptors (MCRs) family.[70a, 71b, 73] This family also includes MC2-, MC3-, MC4- and MC5-receptors. mRNA expression of the five receptors allowed for their localization in various human tissues, summarized in **Table 1.2**.

**Table 1.2**: Melanocortin receptors and their tissue localizations.

| Receptor | Tissues or cell types |
|---|---|
| **MC1R** | Melanocytes, melanoma, macrophages, brain |
| **MC2R** | Adrenal cortex, adipose tissue |
| **MC3R** | Brain, placenta, duodenum, pancreas, stomach |
| **MC4R** | Brain, spinal cord |
| **MC5R** | Skin, adrenal cortex, adipose tissue, skeletal muscle |

The isoform 1 of the MCR is also expressed at leukocytes, where it may mediate an anti-inflammatory action.[67c, 71b] MC2R is expressed in the adrenal cortex, where it mediates the effects of the adrenocorticotropic hormone (ACTH) on steroid secretion. MC3R has been identified in many areas of the central nervous system and peripheral tissues, being involved in energy homeostasis. MC4R is expressed predominantly in the central nervous system and regulates both food intake and sexual function while MC5R is expressed in numerous human peripheral tissues and is mainly involved in exocrine function, particularly sebaceous gland secretion.[71b, 74]

Accurate information about secondary and tertiary structure of MC1R is not available because no crystal structure is available. Although GPCRs, can not be readily crystallized, there are some available templates of the same class delivering information about their secondary and tertiary structures, namely the famous crystal structure of rhodopsin and more recently chemokine (C-X-C motif) receptor 4 (CXCR4) or dopamine D3 receptor (D3R) crystal structures.[75] Hence, MCRs, including MC1R, are classified as class A GPCRs (whose prototype is rhodopsin) due to sequence similarity with the prototype (39-61% homology). Among the structural homologies with GPCRs, MC1R displays an extracellular N-terminus, seven-transmembrane helix joined by three intracellular and three extracellular loops, and the intracellular C-terminal extension.[76] The two-dimensional model of the human melanocortin-1 receptor is depicted in **Figure 1.12**.

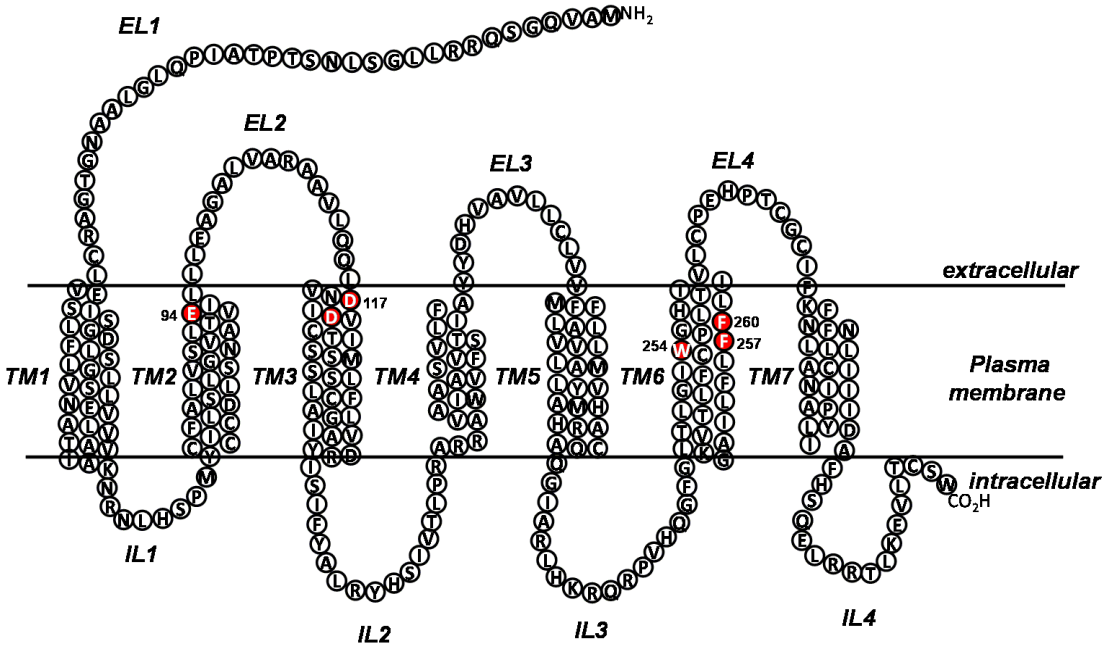


**Figure 1.12**: Schematic representation of the human melanocortin-1 receptor.[76a] The positions for transmembrane (TM) helix, extracellular (EL) loops and intracellular (IL) loops are drawn according to the two-dimensional model of Ringholm et al.[76b] The amino acid sequence corresponds to the wild type consensus (GenBank accession number AF326275). Positions for MC1R binding are shown in red.

The MC1R share the same endogenous ligands with other MCRs, namely with MC3R-MC5R and, therefore, should have similar orthosteric binding (i.e. the receptor area where the endogenous ligand binds).[71b] The orthosteric binding site is located in the transmembrane domains of MC1R, and several positions have been identifided as crucial for ligand binding. The positions are glutamic acid (Glu, E) 94 in TM domain 2, aspartic acid (Asp, D) 117 and 121 in TM 3, tryptophan (Trp, W) 254, phenylalanine (Phe, F) 257 and histidine (His, H) 260 in TM 6 MC1R.[71b]

Among the different signaling pathways described so far, it is noteworthy that MC1R mediates the physiological actions of the endogenous ligand by a Gs-protein dependent activation of the cyclic adenosine monophosphate (cAMP) signaling pathway. The increase of cAMP levels result in the activation of tyrosinase in melanocytes and lead to an increase of melanin production.[74] The mechanism of production and intracellular cAMP accumulation has been used to determine the agonist/antagonist properties of MC1R ligands.[74]

The hormone α-melanocyte-stimulating hormone (α-MSH), a linear tridecapeptide, is the endogenous ligand of MC1R. However, MC1R binds to several natural ligands, which are derived from the same precursor protein (pro-opiomelanocortin – POMC), with the following order of potency: α-MSH > ACTH > β-MSH > γ-MSH.[71a, 76a]

Structure–bioactivity studies have shown that all endogenous ligands contain a conserved $His^6$-$Phe^7$-$Arg^8$-$Trp^9$ sequence that has been attributed to melanocortin receptor selectivity and stimulation.[50, 71, 76a] This high degree of pharmacophore homology makes it difficult to design highly selective ligands for one receptor subtype. Nevertheless, MC1R is known to be expressed at the surface of human melanocytes, and even more at the surface of murine and human melanoma cells, while MC2R-MC5R have higher expression levels in the brain, nervous system. Thus, MC2R-MC5R off-target is unlikely because presumably most agents will not be able to cross the blood brain barrier (BBB).[68a, 77] Taken together, these findings support the development of MC1R targeting strategies without significant adverse effects.

The MC1R targeting strategies described so far involve the design of α-MSH peptide analogs because the receptor has several signaling pathway and non-peptide or small ligands are not available to mimic the physiological action of α-MSH.[74]

#### 1.4.1.2. Radiolabeled α-MSH Analogs

The physiological significance of the α-MSH/ MC1R system in melanoma has fostered considerable research activity over the past decades in the development of peptide based radiotracers for the early detection of this type of skin cancer.

The endogenous peptide hormone α-MSH (**Table 1.3**) is not suitable for receptor imaging due to its very short half-life *in vivo*, about 3 minutes.[78] However, based on the knowledge gained in structure–bioactivity studies for the melonocortin system (α-MSH analogs/ MCR), a great deal of effort has been directed towards the development of potent α-MSH peptide analogs with enhanced biological stability, potency and specificity. **Table 1.3** presents some of the most potent linear and cyclic α-MSH analogs studied.

**Table 1.3**: Sequence of amino acids for α-MSH and some α-MSH analogs.

| PEPTIDES |
|---|
| Ac-Ser-Tyr-Ser-Met$^4$-Glu$^5$-<u>His$^6$-Phe$^7$-Arg$^8$-Trp$^9$</u>-Gly$^{10}$-Lys$^{11}$-Pro$^{12}$-Val$^{13}$-$NH_2$ (**α-MSH**) |
| Ac-Ser-Tyr-Ser- **Nle**$^4$-Glu$^5$-<u>His-**DPhe**$^7$-Arg-Trp</u>-Gly-Lys-Pro-Val-$NH_2$ (**NDP-MSH**) |
| Ac-**Nle**$^4$-**Asp**$^5$-<u>His-**DPhe**$^7$-Arg-Trp</u>-Gly-Lys-$NH_2$ (**NAPamide**) |
| βAla$^3$-**Nle**$^4$-**Asp**$^5$-<u>His-**DPhe**$^7$-Arg-Trp</u>-**Lys**$^{10}$-$NH_2$ (**MSHoct**) |
| Ac-**Cys**$^3$-**Cys**$^4$-Glu$^5$-<u>His-**DPhe**$^7$-Arg-Trp</u>-**Cys**$^{10}$-Lys-Pro-Val-$NH_2$ (**CCMSH**) |
| Ac-**Cys**$^3$-**Cys**$^4$-Glu$^5$-<u>His-**DPhe**$^7$-Arg-Trp</u>-**Cys**$^{10}$-Arg$^{11}$-Pro-Val-$NH_2$ (**CCMSH(Arg$^{11}$)**) |
| Ac-***cyclo*[Cys**$^4$-Glu$^5$-<u>His-**DPhe**$^7$-Arg-Trp</u>-**Cys**$^{10}$]-Lys-Pro-Val-$NH_2$ (**CMSH**) |
| Ac- **Nle**$^4$-***cyclo*[Asp**$^5$-<u>His-**DPhe**$^7$-Arg-Trp</u>-**Lys**$^{10}$]-$NH_2$ (**Melanotan-II: MT-II**) |
| βAla$^3$-**Nle**$^4$-***cyclo*[Asp**$^5$-<u>His-**DPhe**$^7$-Arg-Trp</u>-**Lys**$^{10}$]-$NH_2$ (**βAlaNlecycMSH$_{hex}$**) |
| Ac-**Nle**$^4$-c[<u>**Asp$^5$-N-MeHis$^6$-DPhe$^7$-N-MeArg$^8$-N-MeTrp$^9$-N-MeLys$^{10}$**</u>]-$NH_2$ (**N-Me MTII**) |

Bold: amino acid residues replaced in different analogs relatively to the endogenous peptide (α-MSH); underline: minimal sequence for biological activity.

Initial studies have shown that the minimal sequence of α-MSH required for biological activity is His$^6$-Phe$^7$-Arg$^8$-Trp$^9$. The replacement of Met$^4$ and Phe$^7$ by Nle$^4$ and DPhe$^7$ led to the potent α-MSH analog NDP-MSH with subnanomolar receptor affinity and resistance to enzymatic degradation (**Table 1.3**).[50, 71a, 76a, 79]

Among the short linear peptides, [Ac-Nle$^4$,Asp$^5$,DPhe$^7$]-α$MSH_{4-11}$ (NAPamide, **Table 1.3**) and [βAla$^3$-Nle$^4$,Asp$^5$, DPhe$^7$,Lys$^{10}$]-α$MSH_{4-11}$ (MSHoct, **Table 1.3**) display nanomolar affinity for MC1R.

The introduction of a cyclic constraint can generate peptides with enhanced potency, receptor selectivity and enzymatic stability.[50b] This concept was successfully applied to α-MSH analogs cyclized via disulfide- (e.g. CCMSH, **Table 1.3**), site-specific metal coordination, or lactam-bridge (e.g. MT-II, **Table 1.3**). These peptides have shown enhanced receptor binding affinity and resistance to proteolysis.[50] More recently, a *N*-methylated selective α-MSH analog for hMC1R targeting was reported (**Table 1.3**). All amide bounds in the pharmacophore positions (His-DPhe-Arg-Trp) of the lactam-bridge cyclized peptide are *N*-methylated, except for DPhe. [80]

For potential diagnostic application, the linear analog NDP-MSH was radiolabeled with $^{99m}$Tc and $^{188}$Re using 2-Mercaptoacetylglycylglycyl ($MAG_2$) or the tetrapeptide Ac-Cys-Gly-Cys-Gly (CGCG) as BFCs, respectively. The short linear

peptide MSHoct was also conjugated to 1,4,7,10-tetraazacyclo-dodecane-1,4,7,10-tetraacetic acid (DOTA) and to a pyrazolyl-diamine containing bifunctional chelator (Pz) through the N-terminus and labeled with $^{111}$In and $^{99m}$Tc, respectively.[81] The resulting radiolabeled peptides allowed MC1R visualization in melanoma-bearing mice, but presented an unfavourable uptake in excretory organs.

NAPamide was also conjugated to DOTA and to a Pz bifunctional chelator through Lys$^{11}$ side-chain. The DOTA derivative was labeled with $^{111}$In, $^{68}$Ga and $^{64}$Cu, whereas the pyrazolyl-diamine bifunctional conjugate was labeled with $^{99m}$Tc.[68d, 82] The radiolabeled linear peptides have shown not only moderate tumor uptake but also accumulation of radioactivity in non-target organs, when compared to the family of Re- and Tc-cyclized α-MSH analogs Ac-**M**CCMSH (**M** = Re, $^{99m}$Tc). The Re-peptide analog (ReCCMSH), cyclized through site-specific rhenium coordination, where the metal is stabilized by three Cys$^{3,4,10}$ sulfhydryls and one Cys$^{4}$ amide nitrogen, displayed a receptor-binding affinity of 2.9 nM (**Figure 1.13**).[83]

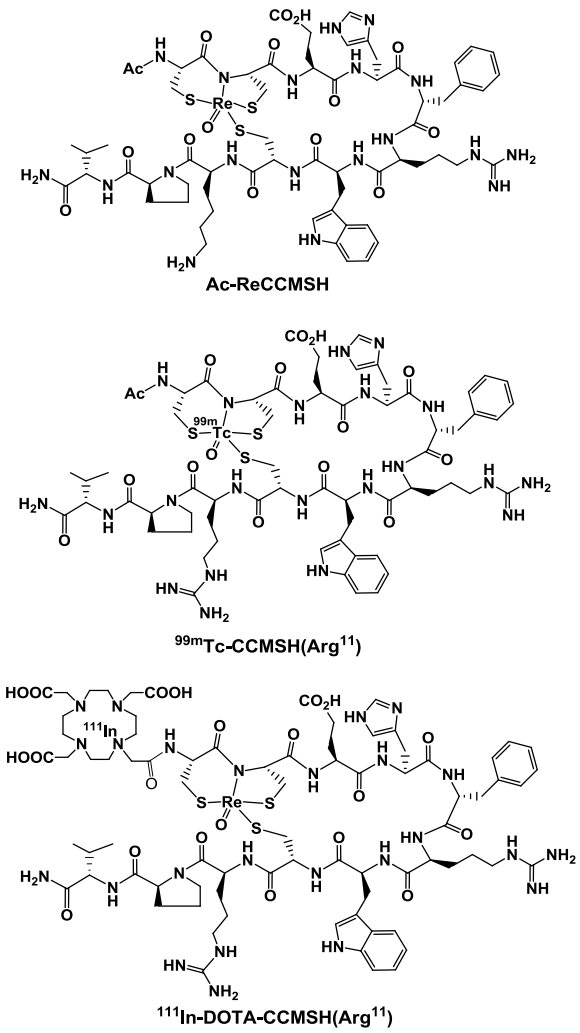


**Figure 1.13**: Structure of Ac-ReCCMSH, $^{99m}$Tc-CCMSH(Arg$^{11}$) and $^{111}$In-DOTA-CCMSH(Arg$^{11}$)

The metal-based cyclization yielded a peptide not only very resistant to chemical and proteolytic degradation but also highly bioactive. The rhenium-free analog, CCMSH, was directly radiolabeled and cyclized by coordination to $^{99m}$Tc(V).[83] Despite the high kidney uptake, the ability of $^{99m}$Tc-CCMSH to target B16F1 melanoma became the proof-of-principle of the potential use of metal-cyclized radiolabeled compounds for melanoma imaging or therapy.

Owing to the good receptor-targeting properties of ReCCMSH, DOTA was conjugated to the N-terminus of the peptide and labeled with $^{111}$In. The $^{111}$In-DOTA-ReCCMSH not only showed a significant tumor uptake but also a high kidney accumulation in B16F1 melanoma-bearing mice.[84]

By comparing the two metal-cyclized CCMSH analogs, $^{111}$In-DOTA-ReCCMSH *versus* $^{99m}$Tc-CCMSH, similar tumor uptake was found, but the Re-cyclized radiopeptide had an enhanced whole-body clearance and a higher tumor/blood ratio.[85] Despite the favorable features of $^{111}$In-DOTA-Re-CCMSH, a relatively high level of radioactivity still remained in the kidneys. Aiming to reduce kidney retention, four new $^{111}$In-DOTA-derivatized Re-CCMSH analogs were designed, with the analog $^{111}$In-DOTA-Re-CCMSH(Arg$^{11}$) (Lys$^{11}$ replaced by Arg, **Figure 1.13**) showing the highest tumor uptake and the lowest kidney retention in murine melanoma model. A similar effect was also found for CCMSH(Arg$^{11}$) cyclized through labeling with $^{99m}$Tc (**Figure 1.13**). Compared to the Re-cyclized analog $^{111}$In-DOTA-Re-CCMSH(Arg$^{11}$), $^{99m}$Tc-CCMSH(Arg$^{11}$) exhibited favorable and comparable tumor targeting properties, and

both allowed clear micro-SPECT/CT images of flank melanoma tumors as well as of B16F10 pulmonary melanoma metastases, with $^{99m}$Tc-CCMSH(Arg$^{11}$) providing images with greater resolution of metastatic lesions.[86]

Among the MC1R-specific probes for PET imaging, DOTA-Re-CCMSH(Arg$^{11}$) was labeled with $^{64}$Cu and $^{86}$Y.[87] Complex $^{64}$Cu-DOTA-Re-CCMSH(Arg$^{11}$) was unstable *in vivo* with release of free $^{64}$Cu. Aiming to improve stability, the DOTA chelator was replaced by 4,11-bis(carboxymethyl)-1,4,8,11-tetraazabicyclo[6.6.2]hexadecane (CBTE2A).[88] The complex $^{64}$Cu-CBTE2A-Re-CCMSH(Arg$^{11}$) presented B16F1 melanoma uptake comparable to $^{64}$Cu-DOTA-Re-CCMSH(Arg$^{11}$) but a significantly higher ratios of tumor to nontarget tissues. *In vivo* studies have also shown that $^{64}$Cu-CBTE2A-Re-CCMSH(Arg$^{11}$) provided better PET images than $^{86}$Y-DOTA-Re-CCMSH(Arg$^{11}$) due to increased tumor retention and kidney clearance. The conjugate DOTA-Re-CCMSH(Arg$^{11}$) was also labeled with $^{68}$Ga, and the resulting complexes displayed lower tumor uptake than the linear α-MSH analog $^{68}$Ga-DOTA-NAPamide in the same melanoma animal model.[89]

An heterobivalent complex, $^{99m}$Tc-RGD-Lys-CCMSH(Arg$^{11}$), was synthesized for dual imaging of integrin and MC1 receptor expressing tumors. Biodistribution studies in B16F1 melanoma-bearing C57BL6 mice have shown a tumor accumulation and retention higher than those found for $^{99m}$Tc-CCMSH(Arg$^{11}$), however, an extremely high kidney uptake was observed.[90]

As an alternative to metal-cyclized α-MSH analogs, a promising cyclization approach based on a lactam-bridge was introduced.[50b] The lactam-based α-MSH analogs with 12-amino acid ring size such as c[Lys-Nle-Glu-His-DPhe-Arg-Trp-Gly-Arg-Pro-Val-Asp] (CycMSH) and GlyGlu-CycMSH were conjugated to DOTA, through the peptide N-terminal, and labeled with $^{111}$In.[91] Both radiopeptides exhibited high receptor-mediated tumor uptake in B16F1 melanoma-bearing mice. The values were comparable to those found for the metal-cyclized $^{111}$In-DOTA-Re-CCMSH, but lower than those found for $^{111}$In-DOTA-Re-CCMSH(Arg$^{11}$). The insertion of a GlyGlu sequence in the basic backbone of CycMSH has reduced kidney accumulation. This result prompted the synthesis of $^{67}$Ga-DOTA-GlyGlu-CycMSH, however, the biological assessment of the radiopeptide revealed higher kidney accumulation than tumor uptake in B16F1 melanoma-bearing mice.[92] To evaluate the effect of DOTA position in the peptide backbone, GlyGlu-CycMSH was acetylated at the N-terminus. DOTA was conjugated

to the Lys residue in the peptide ring and labeled with $^{111}$In. The overall pharmacokinetic profile of the resulting radiopeptide did not improve.[78a]

Using the potent lactam-cyclized MT-II as model, a cyclic derivative with a 6-amino acid ring size, βAla-Nle-c[Asp-His-DPhe-Arg-Trp-Lys]-$NH_2$ ($\beta$AlaNleCycMSH$_{hex}$) was synthesized, conjugated to the Pz chelating unit (**Figure 1.14**), and labeled with *fac*-[$^{99m}$Tc(CO)$_3$]$^+$ moiety.[81b, 93]

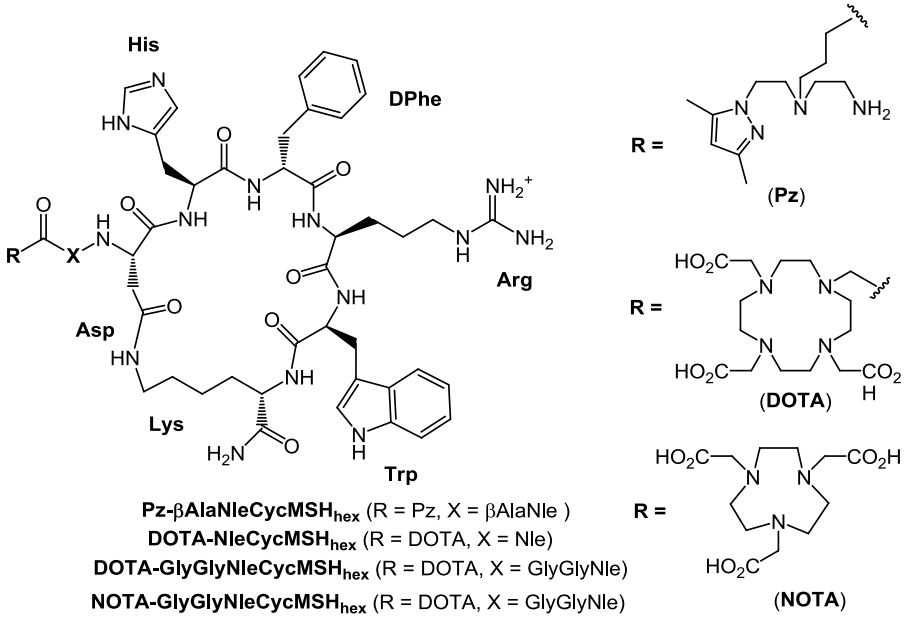


**Figure 1.14**: Lactam bridge-cyclized α-MSH derivatives: structures of Pz-βAlaNleCycMSH$_{hex}$, DOTA-NleCycMSH$_{hex}$, DOTA-GlyGlyNleCycMSH$_{hex}$ and NOTA-GlyGlyNleCycMSH$_{hex.}$

The tumor uptake of $^{99m}$Tc-Pz-βAlaNleCycMSHhex was comparable to that obtained for the lactam-based α-MSH analogs with 12-amino acid ring size in the same animal model.[92]

The macrocyclic chelator DOTA was conjugated to the N-terminus of NleCycMSHhex (**Figure 1.14**) and labeled with $^{111}$In. The resulting radiocomplex, $^{111}$In-DOTA-Nle-CycMSHhex presented a rapid and high tumor uptake, a prolonged tumor retention and a moderate kidney accumulation. When compared to $^{111}$In-DOTA-GlyGlu-CycMSH (12-amino acid ring size), the reduction of the peptide ring size dramatically increased the melanoma uptake and decreased the renal retention.[91, 94] Moreover, $^{111}$In-DOTA-Nle-CycMSHhex displayed a tumor/kidney ratio comparable to the best metal-cyclized radiopeptide $^{111}$In-DOTA-Re-CCMSH(Arg$^{11}$), suggesting a high potential of lactam-based cyclic radiolabeled α-MSH analogs for MC1R melanoma

targeting. Thus, the effects of amino acid linkers on melanoma-targeting and pharmacokinetic properties of $^{111}$In-DOTA-Nle-CycMSHhex were evaluated.[95] The introduction of the −GlyGly− and −GlyGlu− linkers between the DOTA and the Nle-CycMSHhex did not affect the receptor recognition ability of DOTA-GlyGlyNle-CycMSHhex and DOTA-GlyGluNle-CycMSHhex. However, the insertion of −GlyGlu− linkers between DOTA-Nle and the remaining peptide moiety had a negative impact on the MC1R targeting properties of DOTA-NleGlyGlu-CycMSHhex. Biological evalution of these $^{111}$In-labeled peptide in B16F1 melanoma-bearing mice revealed that $^{111}$In-DOTA-GlyGlyNle-CycMSHhex kept its high melanoma uptake while reducing the renal and liver uptake as compared to $^{111}$In-DOTA-Nle-CycMSHhex.

The effect of ring size reduction on melanoma imaging in B16F1 tumor bearing mice was also reported for $^{67}$Ga-labeled CycMSHhex derivatives.[96] Triazacyclononane-1,4,7-triacetic acid (NOTA) or DOTA were conjugated to GlyGlyNle-CycMSHhex and labeled with $^{67}$Ga. The $^{67}$Ga-NOTA-GlyGlyNle-CycMSHhex presented the highest melanoma uptake and tumor/kidney ratios among the radiolabeled α-MSH analogs for melanoma imaging by SPECT.[96]

In an attempt to expand melanoma imaging to PET, NOTA-GlyGlyNle-CycMSHhex and DOTA-GlyGlyNle-CycMSHhex were labeled with $^{64}$Cu.[97] The substitution of DOTA with NOTA dramatically increased the melanoma uptake and decreased the renal and liver uptake of $^{64}$Cu-NOTA-GlyGlyNle-CycMSHhex as compared to $^{64}$Cu-DOTA-GlyGlyNle-CycMSHhex. Moreover, high melanoma uptake coupled with low accumulation in non-target organs suggested $^{64}$Cu-NOTA-GlyGlyNle-CycMSHhex as a lead radiolabeled peptide for future imaging of melanoma by PET.[97]

### 1.4.2. Sentinel Lymph Node

The sentinel lymph node (SLN) is the first node receiving lymphatic drainage directly from a region of primary tumors.[98] Moreover, recent studies demonstrated that SLN shows enhanced lymphangiogenesis even before cancer metastasis and may function as a permissive 'lymphovascular niche' for the survival of metastatic cells.[55] Thus, SLN is regarded as useful prognostic information for some types of cancer, particullary melanoma as 80% of metastasis disseminate through the lymphatic system, while 20% may occur through the blood vasculature or by direct seeding.[99] Nowadays,

the SLN concept is also clinically applied to patients with breast, lung, colon, head and neck cancer.[100]

Current knowledge on the prognostic significance of individual metastatic cells, small metastatic cell clusters or micrometastases (0.2 - 2 mm in diameter) in lymph nodes varies depending on tumor type.[99] The malignant cells disseminating through lymphatic vessels may also produce locoregional metastasis (so-called in transit or satellite lesions) by proliferation *in situ* inside the vessel.[101] In the case of melanoma, treatment follow-up studies indicate that metastases under 0.1 mm in diameter might not have an impact on prognosis. [102] However, larger size metastatic melanoma lesions in lymph nodes correlate with shorter progression-free survival.[99] Thus, SLNs are not only common in melanoma metastization but also associated with increased tumor lethality, as the number of lymph nodes infiltrated with malignant cells have an impact in predicting a patient's survival outcome.

Accurate identification and excision of the SLN by imaging techniques has an important therapeutic and prognostic significance in patients with newly diagnosed cancers. Conventional non-invasive imaging modalities such as X-ray, MRI and US have been clinically explored to quantitatively assess functional lymphatic vasculature and provide whole-patient imaging within human subjects. However, these techniques do not allow cancer staging of lymph nodes and they usually require the administration of high amounts of an unspecific drug.[5b, 103] The high sensitivity of nuclear imaging techniques allows the intradermal administration of a radiopharmaceutical to obtain information about the lymphatic drainage. This technique is called lymphoscintigraphy.[5b]

Traditionally, axillary-lymph-node dissection (ALND) was recommended for patient with sentinel node metastases.[104] Advances on the design of portable gamma-detecting probe improved the accuracy of the lymph node excision through radioguided surgery in a procedure called sentinel lymph node biopsy (SLNB). This technique reduced patient's postoperative morbidity rates when compared to ALND and also enabled tumor staging.[5b, 105] The SLNB is typically performed by injecting a radiolabeled colloid and a blue dye (e.g. Isosulfan Blue®). The radiotracer is used pre- and intraoperatively for anatomical localization of the node with a hand-held gamma-detecting probe and to guide the dissection. The blue dye is typically injected at the beginning of surgery to facilitate the visualization of the lymphatic drainage.[102b] Although there is some debate about the administration route, the colloid is typically

administered intradermally for sentinel lymph node detection (SLND) in melanoma.[54] The radiolabeled particles migrate from the injection site into the lymphatic channel mainly by passive diffusion, and they are cleared from the lymph as foreign matter based on active saturable phagocytosis. However, the accuracy of the biopsy relies heavily on the accuracy of the functional guidance provided during the surgical procedure and on the specific uptake of the radiopharmaceuticals in the SLN.

#### 1.4.2.1. Mannose Receptor

Mannose receptor (MR) belongs to a sub-class of lectin receptors that is highly expressed in mammalian lung macrophages, liver nonparenchymal and parenchymal cells.[106] It is well known to participate in pathogen recognition, clearance of endogenous serum glycoproteins and antigen presentation.[106b]

This extracelullar receptor contains an amino-terminal cysteine-rich domain that recognizes mannose-terminated glycoproteins such as N-acetylgalactosamine.[106b, 107] The strenght and specificity of mannose-lectin interaction is weak due to the flat surface of the receptor. However, binding can be significantly improved by the increase number of carbohydrate molecules that are presented to the receptor.[108] **Figure 1.15** presents the structure of MR bound to 4-sulfated-N-acetylgalactosamine (4-$SO_4$-GalNAc).[109]

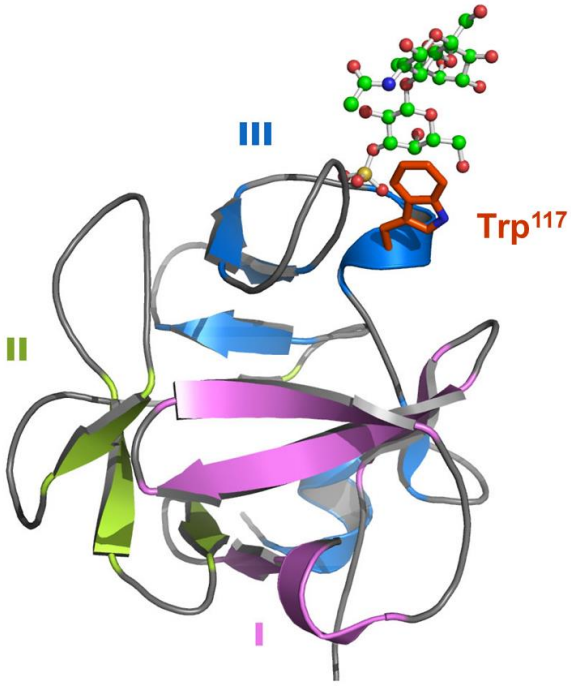


**Figure 1.15**: Mannose receptor structure bound to 4-sulfated-N-acetylgalactosamine (4-$SO_4$-GalNAc). Ribon diagram of MR structure with lobes I, II and III indicated with diferent colors. Dissulphide bounds are yellow and 4-$SO_4$-GalNAc is shown in ball-and-stick representation. $Trp^{117}$ is highlight in orange.[109]

Beyond its function in the innate and adaptive immune system, MR may play a key role in the metastatic behavior of cancer cells as high receptor expression was detected in tumor-associated macrophages.[110] The presence of MR in human lymphatic endothelium, and not in blood vessel endothelium, may also suggest that the entrance of tumor cells in lymphatics might be mediated by the receptor.[111] Morevoer, it has been demonstrated that MR expression can be a specific tool to measure the density of human lymphatic vessels in certain types of tumors.[112] These observations make MR an attractive marker for targeting the SLN.

#### 1.4.2.2. Radiopharmaceuticals for SLN Detection

SLND in nuclear medicine is performed by injecting radiolabeled nanoparticles in the area where a tumor is located.[113] In general, particles smaller than 5 nm leak to the bloodstream and are not ideal to target the lymphatic system, whereas particles

larger than 100 nm are trapped in the interstitial space, resulting in masking of the SLNs that are usually situated only a few centimeters away from the injection site.[103, 114]

The $^{99m}$Tc-antimony trisulfide colloid was the first radiopharmaceutical used for lymphatic mapping, however, several adverse reactions were reported due to the toxicity of the metal. Alternatively, the use of gold ($^{198}$Au) colloids (5–30 nm) was limited by the high radiation dose at the site of injection and the high-gamma energy of gold.[113] Currently, $^{99m}$Tc sulfur colloid ($^{99m}$Tc-SC) and $^{99m}$Tc-labeled human serum albumin (HSA) are used as radiopharmaceuticals for SLND. The particle size of these agents is the most important differential factor dictating the kinetics and their uptake in SLN. In fact, $^{99m}$Tc-SC (e.g. Nanocis®) is available with particle size of ±80 nm and the clearance from the injection site is slow, leading to masked SLNs that are usually situated only a few centimeters away from that area. $^{99m}$Tc-labeled HSA (6-8 nm) rapidly clears from injection sites, however, it travels through the whole lymph node chain to the systemic circulation. Owing to this feature, $^{99m}$Tc-labeled HSA present low SLN extraction rates. Overall, the radiopharmaceuticals currently applied for SLND suffer either from slow clearance rate from the injection sites or low residence times in the SLN or from both. Additionally they are not universally approved by the regulatory authorities for this specific application.

In an attempt to improve SLN uptake, $^{99m}$Tc-labeled dextrans with diferent molecular weights or $^{99m}$Tc-labeled cysteamine dextan were evaluted for SLND, however, unfavorable biological profile was found.[115]

The conjugation of mannose molecules to $^{99m}$Tc-labeled macromolecules like polylysine, albumin, and dextrans showed that the resulting compounds, although of few nanometers in size, can be trapped by the sentinel node in a saturable mode due to their recognition by the MR, either expressed on lymph node macrophages or lymphatic endothelial cells.[106a, 116] As an example **Figure 1.16** shows some of the mannosylated nanocompounds proposed for SLND.

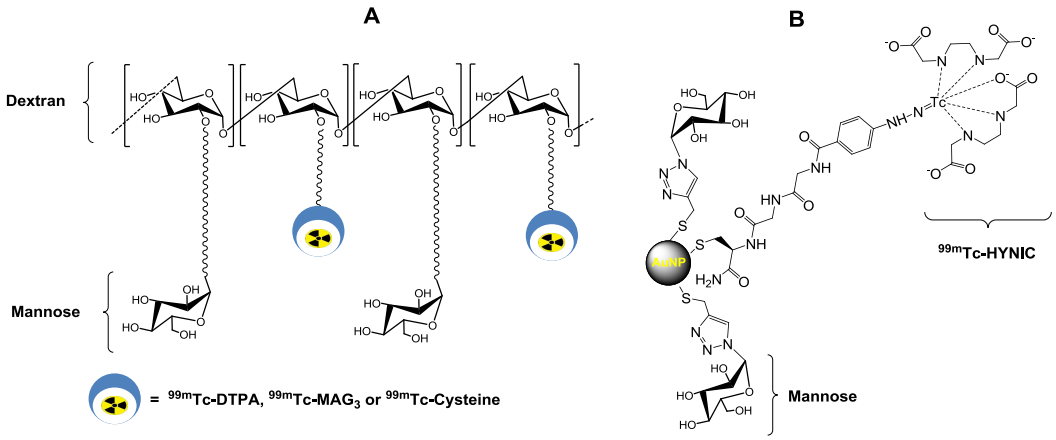


**Figure 1.16**: Schematic representation of $^{99m}$Tc-labeled nanotracers proposed for SLND: A) mannosylated $^{99m}$Tc-labeled dextran derivatives and B) mannosylated $^{99m}$Tc-labeled gold nanoparticle (AuNP).

Among these examples, the mannosylated $^{99m}$Tc-diethylene triaminepentaacetic acid (DTPA)-labeled dextran ($^{99m}$Tc-Tilmanocept) reported by Vera and co-workers, has shown the most promising *in vivo* behavior, being currently in phase 3 clinical trials for SLND in melanoma and breast cancer.[116c, 117] This small particle size (7.1 nm) tracer not only exibits rapid injection site clearance and specific accumulation on SLN, but also low distal node accumulation in a rabbit animal model.

The mannosylated $^{99m}$Tc(I)-cysteine-labeled dextran is one of the few fully characterized compounds proposed for SLND and presents a particle size (8.3 nm) similar to $^{99m}$Tc-Tilmanocept.[118] Biodistribution studies in Wistar rats showed that mannosylated $^{99m}$Tc(I)-cysteine-labeled dextran presents a fast clearance from injection site and high uptake and retention in the SLN.[118-119] Moreover, the biological efficacy of this compound is dose dependent and a low amount (2.5 µg) is required for high SLN uptake with minimal radioactivity accumulation in non-target organs.[119] Although the biological profile is quite similar to $^{99m}$Tc-Tilmanocept, mannosylated $^{99m}$Tc(I)-cysteine-labeled dextran has a shorter synthetic pathway.

AuNPs functionalized with mannose units and 6-Hydrazinopyridine-3-carboxylic acid (HYNIC) were labeled with Tc(V).[120] $^{99m}$Tc(V)-HYNIC-AuNP-mannose was obtained with low radiochemical purity and, after purification, was injected subcutaneously in Wistar rats. Biodistribution results showed that $^{99m}$Tc-HYNIC-AuNP-mannose not only allows a clear visualization of the first lymph node, displaying the highest SLN uptake value among the reported examples, but also

presents a clearance from the injection site similar to $^{99m}$Tc-SC.[120] Mannosylated human serum albumin (MSA) was funcionalized with NOTA and labeled with $^{68}$Ga for PET imaging.[121] Biodistribution results of $^{68}$Ga-NOTA-MSA in mice showed accumulation in the liver and bladder with low uptake in the lymphatic nodes.

In an attempt to improve the efficacy of the clinical procedure that requires the injection of radiocolloid and a dye prior to biopsy, albumin and dextran have been used as scaffolds to design bimodal probes. An alternative to optical detection technology has been found in near-infrared (NIR) field, which allows real-time detection of the lesion to a depth of a few centimeters.[5c, 122] Thus, a NIR fluorophore provides greater sensitivity and depth penetration as compared to the red absorbance of Isosulfan Blue and would enable the excision of the lymph node after radioactive decay.[5c, 123] The incorporation of the NIR fluorophore and a radionuclide in the same imaging agent overcomes the kinetics variation of both individual agents through the lymphatic system, and in the case of a target specific probe, a persistent SLN retention would be imparted by receptor binding even after prolonged interval between the administration of the dual tracer and SLN mapping.[114] Moreover, the synergistic effect of a bimodal imaging probe could enable real-time SLND by radio- or NIR optical guided surgery as well as fluorescent histology. Such hypothesis were confirmed in a comparative study between $^{99m}$Tc-labeled albumin (NanoColl®) and a bimodal probe containing a near infrared fluorophore (indocyanine green – ICG) non-covalently bound to the albumin radiocolloid.[124]

Owing to the good biological properties of mannosylated dextran derivatives mentioned above, Vera and colaborators have reported receptor-targeted fluorescent radiotracers for nuclear and optical imaging techniques such as PET/NIR and SPECT/NIR.[123b, 125] In both cases, cyanine derivative (near infra-red fluorophore) were conjugated to dextran backbone. Biological evaluation has shown a significant uptake of PET/NIR tracer in the first lymph node in mouse animal model. Despite the minimal migration to distal lymph nodes, high amount of activitiy remains at the injection site.[123b] A comparative study between $^{99m}$Tc-Tilmanocept and the SPECT/NIR tracer revealed that the conjugation of NIR fluorophore to dextran backbone did not affect the receptor targeting properties and pharmacokinetics of the macromolecule, allowing clear visualization of the first lymph node in mouse animal model by optical imaging.[125]

# 2

## $^{99m}$Tc(CO)$_3$-labeled Homobivalent α-MSH Analogs for MC1R-Targeting

# 2. $^{99m}$Tc(CO)$_3$-labeled Homobivalent α-MSH Analogs for MC1R-Targeting

## 2.1. Introduction

Multivalent interactions are frequently found in nature where they increase the affinity of weak ligand–receptor interactions such as in the antibody-antigen complex formation or DNA–DNA duplex formation by multiple weak interactions between individual complementary nucleotides.[126] Biophysical modeling also suggests that multivalent interactions can significantly increase specificity because multivalent ligands can bind in ways that are inaccessible to monovalent compounds.[127] The receptor mechanisms that are unique to multivalent ligands are depicted in **Figure 2.1**.

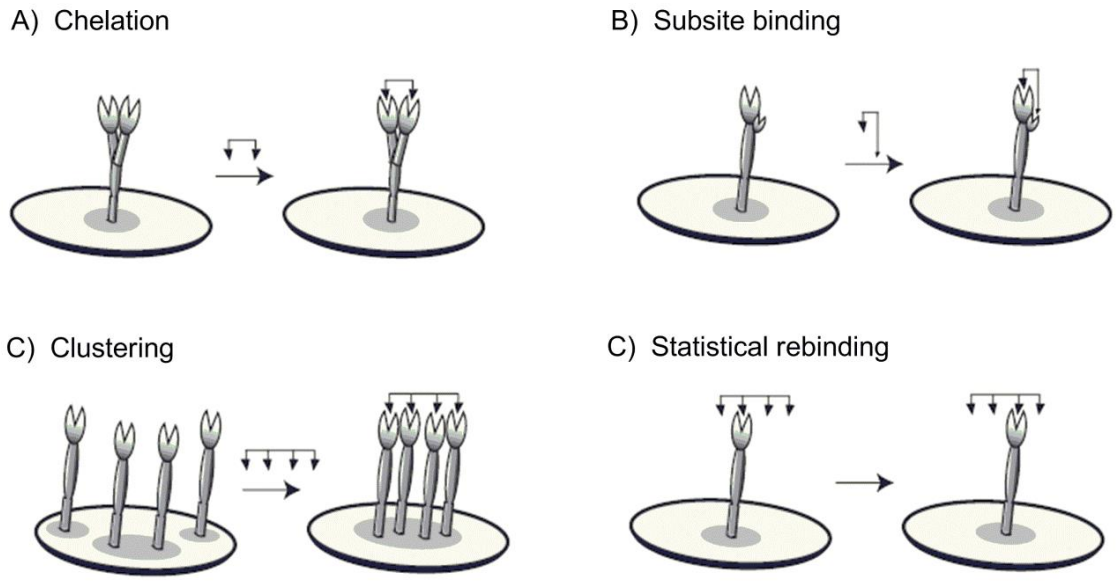


**Figure 2.1**: Receptor binding mechanisms unique to multivalent ligands.[127]

The multivalent approach, which is characterized by the use of constructs displaying multiple copies of a molecular recognition element, aims to enhance the affinity and/or specificity for a target by different mechanisms. Thus, inspired by this principle, multivalent structures have become an attractive strategy for the development of new drugs for diagnosis or therapy. When applied to the design of nuclear probes, this strategy aims to amplify the imaging signal, a crucial issue for a more effective targeted tumor imaging.[50a, 127-128] The most successful examples involve the use of radiolabeled multimeric cyclic RGD peptides, where an increase in peptide multiplicity

significantly enhanced the integrin $\alpha_v\beta_3$ binding affinity with improvement of the tumor targeting ability.[129]

The first examples of α-MSH multivalent constructs comprise a set of various α-MSH molecules coupled to albumin, thyroglobulin and tobacco mosaic virus, which displayed a 1500-fold higher affinity than α-MSH alone.[130] More recently, a comparative study between targeted polymeric micelles decorated with multiple copies of short linear α-MSH analogs showed enhanced MC1R binding affinity when compared to the non-targeted micelles.[77b] However, receptor binding affinity of the functionalized micelles was 10 fold lower than that of the monovalent ligand.

Structure-activity studies have demonstrated that enhanced binding affinity can also be achieved with bivalent constructs.[131] The effect of flexible (polyethylene glycol – PEG) or rigid (phenyl, biphenyl and phenylnaphtyl) linkers with variable length in the affinity of short bivalent α-MSH constructs has been also evaluated. Despite not being conclusive about the optimal linker to span two GPCRs on the melanoma cells, *in vitro* studies have shown that bivalent ligands with a flexible linker (less than 25 Å) displayed 8 to 10 fold higher affinity than the monovalent ligand.[131b] For small rigid phenyl linkers the results have also demonstrated that bivalent constructs displayed 22 fold higher affinity than monovalent ligands, being the effect even more pronounced for mono ligands with low binding affinity.[131a] In spite of the research efforts towards the preparation of bivalent α-MSH constructs with enhanced affinity, few attempts have been made to evaluate their *in vivo* MC1R-targeting properties. Indeed, to the best of the author knowledge, only a few reports on the *in vivo* evaluation of radiolabeled homobivalent α-MSH conjugates have been described.[132] The conjugation of linear α-MSH analogs to BFCs such as DTPA or DOTA gave peptide conjugates with enhanced binding affinity compared to the monovalent counterparts.[132-133] However, the $^{111}$In-DOTA-labeled homodimeric peptide conjugates presented low tumor uptake with unfavorable tumor/normal tissues ratios in B16F1 melanoma-bearing mice.[133]

The encouraging results obtained with the monovalent probe $^{99m}Tc(CO)_3$-pz-**NAPamide** (**Tc4**), which exhibited moderate MC1R tumor uptake and favorable excretion kinetics in B16F1 melanoma bearing mice,[82b] prompted us to explore the bivalent concept. Therefore, aiming at the design of novel peptide-based radioactive probes with improved MC1R-targeting properties and superior tumor to normal tissue ratios, this chapter includes the synthesis and characterization of mono- and homo-bivalent **NAPamide** conjugates (**L4**, **L5** and **L6**) and the corresponding rhenium

complexes (**Re4**, **Re5** and **Re6**). The biological evaluation of the $^{99m}Tc(CO)_3$-labeled homobivalent peptides **Tc5** and **Tc6** is also described and discussed.

## 2.2. Homobivalent NAPamide Conjugates

### 2.2.1. Synthesis and Characterization of the Pyrazolyl-diamine Chelators

The MC1R-binding affinity of bivalent ligands depends not only on the nature of the linkers between the targeting vectors, but also on the distance between those vectors, as mentioned before.[131] Therefore, based on the *tert*-butyloxycarbonyl (Boc)-protected bifunctional chelator **L1-Boc** (**Figure 2.2**), which was used for the preparation of the monovalent **NAPamide** conjugate, we have prepared the bifunctional chelators **L2-Boc** and **L3-Boc**. These compounds, with different overall architecture, contained the pyrazolyl-diamine chelating system ($N_3$ donor atom set) and two carboxylate groups for direct conjugation to **NAPamide**.

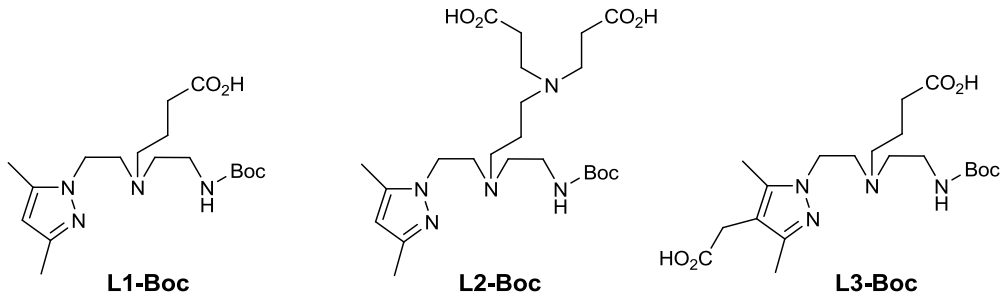


**Figure 2.2:** Pyrazolyl-diamine based bifunctional chelators **L1-Boc** – **L3-Boc**.

**L2-Boc** and **L3-Boc** were synthesized from the corresponding precursors **I** and **II** (**Scheme 2.1**). These precursors were both prepared accordingly to a procedure already described by our group.[51a, 51d, e]

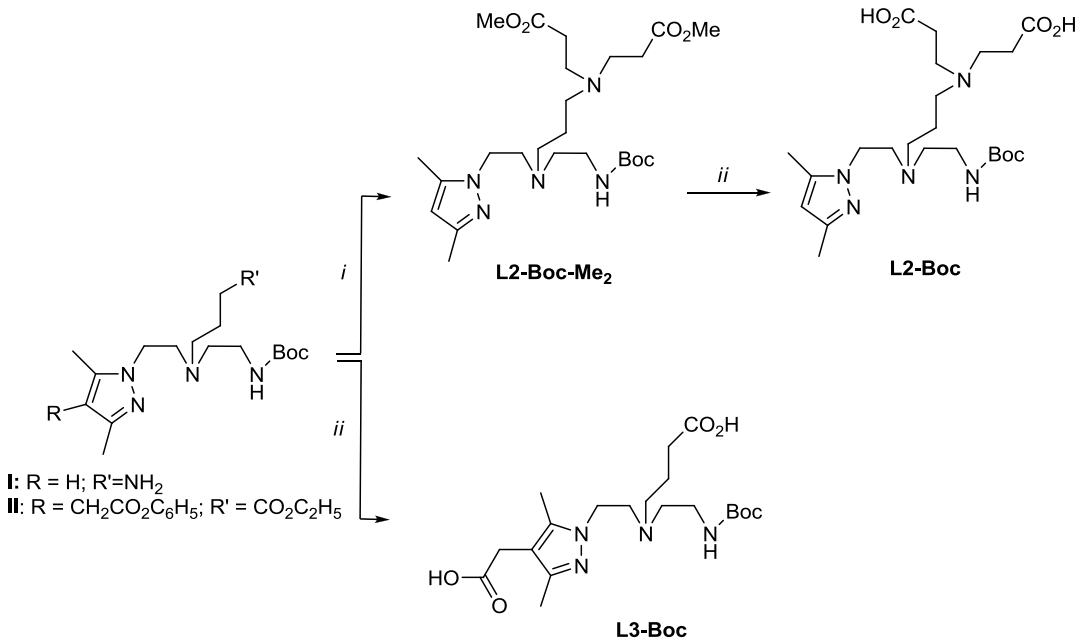


**Scheme 2.1**: Synthesis of **L2-Boc** and **L3-Boc**. (*i*) $CH_2CHCO_2CH_3$, dry MeOH; (*ii*) NaOH, tetrahydrofuran (THF)/$H_2O$.

**L2-Boc** was synthesized in good overall yield (58%) by a aza-Michael addition reaction of the primary amine in **I** with excess methyl acrylate, followed by alkaline hydrolysis of the intermediate diester. **L3-Boc** was prepared by alkaline hydrolysis of precursor **II**.

The bivalent chelators were characterized by the usual analytical techniques in chemistry, including Reversed-Phase High Performance Liquid Chromatography (RP-HPLC), Electrospray Ionization Mass Spectrometry (ESI–MS) and Nuclear Magnetic Resonance (NMR) spectroscopy. The use of 2D-NMR experiments ($^1$H-$^1$H g-COSY and $^1$H-$^{13}$C g-HSQC) was crucial for peak assignment in the NMR spectra, and for the full characterization of the chelators. As an illustrative example, the fully assigned $^1$H-NMR spectrum ($D_2O$) of **L2-Boc** is presented in **Figure 2.3**.

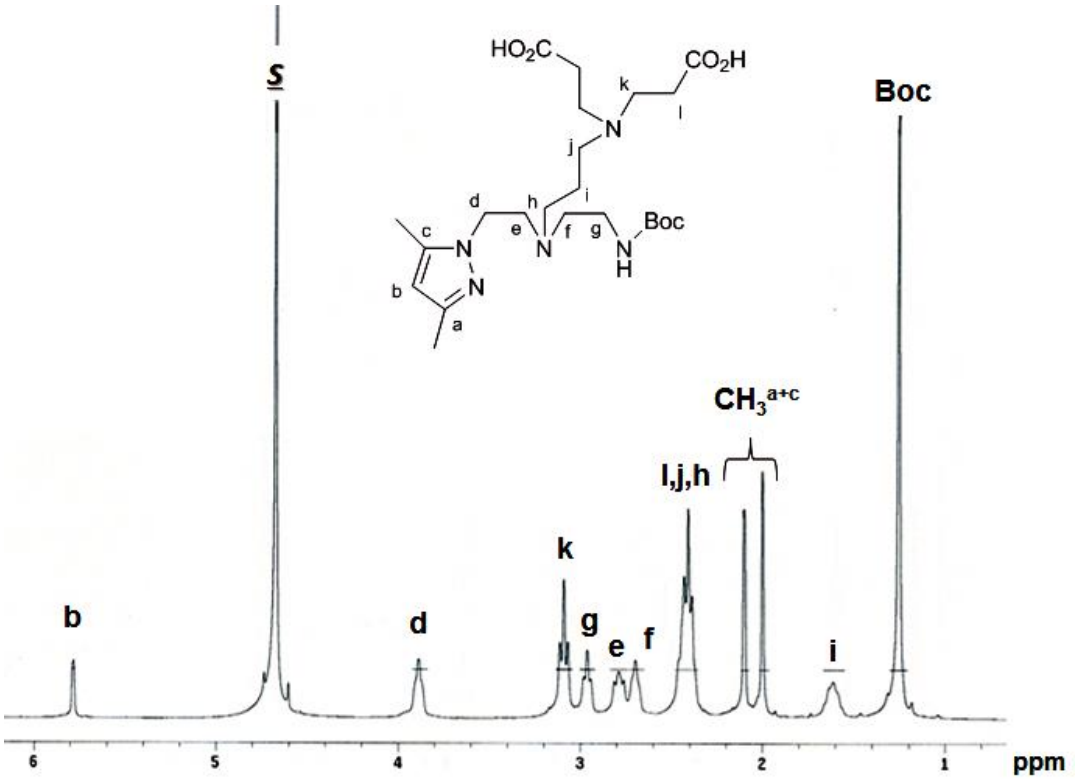


**Figure 2.3**: $^{1}$H-NMR spectrum of **L2-Boc** in $D_2O$ (S = residual water).

It presents the typical sharp singlet peak for the $H^b$ proton (δ 5.78) and the methyl groups of the azolyl-ring (δ 2.10/2.00). Resonances for all methylenic protons of the pyrazolyl-diamine backbone as well as for the pendant arms $H^k$ and $H^l$ were also found.

### 2.2.2. Synthesis and Characterization of NAPamide

The linear α-MSH analog **NAPamide** (Ac-Nle-Asp-His-DPhe-Arg-Trp-Gly-Lys-$NH_2$) as well as the other peptides described in this thesis were prepared through the principle of Solid Phase Peptide Synthesis (SPPS). This synthetic methodology was developed by Bruce Merrifield (Nobel Prize in Chemistry 1984) in the 1950s and 1960s, through the introduction of functionalized solid supports that enable amino acid coupling.[134] The principle of SPPS is briefly illustrated in **Figure 2.4**.

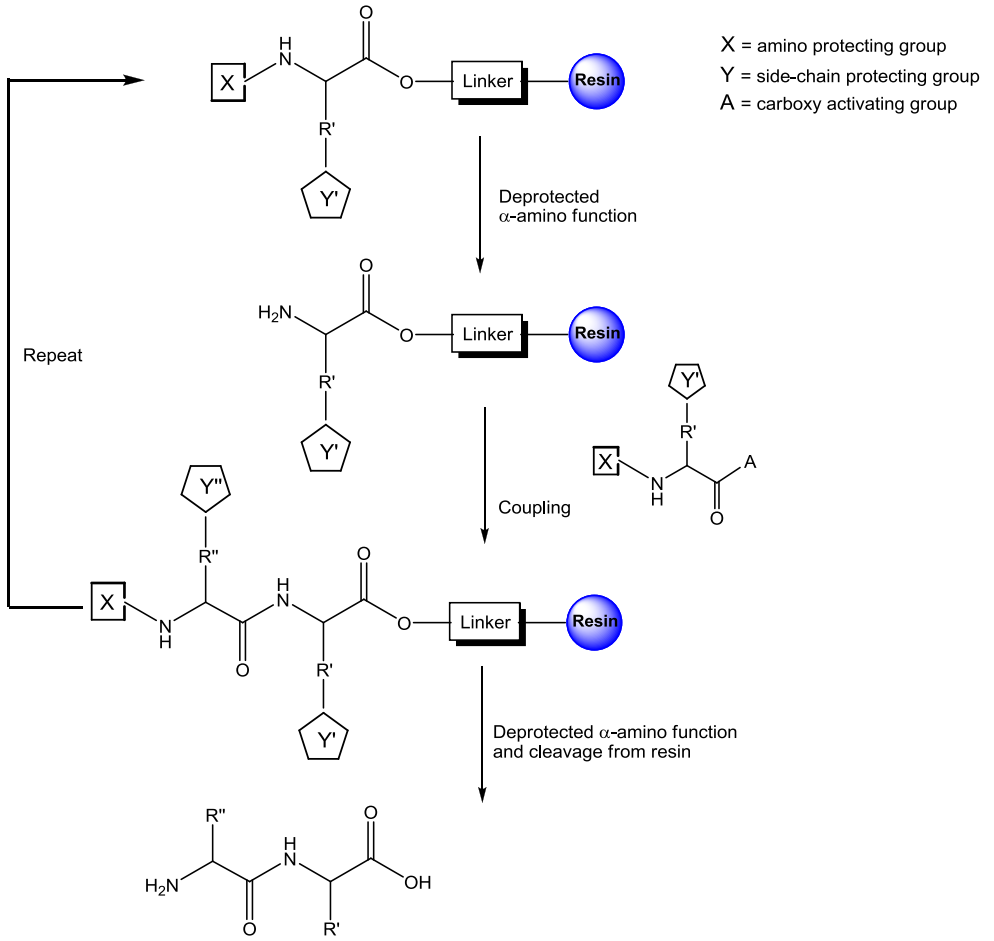


**Figure 2.4**: The solid phase peptide synthesis (SPPS) principle.

SPPS is based on sequential addition (C→N direction) of Nα- and side-chain protected amino acids to a functionalized insoluble polymeric support (resin). Typically, the C-terminal amino acid is first anchored by the carboxylate to the resin via a linker. Then, the Nα-protecting group can be removed without affecting the side-chain protecting groups and the peptide chain is prepared for the next coupling cycle.[134b, 135]

The two most widely used Nα-protecting groups in SPPS are the fluoren-9-ylmethyloxycarbonyl (Fmoc) and the tert-butoxycarbonyl (Boc), each defining an overall strategy for SPPS. The chemical conditions for removal of these transient protecting groups, i.e. base *versus* acid, each define a 'chemical window' of opportunities for the other chemical steps in the overall SPPS strategy.[134b] The Boc strategy, initially introduced by Merrifield, requires trifluoroacetic acid (TFA) or a similar acid for repetitive removal of the Boc groups, and hydrofluoric acid (HF) for peptide cleavage from the solid support. Thus, the Boc strategy also relies on differences in acid lability of the Nα-and side-chain protecting groups. The Fmoc

strategy is often preferred over the Boc strategy for routine synthesis, as the latter normally requires the use of corrosive and toxic HF and the necessity for a HF apparatus. On the contrary, the Fmoc group can be removed under mild conditions with secondary amines, typically 1:4 piperidine–DMF.[134b]

Each peptide or peptide-conjugate synthesis has its own requirements. Indeed, in the case of the homobivalent **NAPamide** constructs, a partially protected peptide (**Pp-NAPamide**) was synthetized to facilitate the preparation of the conjugate in solution and to protect the peptide side-chain functional groups from undesirable side-reaction (**Figure 2.5**). The only reactive group in this peptide precursor is the free primary amine of Lys$^8$, which will be used for conjugation to the chelator.

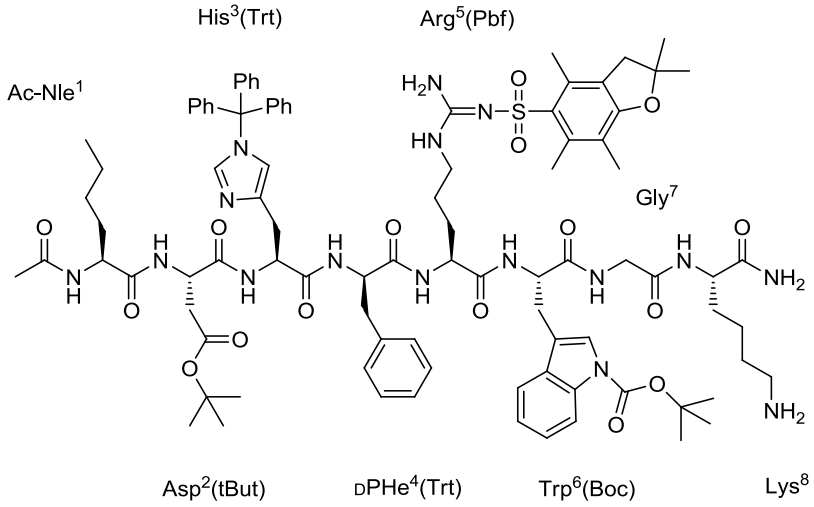


**Figure 2.5:** Schematic representation of **Pp-NAPamide**.

Therefore, a solid-phase support with a hyperacid labile linker (flow-compatible Fmoc-amino-xanthen-3-yloxy-Merrifield resin – Sieber Amide resin) that enables the synthesis of fully or partially protected peptide with amide group at the C-terminus was selected to assemble the peptide sequence. Moreover, the following protecting groups were used for orthogonal protection of the corresponding amino acids side-chain: trityl (Trt) for His, Boc for Trp, *tert*-butyl (*t*-Bu) for Asp, pentamethyl-2,3-dihydrobenzofuran-5-sulfonyl (Pbf) for Arg, and 4-methyltrityl (Mtt) for Lys. The use of the hyperacid sensitive Mtt protecting group and the Sieber Amide resin allows, simultaneously, a selective deprotection of the ε-amino group of Lys and peptide cleavage from the resin after treatment with 1% trifluoroacetic acid (TFA) in

dichloromethane (DCM). Hence, the peptide sequence was prepared by SPPS on a CEM automated 12-channel microwave peptide synthesizer (Liberty®) using standard continuous-flow technology and Fmoc strategy at 0.1 mmol scale. The use of microwave irradiation during the peptide synthesis allowed dramatic time reduction during coupling and Nα-deprotection. Although this synthesis was straightforward, microwave heating has also been proven especially relevant for peptide sequences which might form β-sheet type structures and for sterically difficult couplings.[134b]

After cleavage, appropriate work-up and purification by RP-HPLC (Method D, experimental section **7.2**), the partially protected peptide **Pp-NAPamide** (> 95% purity) was characterized by ESI-MS. The peak found at m/z = 876.1 corresponds to $[M+2H]^{2+}$ of the desired peptide. The minor peak found at m/z = 1507.8 corresponds to a peptide species in which the Trt group was also removed from the His[3] side-chain, showing that diluted solution of TFA have also the ability to remove this protecting group (**Figure 2.6**).

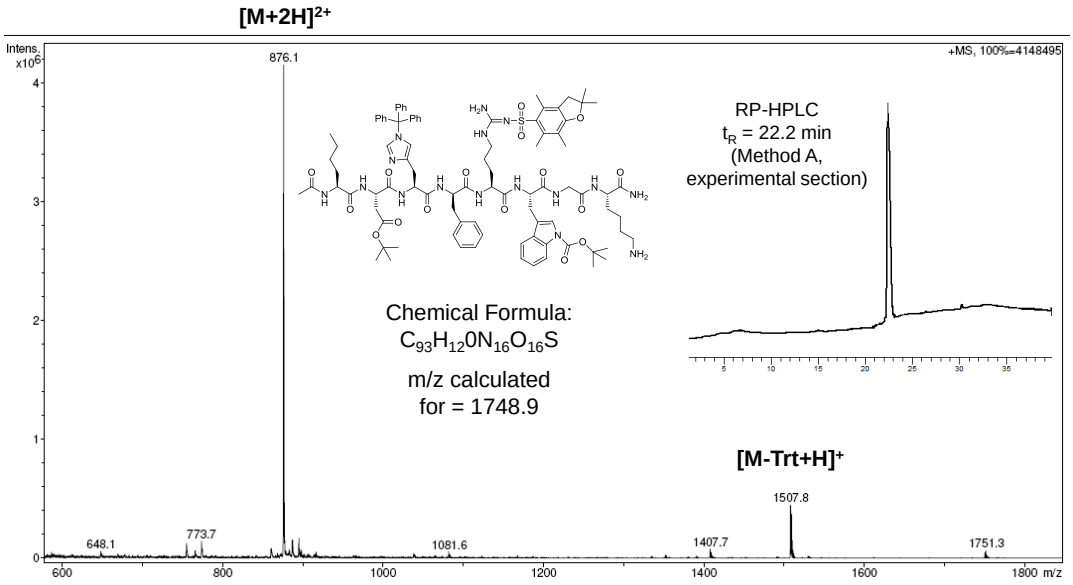


**Figure 2.6**: ESI-MS spectrum and RP-HPLC chromatogram of **Pp-NAPamide**.

We have also prepared the fully unprotected **NAPamide** peptide upon treatment of the protected peptide in the solid support with a standard cocktail solution of 95% TFA, 2.5% triisopropylsilane (TIS), 2.5% $H_2O$. After purification by semi-preparative RP-HPLC, the peptide was fully characterized by ESI–MS and NMR spectroscopy, namely, correlated ($^1$H-$^1$H COSY), total correlated ($^1$H-$^1$H TOCSY), nuclear Overhauser enhancement ($^1$H-$^1$H NOESY), rotating frame nuclear Overhauser ($^1$H-$^1$H ROESY) and heteronuclear single quantum coherence ($^1$H-$^{13}$C and $^1$H-$^{15}$N HSQC) spectroscopy.

The peaks found in the ESI-MS spectrum of **NAPamide** at m/z = 1099.8 and m/z = 550.6 correspond to $[M+H]^+$ and $[M+2H]^{2+}$, respectively.

The signals of the $^1$H-NMR spectrum of the peptide in $H_2O/D_2O$ (9:1 v/v) were assigned by standard sequential assignment methods, which comprises two stages.[136] In the first stage, amino acid spin systems are identified using 2D COSY and 2D TOCSY spectra, and classified to amino acid type. Non-repeated amino acids with unique spin systems are assigned to residue number in this stage (Nle, Arg, Gly and Lys in **NAPamide**). Aromatic rings of His, DPhe and Trp were connected to their correponding AMX spin system by the rotating frame overhause effect (ROE) cross-peaks between the beta/beta' protons and the delta ring protons (δ2 in His, δδ' in DPhe, and δ1 and ε3 in Trp). In this way, all residues of **NAPamide** were fully attributed in the first assignment step.

The $^{13}$C and $^{15}$N resonances were assigned from the cross-correlations observed in the corresponding HSQC between the proton and the bound carbon or nitrogen, respectively. The $^1$H, $^{13}$C and $^{15}$N chemical shifts of **NAPamide** at 2.5 and 25 ºC are listed in the experimental section.

The chemical shift values of the amino acids are conventionally used to predict the structural propensities of peptides and proteins in aqueous solvents.[137] Indeed, the chemical shift deviation (Δδ) of the observed $^1H_{\alpha,}$ $^{13}C_\alpha$ and $^{13}C_\beta$ chemical shift for a given amino acid in a given peptide from its corresponding random coil (RC) value ($\Delta\delta = \delta^{observed} - \delta^{RC}$ ppm) has been used for many years to qualitatively estimate the structure of a peptide.[138]

As depicted in **Figure 2.7**, the chemical shift deviations of $^1H_\alpha$ and $^{13}C_\alpha$ for most residues in the peptide sequence ($\Delta\delta_{H\alpha} < 0.13$ ppm, except for Arg, and $\Delta\delta_{C\alpha} < 0.3$ ppm) are within the range of the RC values (± 0.1 ppm for $^1$H and ± 0.5 ppm for $^{13}$C), suggesting that **NAPamide** might present mainly a random coil conformation in solution.[139]

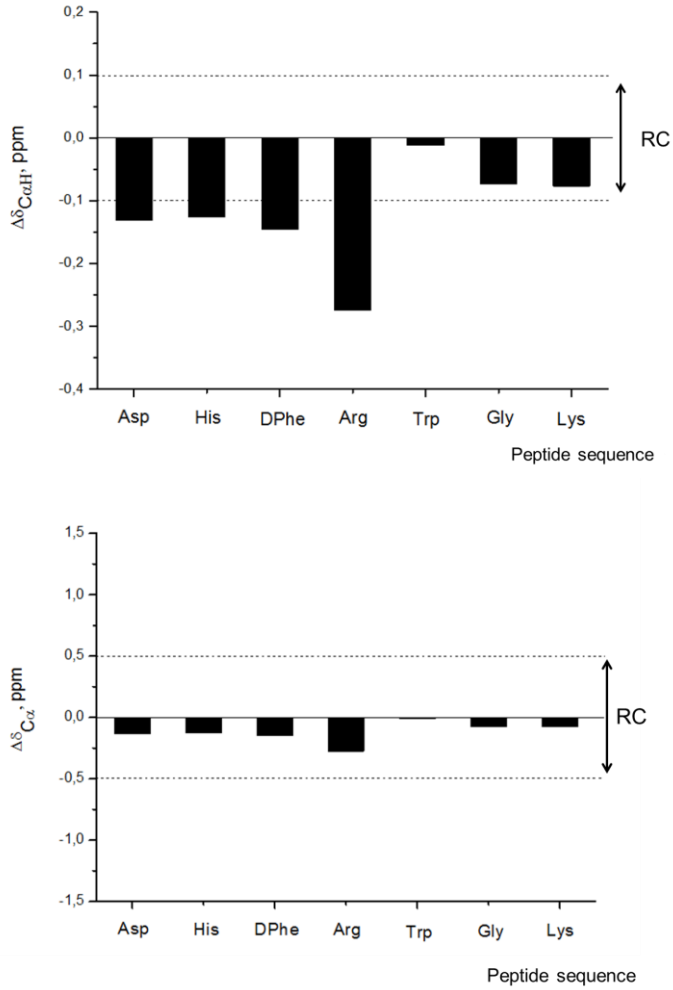


**Figure 2.7**: Histograms showing the chemical shift deviation of $^{1}H_{\alpha}$ (top) and $^{13}C_{\alpha}$ (bottom) values for amino acid residues of **NAPamide** in aqueous solution at pH 2.5 and 5 ºC.

Regular secondary structure elements are more strongly identified from non-sequential nuclear Overhauser effect (NOE), as the NOE cross-peak is observed only when two protons are spatially close (at a distance shorter than 5 Å; NOE intensity depends on $1/r^6$, being r the inter proton distance), and each type of secondary structure element is characterized by a particular pattern of short range NOEs. For instance, α-helices are characterized by a stretch of strong and medium $NH_i$–$NH_{i+1}$ NOEs, and weak $C_{\alpha}H_i$–$NH_{i+1}$ NOEs, sometimes supplemented by $NH_i$–$NH_{i+2}$ and $C_{\alpha}H_i$–$NH_{i+4}$ NOEs. β-strands, on the other hand, are characterized by very strong $C_{\alpha}H_i$–$NH_{i+1}$ NOEs and by the absence of other short-range NOEs involving the NH and $C_{\alpha}H$ protons. β-sheets can be identified and aligned from interstrand NOEs involving the NH, $C_{\alpha}H$, and $C_{\beta}H$ protons.[138]

The NOESY data has shown mainly sequential assignments $C_\alpha H$-$NH_{i+1}$, $C_\beta H$-$NH_{i+1}$ (**Figure 2.8**) suggesting again a random coil conformation for **NAPamide**. The only non-sequential NOE found for the free peptide is a weak $C_\alpha H$-$NH_{i+2}$ NOE cross peak between Nle-His (**Figure 2.8**) present at 5 ºC.

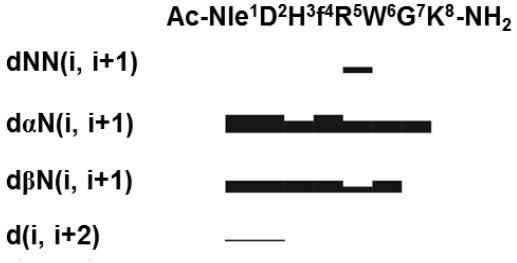


**Figure 2.8**: Summary of the NOE intensities derived from ROESY data observed for **NAPamide** at pH 2.5 and 5 ºC. The height of the bar indicates the strength of the NOE. The NOE volumes were categorized as strong (1.8-3.0 Å), medium (1.8-3.5 Å), or weak (1.8-5.0 Å). "f" stands for DPhe.

### 2.2.3. Synthesis and Characterization of NAPamide Conjugates

**L1-Boc – L3-Boc** were conjugated to **Pp-NAPamide**, via 2-(7-Aza-1H-benzotriazole-1-yl)-1,1,3,3-tetramethyluronium hexafluorophosphate (HATU) activation in the presence of *N*,*N*-Diisopropylethylamine (DIPEA) in a *N*,*N*-dimethylformamide (DMF) solution. The resulting intermediate conjugates were purified by semi-preparative RP-HPLC and the protecting groups were removed with a standard cocktail (95% TFA, 2.5% TIS, 2.5% $H_2O$), giving the final peptide conjugates **L4** – **L6** respectively (**Scheme 2.2**).

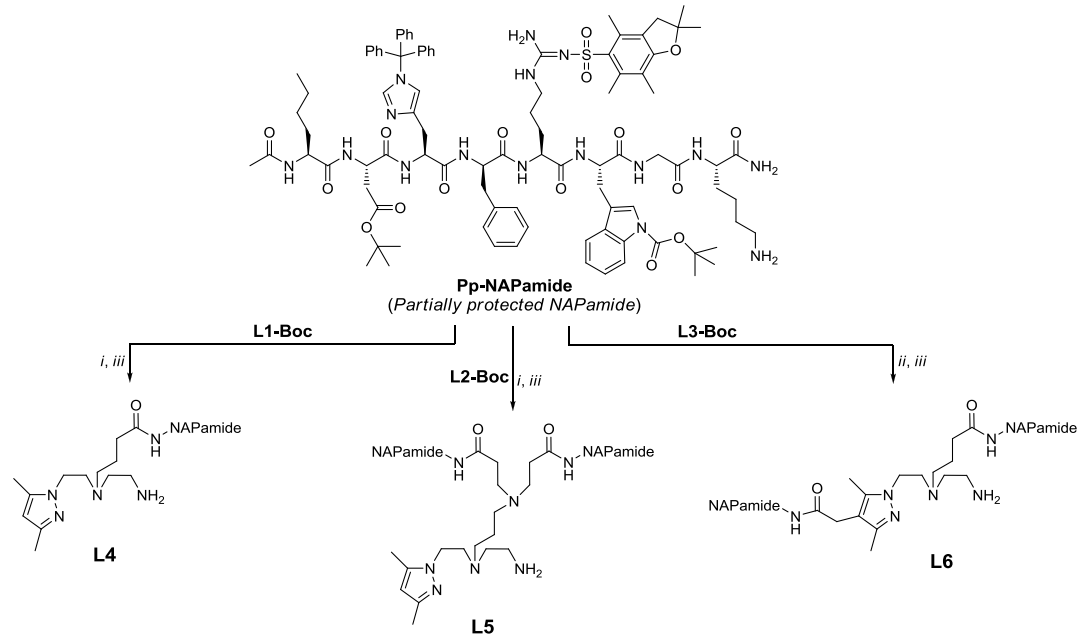


**Scheme 2.2**: Synthesis of mono- and bivalent **NAPamide** conjugates **L4**, **L5** and **L6**. (*i*) HATU, DIPEA, DMF; (*ii*) HATU, DIPEA, Microwave 75W, 50 $^{o}$C, 10 min, DMF; (*iii)* 95% TFA, 2.5% TIS, 2.5% $H_2O$.

The peptide conjugates were characterized by ESI–MS (**Table 2.1**).

**Table 2.1**: Analytical data of the monovalent and bivalent α-MSH derivatives.

| Compound | Formula | Calculated [ion] | Found | $t_R$/min (purity)* |
|---|---|---|---|---|
| **L4** | $C_{65}H_{96}N_{20}O_{12}$ | 1349.8 $[M+H]^{+}$ | 1349.8 | 14.1 (98%) |
| **L5** | $C_{122}H_{177}N_{37}O_{24}$ | 849.5 $[M+3H]^{3+}$ | 849.5 | 15.3 (98%) |
| **L6** | $C_{119}H_{170}N_{36}O_{24}$ | 1244.6 $[M+2H]^{2+}$ | 1244.6 | 15.0 (98%) |

*Method E, experimental section

The monovalent conjugate **L4** was also characterized by multinuclear NMR spectroscopy (2D COSY, TOCSY and NOESY) in $H_2O/D_2O$ (9:1 v/v), which allowed full peak assignment in the NMR spectra. The $^{1}$H, $^{13}$C and $^{15}$N chemical shifts of **L4** are listed in the experimental section, and the correlations found for **L4** are depicted in **Figure 2.9**.

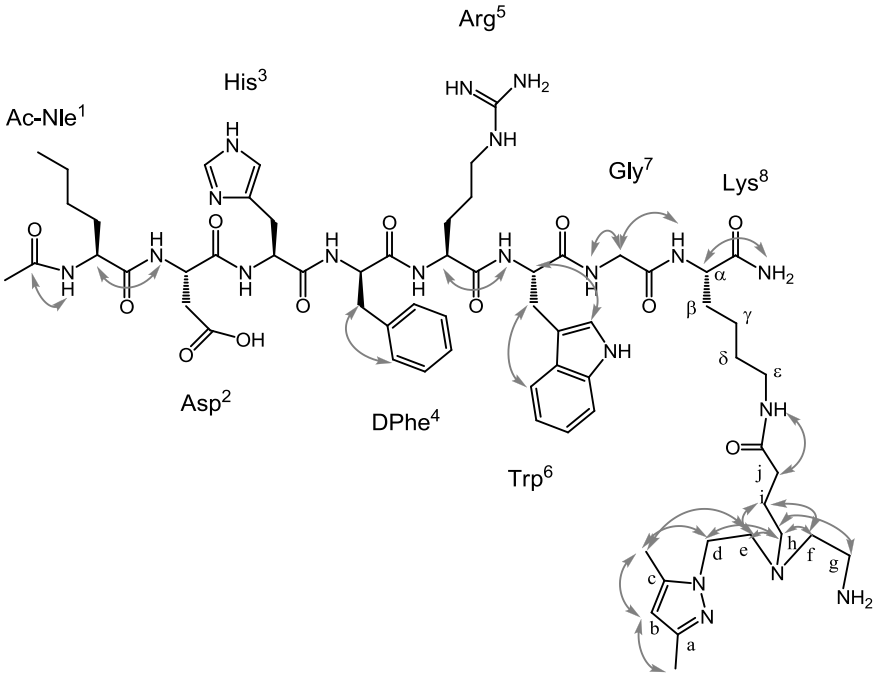


**Figure 2.9**: Schematic representation of **L4**. Arrows represent the observed NOE correlations at pH 2.5 and 5 ºC.

The proton chemical shifts in the $^1$H-NMR spectrum of **L4** at 5 ºC were almost identical ($^1$H: $\Delta\delta^{\text{conjugate-free}} \leq$ -0.1 ppm) to the ones found for the free peptide, except for the methylenic protons of lysine side chain that present a significant deviation ($\Delta\delta_{H\varepsilon\varepsilon'}{}^{\text{conjugate-free}}$ = 0.18 and $\Delta\delta_{H\delta\delta'}$ = -0.16 ppm). The carbon chemical shifts in the $^{13}$C-NMR spectrum of **L4** were also almost identical ($^{13}$C: $\Delta\delta^{\text{conjugate-free}} \leq$ -0.5 ppm) to the free **NAPamide**, while the nitrogen chemical shift of the ε-amino group of the lysine side chain in the conjugate is shifted downfield ($^{15}$N, $\Delta\delta^{\text{conjugate-free}}$ = 57.3 ppm) relatively to the same resonances in the corresponding free analog. These results suggested that the conjugation of the BFC has minor impact on the peptide conformation.

A strong correlation between the methylenic protons ($H^j$) in the aliphatic arm of the chelator and the HN amide of ε-amino group of the lysine side chain at 5 ºC (**Figure 2.9**) was found in the ROE cross-peaks of **L4**. The assignment of the chelator was confirmed by the strong correlation between the methylenic protons in the pyrazolyl-diamine ($H^{a-i}$; **Figure 2.9**).

### 2.2.4. Metallated Homobivalent Peptides of the Type *fac*-[Re(CO)$_3$($\kappa^3$-L)]$^+$

Aiming to assess the influence of metallation of **L4** – **L6** in the MC1R-binding affinity and to characterize the analog $^{99m}$Tc(CO)$_3$-complexes, the metallopeptides **Re4** – **Re6** were synthesized via an indirect method as displayed in **Scheme 2.3**.

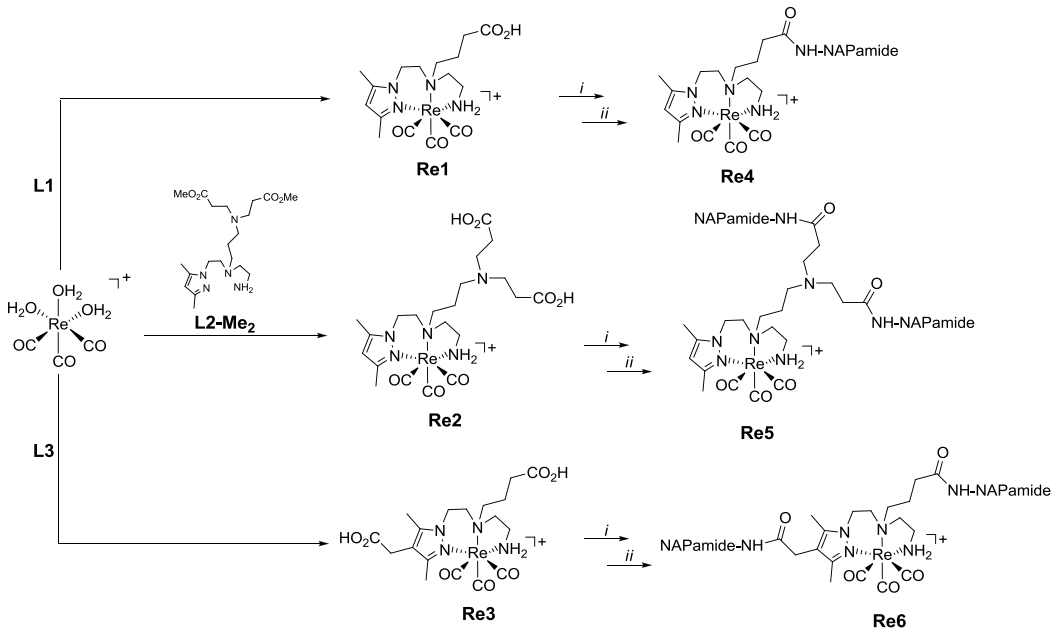


**Scheme 2.3**: Synthesis of the metallated peptides **Re4** – **Re6**. i) **Pp-NAPamide**, DMF/DIPEA/HATU; ii) TFA/TIS/$H_2O$.

Firstly, **L1-Boc**, **L2-Boc-Me$_2$** and **L3-Boc** (see section **2.2.1.**) were treated with a diluted solution of TFA (5% TFA in $CH_2Cl_2$) to yield the corresponding Boc-free bifunctional chelators **L1**, **L2-Me$_2$** and **L3**. These chelators reacted with equimolar amounts of the precursor *fac*-[Re(CO)$_3$($H_2O$)$_3$]Br in refluxing water for 20 h. After purification by preparative RP-HPLC (Method A, experimental section **7.2**), intermediate complexes of the type *fac*-[Re(CO)$_3$($\kappa^3$-**L**)]$^+$ (**Re1**, L = **L1**; **Re2**, L = **L2**; **Re3**, L = **L3**) were obtained as colorless oils in 60%, 73% and 65% yield, respectively. Surprisingly, the methyl ester groups of **L2-Me$_2$** were hydrolyzed under the reaction conditions, as confirmed by the structural characterization of **Re2**.

**Re1** – **Re3** were characterized by the usual analytical techniques, including RP-HPLC, ESI–MS, NMR and infrared (IR) spectroscopy. The use of 2D-NMR experiments ($^1$H-$^1$H g-COSY and $^1$H-$^{13}$C g-HSQC) was crucial for peak assignment in the NMR spectra, and for full characterization of the compounds, as described in the

experimental part. For the sake of example, the $^{1}$H- and $^{13}$C-NMR spectra ($D_2O$) of **Re2** are depicted in **Figure 2.10**.

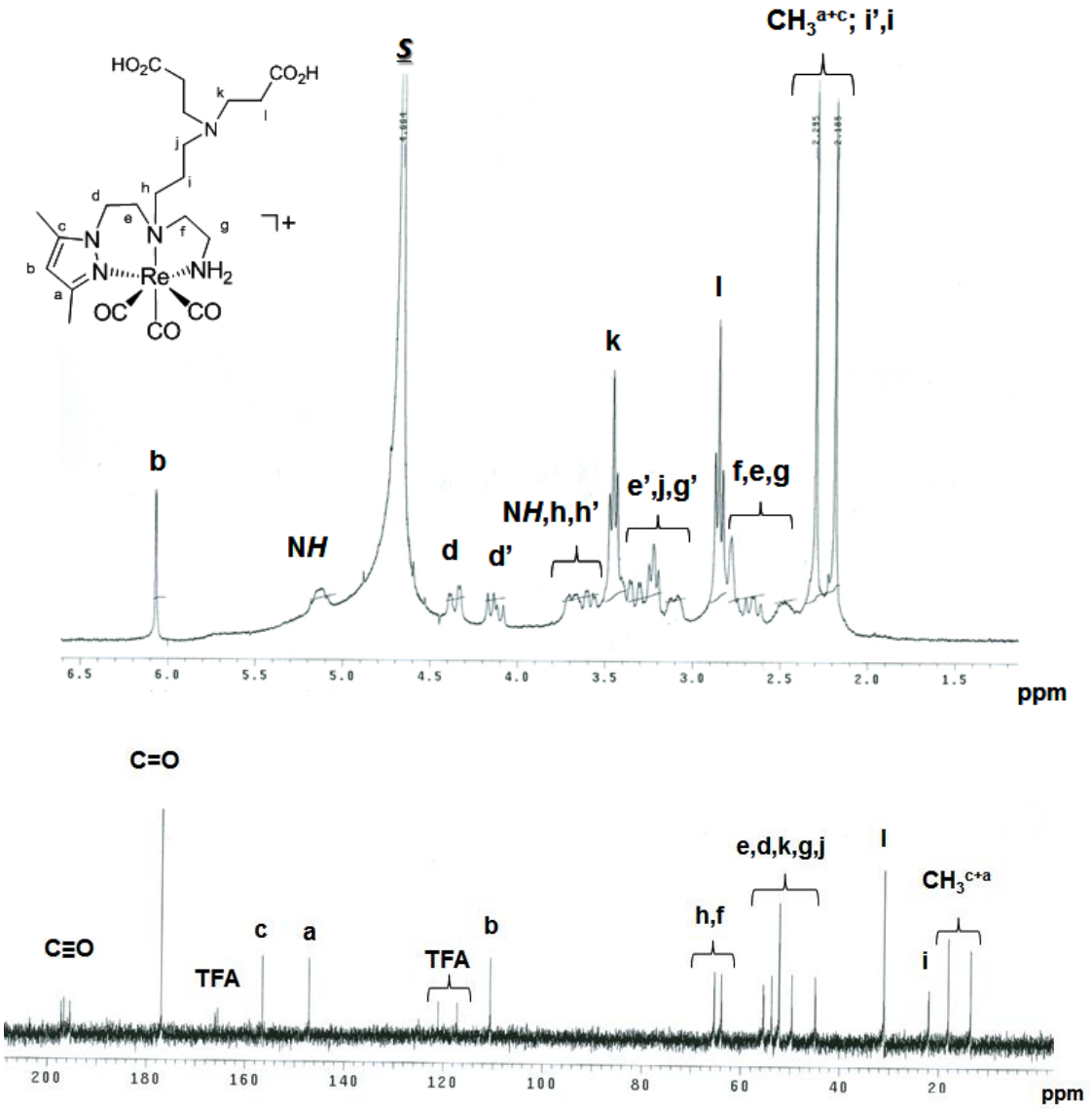


**Figure 2.10**: $^{1}$H-(top) and $^{13}$C-NMR (bottom) spectra of **Re2** in $D_2O$ (S = residual water).

The $^{1}$H-NMR spectrum of **Re2** presented singlet peaks assigned to $H^b$ (δ 6.07) and to the methyl groups of the pyrazolyl ring (δ 2.30/2.14). The $H^b$ and the methyl protons of the pyrazolyl ring were shifted downfield ($H^b$, Δ= 0.29 ppm; Me, Δ = ~0.19 – 0.20 ppm) relatively to the same resonances in the corresponding free chelators, indicating coordination to the metal center. The tridentate coordination mode of the chelator was also confirmed by the splitting of the $NH_2$ protons of the primary amine (δ 5.12 and

δ 3.70), as well as by the splitting of the methylenic protons of the coordinating backbone. For each of these protons, two resonances, integrating for one proton each, were found, due to the diastereotopic character of the methylenic protons after coordination to the metal center (e.g. δ 4.40 $H^{d}$, δ 4.39 $H^{d'}$, δ 3.30 $H^{e}$, δ 2.70 $H^{e'}$, δ 3.08 $H^{g}$, δ 2.48 $H^{g'}$). This behavior, which is a strong evidence of ligand coordination, is similar to other tricarbonyl complexes of the same type.[48c, d] The absence of a sharp singlet at ≈ δ 3.6, assigned to the methyl ester group, indicates that the reaction conditions used lead to ester hydrolysis.

The $^{13}$C-NMR spectrum of **Re2** presented all the expected signals for the proposed structure. The most striking characteristic was the presence of three resonances for the C≡O ligands (δ 197.1, δ 196.6 and δ 195.4) coordinated facially to rhenium, which is common to all complexes. The full assignment of the $^{13}$C resonances was based on $^{1}$H-$^{13}$C g-HSQC. A correlation between the geminal diastereotopic protons and the respective carbons was found.

The metallated peptides **Re4** – **Re6** were prepared by conjugation of the corresponding precursors **Re1** – **Re3** to the free ε-amino group of $Lys^{8}$ in **Pp-NAPamide** (**Scheme 2.3**). After semi-preparative RP-HPLC purification and removal of the side-chain protecting groups with a standard cocktail (95 % TFA, 2.5 % TIS, 2.5 % $H_2O$), **Re4** – **Re6** were characterized by ESI–MS (**Table 2.2**).

**Table 2.2**: Analytical data for **Re4** – **Re6**.

| Compound | Formula | Calculated [ion] | Found | $t_R$/min (purity)* |
|---|---|---|---|---|
| **Re4** | $C_{68}H_{96}N_{20}O_{15}Re$ | 810.8 $[M+2H]^{2+}$ | 810.4 | 15.9 (98%) |
| **Re5** | $C_{125}H_{177}N_{37}O_{27}Re$ | 705.0 $[M+3H]^{3+}$ | 705.0 | 15.4 (98%) |
| **Re6** | $C_{122}H_{170}N_{36}O_{27}Re$ | 920.6 $[M+3H]^{3+}$ | 920.6 | 15.5 (98%) |

* Method E, experimental section

The metallopeptide **Re4** was also characterized by multinuclear NMR spectroscopy, using 2D COSY, TOCSY and NOESY. The $^{1}$H, $^{13}$C and $^{15}$N chemical shifts of **Re4** are listed in the experimental section.

The chemical shift deviations ($^{1}H_{\alpha}$, $^{13}C_{\alpha}$) for some residues of the metallopeptide were determined and compared to the free **NAPamide** and respective peptide conjugate **L4** (**Figure 2.11**)

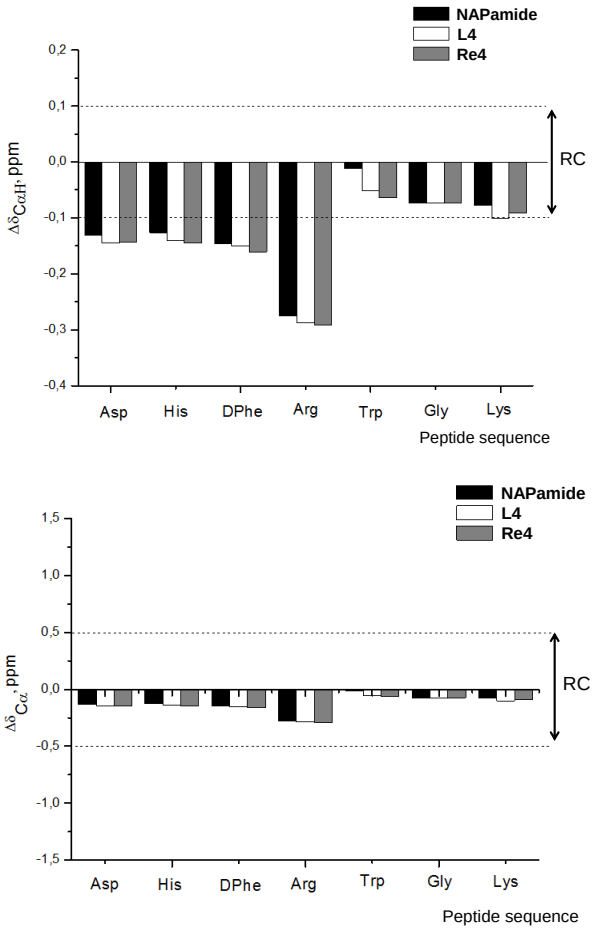


**Figure 2.11**: Histograms showing the chemical shift deviation of $^{1}H_{\alpha}$ (top) and $^{13}C_{\alpha}$ (bottom) values for amino acid residues of **NAPamide** (black bars), **L4** (white bars) and **Re4** (grey bars) in aqueous solution at pH 2.5 and 5 ºC.

The results have shown that the chemical shift deviations of $^{1}H_{\alpha}$ and $^{13}C_{\alpha}$ of most residues in the peptide sequence of **Re4** were similar to the ones found for **NAPamide** indicating that the peptide moiety in the complex might also present a random coil conformation in solution. Moreover, no significant differences were found between the chemical shifts ($^{1}H_{\alpha}$ and $^{13}C_{\alpha}$) of the residues in the free peptide (or **L4**) and **Re4**, indicating that metallation does not affect the conformation of the peptide in solution. The methylenic protons of Lys[8] side chain in **Re4** presented a significant deviation ($\Delta\delta_{H\varepsilon\varepsilon'}$ $^{conjugate\text{-}free}$ = 0.24 and $\Delta\delta_{H\delta\delta'}$ $^{conjugate\text{-}free}$ = -0.12 ppm) from the chemical shifts of free **NAPamide** while the remaining signals were almost identical ($^{1}H$: $\Delta\delta$ $^{conjugate\text{-}free}$ $\leq$ -0.1 ppm).

The carbon chemical shifts of the peptide in **Re4** were also almost identical ($^{13}C$: $\Delta\delta$ $^{conjugate\text{-}free}$ $\leq$ -0.5 ppm) to **NAPamide**, while the nitrogen chemical shift of the ε-

amino group of the $Lys^8$ side chain in the conjugate is shifted downfield ($^{15}N$, $\Delta\delta^{conjugate-free}$ = 58.2 ppm). These results also indicated that the conjugation of the rhenium complex have minor impact on the peptide conformation.

From the observed ROE cross-peaks of **Re4**, the strong correlation between the methylenic protons ($H^j$) in the aliphatic arm of the rhenium complex and the HN amide of ε-amino group of the $Lys^8$ side chain at 5 ºC confirmed peptide conjugation. Moreover, only strong sequential $C_\alpha H\text{-}NH_{i+1}$ correlations were found in the peptide backbone at 5 ºC.

### 2.3. MC1R-Binding Affinity

The receptor-binding affinities of **L4** – **L6** and corresponding metallopeptides **Re4** – **Re6** were assessed in a competitive binding assay using B16F1 murine melanoma cells and [$^{125}$I]-NDP–MSH as a radioligand. The latter was prepared by radioiodination of NDP-MSH using the chloramine-T method as described in the experimental section. Analytical RP-HPLC purification was performed before each assay to minimize the effect of deiodination of [$^{125}$I]-NDP-MSH. Finally, B16F1 cells were incubated at room temperature (25 ºC) with [$^{125}$I]-NDP-MSH (50,000 Cpm in 0.2 mL) and the competitor peptide solution (0.1 mL), yielding a final concentration ranging from $1.9 \times 10^{-5}$ to $1.9 \times 10^{-12}$ M.

The calculated $IC_{50}$ values for all compounds are listed in **Table 2.3**. For the sake of comparison, the $IC_{50}$ values found for α-MSH, NDP–MSH, and free **NAPamide** are also shown.

**Table 2.3**: MC1R binding affinity of α-MSH derivatives.

| Compound | $IC_{50}$ (nM) ± S.D. |
|---|---|
| **α-MSH**$^{140}$ | 1.65 ± 0.18 |
| **NDP-MSH**$^{84}$ | 0.21 ± 0.03 |
| **NAPamide** | 0.78 ± 0.03 |
| **L4** | 0.66 ± 0.13 |
| **L5** | 0.04 ± 0.02 |
| **L6** | 0.16 ± 0.21 |
| **Re4** | 0.03 ± 0.02 |
| **Re5** | 0.15 ± 0.08 |
| **Re6** | 1.14 ± 1.13 |

S.D. = standard deviation

All peptides display high affinity to MC1R with $IC_{50}$ values in the sub- and nanomolar range. The binding affinity of **L4** ($IC_{50}$ = 0.66 ± 0.13 nM) is comparable to that of free **NAPamide** ($IC_{50}$ = 0.78 ± 0.03 nM), demonstrating that conjugation to the BFC did not affect its original MC1R-targeting properties. As envisaged, introduction of a second peptide unit in the same molecule resulted in a significant affinity enhancement. Indeed, the bivalent conjugates **L5** ($IC_{50}$ = 0.04 ± 0.02 nM) and **L6** ($IC_{50}$ = 0.16 ± 0.21 nM) had a 19 and 4 fold increase in affinity at the MC1R, respectively, compared to the monovalent peptide conjugate **L4**. Metallation of the latter resulted in a 20 fold affinity enhancement (**Re4**: $IC_{50}$ = 0.03 ± 0.02 nM), while a slight decrease on the binding affinity of **L5** and **L6** was observed upon metallation (**Re5**: $IC_{50}$ = 0.15 ± 0.08 nM and **Re6**: $IC_{50}$ = 1.14 ± 1.13 nM). Nevertheless, the values found for **Re5** and **Re6** are not only in the nanomolar range but also better or comparable to **NAPamide**, suggesting that both compounds can be potentially adequate for *in vivo* MC1R-targeting.

### 2.4. Radiolabeling with *fac*-[$^{99m}$Tc(CO)$_3$]$^+$ Moiety

Homobivalent peptide conjugates **L5** and **L6** were labeled with $^{99m}$Tc(I) following the methodology already described for **L4**.[82b] As depicted in **Scheme 2.4**, reaction of the conjugates (100 µL, [**L**] = 5 x $10^{-4}$ M) with the organometallic precursor *fac*-[$^{99m}$Tc(CO)$_3$(H$_2$O)$_3$]$^+$ (900 µL) gave the radiometallated peptides of the type *fac*-[$^{99m}$Tc(CO)$_3$($\kappa^3$-**L**)]$^+$ (**Tc5**, L **= L5**, and **Tc6**, L **= L6**) in high yield and high radiochemical purity.

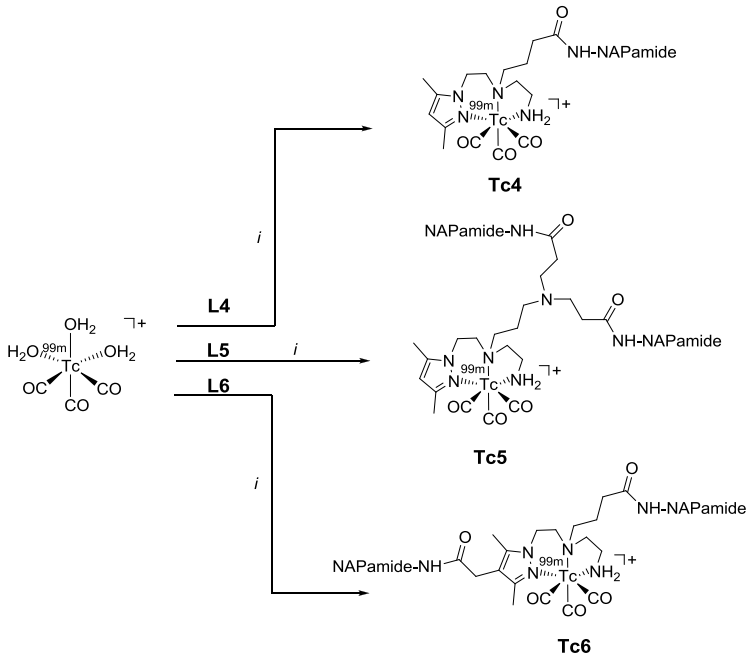


**Scheme 2.4**: Synthesis of **Tc4** – **Tc6**. *i*) 90 ºC, 30 min, pH = 7.

As the concentration of the $^{99m}$Tc(I) complexes is very low ($10^{-8}$ – $10^{-10}$ M), their chemical identification/characterization was made by comparing their RP-HPLC profiles with those of the corresponding Re(I) tricarbonyl complexes, which were synthesized and characterized at the macroscopic level (section **2.2.4.**). In this way, we confirmed that the $^{99m}$Tc(I) complexes corresponded to the expected compounds, which means they present the same structure as the rhenium congeners, being formulated as *fac*-[$^{99m}$Tc(CO)$_3$($\kappa^3$-**L**)]$^+$ (**Tc4**, L = **L4**; **Tc5**, L = **L5**; **Tc6**, L = **L6**). As an example, **Figure 2.12** presents the RP-HPLC profiles of the matched pairs **Re5**/**Tc5** and **Re6**/**Tc6**.

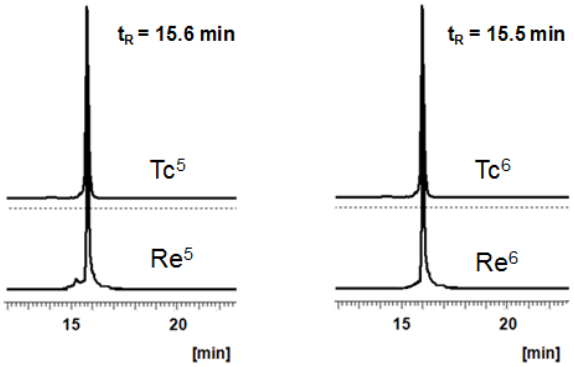


**Figure 2.12**: RP-HPLC chromatograms of **Tc5** and **Tc6** ($\gamma$ - detection)/**Re5** and **Re6** (U.V. detection).

The partition coefficients in octanol-water, expressed in log $P_{o/w}$, have been determined for **Tc4 – Tc6** in physiological conditions (**Table 2.4** and experimental section **7.4**). The results demonstrated the hydrophilic nature of all radiometallated peptides, with complex **Tc6** displaying the highest hydrophilic character.

**Table 2.4**: Log $P_{o/w}$ values for complexes **Tc4** – **Tc6**.

| Radiopeptides | Log $P_{o/w}$ ± S.D. |
|---|---|
| **Tc4** | -0.42 ± 0.01 |
| **Tc5** | -1.34 ± 0.04 |
| **Tc6** | -1.82 ±0.02 |

In order to increase specific activity and maximize cellular and tumor uptake, the radiopeptides **Tc5** and **Tc6** were separated from the corresponding non-metallated conjugates **L5** and **L6** by semi-preparative RP-HPLC. The fraction corresponding to each radiopeptide was collected in a 50 mL Falcon vial containing PBS (biodistribution studies) or MEM (cell studies) with 0.2 % BSA to minimize adsorption phenomena during the evaporation of the elution solvents.

### 2.5. *In Vitro* Stability Studies

The *in vitro* stability studies may help to partially predict the stability of the $^{99m}$Tc(I) complexes *in vivo* towards reoxidation and/or transquelation of the metal by biological substrates. These biological substrates can be proteins, amino acids or other molecules present *in vivo*. Complexes **Tc5** and **Tc6** were challenged in 1 mM solutions of strong coordinating amino acids such as cysteine or histidine. Briefly, 100 µl of $^{99m}$Tc(I) complexes solutions were incubated with 900 µl of cysteine or histidine solutions at 37 °C. After 18 h incubation, aliquots of the solutions were collected and analyzed by RP-HPLC. The results obtained have confirmed a high stability for both $^{99m}$Tc complexes. In fact, no decomposition or reoxidation products were found by RP-HPLC monitoring after incubation of the radioactive complexes.

The stability of **Tc5** and **Tc6** was also assessed in fresh human serum at 37 ºC, and aliquots were analyzed at different time points by RP-HPLC. The results showed that both compounds displayed high serum stability. As an illustrative example, **Figure 2.13** depicts the RP-HPLC chromatographic profile of **Tc6** during the assay.

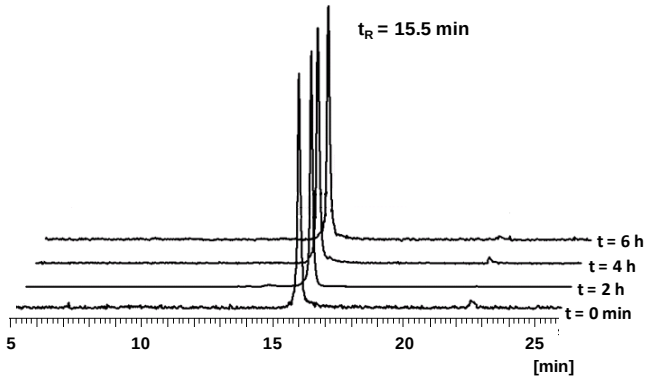


**Figure 2.13**: RP-HPLC chromatograms of **Tc6** after incubation in fresh human serum at different time points.

Together, the stability studies confirmed the high ability of the pyrazolyl-diamine chelating unit to stabilize the core *fac*-[$^{99m}$Tc(CO)$_3$]$^+$, without transmetallation to serum-based proteins or amino acids, and/ or reoxidation to $^{99m}$Tc(VII).

## 2.6. Cell Uptake Studies

For assessing the internalization and specific MC1R-mediated uptake of **Tc5** and **Tc6**, cellular uptake studies were performed in B16F1 murine melanoma cells. The results for internalization were compared with those obtained for the monovalent radiopeptide **Tc4** (**Figure 2.14A**).

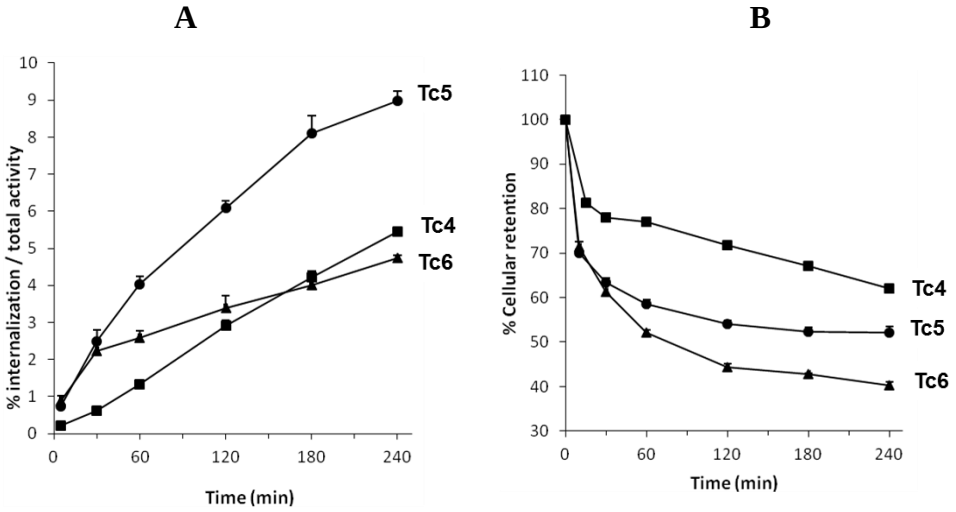


**Figure 2.14**: Internalization (**A**) and retention (**B**) of **Tc4** (*squares*), **Tc5** (*circles*) and **Tc6** (*triangles*) in B16F1 cells at 37 °C. Internalized activity expressed as a percentage of total (applied) activity.

These studies showed that the internalization degree was time-dependent, and both bivalent radiopeptides internalized faster than **Tc4** at short incubation times. The radiopeptide **Tc5** displayed the highest level of internalization (9 % of the total activity at 4 h incubation), whereas **Tc6** displayed moderate internalization, with a pattern similar to the one found for **Tc4** (about 5 % of the applied activity at 4 h incubation).

Cellular retention of **Tc5** and **Tc6** was also evaluated in B16F1 cells at different time points and compared with the results previously described for **Tc4** (**Figure 2.14B**). After 4 h incubation, **Tc5** presented a higher retention value than **Tc6** (52 % and 40 % of the internalized activity, respectively). However, the monovalent radiopeptide **Tc4** had the highest retention with 62 % of the internalized activity still inside the cells after 4 h of incubation.[82b]

To confirm whether the cellular internalization was specific and receptor-mediated, the bivalent radiocomplexes were also incubated in the presence of a high concentration of NDP–MSH, a potent MC1R agonist, to block the MC1Rs. The results of receptor blockade, expressed as a percentage of internalization in the presence and in the absence of NDP–MSH, are displayed in **Figure 2.15**.

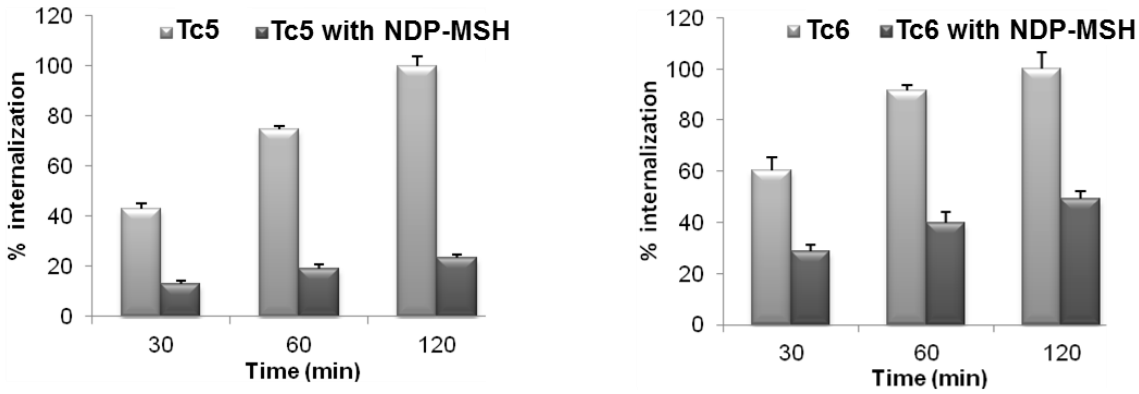


**Figure 2.15**: Receptor-blocking study: inhibition of cellular internalization of **Tc5** (left) and **Tc6** (right) in B16F1 cells by co-incubation with NDP-MSH (3.5μg/well).

Co-incubation with excess NDP–MSH reduced significantly the cellular internalization of **Tc5** and **Tc6** by 70 – 76 % and 50 – 56 %, respectively. These results indicated that the uptake of both radiocomplexes in murine melanoma cells was driven by a MC1R-mediated mechanism.

## 2.7. Biodistribution and *in vivo* Stability of Tc4 – Tc6

The *in vivo* MC1R-targeting properties of **Tc4** – **Tc6** were evaluated in B16F1 melanoma-bearing mice. The primary skin melanoma was generated by implanting subcutaneously 1 x $10^6$ B16F1 cells. Ten to twelve days after the inoculation, tumors reached a weight of 0.2 – 1.0 g. Animals were intravenously injected into the retro-orbital sinus with the radioconjugate diluted in 100 µl of PBS, pH 7.2. The biodistribution was evaluated at 1 h and 4 h post injection (p.i.). **Table 2.5** displays the tissue distribution as percentage of injected activity per gram of organ (% IA/g) as well as total excretion (% IA) of **Tc4** – **Tc6** at 1 h and 4 h p.i.

**Table 2.5:** Biodistribution studies of **Tc4** – **Tc6** in B16F1 murine melanoma-bearing C57BL/6 mice at 1 h and 4 h p.i. (*n* = 3-5).

| Tissue/ organ | % IA/g ± S.D. | | | | | |
|---|---|---|---|---|---|---|
| | **Tc4**[82b] | | **Tc5** | | **Tc6** | |
| | **1h** | **4h** | **1h** | **4h** | **1h** | **4h** |
| **Tumor** | **5.88 ± 2.11** | **4.24 ± 0.94** | **3.02 ± 0.27** | **2.96 ± 0.36** | **2.54 ± 0.30** | **1.81 ± 0.44** |
| Blood | 3.32 ± 0.51 | 1.62 ± 0.64 | 1.36 ± 0.30 | 0.62 ± 0.06 | 2.39 ± 0.61 | 0.49 ± 0.13 |
| **Liver** | **10.8 ± 1.60** | **6.7 ± 2.10** | **45.7 ± 7.10** | **35.3 ± 5.97** | **21.3 ± 0.20** | **10.1 ± 2.20** |
| Intestine | 9.1 ± 0.80 | 14.4 ± 1.6 | 2.75 ± 0.25 | 4.57 ± 1.05 | 1.78 ± 0.02 | 2.82 ± 1.29 |
| Spleen | 1.26 ± 0.20 | 0.88 ± 0.30 | 1.80 ± 0.09 | 2.16 ± 1.01 | 3.12 ± 0.58 | 1.52 ± 0.42 |
| Heart | 0.85 ± 0.10 | 0.58 ± 0.19 | 0.63 ± 0.14 | 0.39 ± 0.03 | 1.01 ± 0.08 | 0.39 ± 0.14 |
| Lungs | 2.88 ± 0.55 | 1.21 ± 0.45 | 1.34 ± 0.14 | 0.67 ± 0.08 | 3.66 ± 0.50 | 0.60 ± 0.10 |
| **Kidney** | **9.7 ± 0.90** | **4.5 ± 2.40** | **33.2 ± 3.30** | **36.8 ± 3.87** | **68.6 ± 6.4** | **72.5 ± 1.1** |
| Muscle | 0.31 ± 0.03 | 0.18 ± 0.14 | 0.24 ± 0.01 | 0.07 ± 0.08 | 0.33 ± 0.03 | 0.1 ± 0.02 |
| Bone | 0.66 ± 0.10 | 0.40 ± 0.20 | 0.61 ± 0.03 | 0.40 ± 0.00 | 0.72 ± 0.07 | 0.31 ± 0.06 |
| Stomach | 2.92 ± 1.70 | 1.06 ± 0.96 | 1.18 ± 0.62 | 0.38 ± 0.04 | 0.88 ± 0.30 | 0.33 ± 0.14 |
| Pancreas | 0.57 ± 0.10 | 0.46 ± 0.32 | 0.31 ± 0.05 | 0.20 ± 0.04 | 0.40 ± 0.02 | 0.43 ± 0.41 |
| **Tumor/normal tissue uptake ratio** | | | | | | |
| Tumor/blood | 1.8 | 2.6 | 2.2 | 4.8 | 1.1 | 3.7 |
| Tumor/muscle | 19.0 | 23.5 | 12.6 | 42.3 | 7.7 | 18.1 |
| Tumor/kidney | 0.60 | 0.94 | 0.09 | 0.08 | 0.037 | 0.03 |
| Total excretion (%) | 57.3 ± 2.7 | 69.1 ± 8.3 | 21.6 ± 1.6 | 32.0 ± 2.8 | 39.9 ± 6.4 | 51.9 ± 1.8 |

The homobivalent radiopeptides **Tc5** and **Tc6** presented lower tumor uptake and a less favorable pharmacokinetic profile than the monovalent radiopeptide **Tc4**. Slower overall excretion was observed for both bivalent radiopeptides, with **Tc5** displaying the worst value, with only 32.0 ± 2.8% of the activity excreted at 4 h p.i.

The radiopeptides **Tc5** and **Tc6** were rapidly cleared from the bloodstream (0.62 ± 0.06 and 0.49 ± 0.13 % IA/g) and major organs, except those related to the excretion pathways at 4 h p.i.

Despite the enhanced *in vitro* affinity, **Tc5** and **Tc6** displayed lower *in vivo* melanoma accumulation (2.96 ± 0.36 and 1.81 ± 0.44 % IA/g at 4 h p.i.) as compared to **Tc4** (4.24 ± 0.94 % IA/g) at the same time point. The *in vivo* targeting properties of both bivalent constructs did not correlate with the cellular internalization data. Indeed, the highest cell internalization level and the moderate retention observed for **Tc5**, together with its nanomolar MC1R-binding affinity, did not lead to an enhancement of tumor uptake relative to **Tc4**. In fact, there was not a positive correlation between the tumor uptake and the number of targeting vectors on the complexes.

In spite of the low tumor uptake observed, **Tc5** displayed the highest tumor retention as 98 % of the radioactivity measured at 1 h was still retained in the tumor after 4 h. These results partially account for the best tumor to blood and tumor to muscle ratios at 4 h p.i. found for **Tc5**.

Unlike **Tc4**, both bivalent radiopeptides showed very high non-specific accumulation and retention in kidneys (33.2 ± 3.3 and 36.8 ± 3.87 % IA/g for **Tc5** and 68.6 ± 6.4 and 72.5 ± 1.1% IA/g for **Tc6** at 1 h and 4 h p.i., respectively). These results, often reported for other radiopeptides, are indicative of pronounced tubular reabsorption, which is likely related to the binding to the multiligand megalin receptor.[81b, 129b, 133, 141] Nevertheless, the non-specific uptake by kidneys could be modulated by the co-administration of cationic amino acids, such as Lys or Arg.[141c, 142]

The high kidney uptake and retention, together with the low tumor uptake led to poor tumor to kidney ratios (e.g., 0.08 and 0.03 for **Tc5** and **Tc6**, respectively, at 4 h p.i.), which were considerably lower than the ratio obtained for the monovalent compound **Tc4** (e.g. 0.94 at 4 h p.i.).

To study the *in vivo* stability of **Tc5** and **Tc6**, urine and blood samples were collected from the sacrificed melanoma-bearing C57BL/6 mice 1 h p.i. of the corresponding radiopeptide. After appropriate treatment, the biological samples were analyzed by RP-HPLC. As an example, the chromatograms of **Tc6** (initial preparation) and the biological samples 1 h after p.i. are shown in **figure 2.16**.

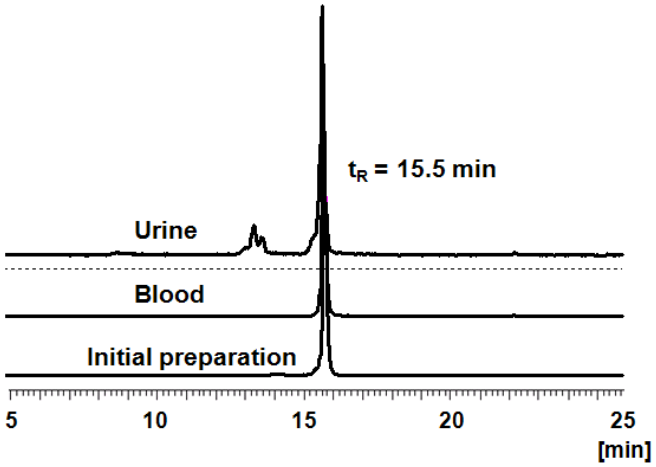


**Figure 2.16**: RP-HPLC γ traces of **Tc6** (initial preparation), blood serum and urine samples collected 1 h after p.i.

*In vivo* stability studies revealed that **Tc5** and **Tc6** were stable in blood serum, as no metabolites could be detected. These results confirmed that metal complexation via the tridentate pyrazolyl-diamine backbone overcomes potential binding/transmetallation to coordinating residues in circulating proteins, such as histidine, cysteine or methionine. In contrast, a small amount (less than 15%) of metabolites with a shorter retention time was found in urine but they were not identified.

## 2.8. Conclusions

The bivalent conjugates **L5** and **L6** presented enhanced *in vitro* MC1R-binding affinity as compared to the monovalent **NAPamide** conjugate (**L4**). Metallation of the bivalent conjugates yielded isostructural complexes of the type *fac*-[$M(CO)_3(\kappa^3$-**L**)] (M = $^{99m}$Tc/Re; **Tc5**/**Re5**, L = **L5**; **Tc6**/**Re6**, L = **L6**), with **Re5** and **Re6** displaying binding affinities in the subnanomolar and nanomolar range, which were still better than or comparable to the binding affinity of **NAPamide**. Cell internalization studies in B16F1 murine melanoma cells has shown that the radiopeptides **Tc5** and **Tc6** internalized via an MC1R-mediated mechanism, with **Tc5** presenting the highest level of internalization.

The biodistribution studies of **Tc4** – **Tc6** in B16F1 melanoma-bearing mice has shown that there was no positive correlation between tumor uptake and valency, even in the case of **Tc5**, which had the highest cellular internalization level and better retention.

# 3

## $M(CO)_3$-labeled Cyclic α-MSH Analogs ($M = {}^{99m}Tc$, Re)

# 3. M(CO)$_3$-labeled Cyclic α-MSH Analogs (M = $^{99m}$Tc, Re)

## 3.1. Introduction

Cyclic peptides present in general enhanced *in vivo* receptor-targeting properties as compared to the linear ones, mainly due to a stable secondary structure that enables a better fit into the receptor pocket.[50] Among the most successful cyclization strategies applied to radiolabeled α-MSH analogs, metal and lactam bridge cyclization resulted in greater tumour uptake and lower kidney uptake than the disulphide bridge cyclization.[50b, 95]

Recently, Grieco et al. have introduced a new family of alkylthioaryl bridge-cyclized peptides formally derived from MT-II and SHU9119, which are a lactam-based cyclized agonist and antagonist of MC1R, respectively (**Figure 3.1**).[143] Among this family, the cyclic analog c[S-$NO_2$-$C_6H_3$-CO-His-DPhe-Arg-Trp-Cys]-$NH_2$ (**PG10N**) emerged as a potent agonist towards MC1R (**Figure 3.1**).

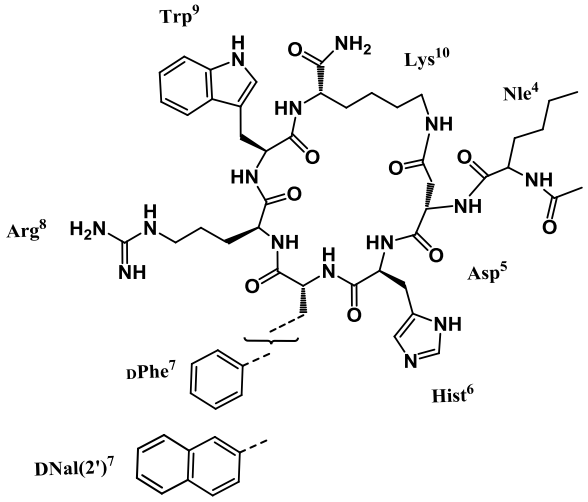


MTII ($IC_{50}$ = 3.5 ± 0.2 nM)
SHU9119 ($IC_{50}$ = 1.3 ± 0.1 nM)

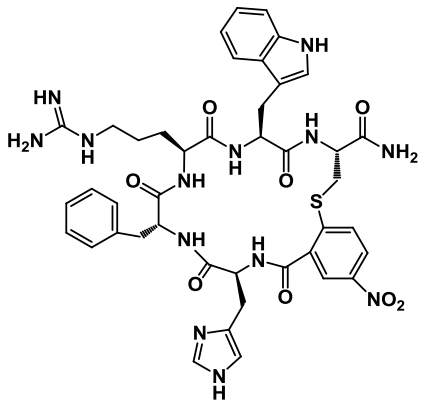

c[S-$NO_2$-$C_6H_3$-CO-His-DPhe-Arg-Trp-Cys]-$NH_2$
(**PG10N**, $IC_{50}$ = 3.7 ± 0.5 nM)

**Figure 3.1**: Schematic representation of the cyclic analog MT-II, SHU9119 and c[S-$NO_2$-$C_6H_3$-CO-His-DPhe-Arg-Trp-Cys]-$NH_2$ (**PG10N**) and their MC1R binding affinity values.[143-144]

The same authors also demonstrated that cyclic peptides containing a cysteine bridge display improved pharmacokinetic and conformational properties when compared to

their cognate peptides.[145] Taken together, these results prompted us to design a (radio)metallated cyclic peptide containing a thioether-bridge within the main ring for *in vivo* MC1R-targeting. Additionally, we have also envisaged the synthesis and biological evaluation of a novel (radio)metallated cyclic peptide containing an amine-bridge instead of a thioether-bridge. In order to prepare the thioether and amine bridge-cyclized α-MSH analogs, our efforts focused on the design of macrocyclic peptides with an appropriate linker to enable conjugation to a bifunctional chelator/metal complex. The incorporation of such linker in the peptide sequence should not affect the MC1R-targeting properties of the cyclic α-MSH analog. Therefore, this chapter describes the synthesis and characterization of the novel thioether and amine bridge-cyclized peptides c[S-$NO_2$-$C_6H_3$-CO-His-DPhe-Arg-Trp-Cys]-Lys-$NH_2$ (**SNBA-MSH$_{hex}$**) and c[NH-$NO_2$-$C_6H_3$-CO-His-DPhe-Arg-Trp-Lys]-Lys-$NH_2$ (**NNBA-MSH$_{hex}$**), respectively, as well as the corresponding peptide conjugates c[S-$NO_2$-$C_6H_3$-CO-His-DPhe-Arg-Trp-Cys]-Lys(Pz)-$NH_2$ (**L7**) and c[NH-$NO_2$-$C_6H_3$-CO-His-DPhe-Arg-Trp-Lys]-Lys(Pz)-$NH_2$ (**L8**). The synthesis, characterization and biological evaluation, including the *in vitro* and *in vivo* MC1R-targeting properties, of the Re/$^{99m}$Tc$(CO)_3$-metallated peptides conjugates is also presented.

### 3.2. Synthesis and Characterization of novel Cyclic α-MSH analogs

Taking into consideration that the conjugation of a bifunctional chelator to the ε-amino group of a Lys side-chain did not affect the MC1R-targeting properties of the resulting **NAPamide** conjugate described in the previous chapter, this amino acid was selected as a suitable linker to be incorporated either at the N- or C-terminus of **PG10N**. Thus, two new linear peptide sequences, **A**: Lys(Boc)-His(Trt)-DPhe-Arg(Pbf)-Trp(Boc)-Cys(Trt)-$NH_2$ and **B**: His(Trt)-DPhe-Arg(Pbf)-Trp(Boc)-Cys(Trt)-Lys(Boc)-$NH_2$, were assembled to the MBHA rink Amide resin by Fmoc-based SPPS in a CEM 12-Channel Automated Peptide Synthesizer (**Scheme 3.1**). The linear sequences were capped with 2-fluoro-5-nitrobenzoic acid (p$NO_2$-BenzAcid) and prior to cyclization, the cysteine protecting group (Trt) was removed selectively with a diluted solution of TFA (**Scheme 3.1**). Cyclization was performed by treatment of the resin-supported peptides with potassium carbonate in DMF (36 h at 25 ºC).

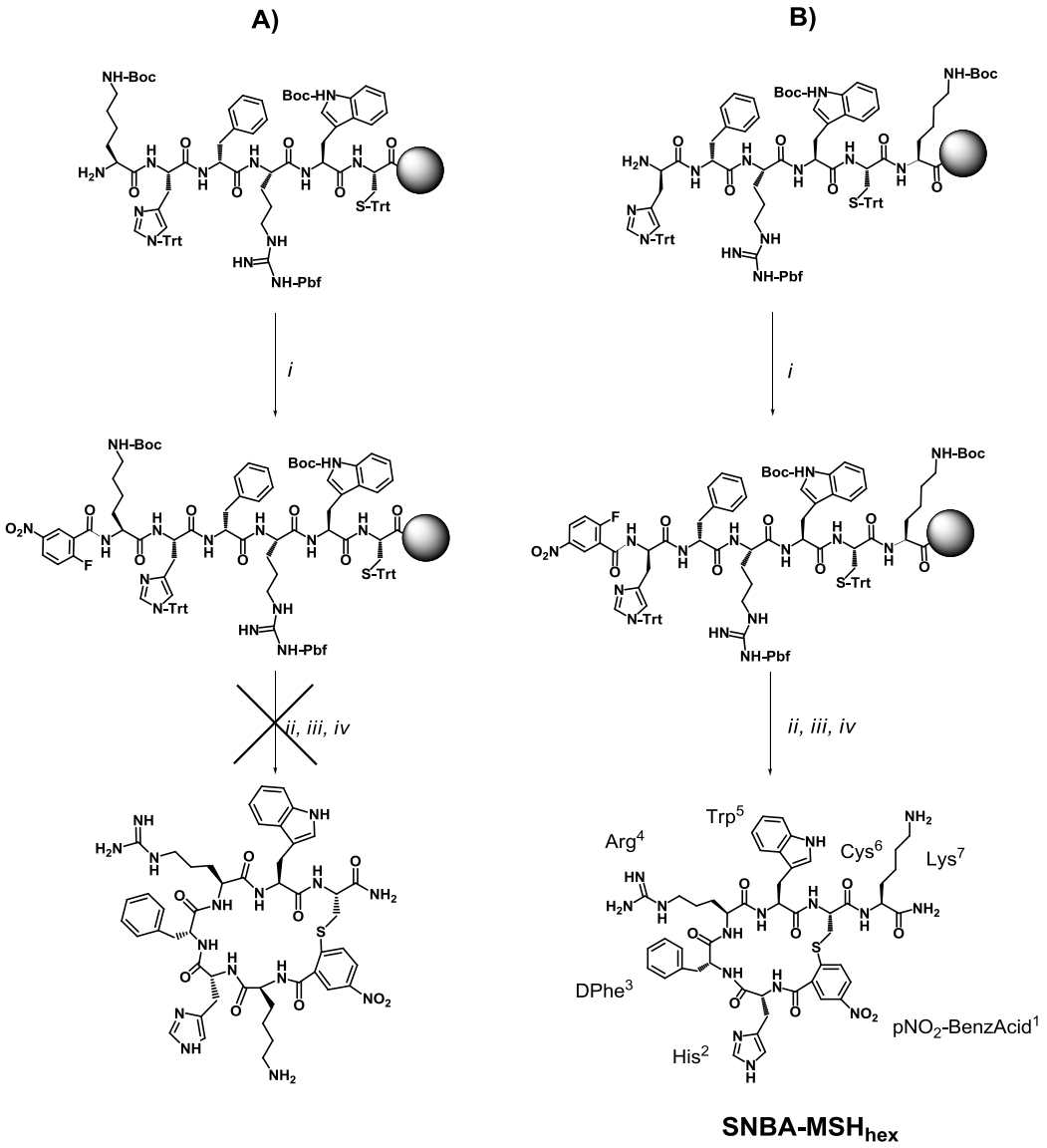


**Scheme 3.1**: Synthesis of a thioether cyclic peptide (**SNBA-MSH$_{hex}$**) containing. *i*) pNO$_2$-BenzAcid, DIPEA, DCM, 3h, r.t.; *ii*) 2% TFA/DCM; *iii*) 5eq. $K_2CO_3$, DMF; *iv*) TFA, TIS, $H_2O$ (95; 2.5 %; 2.5 %).

Both sequences were cleavage from the resin under standard conditions, precipitated with diethyl ether and purified by semi-preparative RP-HPLC, however, the 19-membered cyclic thioether peptide **SNBA-MSH$_{hex}$** was isolated only in the case of sequence **B**. This result suggests that peptide macrocylization may be sterically hindered by the introduction of a Lys at the N- terminus in sequence **A** as opposed to the presence of the same residue at the C- terminus in sequence **B**.

Following the same synthetic methodology, an amine bridge-cyclized peptide was prepared by replacing the nucleophilic promotor Cys$^6$(Trt) with Lys$^6$(ivDde)

(**Figure 3.2**). After removal of the ivDde protecting group with 2 % hydrazine/DMF and subsequent cyclization, the 22-membered cyclic peptide **NNBA-MSH$_{hex}$** was cleaved from the resin under standard conditions, precipitated with diethyl ether and purified by semi-preparative RP-HPLC.

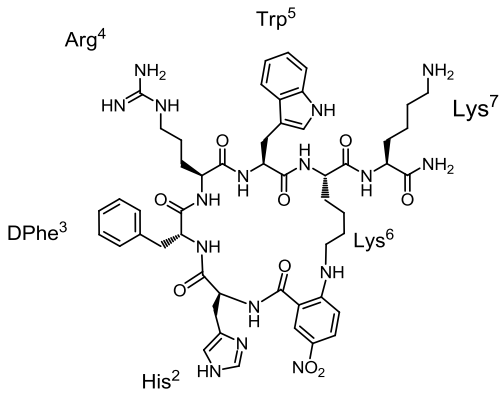


**NNBA-MSH$_{hex}$**

**Figure 3.2**: Schematic representation of amine-bridged cyclic peptide **NNBA-MSH$_{hex}$**.

The peptides **SNBA-MSH$_{hex}$** and **NNBA-MSH$_{hex}$** were characterized by the usual analytical techniques, including RP-HPLC, ESI–MS and NMR spectroscopy ($^1$H-$^1$H COSY, $^1$H-$^1$H TOCSY, $^1$H-$^1$H NOESY, $^1$H-$^1$H ROESY, $^1$H-$^{13}$C and $^1$H-$^{15}$N HSQC). The ESI-MS and RP-HPLC results for both peptides are presented in **Table 3.1**, whereas the $^1$H, $^{13}$C and $^{15}$N data are described in the experimental section (**Tables 7.7** and **7.9**).

**Table 3.1**: Analytical data for **SNBA-MSH$_{hex}$** and **NNBA-MSH$_{hex}$**.

| Compound | Formula | Calculated [ion] | Found | $t_R$/min (purity)* |
|---|---|---|---|---|
| **SNBA-MSH$_{hex}$** | $C_{48}H_{59}N_{15}O_9S$ | 1022.4$[M+H]^+$ | 1022.5 | 9.1 (98%) |
| **NNBA-MSH$_{hex}$** | $C_{51}H_{66}N_{16}O_9$ | 1047.5 $[M+H]^+$ | 1047.5 | 9.3 (98%) |

*Method G, experimental section

As mentioned previously, it is possible to obtain qualitative structural information from $^1H_{\alpha,}$ $^{13}C_\alpha$ and $^{13}C_\beta$ chemical shift values as they are sensitive to the secondary structure of the peptide.[137d] The chemical deviation of $^1H_\alpha$, $^{13}C_\alpha$ and $^{13}C_\beta$ for the aminoacid residues in **SNBA-MSH$_{hex}$** and **NNBA-MSH$_{hex}$** are shown in **Figure 3.3**.

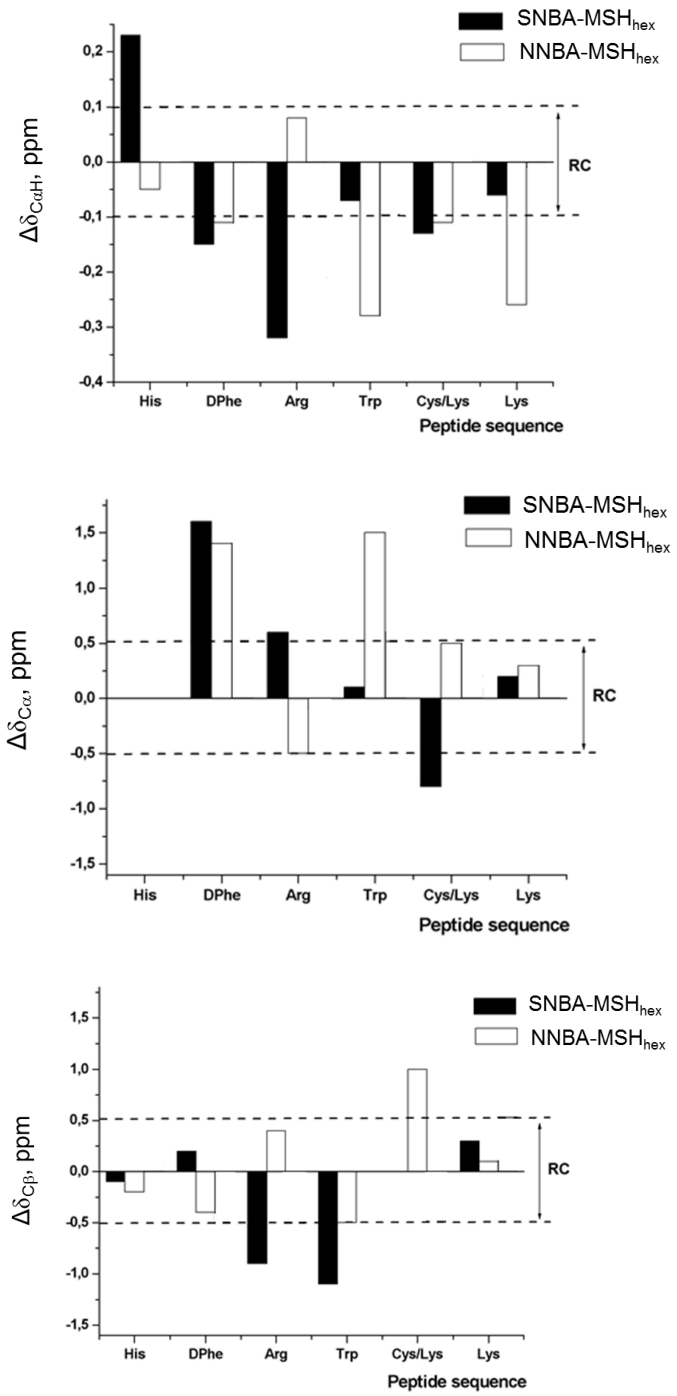


**Figure 3.3:** Histograms showing the chemical deviations ($\Delta\delta_{H\alpha,}$ $\Delta\delta_{C\alpha}$ and $\Delta\delta_{C\beta}$, ppm; being $\Delta\delta = \delta^{observed} - \delta^{RC}$) for amino acid residues of **SNBA-MSH$_{hex}$** (black bars) and **NNBA-MSH$_{hex}$** (white bars), in aqueous solution at pH 2.5 and 5 ºC. Dashed lines indicate the random coil (RC) ranges. Random coil values were taken from Wishart et al.[137a]

The chemical shifts ($^1H_\alpha$, $^{13}C_\alpha$ and $^{13}C_\beta$) of some residues in peptide **SNBA-MSH$_{hex}$** deviated significantly from the random coil values, indicating a turnlike

conformation at the core residues DPhe, Arg, and Trp. Among the side-chain protons, the very large upfield shifts observed for Arg (**Table 3.2**) indicated that these side-chain protons bear anisotropic effects from the ring currents of one or more aromatic side chains in the sequence of **SNBA-MSH$_{hex}$**.

**Table 3.2**: $^{1}$H chemical shifts (ppm) for the Arg side chain of **SNBA-MSH$_{hex}$** and **NNBA-MSH$_{hex}$** in aqueous solution at pH 2.5, 25 ºC. Random coil values were taken from Wishart et al.[139a]

| | **Protons of arginine side-chain** | | |
|---|---|---|---|
| **Peptide** | $H_{\beta\beta'}$ | $H_{\gamma\gamma'}$ | $H_{\delta\delta'}$ |
| **SNBA-MSH$_{hex}$** | 1.12, 1.38 | 0.56, 0.79 | 2.78, 2.78 |
| **NNBA-MSH$_{hex}$** | 1.48, 1.69 | 1.02, 1.22 | 2.48, 2.82 |
| **Random Coil** | 1.76, 1.86 | 1.63, 1.63 | 3.20, 3.20 |

In fact, the cation−π interaction between the positively charged Arg guanidinium group and the indole ring of Trp can contribute to stabilize and fit the peptide structure.[146]

In the case of peptide **NNBA-MSH$_{hex}$**, the chemical shifts ($^{1}H_{\alpha}$, $^{13}C_{\alpha}$ and $^{13}C_{\beta}$) of DPhe, Trp and Lys exhibited significant deviation from the random coil values, indicating also a turn-like conformation. Although the side-chain protons of Arg (**Table 3.2**) were also shifted upfield, the anisotropic effect experienced by these protons is less pronounced in **NNBA-MSH$_{hex}$** than in **SNBA-MSH$_{hex}$**. As reported for other α-MSH analogs, the large anisotropic effect suggested that Arg side chain has a relatively fixed orientation in the case of **SNBA-MSH$_{hex}$**.[147]

Structural features of the peptides can also be deduced from the ROE correlations in the peptide backbone. The intensity of the NOE correlations found for **SNBA-MSH$_{hex}$** and **NNBA-MSH$_{hex}$** backbone are depicted in **Figure 3.4** (top).

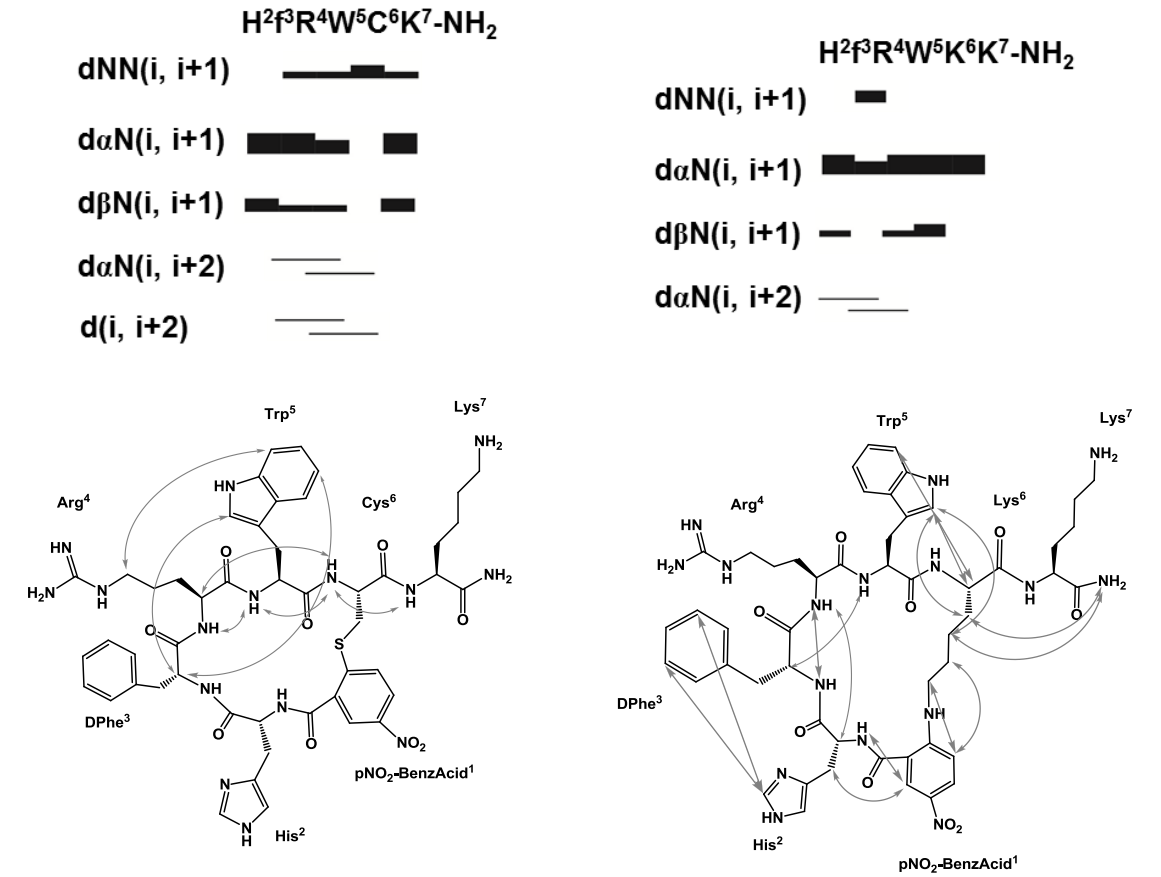


**Figure 3.4**: NOE correlations found for **SNBA-MSH$_{hex}$** and **NNBA-MSH$_{hex}$** backbone (top) at 25 ºC and key NOE cross-peaks present in the ROESY spectra of both peptides (bottom). The height of the bar indicates the strength of the sequential NOE. The NOE volumes were categorized as strong (1.8-3.0 Å), medium (1.8-3.5 Å), or weak (1.8-5.0 Å).

The NOE summary shows the presence of several weak NH-NH$_{i+1}$ (D-Phe$^3$ to Lys$^7$) and medium to strong C$_\alpha$H-NH$_{i+1}$ (His$^2$ to Trp$^5$) NOE correlations in **SNBA-MSH$_{hex}$,** while only one medium NH-NH$_{i+1}$ and one strong C$_\alpha$H-NH$_{i+1}$ correlation were found across the entire peptide backbone of **NNBA-MSH$_{hex}$** (**Figure 3.4**, top). Several weak and medium sequential correlations C$_\beta$H-NH$_{i+1}$ were also found in both peptides, however, the residues involved in these interactions were different. In the case of **SNBA-MSH$_{hex}$,** C$_\beta$H-NH$_{i+1}$ correlations were found for all residues expected between Trp$^5$ and Cys$^6$ while in **NNBA-MSH$_{hex}$** the correlation between D-Phe$^3$ and Arg$^4$ was not observed.

Non-sequential correlations were also found for both peptides, namely $C_\alpha H$-$NH_{i+2}$ (DPhe[3] and Trp[5]), however, an additional weak interaction between Arg[4] and Cys[6] is found in **SNBA-MSH$_{hex}$**, while similar interaction was found between His[2] and Arg[4] in **NNBA-MSH$_{hex}$**.

Correlations between the side chains of the residues in both peptides were also found. The side-chain of Trp[5] is closer to DPhe[3] and Arg[4] side-chain in **SNBA-MSH$_{hex}$**, while in the case of **NNBA-MSH$_{hex}$**, it was pointed in the opposite direction, closer to the Lys[6] side-chain. Furthermore, the imidazole ring of His[2] and the benzyl ring of DPhe[3] were closer in **NNBA-MSH$_{hex}$**, while such correlation was not found in **SNBA-MSH$_{hex}$**. (**Figure 3.4**, bottom)

These interactions contribute for the stabilization of the structural conformation of the peptide. Although the structure adopted by the peptides **SNBA-MSH$_{hex}$** and **NNBA-MSH$_{hex}$** was similar to the structural models of other α-MSH analogs containing the core sequence His-DPhe-Arg-Trp (e.g. **PG10N**, [C[5],C[10]]NDP-MSH$_{5-10}$ and MT-II), which is essential for MC1R recognition, the observed ROE correlations clearly indicated that **SNBA-MSH$_{hex}$** and **NNBA-MSH$_{hex}$** present distinct conformation.[143, 147a] Moreover, the NMR data of the pharmacophore sequence that was more distinct between **SNBA-MSH$_{hex}$** and **NNBA-MSH$_{hex}$** are the chemical shifts of Arg side chain. This finding might be translated into different arrangements of the residue side chain, affecting the interaction **SNBA-MSH$_{hex}$**-receptor.[148]

### 3.3. Peptide Conjugates and Metallopeptides

The Boc-protected bifunctional chelator **L1-Boc** was conjugated to **SNBA-MSH$_{hex}$** and **NNBA-MSH$_{hex}$** via HATU activation in the presence of DIPEA. The resulting intermediate compounds were treated with TFA, yielding the final peptide conjugates **L7** and **L8**, respectively (**Scheme 3.2**).

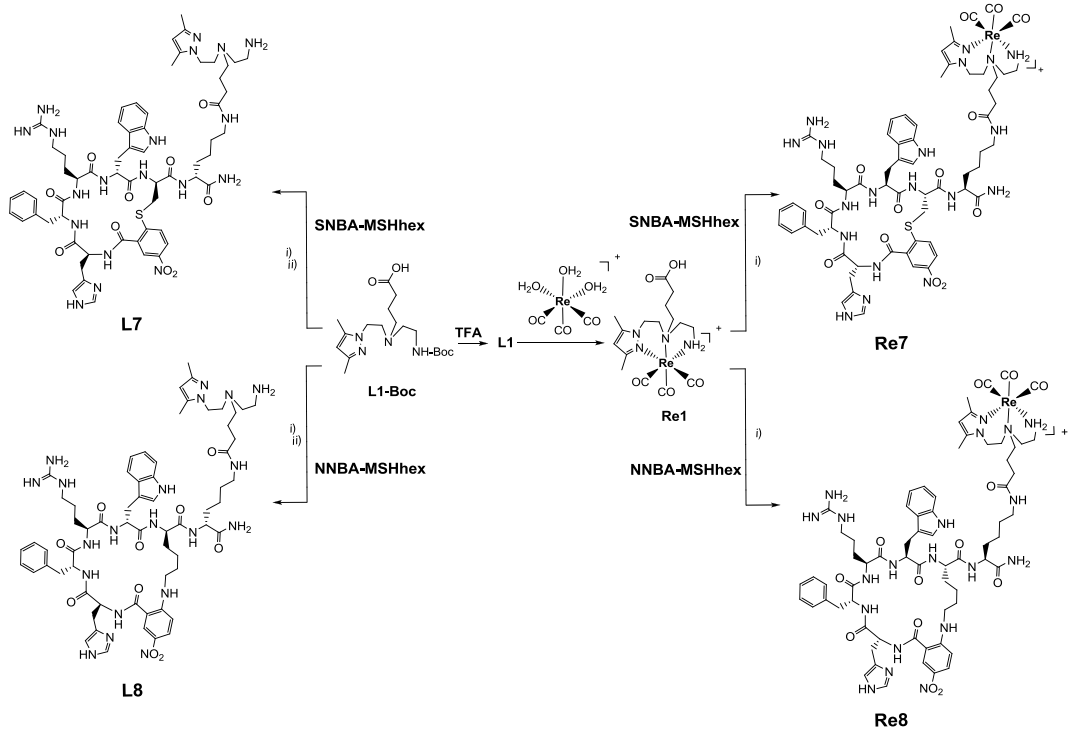


**Scheme 3.2**: Synthesis of **L7**, **L8**, **Re7** and **Re8**. *i*) DMF/DIPEA/HATU; *ii*) TFA/TIS/$H_2O$.

Aiming to evaluate the influence of metallation of **L7** and **L8** in the MC1R-binding affinity and characterize the analogs $^{99m}$Tc(I)-complexes, the ‘‘cold’’ rhenium metallopeptides *fac*-[Re(CO)$_3$($\kappa^3$-**L7**)]$^+$ (**Re7**) and *fac*-[Re(CO)$_3$($\kappa^3$-**L8**)]$^+$ (**Re8**) were also synthesized. These complexes were prepared by conjugation of the free carboxylate group in **Re1** to the Lys side-chain of **SNBA-MSH$_{hex}$** and **NNBA-MSH$_{hex}$,** (**Scheme 3.2**). All compounds were characterized by ESI-MS (**Table 3.3**).

**Table 3.3**: Analytical data for **L7**, **L8**, **Re7** and **Re8**.

| Compound | Formula | Calculated [ion] | Found | $t_R$ / min (purity)* |
|---|---|---|---|---|
| **L7** | $C_{61}H_{81}N_{19}O_{10}S$ | 1272.5 $[M+H]^+$ | 1272.5 | 10.2 (98 %) |
| **Re7** | $C_{64}H_{84}N_{19}O_{13}ReS$ | 772.4 $[M+2H]^{2+}$ | 772.4 | 11.9 (98 %) |
| **L8** | $C_{64}H_{88}N_{20}O_{10}$ | 1297.7 $[M+H]^+$ | 1297.7 | 10.4 (98 %) |
| **Re8** | $C_{67}H_{91}N_{20}O_{13}Re$ | 784.4 $[M+2H]^{2+}$ | 784.4 | 12.1 (98 %) |

*Method G, experimental section

To assess the conformational preferences of the peptide upon conjugation to the chelator and further complexation with the rhenium tricarbonyl core, **L7** and **Re7** were

characterized by NMR spectroscopy ($^{1}$H-$^{1}$H COSY, $^{1}$H-$^{1}$H TOCSY, $^{1}$H-$^{1}$H NOESY, $^{1}$H-$^{1}$H ROESY and $^{1}$H-$^{13}$C as well as $^{1}$H-$^{15}$N HSQC).

After peak assignment in the NMR spectra of **L7** and **Re7** (**Tables 7.10** and **7.12** in experimental section, respectively), the most significant finding was that the majority of the $^{1}$H, $^{13}$C and $^{15}$N chemical shifts of both compounds were practically identical between each other and to the corresponding free peptide. As an example, **Figure 3.5** presents the $^{1}$H,$^{1}$H-TOCSY spectral region of $H_{\alpha}/H_{\beta}$-HN cross-peaks observed for **SNBA-MSH$_{hex}$** and **L7** (left) as well as for **L7** and **Re7** (right).

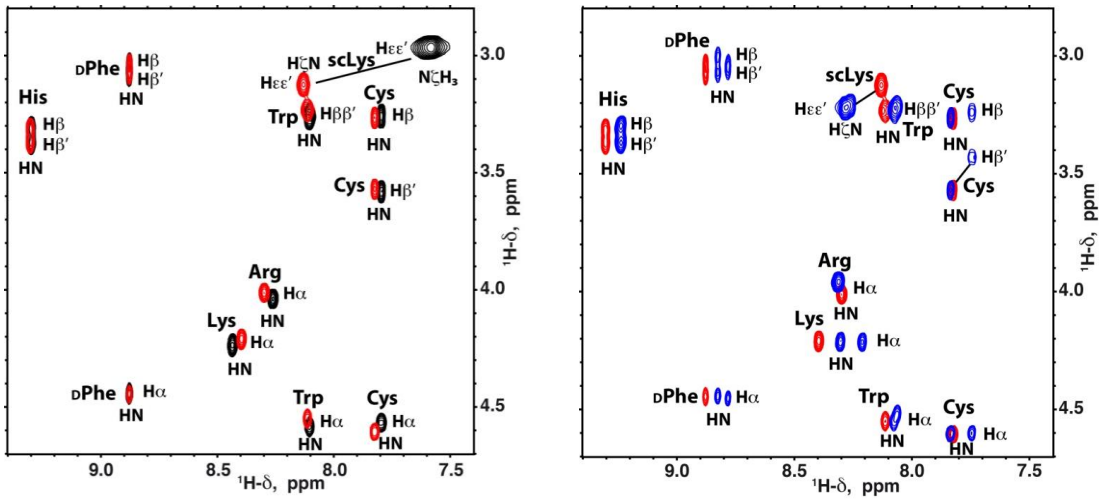


**Figure 3.5**: 2D $^{1}$H,$^{1}$H-TOCSY spectral region showing $H_{\alpha}/H_{\beta}$-HN cross-peaks observed for **SNBA-MSH$_{hex}$** (black contours), **L7** (red contours) and **Re7** (blue contours) in aqueous solution ($H_2O/D_2O$ 9:1 v/v) at pH 2.5 and 5 ºC. The cross-peaks between the $H_{\varepsilon\varepsilon'}$ protons and the amino group of Lys side chain in **SNBA-MSH$_{hex}$** and the corresponding $H_{\zeta}N$ amide to which the chelator is bound in **L7** and **Re7** are also shown.

The largest differences in chemical shift corresponded, as expected, to the Lys side chain to which the chelator is conjugated, and to the very sensitive HN protons, which even so change less than 0.05 ppm between **SNBA-MSH$_{hex}$** and the conjugate **L7**. In contrast to **SNBA-MSH$_{hex}$** and **L7**, the metallated peptide **Re7** exhibited two sets of signals for some protons (**Figure 3.5**, **Tables 7.10**, **7.12** and **7.13** in experimental section, respectively), which indicated the coexistence of two isomeric species, **Re7a** and **Re7b**, as previously reported for other Re(I) complexes.[149] Based on volume integration of TOCSY signals, the two isomers were almost equally populated (53 and 47% at 5 ºC, and 51 and 49% at 25 ºC). Interestingly, the peptide moiety showed similar

conformational behavior in the two species, as derived from the examined NMR parameter. The chemical shift deviations observed for the $^{1}H_{\alpha}$, $^{13}C_{\alpha}$ and $^{13}C_{\beta}$ backbone atoms also demonstrated that the conformational behavior of peptide moiety was identical in **L7** and **Re7** population (**Figure 3.6** and **3.7**).

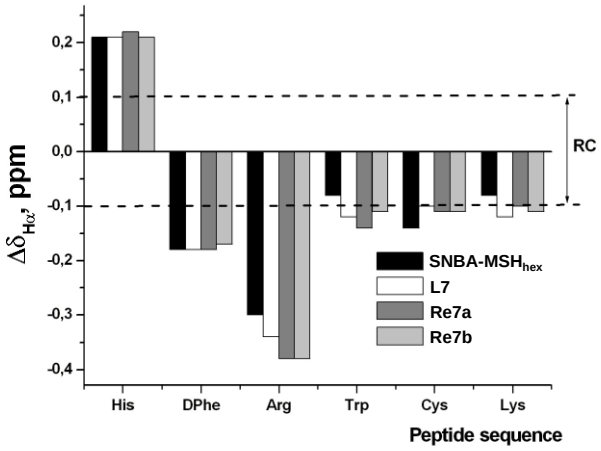


**Figure 3.6**: Histogram showing the $\Delta\delta_{H\alpha}$ ($\Delta\delta_{H\alpha} = \delta_{H\alpha}^{observed} - \delta_{H\alpha}^{RC}$, ppm) values for amino acid residues of **SNBA-MSH$_{hex}$** (black bars), **L7** (white bars), and the two **Re7** isomers (**Re7a** and **Re7b**; grey bars) in aqueous solution at pH 2.5 and 5 ºC. Dashed lines indicate the random coil (RC) range. Random coil values were taken from Wishart et al.[137a]

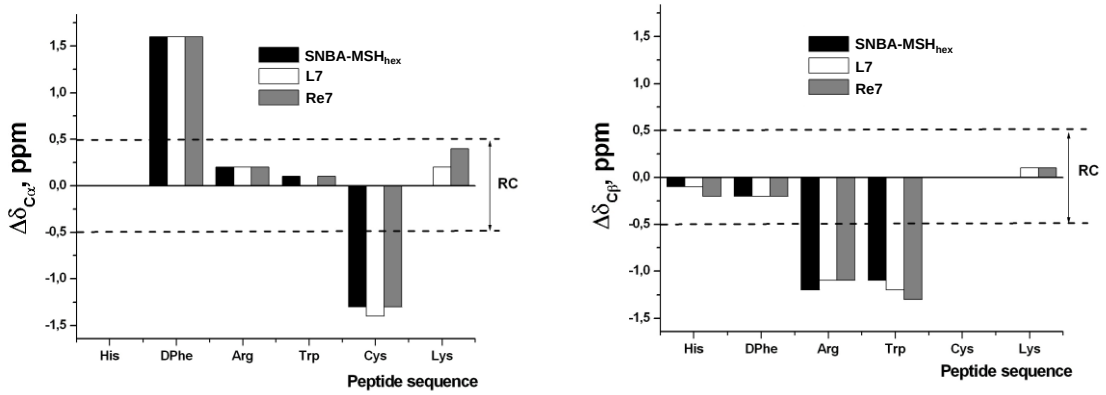


**Figure 3.7**: Histograms showing the $\Delta\delta_{C\alpha}$ ($\Delta\delta_{C\alpha} = \delta_{C\alpha}^{observed} - \delta_{C\alpha}^{RC}$, ppm), and $\Delta\delta_{C\beta}$ ($\Delta\delta_{C\beta} = \delta_{C\beta}^{observed} - \delta_{C\beta}^{RC}$, ppm) for amino acid residues of **SNBA-MSH$_{hex}$** (black bars), **L7** (white bars), and **Re7** (grey bars) in aqueous solution at pH 2.5 and 5 ºC. Dashed lines indicate the RC ranges. $^{13}$C-chemical shift values for $C_{\alpha}$ and $C_{\beta}$ carbons are identical for the two **Re7** species (**Tables 7.10** and **7.12** in experimental section). RC values were taken from Wishart et al.[137a]

Among the side chain protons, the anisotropic effect experienced by the Arg side chain protons ($H_{\beta\beta'}$, $H_{\gamma\gamma'}$, $H_{\delta\delta'}$) was found for all the compounds containing the alkylthioaryl bridge-cyclized moiety (**SNBA-MSH$_{hex}$**, **L7** and **Re7**). Moreover, the $^{1}$H chemical shift deviations increased from 25 ºC to 5 ºC, suggesting that the structure adopted by **SNBA-MSH$_{hex}$** and by the peptide moiety in **L7** and **Re7** was stabilized at low temperature.

### 3.4. MC1R-Binding Affinity

The $IC_{50}$ values determined for **L7**, **L8**, **Re7**, **Re8** as well as for the precursors **PG10N**, **SNBA-MSH$_{hex}$** and **NNBA-MSH$_{hex}$** are listed in **Table 3.4**.

**Table 3.4**: MC1R binding affinities of cyclic α-MSH analogs.

| Compound | $IC_{50}$ (nM) ± S.D. |
|---|---|
| **PG10N**[143] | 3.7 ± 0.5 |
| **SNBA-MSH$_{hex}$** | 1770±480 |
| **L7** | 430 ± 60 |
| **Re7** | 690 ± 250 |
| **NNBA-MSH$_{hex}$** | 51 ± 12 |
| **L8** | 179 ± 39 |
| **Re8** | 176 ± 5 |

The introduction of an additional Lys residue at the C-terminus of **PG10N** sequence led to the analog **SNBA-MSH$_{hex}$** that presented 486 fold less affinity than the parent peptide. Replacement of the alkylthioaryl-bridge in **SNBA-MSH$_{hex}$** by and alkylaminoaryl-bridge gave the 22-membered macrocyclic peptide **NNBA-MSH$_{hex}$** which presented 10 fold less affinity than **PG10N**, but displayed higher affinity than **SNBA-MSH$_{hex}$**.

Conjugation of the chelator to **SNBA-MSH$_{hex}$** led to an improvement of the binding affinity of the resulting peptide conjugate **L7**, however, the $IC_{50}$ value was still 116 fold higher than the one found for the parent peptide **PG10N**. Unlike **SNBA-MSH$_{hex}$**, the MC1R binding affinity of **NNBA-MSH$_{hex}$** decreased upon conjugation to the chelator since the resulting peptide conjugate **L8** presented 3.5 fold less affinity.

The metallation of **L7** and **L8** with the organometallic core *fac*-$[Re(CO)_3]^+$ did not lead to a significant decrease of binding affinity towards MC1R, as concluded by comparing the $IC_{50}$ values of **Re7** ($IC_{50}$ = 690 ± 250 nM) and **Re8** ($IC_{50}$ = 176 ± 5 nM)

with those of the respective non-metallated conjugates (**L7**: $IC_{50}$ = 430 ± 100 nM) and (**L8**: $IC_{50}$ = 179 ± 39 nM).

Brought together, the binding affinity results has shown that **SNBA-MSH$_{hex}$** and **NNBA-MSH$_{hex}$** present distinct MC1R targeting properties. As discussed previously in the NMR characterization of both peptides, this finding could be ascribed to the conformational structure of the peptides in solution, in particular, to the orientation of the Arg side chain.

As already mentioned, the most interesting finding was related to the fact that metallation of the peptide conjugates did not affect binding at the MC1R as concluded by comparing the $IC_{50}$ values of **L7** and **L8** to those of the respective complexes **Re7** and **Re8**. The NMR characterization of **SNBA-MSH$_{hex}$** and **Re7** corroborated this result, as the majority of the $^{1}$H, $^{13}$C and $^{15}$N chemical shifts were practically identical in both compounds.

### 3.5. Radiolabeling with the *fac*-[$^{99m}$Tc(CO)$_3$]$^+$ Moiety

The radioactive complexes *fac*-[$^{99m}$Tc(CO)$_3$(κ$^3$-**L7**)]$^+$ (**Tc7**) and *fac*-[$^{99m}$Tc(CO)$_3$(κ$^3$-**L8**)]$^+$ (**Tc8**), structural analogs of **Re7** and **Re8**, were obtained in almost quantitative yield (> 98%) upon reaction of the peptide conjugates **L7** and **L8** (100 μL, [**L**] = 5 – 8 x $10^{-5}$ M) with the precursor *fac*-[$^{99m}$Tc(CO)$_3$(H$_2$O)$_3$]$^+$ (900 μL) at 75 °C (**Figure 3.8**).

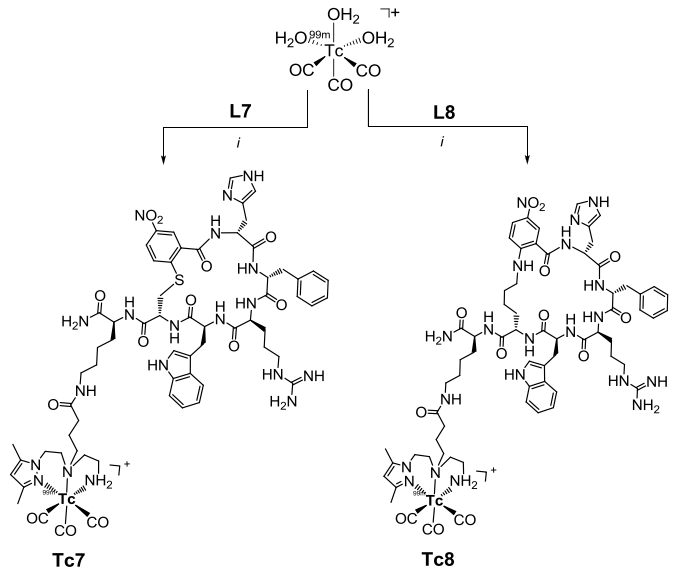


**Figure 3.8:** Synthesis of the radiopeptides **Tc7** and **Tc8**. *i*) 75 ºC, 30 min, pH = 7.

With the aim of increasing the specific activity of the $^{99m}$Tc(I)-labeled peptides to maximize their MC1R-binding ability, the radiopeptides were separated from the free peptide conjugates by semi-preparative RP-HPLC. The fractions corresponding to the radioconjugate were collected in Falcon vials containing PBS for biodistribution studies and cell internalization studies. The purity/ stability of the radioconjugates was evaluated by RP-HPLC and ITLC. It has been found that no oxidation or colloid formation took place under those conditions, and only one species was observed by HPLC and ITLC.

To assess the (hydro)/lipophylic nature of the radiocomplexes, the partition coefficient of **Tc7** and **Tc8** were determined in physiological conditions (experimental section **7.4**). The results, displayed in **Table 3.5**, has shown that all radiopeptides present a moderate hydrophilic character.

**Table 3.5**: Retention time (RP-HPLC) and log $P_{o/w}$ values for **Tc7** and **Tc8**.

| Radiopeptides | $t_R$/min (purity)* | log $P_{o/w}$ ± S.D. |
|---|---|---|
| **Tc7** | 12.2 min (98%) | − 0.34 ± 0.03 |
| **Tc8** | 12.3 min (98%) | − 0.80 ± 0.05 |

*Method H, experimental section

The identification/ characterization of **Tc7** and **Tc8** was accomplished by comparing their γ-traces with the U.V. traces of the respective rhenium compounds **Re7** and **Re8**. As an example, **Figure 3.9** presents the RP-HPLC chromatographic profiles obtained for **Tc7** and **Re7**.

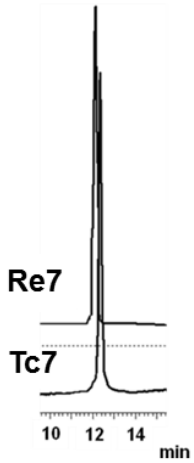


**Figure 3.9**: RP-HPLC chromatographic profiles for **Tc7** (γ - detection) and respective "cold" surrogate **Re7** (U.V. detection, 220 nm).

### 3.6. *In vitro* Stability Studies

The stability of **Tc7** and **Tc8** was assessed in fresh human serum at 37 ºC. Aliquots were analyzed at different time points by RP-HPLC (Method H, experimental section). As depicted in **Figure 3.10**, both compounds displayed high serum stability with negligible degradation.

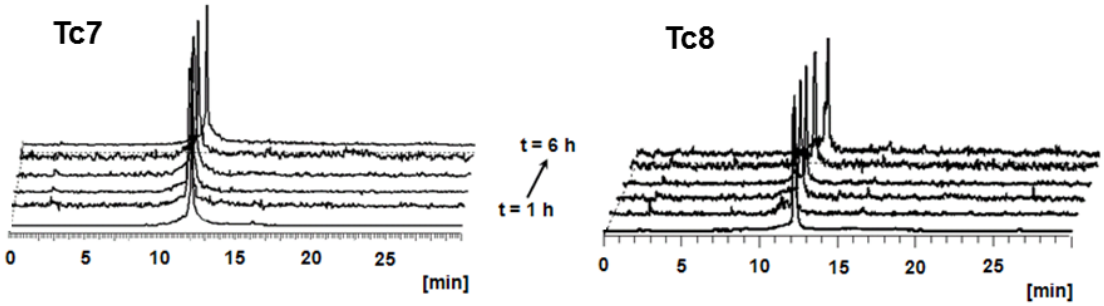


**Figure 3.10**: RP-HPLC profiles of **Tc7** and **Tc8** in fresh human serum at different time points at 37 ºC.

### 3.7. Cell Uptake Studies

The degree of internalization and retention of **Tc7** and **Tc8** was assessed in B16F1 murine melanoma cells. The results has shown that cellular uptake was time-dependent for both radiopeptides at 37 ºC, as displayed in **Figure 3.11**.

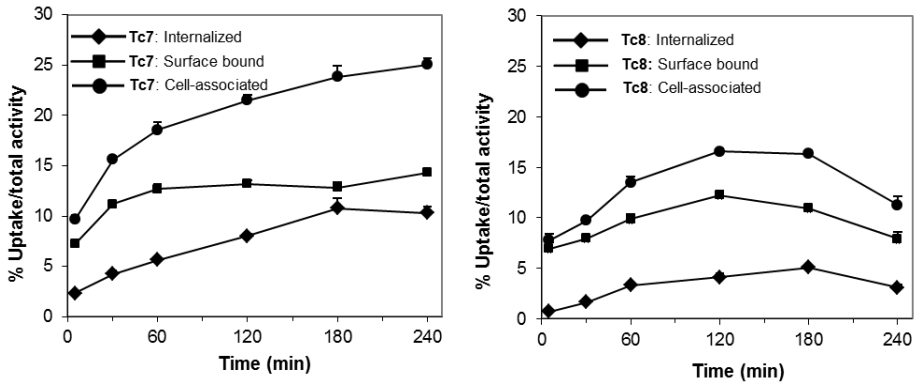


**Figure 3.11**: Internalization of **Tc7** and **Tc8** in B16F1 cells at different time points at 37 ºC. Internalized and surface-bound activities expressed as a percentage of applied activity.

High to moderate cellular uptake was attained for both radiopeptides, with **Tc7** presenting the highest internalization level at 3 h after incubation, when ca. 10 % of the total applied radioactivity was internalized by the cells. Despite presenting a lower internalization degree, the radiopeptide **Tc8** still presented a significant internalization (ca 5 % at 3 h after incubation), comparable to previously described cyclic $^{99m}$Tc-labeled α-MSH analogs.[68a]

With regard to the radioactivity associated to the membrane (surface-bound), only a small difference was observed between the two radiopeptides, with **Tc7** and **Tc8** reaching maximum values at 4 h (14.3 %) and 2 h (12.3%) after incubation, respectively.

The cellular retention of the radioconjugates was also evaluated in the same cell line, after 3 h of internalization at 37ºC (**Figure 3.12**). A moderate and similar retention was observed for **Tc7** and **Tc8**, with ca. 50 % of the internalized activity still remaining inside the cells after 2 h.

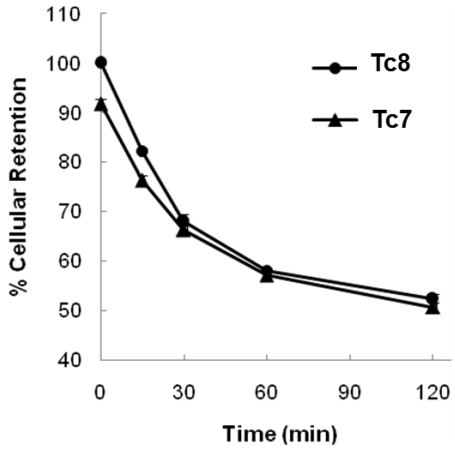


**Figure 3.12**: Cellular retention of internalized **Tc7** and **Tc8** radiopeptides in B16F1 cells at different time points at 37 ºC.

Brought together, the significant cell internalization degree and the moderate retention of **Tc7** and **Tc8** in murine melanoma cells prompted us to assess the tumor targeting properties of those radiopeptides in a B16F1 melanoma-bearing mouse model.

### 3.8. Biodistribution and *In Vivo* Stability

The *in vivo* MC1R-targeting properties of **Tc7** and **Tc8** were evaluated in B16F1 melanoma-bearing mice. **Table 3.6** summarizes the tissue distribution obtained for both radiopeptides as % IA/g at 1 h and 4 h p.i.

**Table 3.6**: Biodistribution of **Tc7** and **Tc8** in B16F1 melanoma-bearing C57BL/6 mice at 1h and 4h p.i. The results are presented as % IA/g (mean ± S.D., n=3-4).

| **% IA/g ± S.D.** | | | | |
|---|---|---|---|---|
| **Tissue/ organ** | **Tc7** | | **Tc8** | |
| | **1h** | **4h** | **1h** | **4h** |
| **Tumor** | **2.33 ± 0.89** | **1.38 ± 0.18** | **2.63 ± 0.50** | **2.47 ± 0.70** |
| Blood | 3.8 ± 1.1 | 2.6 ± 1.2 | 8.0 ± 1.0 | 3.9 ± 0.2 |
| **Liver** | **29.8 ± 4.6** | **30.9 ± 4.2** | **40.2 ± 4.8** | **24.3 ± 1.7** |
| Intestine | 7.2 ± 1.5 | 11.7 ± 3.1 | 5.8 ± 1.2 | 10.5 ± 1.1 |
| Spleen | 3.3 ± 2.2 | 4.6 ± 3.9 | 7.5 ± 0.6 | 5.1 ± 0.3 |
| Heart | 2.2 ± 0.3 | 1.3 ± 0.2 | 3.8 ± 0.3 | 2.0 ± 0.3 |
| Lung | 4.7 ± 0.5 | 3.0 ± 2.0 | 8.8 ± 0.7 | 4.7 ± 0.2 |
| **Kidney** | **23.2 ± 2.4** | **10.0 ± 3.3** | **18.4 ± 2.1** | **9.7 ± 1.1** |
| Muscle | 0.5 ± 0.1 | 0.18 ± 0.16 | 0.67 ± 0.06 | 0.41 ± 0.08 |
| Bone | 1.1 ± 0.4 | 0.45 ± 0.37 | 1.9 ± 0.2 | 1.5 ± 0.3 |
| Stomach | 2.4 ± 0.6 | 1.5 ± 0.9 | 2.7 ± 1.0 | 1.0 ± 0.2 |
| Pancreas | 2.0 ± 1.3 | 2.5 ± 2.5 | 1.1 ± 0.1 | 1.0 ± 0.1 |
| **Uptake ratio of tumor/normal tissue** | | | | |
| Tumor/blood | 0.61 | 0.53 | 0.33 | 0.63 |
| Tumor/muscle | 4.7 | 7.7 | 3.9 | 6.0 |
| Tumor/kidney | 0.10 | 0.14 | 0.14 | 0.25 |
| Total Excretion (%) | 10.8 ± 9.5 | 21.4 ± 4.6 | 13.0 ± 1.1 | 27.7 ± 1.3 |

The biodistribution results correlated well with the low affinity for the MC1R, as evidenced by the low tumor uptake values found for **Tc7** (2.33 ± 0.89 % IA/g) and **Tc8** (2.63 ± 0.50 % IA/g) at 1 h p.i. Furthermore, **Tc7** and **Tc8** showed an unfavorable biodistribution profile, with a slow clearance from the bloodstream and a very low overall excretion from whole animal body as only 21.4 % and 27.7 % of total activity, respectively, was eliminated after 4 h p.i. Although occuring some renal excretion, the hepatobiliary excretion pathway played a prominent role as seen by the high liver accumulation (**Tc7**: 30.4 ± 5.2 % IA/g and **Tc8**: 40.2 ± 4.8 % IA/g, at 1 h p.i.).

Urine and blood samples were collected from the sacrificed C57BL/6 mice 1 h p.i. to assess the *in vivo* stability of the corresponding radiopeptides. After appropriate treatment, the biological samples were analyzed by RP-HPLC. As an example, the

chromatograms of **Tc8** (initial preparation) and of the biological samples at 1 h p.i. are shown in **Figure 3.13**.

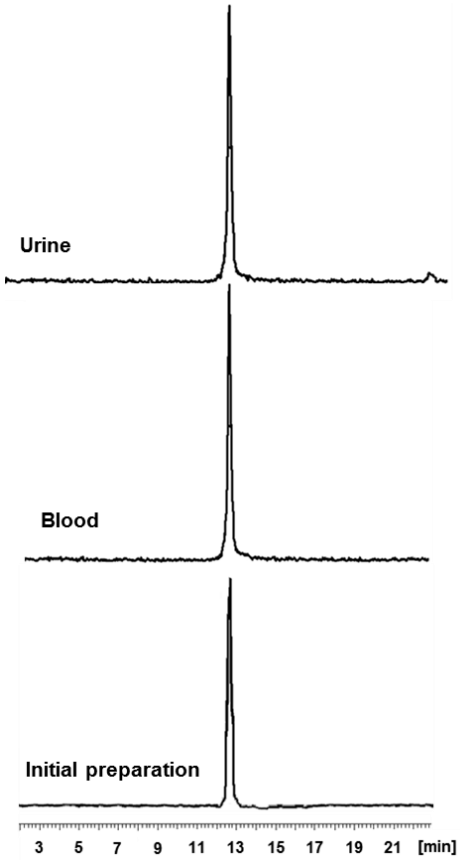


**Figure 3.13**: RP-HPLC γ traces of **Tc8** (initial preparation), blood serum and urine samples collected 1 h after p.i.

The *in vivo* stability studies demonstrated that **Tc7** and **Tc8** were stable in blood serum, as no metabolites could be detected.

### 3.9. Conclusions

We have designed novel thioether (**SNBA-MSH$_{hex}$**) and amine bridge-cyclized (**NNBA-MSH$_{hex}$**) α-MSH derivatives bearing a Lys linker at the C-terminus. Conjugation of a bifunctional chelator to the ε-amino group of Lys gave peptide conjugates **L7** and **L8**. Reaction of the previously described rhenium precursor *fac*-$[Re(CO)_3(k^3\text{-}\mathbf{L1})]^+$ (**Re1**) with **SNBA-MSH$_{hex}$** and **NNBA-MSH$_{hex}$** gave the corresponding metallopeptides **Re7** and **Re8**.

Competitive binding assays has shown that the MC1R targeting properties of **SNBA-MSH$_{hex}$** were lower as compared to the cognate analog **PG10N**. Moreover,

**SNBA-MSH$_{hex}$** also bound to the MC1R with lower affinity than **NNBA-MSH$_{hex}$**. NMR studies indicated that such difference could be ascribed to the orientation of the Arg side chain in the pharmacophore sequence, which is in agreement with a recent study.[148] Furthermore, NMR structural analysis of the alkylthioaryl bridge-cyclized peptide derivatives **L7** and **Re7** demonstrated that the structural features of the peptide moiety remain unchanged upon conjugation of the chelating unit to the Lys side chain or upon incorporation of the metal fragment into the peptide conjugate.

Biodistribution studies in a B16F1 melanoma-bearing mouse model has shown that both radiopeptides were stable *in vivo*, however, their tumor targeting and pharmacokinetic properties were unfavorable. The tumor targeting correlated well with the low *in vitro* affinity of the rhenium surrogates **Re7** and **Re8** for the MC1R.

# 4

## Modulation of the Pharmacokinetic Properties of $^{99m}Tc(CO)_3$-labeled βAlaNleCycMSHhex

# 4. Modulation of the Pharmacokinetic Properties of $^{99m}Tc(CO)_3$-labeled βAlaNleCycMSHhex

## 4.1. Introduction

The $^{99m}Tc(CO)_3$-labeled cyclic peptide **βAlaNleCycMSHhex** (**Tc9**), previously described by our group,[81b] presented high tumor uptake (11.3 ± 1.8 % IA/g) at 4 h p.i. in B16F1 melanoma-bearing mice (**Figure 4.1**). However, it showed a slow overall excretion rate and high accumulation in excretory organs (32.1 ± 1.6 and 22.9 ± 1.2 % IA/g for kidney and liver, respectively).

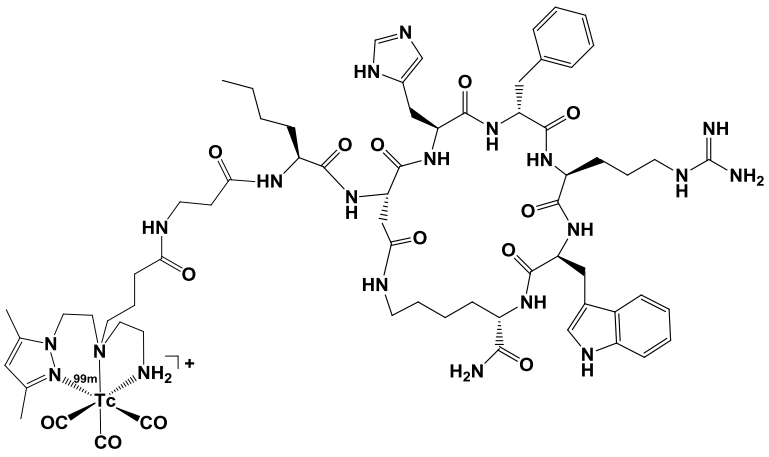

**Figure 4.1**: Schematic representation of **Tc9**.

Aiming to improve the pharmacokinetic profile of this radiopeptide, we decided to modify its physicochemical properties (e.g. hydrophilicity and molecular weight) through structural modifications in the ring substitution pattern of the pyrazolyl-diamine chelating unit. Such data could provide a better insight into the structural factors that influence melanoma uptake, overall excretion rate, and tumor/non-target organs ratios in melanoma bearing mice.

This chapter describes the synthesis and characterization of Boc-protected pyrazolyl-diamine based bifunctional chelators **L10-Boc** – **L12-Boc**, as well as peptide conjugates **L13** – **L15**, which contain the lead peptide **βAlaNleCycMSHhex**. The biological properties of novel $^{99m}Tc(CO)_3$-labeled **βAlaNleCycMSHhex** analogs **Tc13**, **Tc14** and **Tc15** are also reported

## 4.2. $M(CO)_3$-Complexes (M = Re, $^{99m}$Tc) Anchored by Pyrazolyl-Diamine-Based Chelators

### 4.2.1. Synthesis and Characterization of the Bifunctional Chelators

We have introduced the three novel Boc-protected bifunctional chelators **L10-Boc – L12-Boc** with different azolyl-ring substitution patterns (**Figure 4.2**). They contain a common $N_3$ donor atom set for stabilization of the organometallic core *fac*-$[M(CO)_3]^+$ (M = Re, $^{99m}$Tc) and a central propyl-carboxylate spacer for peptide conjugation.

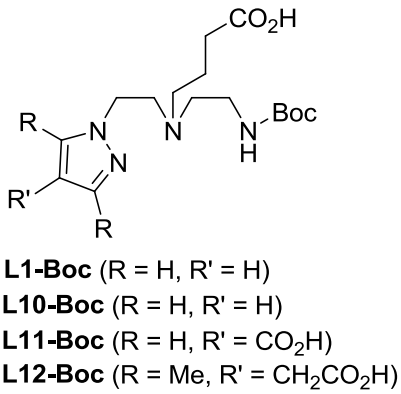


**Figure 4.2**: Boc-protected Bifunctional chelators **L1-Boc** and **L10-Boc – L12-Boc.**

The synthetic pathway for these compounds is shown in **Scheme 4.1**. **L10-Boc – L12-Boc** were prepared by alkylation of the central secondary amine of the respective precursors **III**, **IV** and **V** with ethyl 4-bromobutanoate, followed by basic hydrolysis of the corresponding intermediate compounds **VI**, **VII** and **VIII**.[48d, 150]

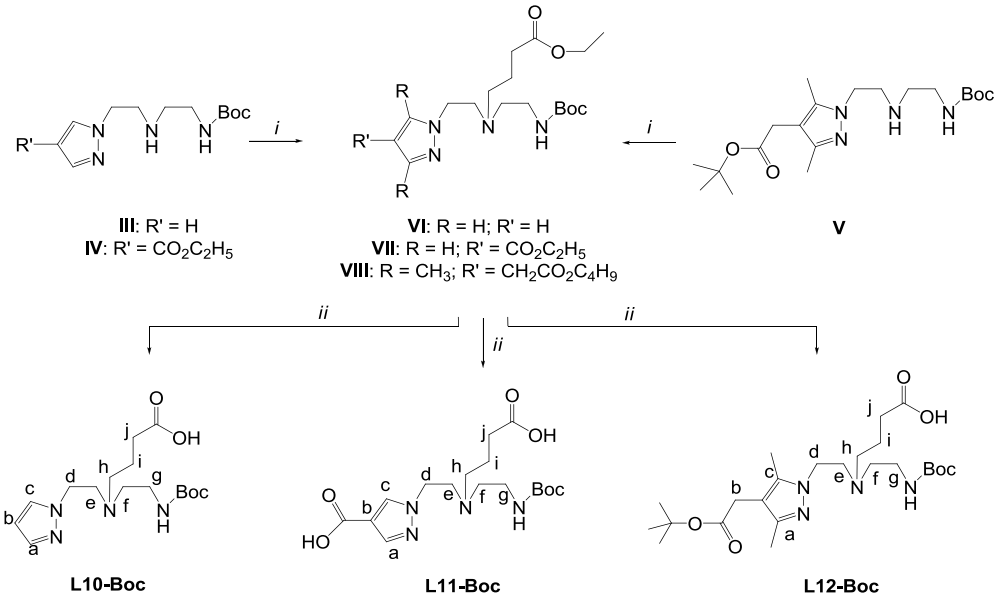


**Scheme 4.1**: Synthesis of the bifunctional chelators **L10-Boc, L11-Boc** and **L12-Boc**. *i*) $Br(CH_2)_3CO_2Et$, $K_2CO_3$, KI, $CH_3CN$; *ii*) NaOH, $THF/H_2O$, r.t., overnight; (*identification system for NMR assignments is displayed).*

All compounds were characterized by the usual analytical techniques in chemistry, including RP-HPLC, NMR spectroscopy and ESI-MS. 2D-NMR experiments ($^1H$-$^1H$ g-COSY and $^1H$-$^{13}C$ g-HSQC), which allowed full peak assignment in the NMR spectra. As an example, we present the $^1H$-NMR spectrum ($D_2O$) of **L11-Boc** in **Figure 4.3.** The spectrum presents the protons of the azolyl-ring at δ 7.84/ 7.67, and a sharp singlet peak for the methylenic protons of the Boc protecting group at δ 3.2.

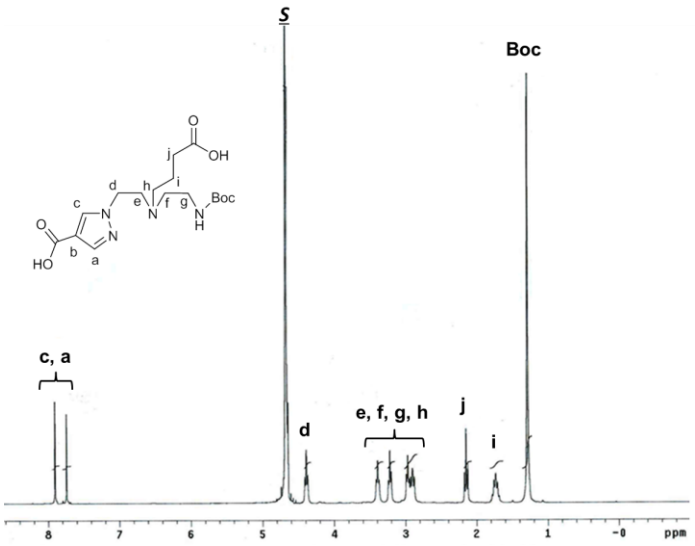


**Figure 4.3**: $^1H$-NMR spectrum of compound **L11-Boc** in $D_2O$ (S = residual water).

Resonances for all methylenic protons of the pyrazolyl-diamine backbone and propyl-carboxylate spacer were also found and fully assigned. The $^{13}$C-NMR spectra of the chelators presented signals corresponding to all the carbon nuclei.

### 4.2.2. Synthesis and Characterization of the Re(CO)$_3$-Complexes

The Boc deprotection of **L10-Boc**, **L11-Boc** and **L12-Boc** under standard conditions gave the bifunctional chelators **L10**, **L11** and **L3**, respectively. It is noteworthy that the preparation of **L3** has already been described in section **2.2.4** using, however, a different synthetic pathway.

Reaction of **L3**, **L10** and **L11** with equimolar amounts of the precursor *fac*-[Re(CO)$_3$(H$_2$O)$_3$]Br in refluxing water, gave, after purification by preparative RP-HPLC (Method A, experimental section), complexes of the type *fac*-[Re(CO)$_3$($\kappa^3$-**L**)]$^+$ (**Re3**, L = **L3**; **Re10**, L = **L10**; **Re11**, L = **L11**) (**Scheme 4.2**).

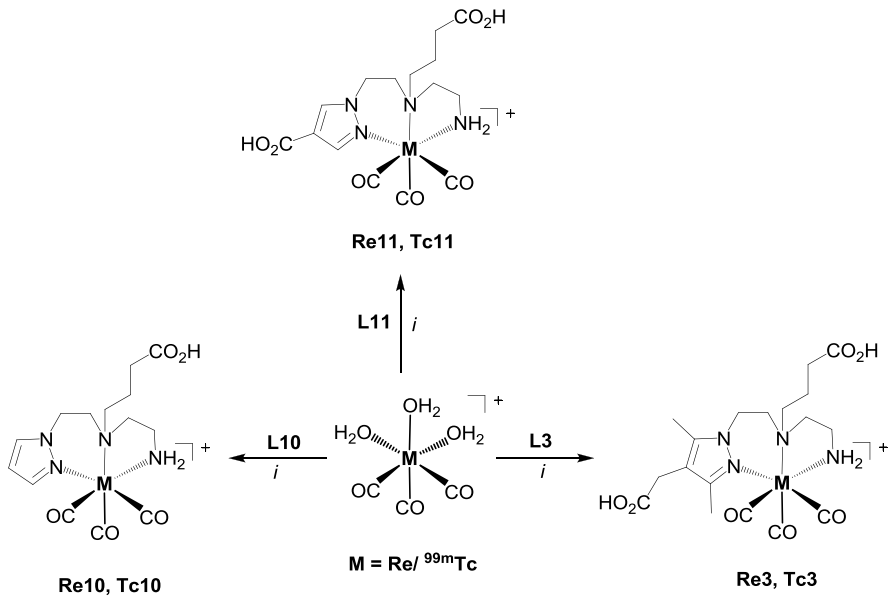


**Scheme 4.2**: Synthesis of complexes **Re3/Tc3**, **Re10/Tc10** and **Re11/Tc11**. *i*) $H_2O$, reflux, overnight (M = Re) or $H_2O$, 100 °C, 30 min (M = $^{99m}$Tc).

The complexes **Re3**, **Re10** and **Re11**, non-radioactive surrogates of the corresponding **Tc3**, **Tc10** and **Tc11** (**Scheme 4.2**), were fully characterized by IR and NMR spectroscopy, ESI-MS, and RP-HPLC. As in the case of the bifunctional chelators, the use of 2D-NMR experiments ($^1$H-$^1$H g-COSY and $^1$H-$^{13}$C g-HSQC) was crucial for peak assignment in the NMR spectra.

The $H^{a, c}$ and the $H^{b}$ of the pyrazolyl ring in **Re10** were shifted downfield ($H^{a,c}$, Δ= ~0.30 – 0.20 ppm; $H^{b}$, Δ= ~0.25 – 0.10 ppm) relatively to the same resonances in the corresponding free chelator, indicating coordination to the metal center. Similar behavior was also found for the $H^{a, c}$ of the pyrazolyl ring in **Re11** ($H^{a, c}$, Δ= ~0.20 ppm) as well as for the the methyl protons of the pyrazolyl ring in **Re3** (Me, Δ = ~0.14 – 0.08 ppm).

The tridentate coordination mode of the chelators was confirmed by the splitting of the protons of the primary amine (δ 5.03 and δ 3.61, **Re3**; δ 5.07 and δ 4.10, **Re10**; δ 5.11 and δ 4.22, **Re11**), as well as by the splitting of the methylenic protons of the coordinating backbone. For each of these protons, two resonances, integrating for one proton each, were found, due to the diastereotopic character of the methylenic protons after coordination to the metal center (e.g. δ 4.33 $CH^{d}$, δ 4.07 $CH^{d'}$, δ 3.33 $CH^{e}$, δ 2.53 $CH^{e'}$ for **Re3**; δ 4.52 $CH^{d}$, δ 4.37 $CH^{d'}$, δ 3.42 $CH^{e}$, δ 2.70 $CH^{e'}$ for **Re10**; δ 4.54 $CH^{d}$, δ 4.46 $CH^{d'}$, δ 3.56 $CH^{e}$, δ 2.69 $CH^{e'}$ for **Re11**). This behavior, which is a strong evidence of ligand coordination, has been already observed in other tricarbonyl complexes of the same type previously described.[48c, d] The $^{13}$C-NMR spectra presented all the expected signals for the proposed structures, which include three resonances for the C≡O ligands coordinated facially to rhenium (δ 196.3, δ 195.8 and δ 194.8 ppm for **Re3**; δ 195.1, δ 194.6 and δ 193.1 for **Re10**; δ 194.6, δ 194.1 and δ 192.3 for **Re11**).

The $^{1}$H-NMR and $^{13}$C-NMR spectra of **Re11** with corresponding peak assignment are presented in **Figure 4.4** as an illustrative example.

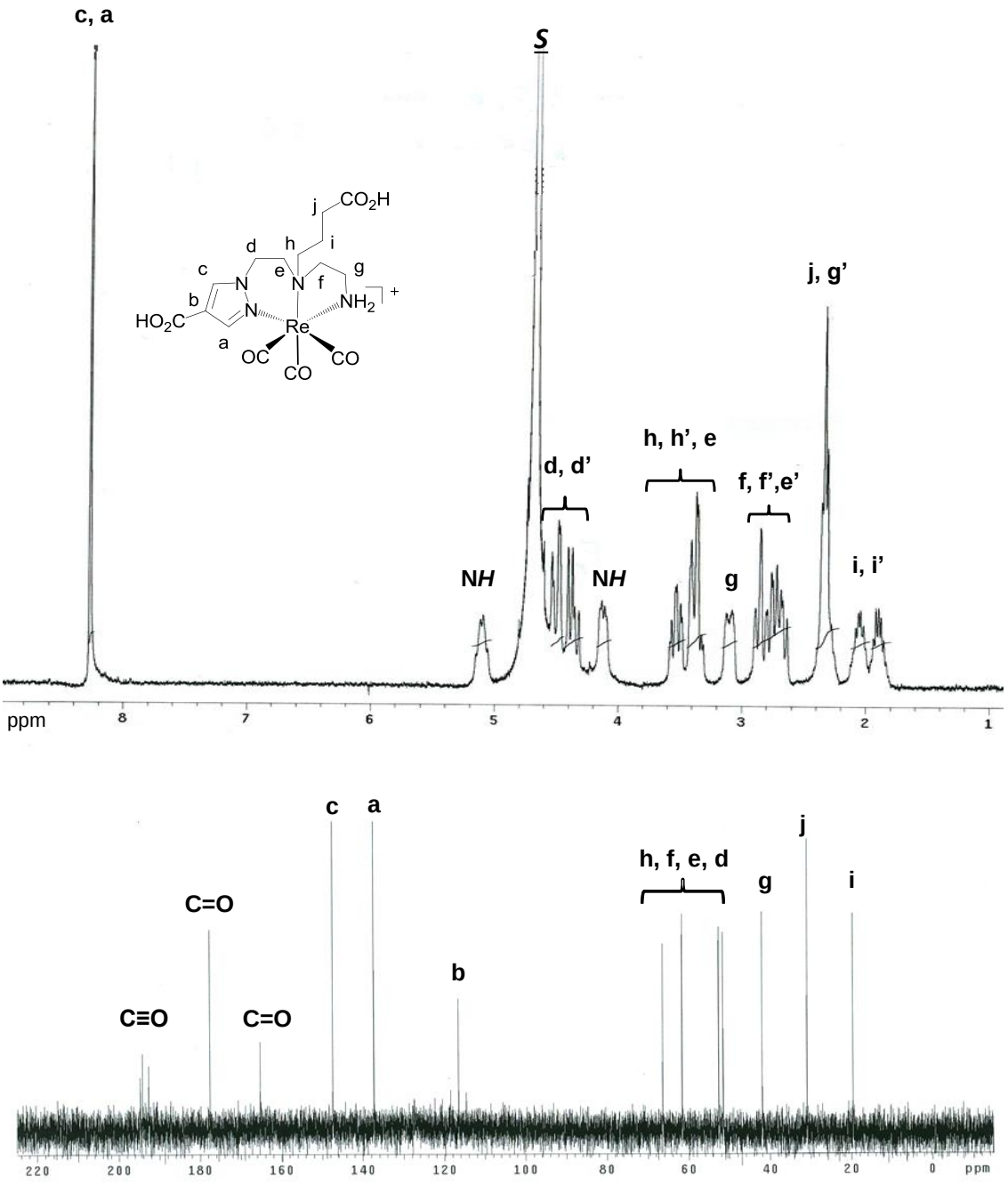


**Figure 4.4**: $^{1}$H-NMR (top) and $^{13}$C-NMR (bottom) spectra of **Re11** in $D_2O$.

The facial arrangement of the carbonyl groups in the complexes was confirmed by the strong C≡O stretching bands in the IR spectra (2028s and 1927s cm$^{-1}$, **Re3**; 2030s and 1920s cm$^{-1}$, **Re10**; 2031s and 1925s cm$^{-1}$, **Re11**), being within the ranges normally found for other complexes with the "*fac*-Re(CO)$_3$" moiety.[48]

### 4.2.3. Synthesis and Characterization of the $^{99m}Tc(CO)_3$-Complexes

The radioactive complexes **Tc3**, **Tc10** and **Tc11** were prepared in high yield (> 95 %) by reaction of **L3**, **L10** and **L11** (100 µL, [**L**] = $10^{-4}$ M) with *fac*-$[^{99m}Tc(CO)_3(H_2O)_3]^+$ (900 µL) in aqueous solution at 100 °C for 30 min (**Scheme 4.2**).

The chemical identity of the complexes *fac*-$[^{99m}Tc(CO)_3(\kappa^3\text{-}\mathbf{L})]^+$ (**Tc3**, L = **L3**; **Tc10**, L = **L10**; **Tc11**, L = **L11**) was confirmed by comparing their RP-HPLC profiles (Method A, experimental section) with those of the corresponding rhenium analogs **Re3**, **Re10** and **Re11**. As an example, the RP-HPLC chromatogram of the complexes **Tc3**/**Re3** is displayed in **Figure 4.5**.

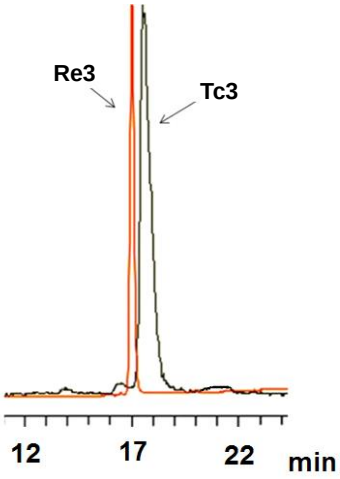


**Figure 4.5**: RP-HPLC traces of **Re3** (U.V. detection, 254 nm) and **Tc3** (γ detection).

The hydrophilic nature of **Tc3**, **Tc10** and **Tc11** was determined by the partition coefficient ($P_{o/w}$) in the biphasic system octanol/PBS (experimental section, **7.4**). The radiocomplexes present a hydrophilic nature (**Tc3**: -1.82 ± 0.02, **Tc10**: - 1.23 ± 0.02, **Tc11**: -2.22 ± 0.03) and the presence of an additional carboxylate in the azolyl-ring enhanced such property.

To ascertain the *in vitro* stability, complexes **Tc3**, **Tc10** and **Tc11** were incubated with a large excess of cysteine or histidine (37 °C for 18 h). Aliquots of these solutions were analyzed at different time points by analytical RP-HPLC (Method A, experimental section). The results have shown that all complexes were highly stable, since no decomposition or reoxidation to $[^{99m}TcO_4]^-$ occured.

### 4.2.4. Biodistribution and *In Vivo* Stability Studies

The biological behavior of **Tc3**, **Tc10** and **Tc11** was studied in healthy CD/1 mice to evaluate their pharmacokinetics and *in vivo* stability at 1 h, and 4 h p.i. Tissue distribution data of these complexes is presented in **Table 4.1**.

**Table 4.1**: Biodistribution (% IA/g) and total excretion (% IA) of the complexes **Tc3**, **Tc10** and **Tc11** in CD/1 mice, 1 h and 4 h p.i.

| | % IA/g ± S.D. | | | | | |
|---|---|---|---|---|---|---|
| **Tissue/ organ** | **Tc3** | | **Tc10** | | **Tc11** | |
| | **1h** | **4h** | **1h** | **4h** | **1h** | **4h** |
| Blood | 1.10 ± 0.20 | 0.90 ± 0.60 | 0.52 ± 0.08 | 0.15 ± 0.01 | 0.26 ± 0.06 | 0.15 ± 0.02 |
| Liver | 3.90 ± 1.00 | 4.80 ± 1.00 | 9.61 ± 1.40 | 2.72 ± 0.25 | 1.24 ± 0.19 | 0.96 ± 0.27 |
| Intestine | 12.60 ± 0.80 | 13.30 ± 1.90 | 4.54 ± 0.87 | 7.06 ± 0.44 | 3.87 ± 0.54 | 3.35 ± 0.49 |
| Spleen | 0.36 ± 0.05 | 0.38 ± 0.21 | 0.31 ± 0.03 | 0.12 ± 0.01 | 0.44 ± 0.10 | 0.22 ± 0.04 |
| Heart | 0.44 ± 0.04 | 0.37 ± 0.18 | 0.27 ± 0.00 | 0.10 ± 0.01 | 0.06 ± 0.03 | 0.05 ± 0.01 |
| Lung | 0.70 ± 0.10 | 0.45 ± 0.34 | 0.45 ± 0.03 | 0.18 ± 0.01 | 0.19 ± 0.07 | 0.09 ± 0.05 |
| Kidney | 2.00 ± 0.60 | 3.30 ± 0.30 | 11.12 ± 2.13 | 2.34 ± 0.15 | 2.95 ± 0.79 | 0.42 ± 0.05 |
| Muscle | 0.20 ± 0.02 | 0.24 ± 0.04 | 0.14 ± 0.01 | 0.05 ± 0.00 | 0.12 ± 0.16 | 0.02 ± 0.00 |
| Bone | 0.24 ± 0.03 | 0.26 ± 0.04 | 0.16 ± 0.03 | 0.06 ± 0.00 | 0.09 ± 0.03 | 0.03 ± 0.01 |
| Stomach | 1.10 ± 0.60 | 1.00 ± 0.30 | 0.64 ± 0.19 | 0.31 ± 0.12 | 0.11 ± 0.08 | 0.11 ± 0.04 |
| Excretion % | 41.40 ± 3.80 | 44.50 ± 2.70 | 52.5 ± 3.8 | 70.7 ± 2.4 | 80.8 ± 2.40 | 85.30 ± 2.00 |

The main differences in the biodistribution profile of **Tc3**, **Tc10** and **Tc11** were related to the clearance from tissues as well as to the rate of overall excretion. No preferential uptake in the main organs or tissues was observed, except those involved in the excretory routes (liver, intestines and kidney). The radiocomplex **Tc11** has shown a faster clearance from the main organs, an enhanced overall excretion (**Tc11**: 85.30 ± 2.00 % IA/g; **Tc10**: 70.7 ± 2.4 % IA/g; **Tc3**: 44.50 ± 2.70 % IA/g; 4 h p.i.), and a higher hepatobiliary clearance.

There was no significant uptake in the stomach, indicating a high stability of the complexes to reoxidation. Analysis of murine serum and urine samples by RP-HPLC showed no pertechnetate or other decomposition products, being complexes **Tc3**, **Tc10** and **Tc11** the only species present. Taken together, these results demonstrated the *in vivo* stability of the complexes.

## 4.3. Lactam Bridge-Cyclized α-MSH Peptide Conjugates

### 4.3.1. Synthesis and Characterization of $\beta$AlaNleCycMSH$_{hex}$

The linear sequence Fmoc-Asp(Dmab)-His(Trt)-DPhe-Arg(Pbf)-Trp(Boc)-Lys(ivDde)-$NH_2$ was assembled to a MBHA Rink Amide resin by Fmoc-based Solid Phase Peptide Synthesis (SPPS) in a CEM 12-Channel Automated Peptide.

The peptidyl resin was treated with a freshly prepared mixture of hydroxylamine hydrochloride and imidazole in *N*-methylpyrrolidone (NMP) to accomplish a selective and simultaneous removal of the ODmab and ivDde side chain protecting groups.[93] Condensation of the Asp and Lys side chains to form the intramolecular lactam bridge was carried out using a large excess of (benzotriazol-1-yloxy)tripyrrolidinophosphonium hexafluorophosphate (PyBop: 6 equiv), DIPEA (12 equiv), and 1-hydroxybenzotriazole (HOBt: 6 equiv) for 36 h (negative Kaiser test). After lactamization, normal assembly of the remaining peptide chain was resumed up to the quantitative incorporation of the residues Nle and βAla.

Cleavage of the protected Fmoc-peptide from the solid support was performed by treatment of the peptidyl resin with TFA containing 2.5 % $H_2O$ and 2.5 % triisopropylsilane. The crude product was purified by RP-HPLC and **Fmoc-βAlaNleCycMSH$_{hex}$** was obtained as a white solid that was characterized by ESI-MS (found m/z for $[M+H]^+$: 1275.6; calcd. for $C_{66}H_{82}N_{16}O_{11}$ = 1274.6). RP-HPLC (Method J, experimental section): 99 % ($t_R$ = 25.8 min).

Removal of the Fmoc group in **Fmoc-βAlaNleCycMSH$_{hex}$** with piperidine/DMF gave **βAlaNleCycMSH$_{hex}$** as a white solid after evaporation of the solvent and washing with cold ethyl ether. The peptide was dried under nitrogen flow, dissolved in water, lyophilized and characterized by ESI-MS. In the ESI-MS spectra, the peak found at m/z = 1053.6, m/z = 527.4 and m/z = 264.3 correspond to $[M+H]^+$, $[M+2H]^{2+}$ and $[M+4H]^{4+}$, respectively (**Figure 4.6**).

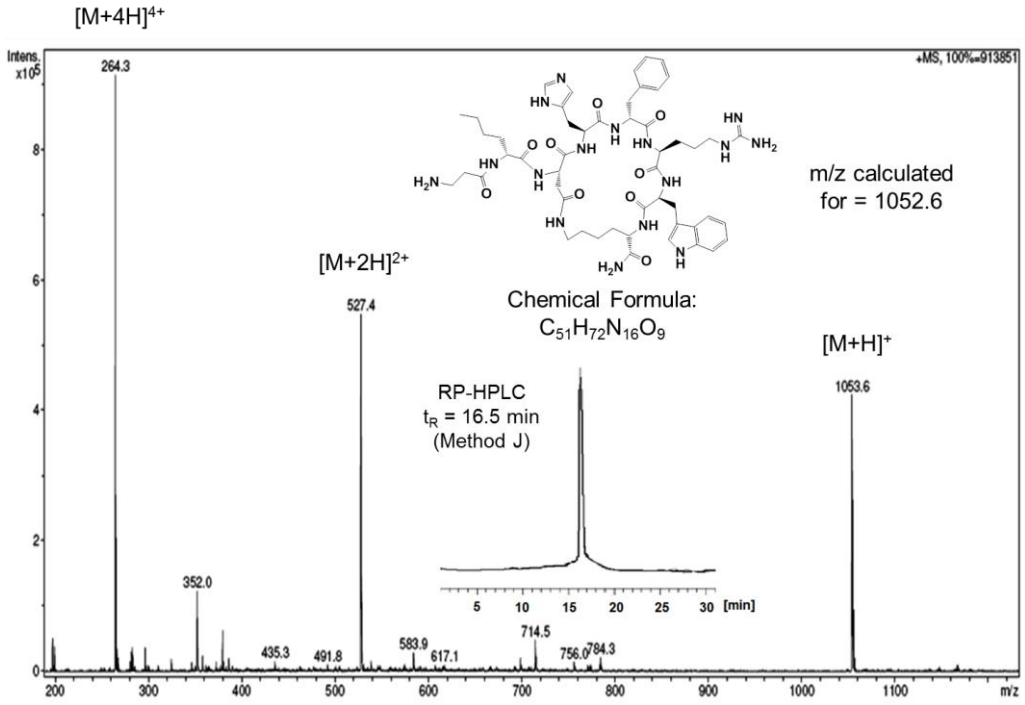


**Figure 4.6**: ESI-MS spectra and RP-HPLC chromatogram of **βAlaNleCycMSH$_{hex}$**.

### 4.3.2. Synthesis and Characterization of the βAlaNleCycMSH$_{hex}$ Conjugates

The chelators **L1-Boc**, **L10-Boc** – **L12-Boc** were conjugated to **βAlaNleCycMSH$_{hex}$** via HATU activation in the presence of DIPEA in a DMF solution, yielding intermediate conjugates, which, upon treatment with TFA gave the final conjugates **L9** and **L13 – L15**, respectively (**Scheme 4.3**).

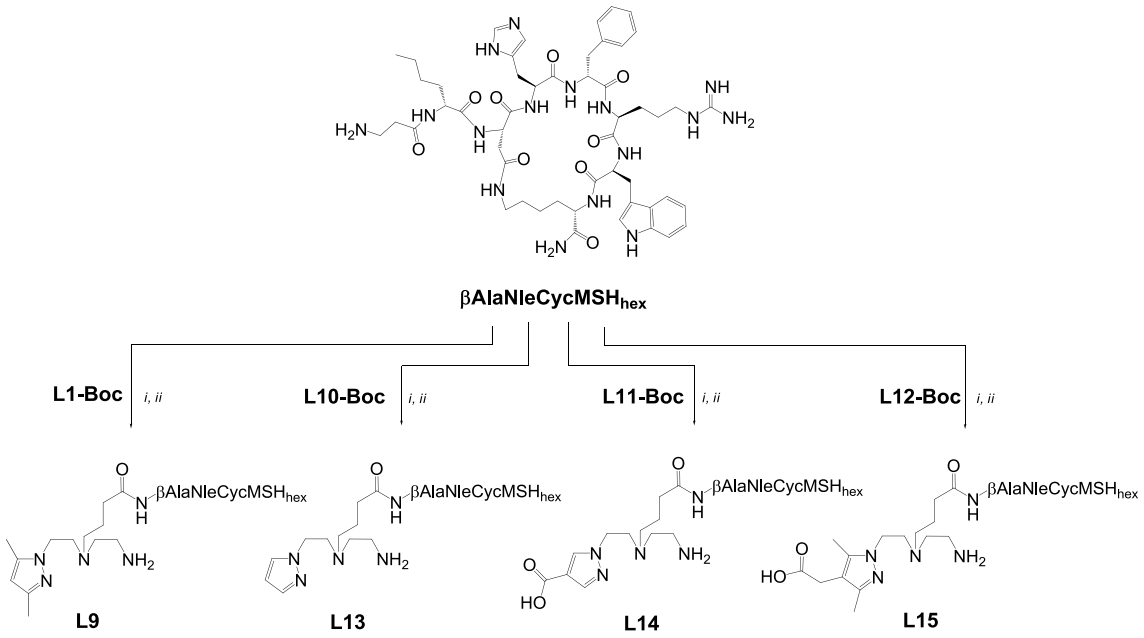


**Scheme 4.3**: Synthesis of the peptide conjugates **L9**[81b] and **L13** – **L15**. *i*) HATU, DIPEA, DMF; *ii*) 95 % TFA, 2.5 % TIS, 2.5 % $H_2O$.

The peptide conjugates were purified by semi-preparative RP-HPLC and characterized by ESI-MS (**Table 4.2**).

**Table 4.2**: Analytical data for the α-MSH peptide conjugates.

| Compound | Molecular formula | Calculated [ion] | Found | $t_R$/min (purity)* |
|---|---|---|---|---|
| **L13** | $C_{62}H_{90}N_{20}O_{10}$ | 639.2 $[M+2H]^{2+}$ | 638.4 | 13.3 (98%) |
| **L14** | $C_{63}H_{90}N_{20}O_{12}$ | 442.5 $[M+3H]^{3+}$ | 442.8 | 12.7 (98%) |
| **L15** | $C_{66}H_{96}N_{20}O_{12}$ | 682.3 $[M+2H]^{2+}$ | 681.8 | 11.2 (98%) |

*Method I, experimental section

Owing to the existence of two free carboxylate groups in **L11-Boc**, one at the pyrazole ring and the other at the pendant aliphatic arm, there are two likely conjugation positions for the peptide. To clarify this point, solution NMR studies ($^1H$-$^1H$ COSY, $^1H$-$^1H$ TOCSY, $^1H$-$^1H$ NOESY, $^1H$-$^1H$ ROESY, $^1H$-$^{13}C$ and $^1H$-$^{15}N$ HSQC) for **L11** and **L14** have been performed. After assigning the resonances in the spectra of **L11** and **L14**, we found that the chemical shifts of the carbon atoms of the pyrazolyl ring in **L11** and **L14** were almost identical ($^{13}C$: $|\Delta\delta^{free\text{-}bound}| \leq 0.5$ ppm; **Tables 7.14** and **7.15** at experimental section, respectively) while a significant difference was found for the methylene carbons of the aliphatic chain (1.1 and 1.7 ppm for methylene carbons $C^i$ and $C^j$, respectively; **Tables 7.14** and **7.15**), indicating that the conjugation occurs by the

carboxylate group at the aliphatic arm. Stronger and further support to this conclusion was attained from the ROE cross-peaks observed between **L11** and the peptide moiety that involve protons from the aliphatic arm of **L11**, but not from the pyrazolyl ring. The observed ROE cross-peaks were a strong cross-peak between the $H^j$ protons of **L11** and the HN amide of βAla[1], a medium-weak cross-peak between the $H^i$ protons of **L11** and the HN amide of βAla[1], and a weak cross-peak between the $H^j$ protons of **L11** and the $H_\alpha$ proton of βAla[1] (**Figure 4.7**). None of the ROE cross-peaks expected for the peptide moiety if conjugated through the carboxylate at the pyrazolyl ring were present.

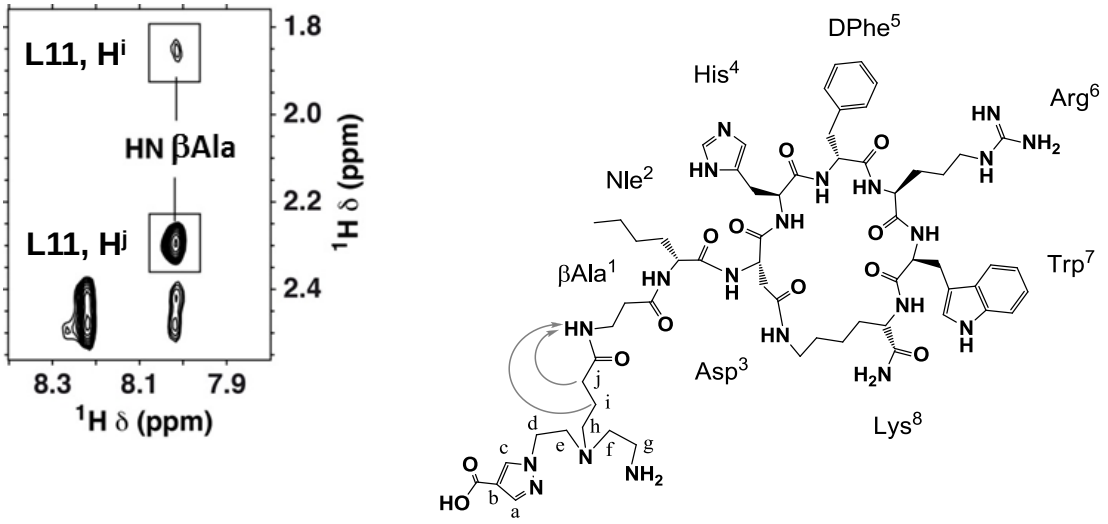


**Figure 4.7**: Selected ROESY spectral region (left) of **L14** in aqueous solution ($H_2O$/ $D_2O$ 9/1 v/v) at pH 2.5 and 25 °C and key correlations (right) observed between **L11** and the NH of βAla (arrow).

Brought together, the NMR parameters (ROEs and $^{13}$C-NMR chemical shifts) indicated the conjugation of the peptide through the carboxylate group of the central tertiary amine.

### 4.3.3. MC1R-Binding Affinity

The binding affinity of the cyclic α-MSH derivatives to the MC1R were evaluated in a competitive binding assay in B16F1 cells, using [$^{125}$I]-NDP-αMSH as radioligand. The $IC_{50}$ values for the peptide conjugates as well as for **βAlaNleCycMSH$_{hex}$** are listed in **Table 4.3**.

**Table 4.3**: Binding affinity for the α-MSH analog and peptide conjugates.

| Compound | IC50 (nM) ± S.D. |
|---|---|
| **βAlaNleCycMSH$_{hex}$** | 0.05 ± 0.02 |
| **L9** | 0.02 ± 0.05 |
| **L13** | 0.02 ± 0.01 |
| **L14** | 0.04 ± 0.01 |
| **L15** | 0.16 ± 0.10 |

The conjugation of the chelators to **βAlaNleCycMSH$_{hex}$** ($IC_{50}$ = 0.05 ± 0.02 nM) led to a slight improvement of the binding affinity in the case of **L9** ($IC_{50}$ = 0.02 ± 0.05 nM), **L13** ($IC_{50}$ = 0.02 ± 0.01 nM) and **L14** ($IC_{50}$ = 0.04 ± 0.01 nM), and a slight decrease in the case of **L15** ($IC_{50}$ = 0.16 ± 0.1nM).

## 4.4. Radiolabeling with *fac*-[$^{99m}Tc(CO)_3$]$^+$ Moiety

Reaction of the peptide conjugates **L9**, **L13** – **L15** (50 μL, [**L**] = $10^{-4}$ M) with the organometallic precursor *fac*-[$^{99m}Tc(CO)_3(H_2O)_3$]$^+$ (450 μL) gave the radiometallated peptides **Tc9**, **Tc13** – **Tc15** (**Scheme 4.4**) that were analyzed by RP-HPLC (**Table 4.4**).

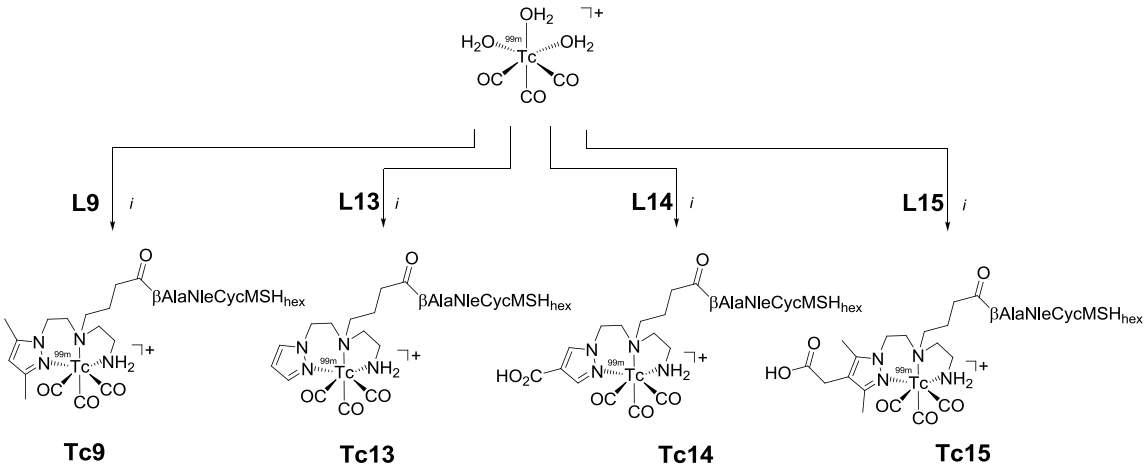


**Scheme 4.4**: Synthesis of the radiopeptides **Tc9**[81b] and **Tc13** – **Tc15**. *i*) 90 ºC, 20 min, pH = 7.

**Table 4.4**: Analytical data for the radiopeptides.

| Radiopeptides | $t_R$(min)* | log $P_{o/w}$ |
|---|---|---|
| **Tc9**[81b] | 12.7 | + 0.19 ± 0.01 |
| **Tc13** | 11.9 | − 0.93 ± 0.01 |
| **Tc14** | 10.6 | − 1.11 ± 0.02 |
| **Tc15** | 11.2 | − 0.88 ± 0.04 |

*Method H, experimental section

The partition coefficients, expressed in log $P_{o/w}$, were determined for **Tc9**, **Tc13** – **Tc15** by the ‘‘shake flask’’ method, in physiological conditions (**Table 4.4**).[151] The log $P_{o/w}$ values demonstrated the hydrophilic nature of the novel radiometallated peptides as compared to the previously described **Tc9** (+ 0.19 ± 0.01) with complex **Tc14** displaying the highest hydrophilic character (log $P_{o/w}$ = -1.11 ± 0.02).

To increase the specific activity, the radiopeptides were separated from the respective non-labeled peptide conjugates by RP-HPLC. As an example, **Figure 4.8** presents the retention times of conjugate **L15** ($t_R$ = 11.2 min) and **Tc15** complex ($t_R$ = 17.9 min) that were sufficient different to allow a good separation by RP-HPLC.

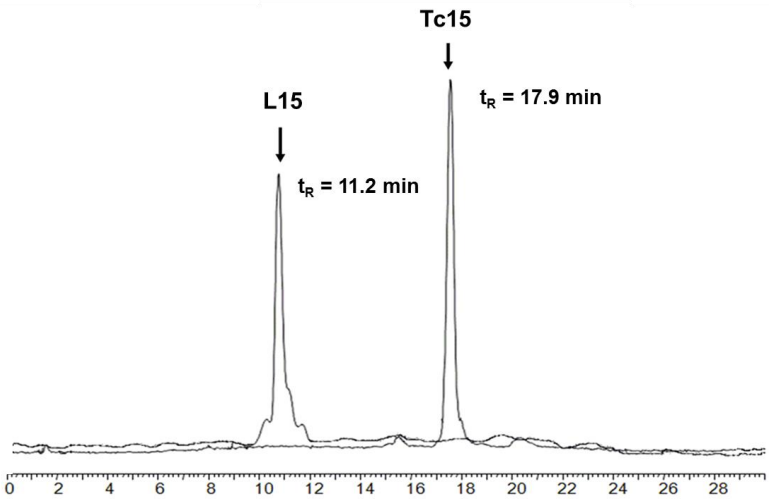


**Figure 4.8**: Superimposition of the RP-HPLC chromatograms of **L15** (U.V. detection) and **Tc15** (gamma detector), using Method J (experimental section **7.2**).

The activity corresponding to the radiopeptides **Tc13**-**Tc15** was collected in a Falcon flask, containing PBS. The pH of the final solution was adjusted to 7.4 with NaOH 0.1 M, for biodistribution and internalization studies. The product was controlled

by analytical RP-HPLC (Method J) to confirm its purity and stability after purification and concentration.

The stability of the radiopeptides was assessed in human serum at 37 °C and aliquots were analyzed at different time points by RP-HPLC. The results showed that all radiopeptides displayed high stability with negligible degradation. As an example, **Figure 4.9** depicts the RP-HPLC chromatographic profile of **Tc14** during the assay.

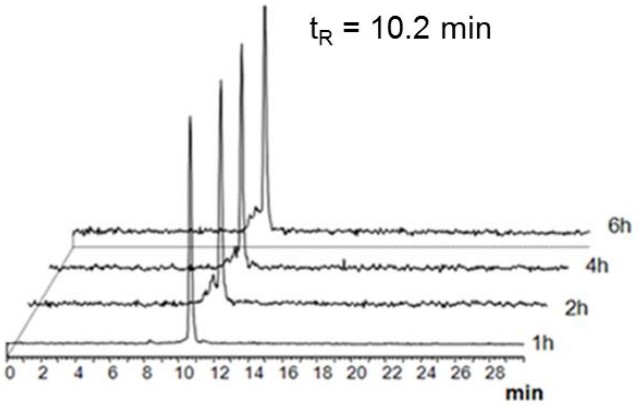


**Figure 4.9**: RP-HPLC chromatograms of **Tc14** after incubation in human serum at different time points (37 ºC).

The radiopeptides were also stable in cysteine and histidine solutions since no degradation or trans-chelation products were observed even after 6 h incubation at 37 °C.

### 4.5. Cell Uptake Studies

Aiming to predict the tumor-targeting properties of **Tc13** – **Tc15**, internalization studies in B16F1 murine melanoma cells have been performed at 37 ºC, and the results are presented in **Figure 4.10**.

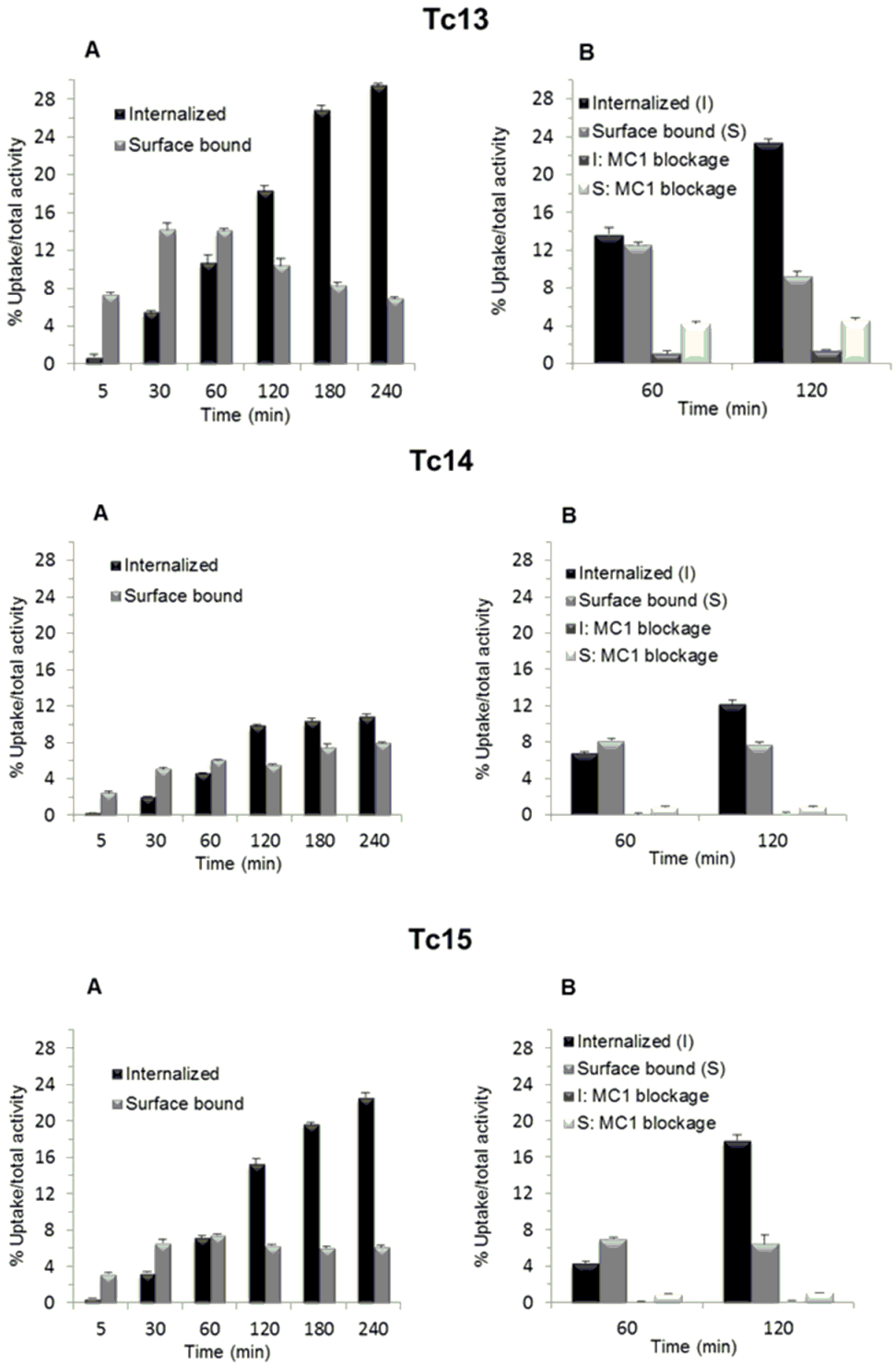


**Figure 4.10**: (**A**) Internalization of the radioconjugates **Tc13** – **Tc15** in B16F1 murine melanoma cells at different time points at 37 ºC. (**B**) Effect of MC1R-saturation with NDP-MSH (3.5 µg/well) on the internalized and the surface bound radioconjugates. Internalized and surface bound activity expressed as a percentage of total activity.

The radioconjugates **Tc13** – **Tc15** exhibited high levels of time-dependent internalization. The highest level of internalization was reached for complex **Tc13** after 4 h incubation at 37 ºC, with 29.4 ± 0.3 % of the total activity being internalized in B16F1 cells, which corresponds to 81.0 ± 0.4 % of the cell-associated activity (**Figure 4.10A**). At the same time point, 10.8 ± 0.3 % and 22.6 ± 0.5 % of the applied activity of **Tc14** and **Tc15** was internalized in B16F1 cells, corresponding to 57.8 ± 0.5 % and 78.6 ± 0.4 % of cellular uptake of **Tc14** and **Tc15**, respectively.

To evaluate the specificity of cellular uptake, internalization studies of **Tc13** – **Tc15** in B16F1 cells at 1 h and 2 h (37 ºC) were also performed with co-incubation with NDP-MSH (3.5 μg/ well), a α-MSH analog with high affinity for MC1R (0.21 nM). *In vitro* MC1R-saturation data is represented in **Figure 4.10B**. In the presence of NDP-MSH ($IC_{50}$ = 0.21 nM), the internalization of all radioconjugates was inhibited, being almost complete for **Tc14** and **Tc15** with a reduction of 99 % of internalized activity at 2 h after incubation *versus* 94 % for **Tc13**. The cell surface-bound activity of **Tc14** and **Tc15** was also highly reduced in the presence of NDP-MSH (90 % and 87 % of inhibition after 1 h; 89 % and 84 % of inhibition after 2h, respectively). Lower inhibition values were found for **Tc13** (66 and 50 % at 1 h and 2 h, respectively) indicating a higher non-specific binding to cell membrane. Taken together, these results suggested that the MC1R targeting properties was preserved upon radiometallation, as all radiopeptides displayed high level of time dependent internalization in murine B16F1 melanoma cells which was inhibited by receptor-saturation with NDP-MSH.

The cellular retention of **Tc13** – **Tc15** was evaluated at different time points, after 3 h internalization in B16F1 cells at 37 ºC (**Figure 4.11**). Good retention values were found for all compounds, and **Tc15** presented the best value with 62 % of the internalized activity still remaining inside the cells after 4 h. The radiopeptides **Tc13** and **Tc14** presented a similar behavior with 48 and 50 % of the internalized activity retained in the cells.

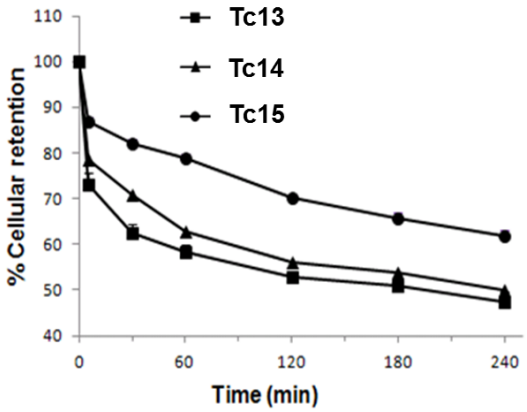


**Figure 4.11**: Cellular retention of internalized radioconjugates **Tc13** – **Tc15** in B16F1 melanoma cells over time at 37 ºC.

### 4.6. Biodistribution and *In Vivo* Stability

The *in vivo* MC1R-targeting properties of all radiopeptides were evaluated in B16F1 melanoma-bearing mice. **Table 4.5** presents the tissue distribution (% IA/g) of **Tc13** – **Tc15** in comparison with **Tc9**,[81b] at 1 h and 4 h p.i., as well as the data corresponding to radioconjugates **Tc14** and **Tc15** co-injected with NDP-MSH.

**Table 4.5**: Biodistribution studies of **Tc9** and **Tc13** – **Tc15** in B16F1 murine melanoma-bearing C57BL/6 mice at 1 and 4h p.i. (*n* = 3-5).

| | % IA/ g ± S.D. | | | | | | | | | |
|---|---|---|---|---|---|---|---|---|---|---|
| **Tissue/organ** | **Tc9**[81b] | | **Tc13** | | **Tc14** | | | **Tc15** | | |
| | **1 h** | **4 h** | **1 h** | **4 h** | **1 h** | **4 h** | **1h with NDP*** | **1 h** | **4 h** | **1h with NDP*** |
| **Tumor** | **9.26 ± 0.83** | **11.31 ± 1.83** | **9.90 ± 1.10** | **9.51 ± 1.34** | **11.82 ± 3.91** | **4.15 ± 0.53** | **1.69 ± 0.02** | **10.55 ± 1.83** | **6.15 ± 1.00** | **2.35 ± 0.46** |
| Blood | 2.71 ± 0.64 | 1.67 ± 0.24 | 1.82 ± 0.05 | 0.77 ± 0.09 | 0.65 ± 0.14 | 0.49 ± 0.01 | 0.84 ± 0.10 | 0.92 ± 0.05 | 0.41 ± 0.06 | 2.80 ± 0.64 |
| **Liver** | **42.19 ± 5.05** | **22.86 ± 1.17** | **23.97 ± 3.67** | **7.09 ± 0.42** | **2.96 ± 1.15** | **1.87 ± 0.17** | **4.33 ± 0.25** | **5.08 ± 0.12** | **2.13 ± 0.23** | **6.69 ± 1.46** |
| Intestine | 5.17 ± 0.91 | 8.45 ± 0.76 | 8.24 ± 1.04 | 10.59 ± 2.78 | 0.84 ± 0.26 | 1.60 ± 0.31 | 0.99 ± 0.36 | 2.28 ± 0.11 | 3.87 ± 0.54 | 1.81 ± 0.37 |
| Spleen | 2.54 ± 0.28 | 2.24 ± 0.37 | 7.67 ± 0.66 | 3.91 ± 0.38 | 0.44 ± 0.05 | 0.24 ± 0.03 | 0.83 ± 0.41 | 0.65 ± 0.04 | 0.28 ± 0.08 | 1.77 ± 0.73 |
| Heart | 1.04 ± 0.19 | 0.48 ± 0.07 | 2.85 ± 0.16 | 1.25 ± 0.07 | 0.29 ± 0.02 | 0.24 ± 0.09 | 0.51 ± 0.08 | 0.33 ± 0.11 | 0.15 ± 0.03 | 1.41 ± 0.40 |
| Lung | 3.85 ± 0.46 | 1.54 ± 0.16 | 7.16 ± 1.47 | 3.23 ± 0.59 | 0.78 ± 0.07 | 0.46 ± 0.26 | 0.57 ± 0.65 | 0.91 ± 0.19 | 0.31± 0.03 | 2.65 ± 0.83 |
| **Kidney** | **71.06 ± 6.44** | **32.12 ± 1.57** | **24.86 ± 1.80** | **4.02 ± 0.17** | **7.72 ± 1.33** | **2.97 ± 0.28** | **13.03 ± 1.19** | **2.98 ± 0.59** | **0.87 ± 0.14** | **9.83 ± 4.29** |
| Muscle | 0.35 ± 0.07 | 0.19 ± 0.08 | 0.49 ± 0.05 | 0.15 ± 0.01 | 0.16 ± 0.02 | 0.05 ± 0.01 | 0.25 ± 0.07 | 0.17 ± 0.01 | 0.04 ± 0.02 | 0.69 ± 0.30 |
| Bone | 1.14 ± 0.19 | 0.70 ± 0.13 | 0.99 ± 0.09 | 0.39 ± 0.03 | 0.33 ± 0.02 | 0.16 ± 0.06 | 0.45 ± 0.11 | 0.43 ± 0.20 | 0.11 ± 0.01 | 0.93 ± 0.25 |
| Stomach | 1.97 ± 0.75 | 0.88 ± 0.46 | 2.92 ± 0.72 | 0.32 ± 0.10 | 1.12 ± 0.39 | 0.07 ± 0.00 | 1.08 ± 0.17 | 1.32 ± 0.38 | 0.18 ± 0.07 | 1.69 ± 0.11 |
| Pancreas | 0.73 ± 0.32 | 0.39 ± 0.10 | 0.76 ± 0.05 | 0.26 ± 0.06 | 0.22 ± 0.02 | 0.09 ± 0.00 | 0.43 ± 0.08 | 0.16 ± 0.02 | 0.07 ± 0.02 | 0.98 ± 0.17 |
| **Tumor: normal tissue uptake ratio** | | | | | | | | | | |
| Tumor/blood | 3.4 | 6.8 | 5.4 | 12.3 | 18.2 | 8.5 | | 11.5 | 15 | |
| Tumor/muscle | 26.5 | 61.4 | 20.2 | 63.4 | 73.9 | 83 | | 62.0 | 153.7 | |
| Tumor/kidney | 0.13 | 0.35 | 0.40 | 2.36 | 1.53 | 1.4 | | 3.5 | 7.1 | |
| Tumor/liver | 0.22 | 0.49 | 0.41 | 1.34 | 3.99 | 2.2 | | 2.08 | 2.89 | |
| Total Excretion (%) | 14.2 ± 2.3 | 37.4 ± 2.4 | 27.6 ± 1.3 | 56.5 ± 7.0 | 73.9 ± 1.9 | 69.7 ± 1.7 | 63.4 ± 8.3 | 74.3 ± 2.4 | 83.7 ± 2.8 | 36.2 ± 22.6 |

** coinjection of the radioconjugate with NDP-MSH*

All radiopeptides exhibited rapid, high and comparable tumor uptake at 1 h p.i., with 11.82 ± 3.91 % IA/g for **Tc14**, 10.55 ± 1.83 % IA/g for **Tc15** and 9.90 ± 1.10 % IA/g for **Tc13**.

The kidney and liver uptakes of **Tc13 – Tc15** were significantly reduced when compared to **Tc9**. In fact, **Tc14** presented the lowest liver uptake at 1 h and 4 h p.i., with 2.96 ± 1.15 % IA/g and 1.87 ± 0.17 % IA/g, respectively. **Tc15** presented the lowest kidney accumulation at the same time points, with 2.98 ± 0.59 % IA/g and 0.87 ± 0.14 % IA/g, respectively. Furthermore, **Tc14** and **Tc15** were rapidly cleared from body with comparable and high excretion values (73.9 ± 1.9 % and 74.3 ± 2.4 % at 1 h p.i., respectively). This biological behavior of **Tc14** and **Tc15** could be ascribed to a reduction of the net positive charge of the radiopeptides due to the presence of a carboxylate group in the pyrazolyl ring of the chelator. This modification improved the tumor to excretory organs ratio of both peptides, displaying **Tc15** the highest tumor to kidney ratio value ( 7.1) among the all labeled lactam bridge-cyclized radiopeptides described in the literature, at 4 h p.i.[78a, 92, 94-96]

To evaluate the *in vivo* MC1R-binding specificity of **Tc14** and **Tc15**, the radioconjugates were co-administrated with cold NDP-MSH (20µg/mice) in B16F1 melanoma-bearing mice. As expected from the cell studies, MC1R-saturation with this potent agonist led to a very important reduction in the tumor uptake of **Tc14** (from 11.82 ± 3.91 to 4.15 ± 0.53 % IA/g) and **Tc15** (from 10.55 ± 1.83 to 2.35 ± 0.46 % IA/g), without significant changes in the biodistribution profile of the radioconjugates.

Owing to the favorable biodistribution properties of **Tc14** and **Tc15**, their melanoma imaging properties were further evaluated. **Figure 4.12** presents planar scintigraphic images of B16F1 murine melanoma-bearing C57BL/6 mice injected with **Tc14** and **Tc15** at 1 h p.i. Images were consistent with the biodistribution results, showing lower liver uptake for **Tc14** and lower kidney uptake for **Tc15**.

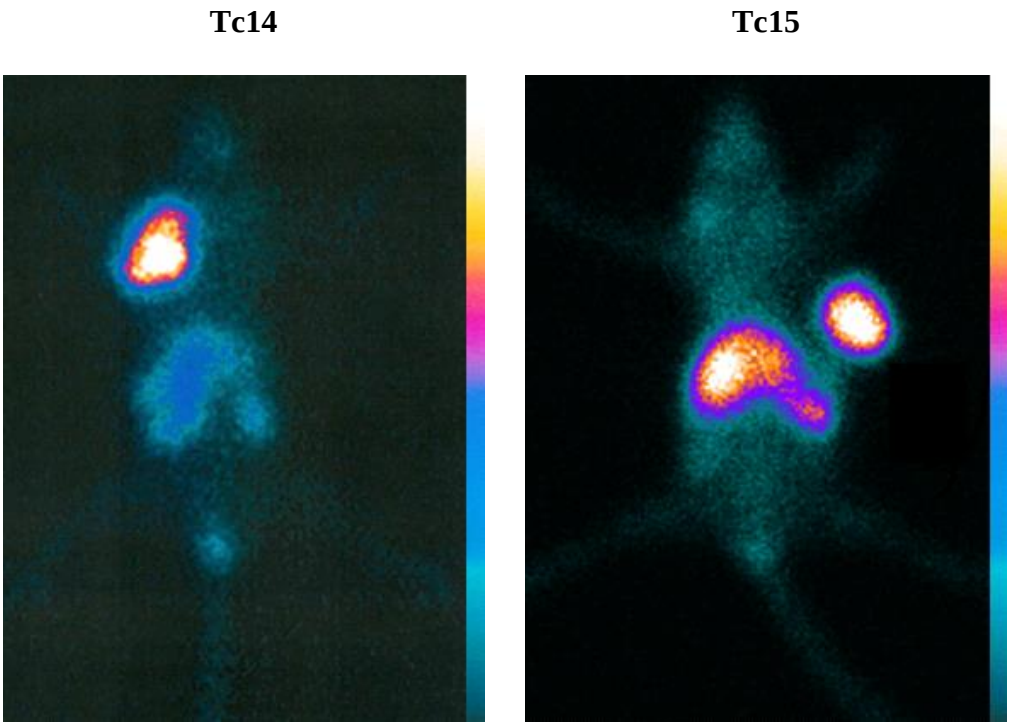


**Figure 4.12**: Planar scintigraphic images of B16F1 murine melanoma-bearing C57BL/6 mice injected with **Tc14** and **Tc15** at 1 h p.i.

Moreover, the enhanced tumor/kidney and tumor/liver ratios for both compounds generated high contrast between tumor and background allowing a clear visualization of melanoma.

To study the *in vivo* stability, urine and blood samples as well as tumor, kidney and liver homogenates were collected from the sacrificed melanoma-bearing C57BL/6 mice 1 h and 4 h p.i. of the corresponding radiopeptide. After appropriate treatment, the biological samples were analyzed by RP-HPLC.

The analysis of tissue samples collected from sacrificed mice has shown that all radiopeptides were stable in blood serum, tumor and liver homogenates, as no metabolites could be detected after 4 h p.i. At this time point, new species with lower retention time, corresponding to hydrophilic metabolites (not identified), were detected in kidney homogenate and urine. As an example, **Figure 4.13** displays RP-HPLC profile of tumor, kidney and liver homogenate samples collected from animal injected with **Tc14**, at 1 h and 4 h p.i.

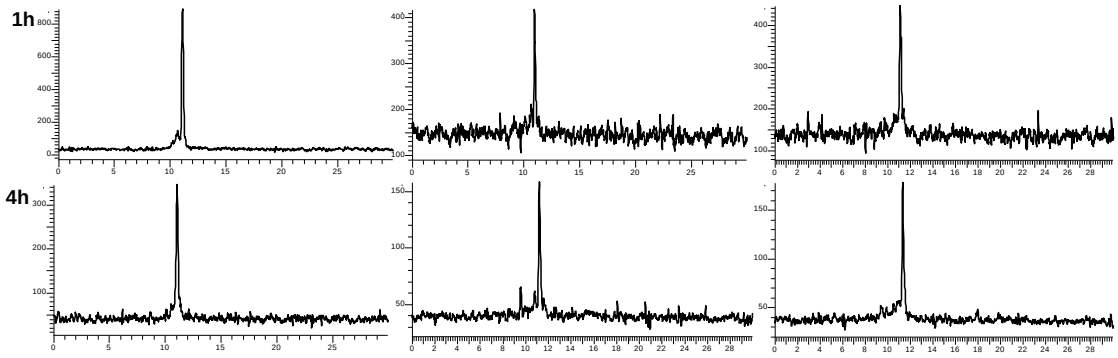


**Figure 4.13**: RP-HPLC γ traces of homogenate samples from tumor (left column), kidney (center column) and liver (right column) collected from melanoma-bearing C57BL/6 injected with **Tc14** at 1 h and 4 h p.i.

## 4.7. Conclusions

The main goal of the study presented in this chapter was to improve the overall biological profile of the $^{99m}Tc(CO)_3$-labeled **βAlaNleCycMSH$_{hex}$**. Such improvement was determined by the structural modifications in the azolyl-ring substitution pattern of the new compounds.

The introduction of a carboxylate group in the azolyl-ring of the chelator shifted the excretion pathway of the radiopeptides **Tc14** and **Tc15** from mainly hepatobiliar towards mainly renal leading to a striking kidney and liver uptake reductions (> 90%, at 4 h p.i.) and improved notably the excretion rate. Such effect taken together with the good in vivo MC1R-targeting properties enhanced significatively the uptake ratios of tumor to excretory organs

The relevant biological properties of **Tc14** and **Tc15** at the pre-clinical level highlights the potential usefulness of both compounds as melanoma imaging agents in humans.

# 5

## Mannosylated Dextran Derivatives for SLND

# 5. Mannosylated Dextran Derivatives for SLND by SPECT/CT and SPECT/NIR Imaging

## 5.1. Introduction

Radiolabeled mannosylated nanoparticles have been considered potential receptor-specific diagnostic agents for SLND. Among them, $^{99m}$Tc-Tilmanocept, a mannosylated $^{99m}$Tc-diethylene triaminepentaacetic acid (DTPA)-labeled dextran has shown the most promising *in vivo* behaviour, being currently in Phase 3 clinical trials.[152] However, from the chemical and radiochemical point of view, DTPA is not an ideal bifunctional chelator to stabilize Tc, as the chemistry of this metal with DTPA is not well defined, existing some controversial about the nature of the complex formed at non carrier added (n.c.a.) level.[27, 37, 153]

Profiting from the versatility of the $^{99m}$Tc-tricarbonyl technology as well as from the superior coordination properties of the pyrazolyl-diamine-based chelators,[48a, 48d] we aimed at contributing for the synthesis of highly stable and chemically defined $^{99m}$Tc(CO)$_3$-labeled dextran-based nanocompounds for SLND. Furthermore, we have also decided to expand this technology to the synthesis of bimodal probes for SLND by SPECT and near infrared (NIR) optical imaging.

This chapter describes the synthesis, characterization and biological evaluation of $^{99m}$Tc(CO)$_3$-labeled mannosylated dextran polymers for SLND by SPECT. We will also describe a bimodal probe for SPECT/NIR optical imaging of SLN.

## 5.2. Synthesis and Characterization of Mannosylated Dextran Bearing a Pyzazolyl-Diamine Chelator

Following a multistep synthetic pathway, we have functionalized dextran with a similar number of mannose units (Y = 13 units/mol dextran) and with a different number of pyrazolyl-diamine chelators (**L18**, X = 4 and **L19**, X = 8 units/ mol dextran) to stabilize the *fac*-[M(CO)$_3$]$^+$ moiety (M = $^{99m}$Tc, Re) (**Scheme 5.1**).[154]

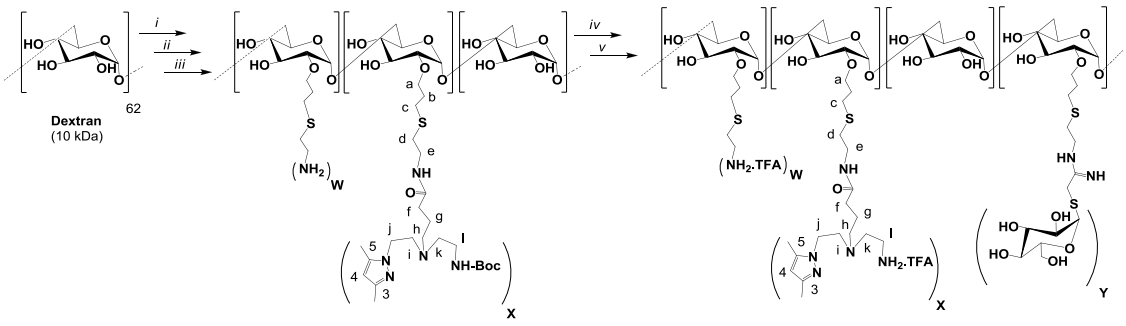


**Scheme 5.1**: Synthesis of mannosylated dextran derivatives bearing pyrazolyl-diamine and mannose units.[154] *i*) $BrC_3H_5$, NaOH (2.5 M), $H_2O$; *ii*) $NH_2(CH_2)_2SH$, $(NH_4)_2S_2O_8$, DMSO; *iii*) **L1-Boc**, 1-ethyl-3-(3-dimethylaminopropyl) carbodiimide (EDC), N-hydroxysuccinimide (NHS), borate buffer 0.1 M, pH 9; *iv*) 2-imino-2-methoxethyl-1-thio-β-D-mannoside (IME-thiomannose) 0.1 M borate buffer, pH 9; *v*) TFA/$H_2O$.

The high purity of the nanocompounds **L18** and **L19** was confirmed by SEC-HPLC at 220nm (method L, see experimental section). In fact, the chromatograms of both compounds present only one species, which appear at 14.4 min for **L18** and 14.6 min for **L19**. The number of units (bifunctional chelator and mannose) per mol of dextran in both cases was estimated based on the intensity ratio of the $^1$H-NMR peaks assigned to the mannose anomeric proton (δ 5.22), the methyl groups of the azolyl ring (3,5-$Me_2$Pz: δ 2.08, δ 1.98) and the protons adjacent to free amine of the dextran backbone (δ 2.74, He).[154]

## 5.3. M(CO)$_3$-Mannosylated Dextran (M = Re, $^{99m}$Tc)

### 5.3.1. Synthesis and Characterization of Re(CO)$_3$-Mannosylated Dextran

The rhenium-containing mannosylated dextrans **Re18** and **Re19** were prepared by reacting *fac*-[$Re(CO)_3(H_2O)_3$]Br with **L18** and **L19**, respectively, using a rhenium precursor/chelator molar ratio of 4:1 (**Scheme 5.2**). These metallated nanocompounds have been prepared to characterize the radiometallated compounds **Tc18** and **Tc19** described in section **5.3.2**.

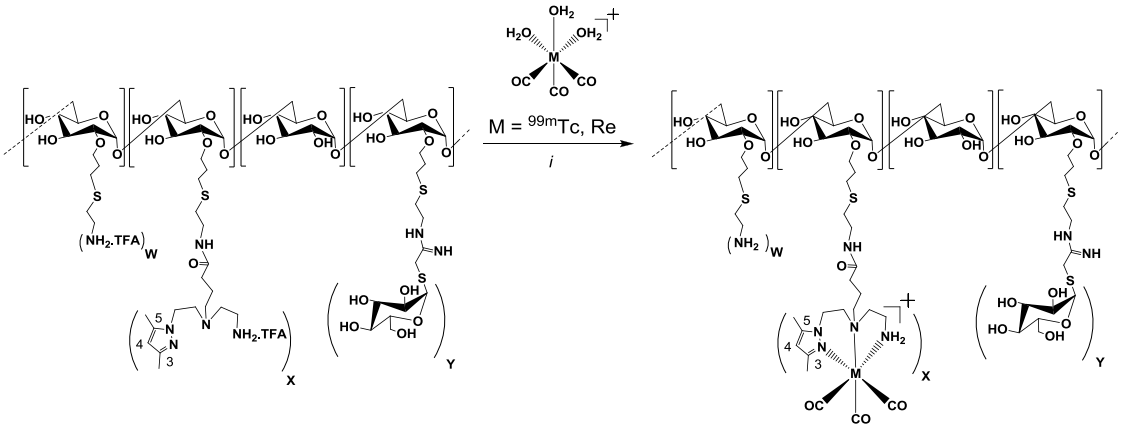


**Scheme 5.2**: Synthesis of *fac*-[M(CO)$_3$($\kappa^3$-**L**)] (M = $^{99m}$Tc/Re: **Tc18/Re18**, L = **18**; **Tc19/Re19**, L = **19**); i) $H_2O$, 50 ºC, 16 h (M = Re) or 100 °C, 10 min (M =$^{99m}$Tc).

The reactions were performed at 50 ºC to prevent polymer degradation. The kinetics of these reactions was slow and their progress was monitored by RP-HPLC and $^1$H-NMR spectroscopy at different time points (1 h, 6 h and 16 h). As an example, **Figure 5.1** shows the RP-HPLC chromatograms (Method M, experimental section **7.2**) and $^1$H-NMR spectra for one of these reactions at 1 h and 16 h.

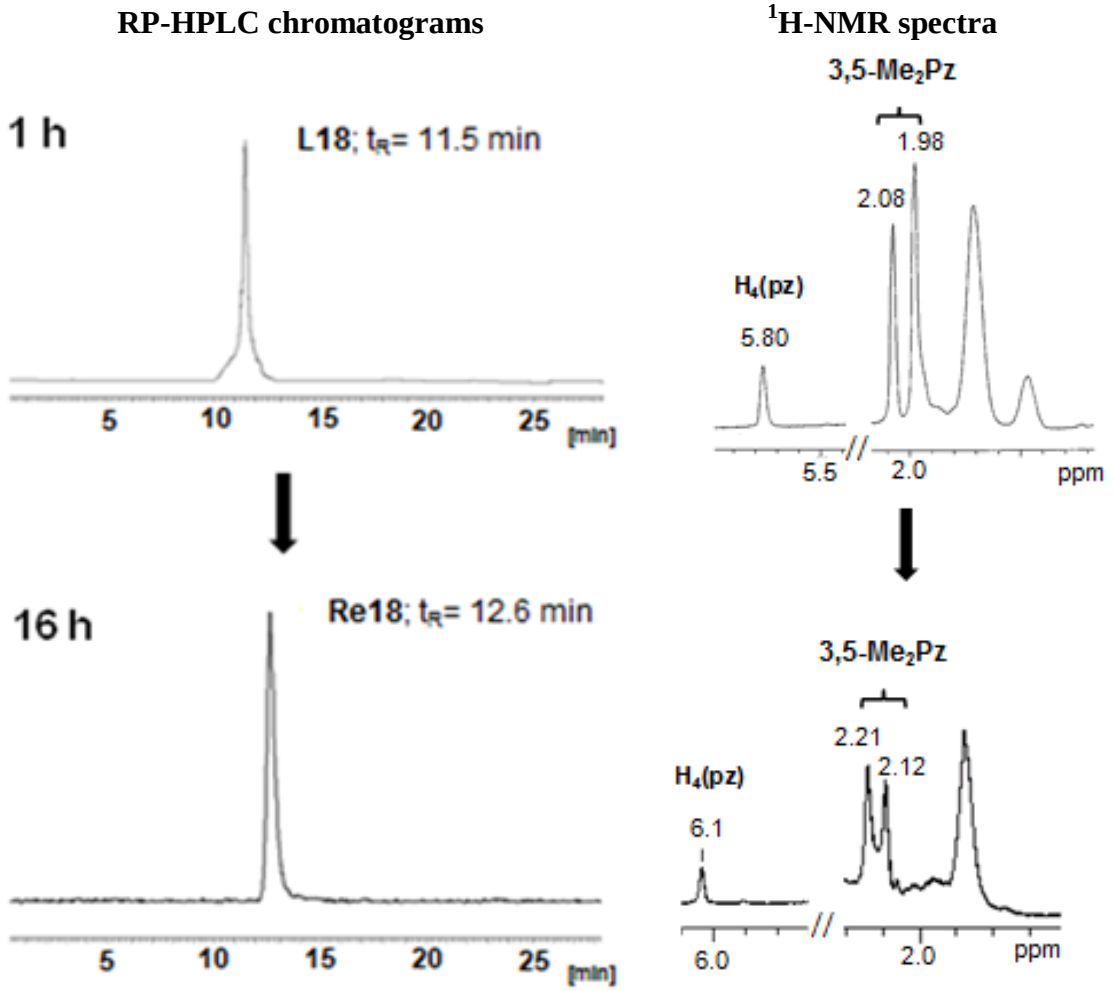


**Figure 5.1**: Progression of the reaction of *fac*-$[Re(CO)_3(H_2O)_3]Br$ with **L18**: RP-HPLC chromatograms (λ = 220 nm) and $^1$H-NMR data of the mixture at 1 h and 16 h after reagents addition.

From all the peaks of the pyrazolyl-diamine chelator in the $^1$H-NMR spectrum, only the ones assigned to $H_4$(Pz) and the methyl groups of the pyrazolyl-ring (3,5-$Me_2$Pz) were used to evaluate the progress of the reaction. After 1 h, the chemical shifts of $H_4$(Pz) (δ 5.8) and of 3,5-$Me_2$Pz groups (δ 2.08 and δ 1.98) presented values that correspond to the ones found for the free conjugate **L18**, indicating that no metallation has taken place. In addition, only one species was detected by RP-HPLC with a retention time identical to the one presented by **L18** ($t_R$ = 11.5). After 6 h, $^1$H-NMR analysis showed that some metallation has taken place, but some uncoordinated ligand could still be detected (results not shown). Only after 16 h the reaction was complete, as indicated by the three peaks that appear in the $^1$H-NMR spectrum at δ 6.10, δ 2.21 and δ 2.12 assigned to $H_4$(Pz) and 3,5-$Me_2$Pz groups of **Re18**. The chemical shift of these

peaks clearly confirmed the coordination of the metal to the chelating unit when compared with the same ressonances in the $^{1}$H-NMR spectrum of **L18**. **Re18** was also analyzed by SEC- and RP-HPLC and, in both cases, only one peak was present at 14.4. min and 12.6 min, respectivelly.

In the $^{13}$C-NMR spectra of **Re18** and **Re19**, the peaks due to the carbonyl groups of the *fac*-$[Re(CO)_3]^+$ core could also be assigned in the expected range (**Re18**: δ 195.2, δ 194.7 and δ 193.1; **Re19**: δ 195.4, δ 194.9 and δ 193.2).

The presence of the organometallic core in **Re18** and **Re19** was also confirmed by the IR data, where strong stretching bands due to ν(C≡O) could be found in the range 2027 - 1998 cm$^{-1}$. These ν(C≡O) stretching bands are shifted to slightly higher wavenumbers as compared to the rhenium tricarbonyl precursor (ν(C≡O), 2025 - 1941 cm$^{-1}$) (**Figure 5.2**).[48a, 155]

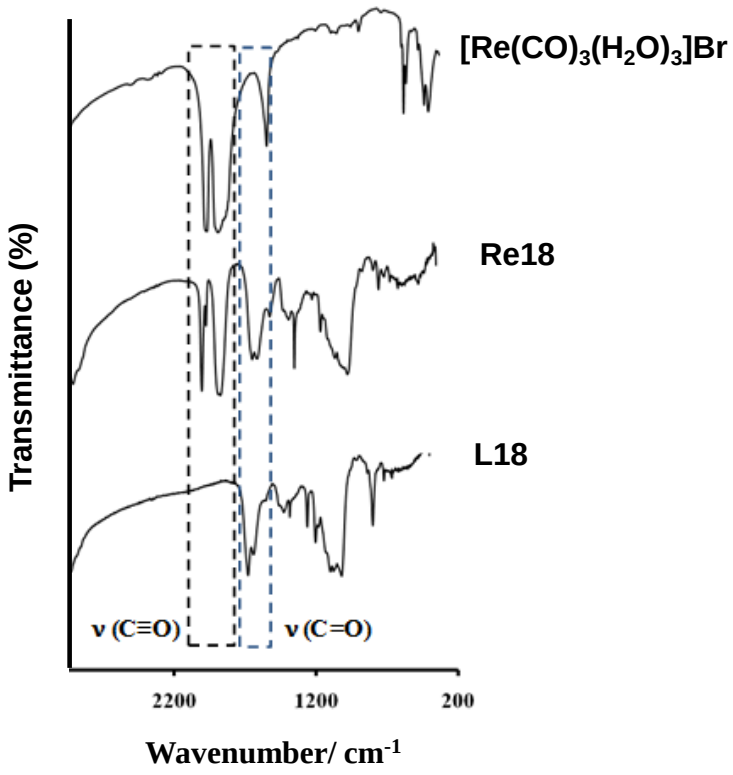


**Figure 5.2**: IR spectra of $[Re(CO)_3(H_2O)_3]Br$, **Re18** and L**18**.

The metallated polymers **Re18** and **Re19**, the corresponding precursors **L18** and **L19**, as well as the dextran precursor (M.W. = 10 kDa) were also characterized by dynamic light scattering (DLS), atomic force microscopy (AFM) and laser Doppler velocimetry (LDV).

The hydrodynamic diameter and the zeta potential were determined in PBS 0.01 M, pH 7.4, in order to mimic the radiolabeling conditions (section **5.3.2**). As an example, **Figure 5.3** shows the size distribution histograms obtained for **Re18** and **Re19**.

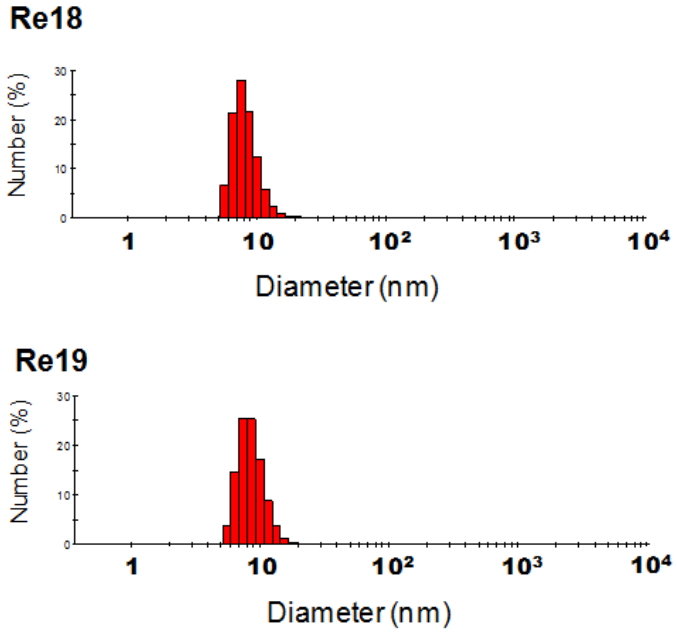


**Figure 5.3**: Hydrodynamic diameter of **Re18** (8.4 ± 0.5 nm) and **Re19** (8.7 ± 0.3 nm), determined by DLS (detection angle of 173º).

The final composition of the dextran derivatives, their physical parameters and the calculated molecular weight for each polymer are summarized in **Table 5.1**.

**Table 5.1**: Group density, hydrodynamic diameter, zeta potential and calculated molecular weight of dextran, **L18**, **L19**, **Re18** and **Re19**.

| Compound | Group density (units/mol dextran) | | | Diameter* (nm) | Zeta potential* (mV) | M. W. calculated (g/ mol) |
|---|---|---|---|---|---|---|
| | amine | **Pz** | Mannose | | | |
| **Dextran** | - | - | - | 4.3 ± 0.4 | -9.9 ± 0.5 | 10000 |
| **L18** | 13 | 4 | 13 | 7.0 ± 0.3 | 6.6 ± 0.3 | 19231 |
| **L19** | 9 | 8 | 13 | 7.0 ± 0.7 | 7.3 ± 0.6 | 20231 |
| **Re18** | 13 | 4 | 13 | 8.4 ± 0.5 | 7.1 ± 0.7 | 19850 |
| **Re19** | 9 | 8 | 13 | 8.7 ± 0.3 | 7.1 ± 0.1 | 21479 |

* mean ± S.D.

The hydrodynamic diameter of the polymeric compounds increased with the dextran backbone functionalization. However, the number of pyrazolyl-diamine chelating units (4 *versus* 8) did not affect significantly their size, as shown by the results obtained for **L18** and **L19** (**Table 5.1**). A slight increase of the particles size was also found (**Re18**: 8.4 ± 0.5 nm; **Re19**: 8.7 ± 0.3 nm) upon metallation of **L18** and **L19**.

Analysis by AFM, after dispersion on mica substrates, gave molecular diameters of c.a. 4 nm (A), 12 nm (B), and 8-16 nm (C) for dextran, **Re18** and **Re19**, respectively (**Figure 5.4**).

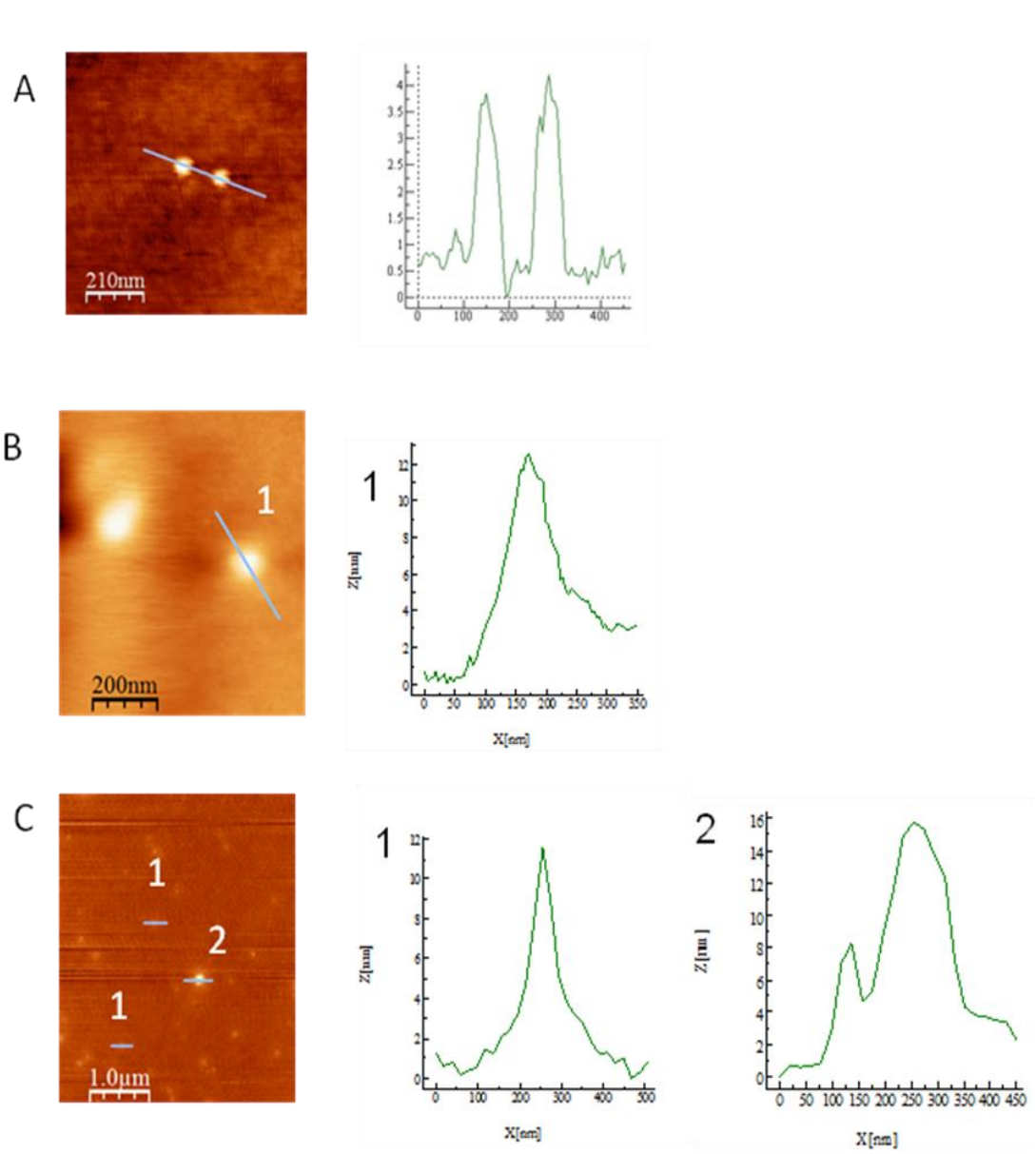


**Figure 5.4**: Height-scaled AFM images and corresponding line profiles of **dextran** (A), **Re18** (B) and **Re19** (C).

AFM and DLS molecular measurements are similar for dextran, while the small difference found for **Re18** might be ascribed to a possible interaction between the polymer and the solid support during sample deposition. In the case of **Re19**, the dispersion found in AFM measurements may indicate some aggregation during sample preparation or deposition.

Zeta potential measurements indicated an overall negative charge for dextran (-9.9 ± 0.5 mV), which changed drastically upon functionalization (**L18**: + 6.6 ± 0.3 mV, **L19**: + 7.3 ± 0.6 mV). However, the overall charge of the polymeric compounds was not significantly affect by metallation (**Re18**: + 7.1 ± 0.7 mV, **Re19**: + 7.1 ± 0.1 mV).

### 5.3.2. Synthesis and Characterization of $^{99m}Tc(CO)_3$-Mannosylated Dextran

The radioactive nanocompounds **Tc18** and **Tc19** were prepared by reaction of the precursor *fac*-$[^{99m}Tc(CO)_3(H_2O)_3]^+$ with the respective mannosylated dextran derivatives **L18** and **L19** during 10 min at 100 ºC (**Scheme 5.2**).

Aiming to maximize the specific activity of the radioactive compounds, the amount of **L18** and **L19** was optimized t 50-100 µg (final concentration: 2.3 – 4.5 x $10^{-6}$ M) without compromising the labeling yield.

The radiochemical purity of **Tc18** and **Tc19** was monitored by SEC-, RP-HPLC (method M, experimental section **7.2**) and ITLC (experimental section, **7.2**). SEC-HPLC analysis of **Tc18** and **Tc19** showed formation of a major product (> 98%) and the absence of aggregation or smaller particles.

To monitor colloidal impurities or polymeric aggregates above the SEC-HPLC cut-off, a solution of **Tc18** or **Tc19** was applied on a sephadex G-25 gel filtration column previously equilibrated with saline solution. After elution with saline solution, these columns were scanned to check the presence of aggregates. The radiochromatograms of the scanned columns show that no radioactivity was detected at the application point, indicating the absence of aggregates ($R_f$ = 0) in both radioactive preparations. The chromatograms show only one peak in the front of the solvent, which were identified as **Tc18** or **Tc19**. As an example, **Figure 5.5** presents the radiochromatogram of a scanned column after elution of **Tc19** with 5 mL of saline solution.

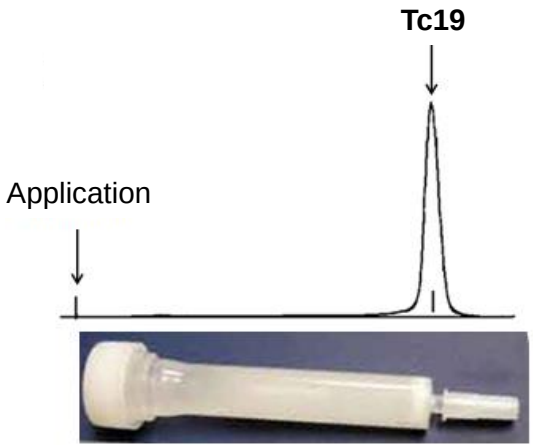


**Figure 5.5**: Scan of sephadex G-25 gel filtration column, after elution of **Tc19** with saline solution.

The RP-HPLC chromatograms of **Tc18** ($t_R$ =12.2 min) and **Tc19** ($t_R$ =12.2 min) have shown only one species as no other radiochemical impurity could be detected.

The high radiochemical purity (> 95 %) of **Tc18** and **Tc19** was also confirmed by ITLC, as no $[TcO_4]^-$ or *fac*-$[^{99m}Tc(CO)_3(H_2O)_3]^+$ were detected ($R_f$ = 1). For the sake of example, **Figure 5.6** presents the RP-HPLC and ITLC chromatograms obtained for **Tc18**.

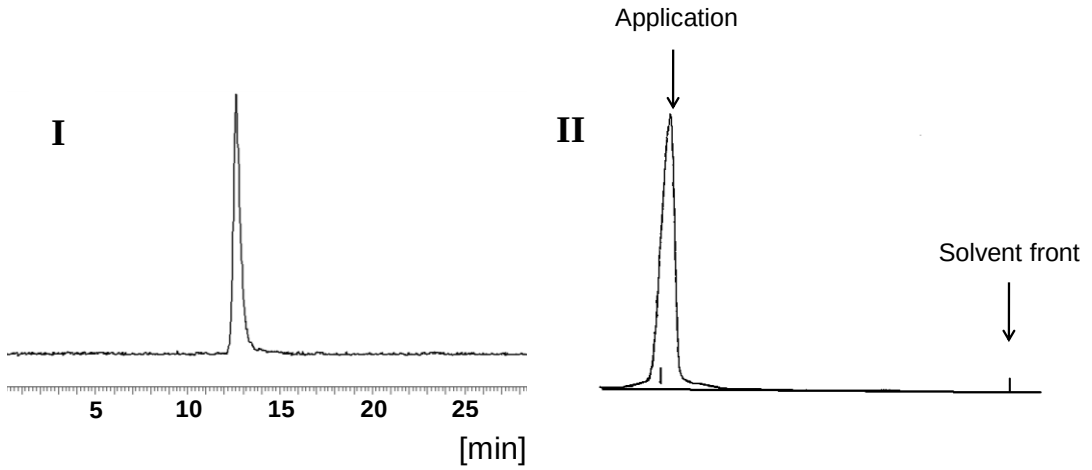


**Figure 5.6**: Radiochromatograms of **Tc18**: **I** – RP-HPLC ($t_R$ = 12.2 min); **II** – ITLC (**Tc18**, $R_f$ = 0).

Structural characterization of the radioactive compounds was done by comparing the chromatographic profile (γ-detection) of **Tc18** and **Tc19** with that of the corresponding surrogates **Re18** and **Re19** (U.V. detection). As an example, **Figure 5.7** displays the RP-HPLC chromatograms obtained for **Tc18** and **Re18**.

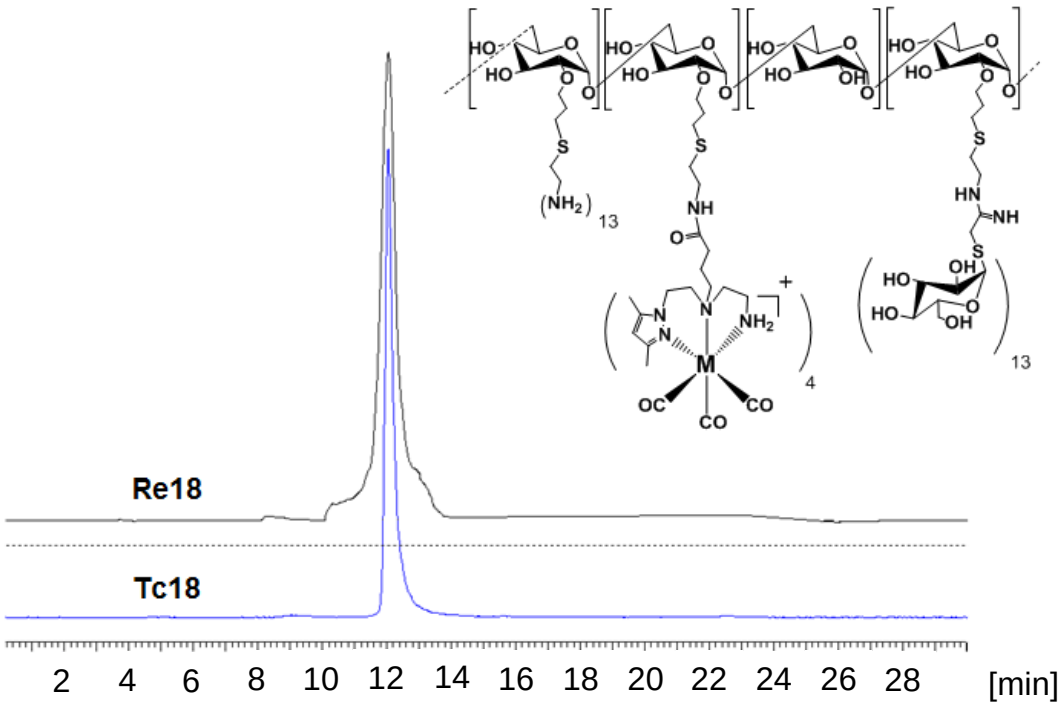


**Figure 5.7**: RP-HPLC chromatograms of **Tc18** (γ detection) and **Re18** (U.V. detection).

To evaluate the stability of **Tc18** and **Tc19** towards transchelation, both compounds were incubated with a large excess of cysteine and histidine (1:100). Aliquots of these solutions were analyzed at different time points (1 h, 3 h and 6 h) by RP-HPLC (method M) and the results demonstrated that **Tc18** and **Tc19** are highly stable under the tested conditions.

### 5.4. Biodistribution Studies

The biological properties of **Tc18** and **Tc19** were evaluated in a Wistar rat model. **Tc18** and **Tc19** were injected subcutaneously (20 µg of the polymer in 50 µL, ≈ 3.7 MBq) in the footpad region, after anesthesia of the animal with a mixture of xylazine (70 mg/kg) and ketamine (7 mg/kg). The area of injection was massaged gently

with a strip of gauze pad for 2 min to facilitate movement of the radiotracer from the injection site.

**Table 5.2** summarizes the distribution of **Tc18** and **Tc19** in each organ as a percentage of the injected activity (% IA/organ) at different time points.

**Table 5.2**: Biodistribution data for **Tc18** and **Tc19** in Wistar rat model at different time points (n = 3-5).

| | **% IA/organ ± S.D.** | | | | | | | |
|---|---|---|---|---|---|---|---|---|
| | **Tc18** | | | | **Tc19** | | | |
| **Tissue/organ** | **15 min** | **30 min** | **1 h** | **3 h** | **15 min** | **30 min** | **1 h** | **3 h** |
| **Liver** | **2.57 ± 1.17** | **4.06 ± 0.32** | **4.80 ± 1.03** | **6.49 ± 0.09** | **2.42 ± 0.47** | **3.74 ± 0.17** | **5.44 ± 1.06** | **6.84 ± 0.01** |
| Intestine | 0.45 ± 0.10 | 0.59 ± 0.04 | 0.75 ± 0.06 | 0.95 ± 0.17 | 0.55 ± 0.07 | 1.21 ± 0.11 | 0.61 ± 0.57 | 1.28 ± 0.17 |
| Stomach | 0.12 ± 0.03 | 0.18 ± 0.01 | 0.30 ± 0.05 | 0.52 ± 0.17 | 0.15 ± 0.03 | 0.27 ± 0.01 | 0.42 ± 0.01 | 0.74 ± 0.07 |
| **Kidney** | **0.56 ± 0.19** | **0.82 ± 0.02** | **1.12 ± 0.27** | **1.20 ± 0.01** | **0.53 ± 0.02** | **0.94 ± 0.01** | **1.18 ± 0.20** | **1.67 ± 0.28** |
| Heart | 0.06 ± 0.02 | 0.07 ± 0.00 | 0.06 ± 0.01 | 0.06 ± 0.02 | 0.04 ± 0.01 | 0.08 ± 0.02 | 0.09 ± 0.00 | 0.09 ± 0.03 |
| Lung | 0.48 ± 0.27 | 0.65 ± 0.01 | 0.83 ± 0.16 | 0.65 ± 0.04 | 0.32 ± 0.01 | 0.35 ± 0.05 | 0.43 ± 0.03 | 0.60 ± 0.07 |
| Spleen | 0.12 ± 0.07 | 0.18 ± 0.08 | 0.32 ± 0.10 | 0.31 ± 0.04 | 0.12 ± 0.03 | 0.20 ± 0.10 | 0.25 ± 0.11 | 0.45 ± 0.04 |
| Blood (whole) | 0.97 ± 0.34 | 1.47 ± 0.08 | 0.91 ± 0.02 | 0.96 ± 0.37 | 2.14 ± 0.01 | 2.86 ± 1.72 | 1.72 ± 0.81 | 1.55 ± 0.65 |
| **1st Node (Popliteal)** | **3.96 ± 0.87** | **7.43 ± 1.59** | **6.71 ± 2.35** | **5.98 ± 1.68** | **4.43 ± 0.27** | **4.31 ± 0.27** | **7.53 ± 0.69** | **5.21 ± 0.78** |
| **2nd Node (Inguinal)** | **0.83 ± 0.05** | **3.15 ± 0.83** | **2.59 ± 1.06** | **1.41 ± 0.50** | **1.09 ± 0.40** | **1.41 ± 0.28** | **0.41 ± 0.15** | **0.59 ± 0.14** |
| Injection site | 89.06 ± 0.28 | 80.93 ± 2.87 | 83.85 ± 1.37 | 79.50 ± 5.02 | 89.14 ± 2.09 | 87.24 ± 3.06 | 81.58 ± 0.35 | 81.13 ± 0.01 |
| **PE %** | **78.60 ± 3.39** | **57.85 ± 2.19** | **61.81 ± 2.42** | **76.65 ± 1.73** | **68.55±1.35** | **76.27±5.07** | **94.47±2.45** | **87.81±3.75** |

Both radiolabeled nanocompouds show appreciable accumulation in the popliteal node (which serves as the sentinel lymph node in this protocol), occurring the highest radioactivity uptake between 30-60 min p.i. with a major portion of this retained up to 180 min p.i.

The popliteal extraction (PE) is a parameter that predicts the suitability of a preparation to be used for SLND. The PE is determined according to the following equation:[116c]

$$\text{PE (\%)} = \frac{\text{\% IA (popliteal) - \% IA (inguinal)}}{\text{\% IA (popliteal)}} \times 100 \qquad (\mathbf{1})$$

The PE values determined for both compounds highlights the potential of **Tc19** (% PE: 94.47 ± 2.45 %) for SLND, as it presents higher extraction of the first node than **Tc18** (% PE: 61.81 ± 2.42 %) at 1 h p.i.

The SPECT/CT image obtained for **Tc19** (**Figure 5.8**) has shown a clear delineation of the popliteal (sentinel) lymph node with minimal spread to secondary lymph node. However, a significant amount of radioactivity remains at the injection site at 1 h p.i.

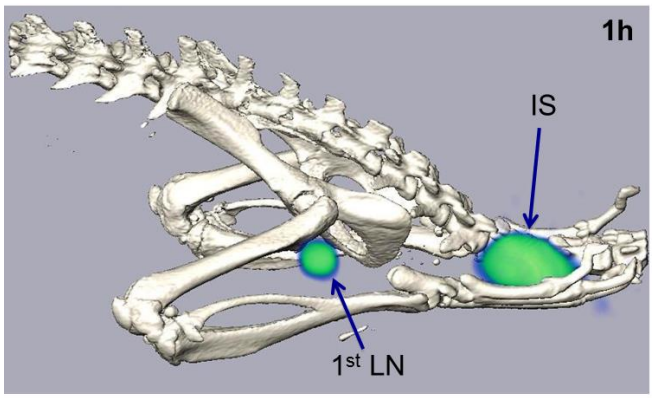


**Figure 5.8**: SPECT/CT image obtained for **Tc19** in a Wistar rat, at 1 h p.i.; IS, injection site; 1st LN, popliteal lymph node. Image performed Prof. Yasushi Arano (Chiba University, Department of Molecular Imaging and Radiotherapy, Japan) under the "Co-ordinated Research Project on the Development of $^{99m}$Tc Radiopharmaceuticals for Cancer Diagnosis and Sentinel Node Detection" sponsored by the IAEA.

Taken together, the biological data renders **Tc19** as a very favorable radiotracer for SLN imaging.

The *in vivo* specificity of the radiolabeled polymers was evaluated by comparing the biological profile of the non-mannosylated (**Tc17**) and mannosylated compounds (**Tc19**) in the same animal model. **Tc17** was obtained by the same labeling procedure described for **Tc18** and **Tc19**, using the Boc-deprotected precursor described in **Scheme 5.1**. Biodistribution of both compounds was evaluated at 3 h p.i (**Table 5.3**).

**Table 5.3**: Biodistribution data for **Tc17** and **Tc19** in a Wistar rat model (3 h p.i.).

| **Organ** | **% IA/organ ± S.D.** | |
|---|---|---|
| | **Tc17** | **Tc19** |
| **Liver** | **0.48 ± 0.41** | **6.84 ± 0.01** |
| Intestine | 0.57 ± 0.68 | 1.28 ± 0.17 |
| Stomach | 0.04 ± 0.05 | 0.74 ± 0.07 |
| **Kidney** | **0.14 ± 0.08** | **1.67 ± 0.28** |
| Heart | 0.01 ± 0.01 | 0.09 ± 0.03 |
| Lungs | 0.02 ± 0.02 | 0.60 ± 0.07 |
| Spleen | 0.02 ± 0.01 | 0.45 ± 0.04 |
| Blood(whole) | 0.16 ± 0.16 | 1.55 ± 0.65 |
| **1$^{st}$ Node (Popliteal)** | **0.34 ± 0.35** | **5.21 ± 0.78** |
| **2$^{nd}$ Node (Inguinal)** | **0.13 ± 0.50** | **0.59 ± 0.14** |
| Injection site | 80.42 ± 0.60 | 81.13 ± 0.01 |
| **PE %** | 61.76 ± 0.40 | 87.81 ± 3.75 |

Analysis of the biodistribution results shows that **Tc17** presents almost no uptake in the popliteal node and a lower PE value as compared to **Tc19**, highlighting the importance of mannose and MR for accurate detection of SLND.

## 5.5. Bimodal Probe for SPECT/CT and NIR Optical Imaging

### 5.5.1. Synthesis and Characterization of Mannosylated Dextran Bearing a Pyrazolyl-Diamine Chelator and a NIR Fluorophore

Among the compounds currently explored for NIR optical imaging,[5c, 156] we have selected a small organic fluorophore from the cyanine family (IR775-Cl) to be attached to the lead compound **L19-Boc**. The dextran based compound bearing pyrazolyl-diamine chelator, mannose and fluorophore units (**L20**) was synthesized from **L19-Boc**, following the synthetic procedure depicted in **Scheme 5.3**.

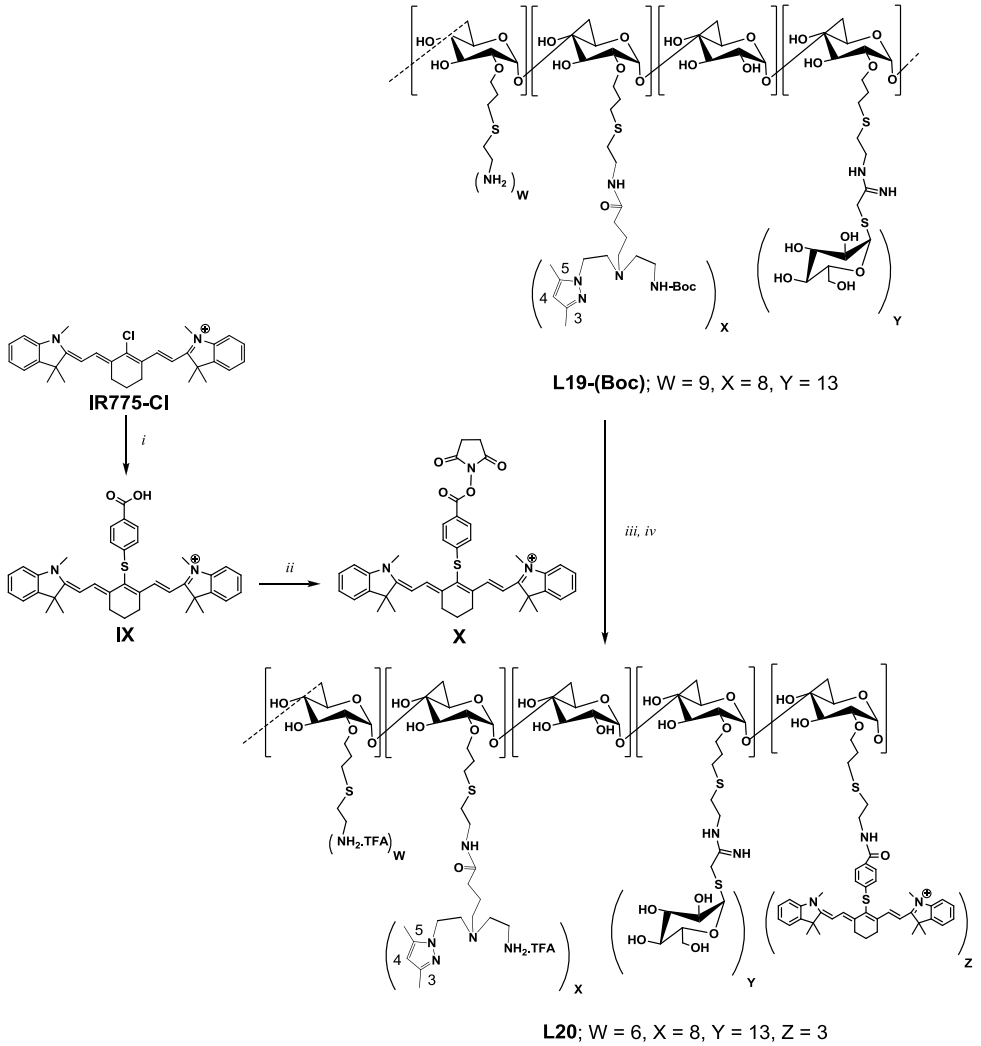


**Scheme 5.3**: Synthesis of **L20**. *i*) 4-mercaptobenzoic acid, DMF; *ii*) EDC, NHS, DCM; *iii*) DMSO/ borate buffer, 0.1 M, pH 9 (1:1), *iv*) TFA.

Firstly, we performed the alkylation of the 4-mercaptobenzoic acid with chloro-substituted heptamethine cyanine IR775-Cl to obtain the precursor **IX** in almost quantitative yield. This compound was activated with EDC/NHS to give compound **X,** which was added to the free amines of **L19-Boc** in a 5:1 molar ratio to maximize the number of fluorophores per mol/dextran. After dialysis, the resulting conjugate was purified by sephadex G-25 gel filtration. The purified product reacted with TFA to remove the Boc-protecting group, providing **L20** in moderate overall yield (35%).

Conjugation of the fluorophore to the dextran backbone was confirmed by SEC- and RP-HPLC (Method L and Method M, respectively; experimental section **7.2**). In both cases, only one peak was observed in the chromatograms of **L20** with a retention time of 11.2 min for SEC-HPLC and 15.6 min for RP-HPLC at 760 nm. The chromatograms also indicated that there was no free fluorophore (**IX**, SEC-HPLC: $t_R$ = 29.1 min; RP-HPLC: $t_R$ = 19.2 min). **L20** was also analyzed by SEC-HPLC and RP-HPLC at 220 nm to check the presence of any impurity or precursor (**L19**: SEC-HPLC, $t_R$ = 14.6 min; RP-HPLC, $t_R$ = 12.2 min). As can be seen in **Figure 5.9**, the chromatograms obtained for **L20** show the presence of only one peak.

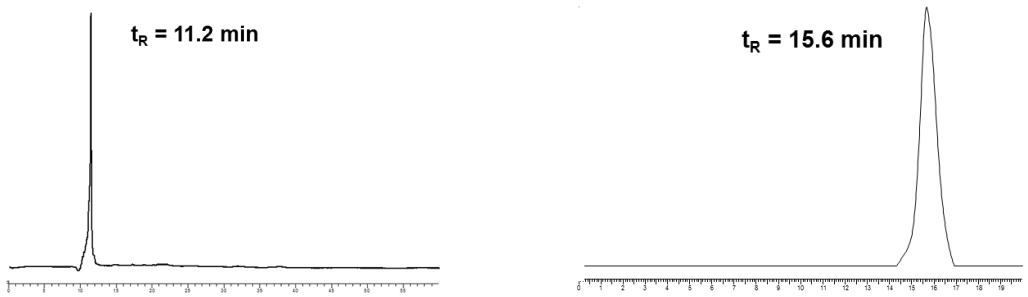


**Figure 5.9**: SEC- (left) and RP-HPLC (right) chromatograms of **L20**, using Methods L and M, respectively.

Compound **L20** was characterized by NMR spectroscopy and spectrophotometry (see experimental section **7.3.55**).For the sake of example, the $^1$H-NMR spectrum ($D_2O$) obtained for **L20** is depicted in **Figure 5.10**.

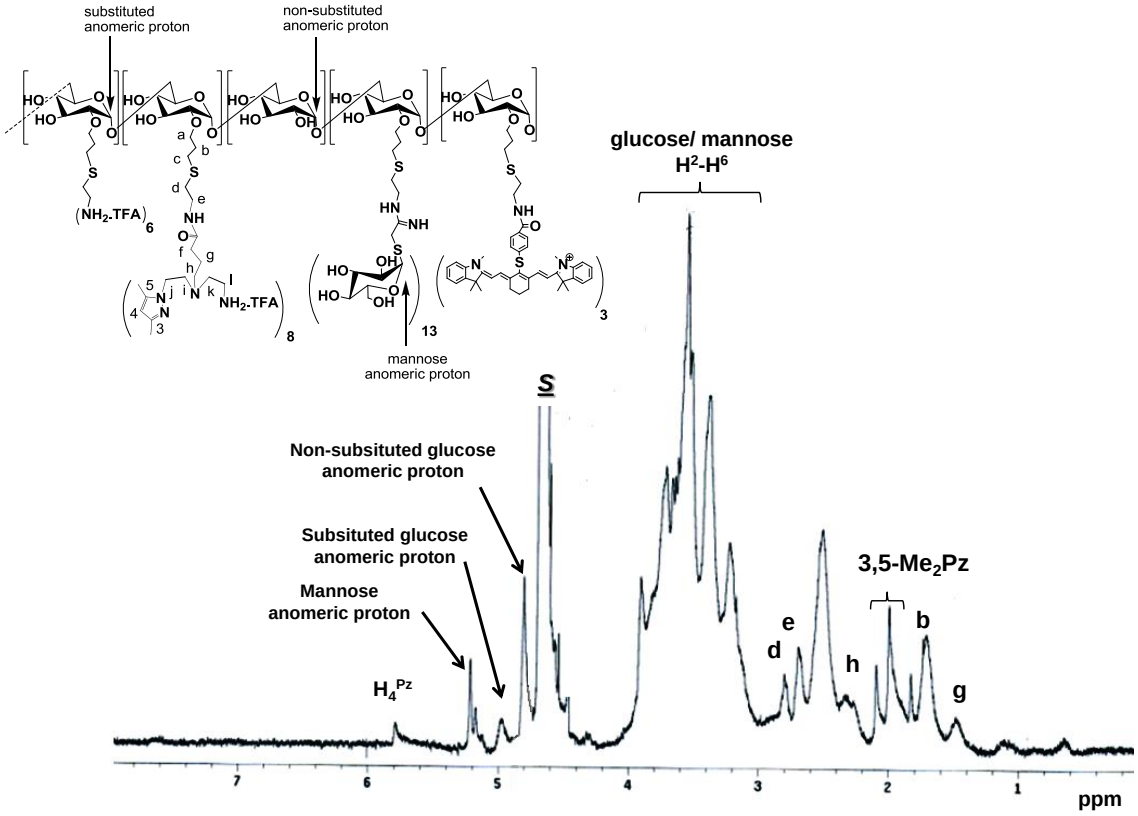


**Figure 5.10**: $^{1}$H-NMR spectrum of **L20** in $D_2O$ (identification system for NMR assignments is displayed).

The spectrum presented several characteristic peaks of the dextran backbone, which could be clearly assigned, namely the anomeric protons of the substituted and non-substituted glucose units (δ 5.06 and δ 4.80, respectively), the mannose anomeric proton (δ 5.30) and some peaks of the bifunctional chelator ($H^h$: δ 2.34; 3,5-$Me_2$Pz: δ 2.10, δ 2.00; $H^g$: δ 1.48).

Typically, the number of units conjugated to dextran backbone was determined based on to the intensity ratio of the peaks corresponding to each unit (e.g. bifunctional chelator and/or mannose) and the protons adjacent to free amines ($H^e$: δ 2.70). However, no evident peaks corresponding to the protons of the NIR fluorophore could be assigned in the spectrum of **L20**. Taking into account other results reported in the literature,[157] the absence of the fluorophore signals in the $^{1}$H-NMR spectrum could be ascribed to some aggregation in water. Such aggregation was corroborated by spectrophotometric characterization of **L20**. Indeed, the absorption spectrum of **L20** dissolved in water (**Figure 5.11**, dashed line) showed a relatively strong band at 723 nm that has been

described as an aggregate form of the fluorophore, while the monomeric species presented a maximum at 797 nm.[158]

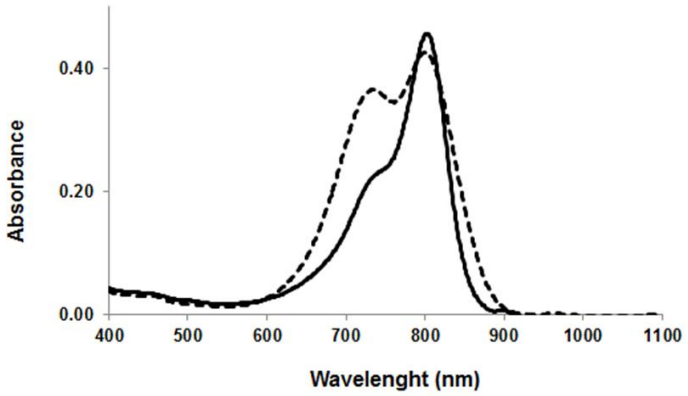


**Figure 5.11**: Absorption spectra of 1 nM solutions of **L20** in water (dashed line) showing the aggregate form at 723 nm and the monomeric form at 797 nm. Only the monomeric form is found at 802 nm in 20% DMSO aqueous solution (solid line).

As can be seen in **Figure 5.11** (solid line) when **L20** was dissolved in 20% DMSO aqueous solution, the most intense band in the absorption spectrum appears at 802 nm and corresponded to monomeric form of the fluorophore. The short wavelength shoulder visible in this absorption spectrum of **L20** is a common feature of virtually all cyanine based fluorophores and is observed in less polar solvents such as DMSO and MeOH where there is no tendency for aggregation.[158] This behavior has been studied intensively for protein and antibody conjugates with lipophilic fluorescent labels, mainly fluorophores of the cyanine type.[159]

Based on these results, one can hypothesized that the absence of fluorophore signals on the $^{1}$H-NMR spectrum of **L20** in deuterated water might be due to the limited tumbling motion of the aggregate form, which hampers the signal resolution of the protons.

In the $^{1}$H-NMR spectrum of **L20** in $D_2O$/DMSO (1:0.2 v/v) we could observe some peaks (δ 8.21 – 7.06) that were certainly due to the aromatic protons of the fluorophore. However, some key peaks in the range of δ 3.00 - 2.10, namely the ones due to the protons adjacent to free amines ($H^e$: δ 2.70) and to the methyl groups of the bifunctional chelator (δ 2.20-2.10), could not be assigned, preventing the use of NMR data to estimate the number of fluorophores per mol of dextran in **L20**.

As an alternative method to NMR spectroscopy, we have used spectrophotometry to estimate the number of NIR fluorophore units per mol of dextran, following equation **2**:

$$\text{Fluorophore number/mol dextran} = \frac{[\text{Fluorophore}]}{[\text{Glucose}]} \times N \qquad (\mathbf{2});$$

where: [Fluorophore] = fluorophore concentration;
[Glucose] = glucose concentration;
N = 62; average number of glucose units in 10 kDa dextran.

The fluorophore concentration in **L20** was determined by spectrophotometry from interpolation of a standardized curve, using known quantities of the precursor **IX** (see experimental section **7.3.52**). The molar extinction coefficient of **IX** in a 20% DMSO aqueous solution was 125052 L $mol^{-1}$ $cm^{-1}$ at 795 nm. At this wavelenght, 20 µg of **L20** dissolved in a 20% DMSO aqueous solution contain 1.3 ± 0.02 µM of fluorophore (see experimental section **7.3.55**).

The glucose concentration of **L20** was determined by a colorimetric assay. Using known amounts of glucose as standard (see experimental section **7.3.55**),[160] we obtained a standard curve and the concentration of glucose in 20 µg of **L20** was determined from interpolation. Based on three determinations, **L20** contain 21.0 ± 0.03 µM of glucose. Thus, the estimated molar ratio of fluorophores per molecule of dextran in **L20** was found to be 3 ± 1 units.

The physical properties of **L20** were also determined in 0.01 M PBS, pH 7.4, to mimic the labeling conditions. Zeta potential measurements showed that the superficial charge of **L20** is negative (-2.3 ± 0.4 mV) and DLS measurements showed that the hydrodynamic diameter was 17.7 ± 2.0 nm (**Figure 5.12**). The latter result indicates an increase of the particle size upon functionalization of dextran derivative **L19** with the fluorophore.

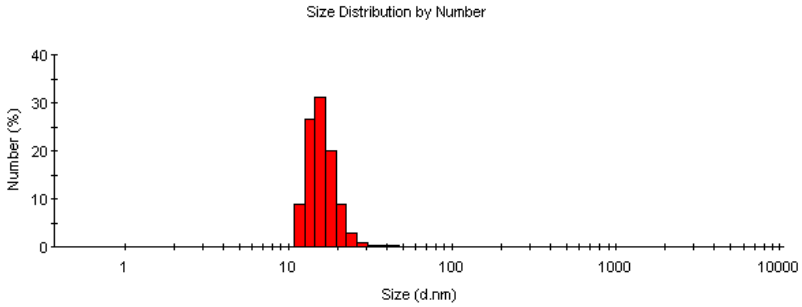


**Figure 5.12**: Hydrodynamic diameter of **L20** in 0.01 M PBS, pH 7.4.

### 5.5.2. *In Vivo* Fluorescence Properties

In close collaboration with Prof. Vicky Caveliers and Prof. Tony Lahoutte from the Free University of Brussels (VUB), the *in vivo* fluorescence properties of **L20** were evaluated in a Wistar rat model, after subcutaneous injection (1 nmol) in the left rear footpad. Optical imaging of the left rear leg were acquired at different time points (5 min, 10 min, 15 min, 30 min, 45 min, 60 min and 20 h). As depicted in **Figure 5.13**, the amount administered to the animals provide sufficient signal to visualize the first lymph node based on the fluorescence component of **L20**, 5 min p.i. No other lymph nodes were detected by NIR optical imaging, even at 20 hours p.i.

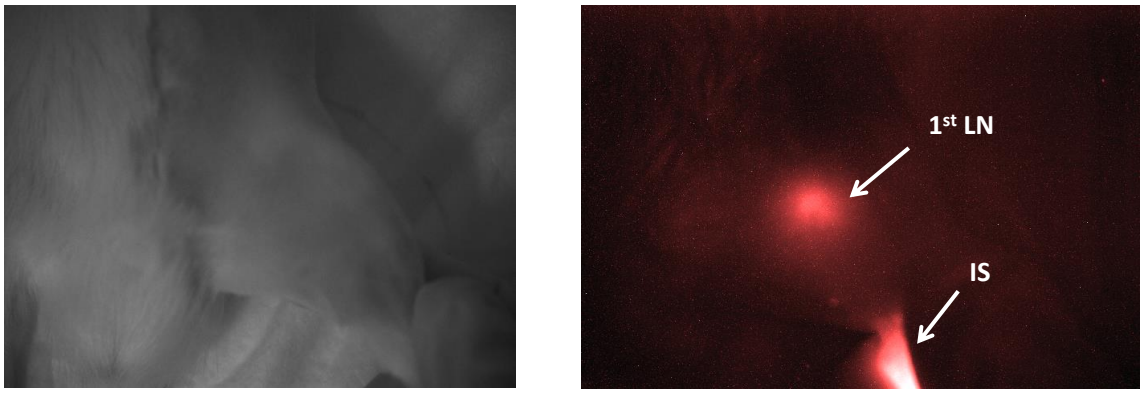


**Figure 5.13**: Bright field image (left) and NIR image (right) of Wistar rat injected with **L20** (exposure time 350 ms), at 1h p.i.; IS, injection site; 1st LN, popliteal (sentinel) lymph node.

## 5.6. $M(CO)_3$-Mannosylated Dextran (M = Re, $^{99m}$Tc) Bearing NIR Fluorophore

### 5.6.1. Synthesis and Characterization of $Re(CO)_3$-Mannosylated Dextran Bearing NIR Fluorophore

The metallated polymer bearing a NIR fluorophore (**Re20**) was prepared by reacting **Re19** with the activated succinimide ester **X** (**Scheme 5.4**).

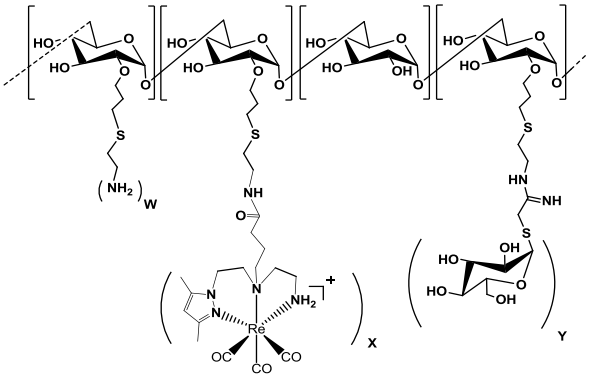

**Re19**; W = 9, X = 8, Y = 13

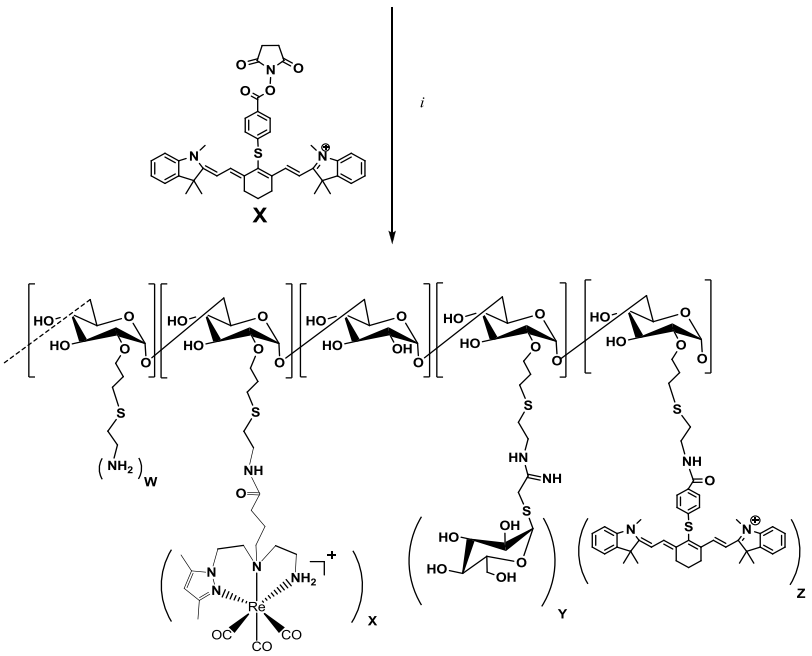

**Re20**; W = 6, X = 8, Y = 13, Z = 3

**Scheme 5.4**: Synthesis of **Re20**; *i*) DMSO/ borate buffer, 0.1 M, pH 9 (1:1), 8 h, r.t.

After purification by shepadex G-25 filtration, **Re20** was characterized by SEC- and RP-HPLC. In both cases, one peak was observed in the chromatograms of **Re20** with a retention time of 11.3 min for SEC-HPLC and 15.2 min for RP-HPLC at 760 nm. The chromatograms also shown the absence of free fluorophore (**IX**, SEC-HPLC: $t_R$ = 29.1 min; RP-HPLC: $t_R$ = 19.2 min). Morevoer, **Re20** was also analyzed by SEC-HPLC and RP-HPLC at 220 nm to check the presence of any impurity or precursor (**Re19**: SEC-HPLC, $t_R$ = 14.6 min; RP-HPLC, $t_R$ = 12.2 min). As can be seen in **Figure 5.14**, the SEC- and RP-HPLC chromatograms obtained for **Re20** shows the presence of only one peak.

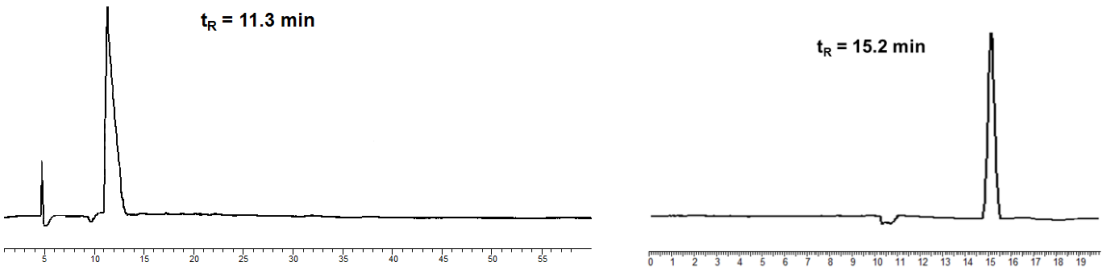


**Figure 5.14**: SEC-(left) and RP-HPLC (right) chromatogram of **Re20** at 220 nm, using method L and M (see experimental section **7.2**), respectively.

Following the methodology described for **L20**, the number of fluorophore units per molecule of dextran in **Re20** was found to be 3 ± 1 unit (see experimental section **7.3.56**).

Compound **Re20** was also characterized by DLS and LDV. The hydrodynamic diameter of **Re20** was 22.5 ± 2.9 nm, while the superficial charge was negative, - 7.7 ± 2.5 mV.

### 5.6.2. Synthesis and characterization of $^{99m}Tc(CO)_3$-Mannosylated Dextran Bearing NIR Fluorophore

The bimodal tracer **Tc20** was obtained in almost quantitative yield (> 98%) upon reaction of *fac*-$[^{99m}Tc(CO)_3(H_2O)_3]^+$ with the conjugate **L20** (final concentration: 4 x $10^{-6}$ M) (**Scheme 5.5**).

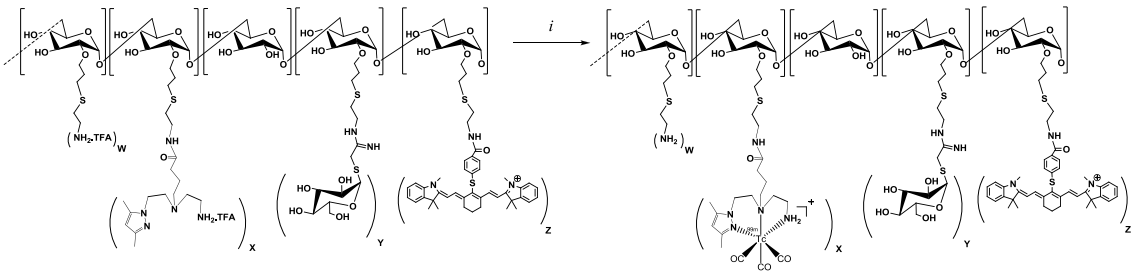


**L20**; W = 6, X = 8, Y = 13, Z = 3

**Tc20**; W = 6, X = 8, Y = 13, Z = 3

**Scheme 5.5**: Synthesis of **Tc20**. *i*) *fac*-[$^{99m}$Tc(CO)$_3$(H$_2$O)$_3$]$^+$, 90 ºC, 10 min, pH = 7

The purity/stability of the radiocompound was evaluated by RP-HPLC ($t_R$ = 15.6 min, method M) and ITLC ($R_f$ = 1) chromatography. In both cases, the chromatograms have shown only one species, confirming that no precursors and/or oxidation species were present.

The identification/characterization of **Tc20** was accomplished by RP-HPLC, comparing the γ-trace with the U.V. trace of the rhenium analog **Re20** (**Figure 5.16**).

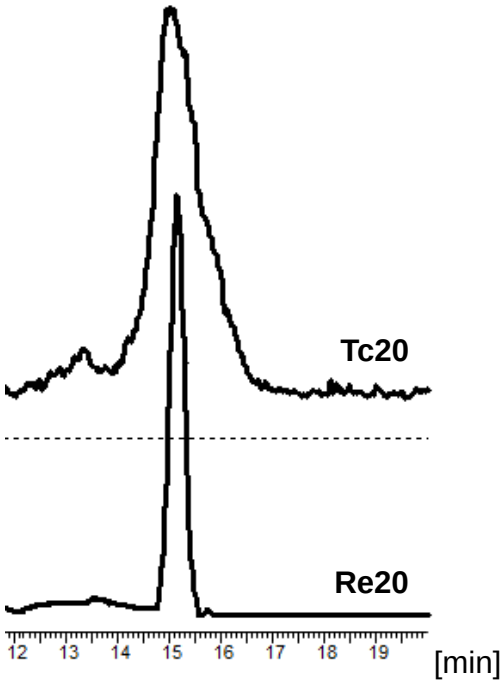


**Figure 5.15**: RP-HPLC (Method M) chromatographic profiles of **Tc20** (γ - detection) and respective cold surrogate **Re20** (U.V. detection, 220 nm).

Before biodistribution studies, we have decided to evaluate the impact of the labeling conditions on the fluorescence properties of **Tc20**. Thus, equimolar solutions (2 x $10^{-11}$ mol) of **L20** and **Tc20** that were prepared and applied (20 µL) on a ITLC. The emitted fluorescence signal of triplicate samples was measured in a Odyssey IR imaging system using 700- and 800-nm channels. **Figure 5.15** shows the fluorescent intensity of both compounds.

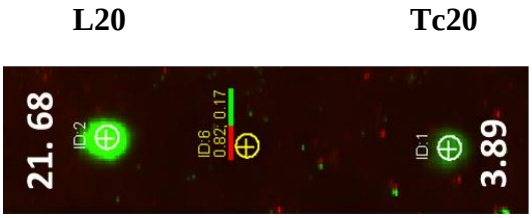


**Figure 5.16**: Fluorescence intensity of **L20** (left) and **Tc20** (right); background (center) in a Odyssey IR imaging system with 700- and 800-nm channels.

The results showed that the NIR fluorescence properties of **Tc20** decreased (≈ 87 %) as compared to **L20**, suggesting that the high temperature (100 ºC) used to prepare **Tc20** could lead to degradation of the fluorophore.

### 5.7. Biodistribution Studies

Following the procedure described for **Tc18** and **Tc19**, *in vivo* evaluation of **Tc20** was also carried out in Wistar rat model. The animals were injected subcutaneously with **Tc20** (≈ 1 nmol) and images were acquired at different time points. **Figure 5.17** shows a SPECT/CT image of one animal acquired at 1 h p.i.

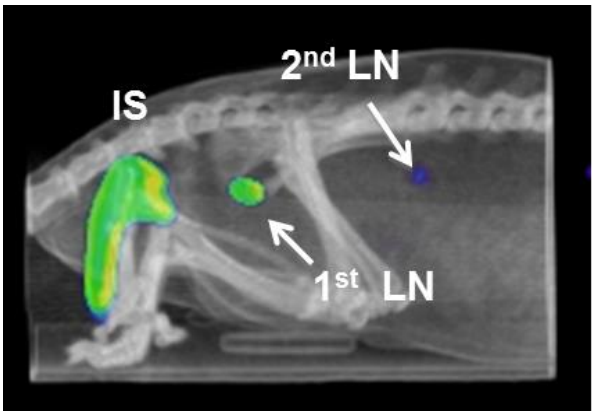


**Figure 5.17**: SPECT/CT image of a Wistar rat injected subcutaneously with **Tc20** at 1 h p.i.; IS, injection site; 1st LN, popliteal (sentinel) lymph node; 2nd LN, inguinal (secondary) lymph node.

The SPECT/CT image showed a clear delineation of the sentinel node with an high degree of specific retention and minimal spread of **Tc20** to other regions. The image compared well with the SPECT/CT image obtained for **Tc19** (**Figure 5.8**) at the same time point.

Traditional *ex-vivo* biodistribution was performed at 3 h p.i. and the tissue distribution of **Tc20** was determined (**Table 5.4**).

**Table 5.4**: Biodistribution data for **Tc20** in Wistar Rat model at 3h p.i. (n = 3).

| **Organ** | **% IA/organ ± S.D.** |
|---|---|
| | **3h** |
| **Liver** | **1.81 ± 0.46** |
| Intestine | 0.34 ± 0.17 |
| Stomach | 0.01 ± 0.01 |
| **Kidney** | **0.46 ± 0.1** |
| Heart | 0.02 ± 0.01 |
| Lungs | 0.03 ± 0.02 |
| Spleen | 0.02 ± 0.01 |
| Blood(whole) | 0.23 ± 0.2 |
| **1st Node (Popliteal)** | **3.87 ± 0.63** |
| **2nd Node (Inguinal)** | **0.40 ± 0.20** |
| Injection site | 86.73 ± 0.92 |
| **PE (%)** | **89.66 ± 0.03** |

The biodistribution results showed an appreciable accumulation of **Tc20** in the popliteal (sentinel) node while much less activity was found in the inguinal lymph node or other organs, at 3h p.i. These data compared well with the biodistribution of **Tc19**

(**Table 5.2**), indicating that the conjugation of fluorophore to **Tc19** did not affect the pharmacoknetic profile of the polymer. Indeed, the bimodal probe **Tc20** presented a high PE value (89.66 ± 0.03 %), comparable to **Tc19** (87.81 ± 3.75 %). Moreover, **Tc19** and **Tc20** presented also other common features, namely similar accumulation in the injection site (**Tc20**: 86.7 ± 0.92 % IA/organ; **Tc19**: 81.13 ± 0.01 % IA/organ) and minimal spread to non-target organs.

The NIR fluorescence signal of the bimodal probe **Tc20** enabled also the localization of the popliteal lymph node by optical imaging with a FLuoBeam800 imaging system (FluOptics). **Figure 5.18** shows the NIR optical image of a left rear footpad of a Wistar rat injected subcutaneously with **Tc20** at 3 h p.i.

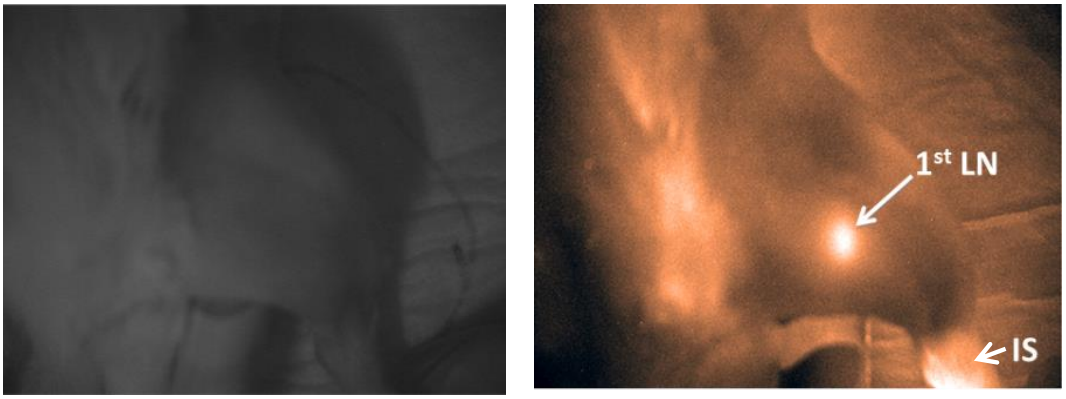


**Figure 5.18**: Bright field (left) and NIR optical imaging (right) image of Wistar rat leg injected with 1 nmol of **Tc20** (exposure time 750 ms), at 3 h p.i. The white arrow indicates the localization of the dual tracer in the popliteal lymph node. IS, injection site.

These results indicated that gamma radiation and NIR fluorescence signal emitted by the bimodal probe **Tc20** (4 µM) allowed SPECT and NIR optical imaging of the lymph node.

After 3 h p.i., the animals were sacrified and the NIR fluorescence signal of **Tc20** enabled a rapid and simple image-guided surgical excision of the lymph nodes by real-time optical imaging. **Figure 5.19** shows *ex-vivo* NIR optical images of the 1$^{st}$ and 2$^{nd}$ LN.

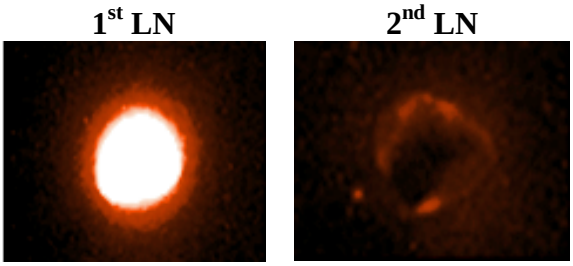


**Figure 5.19**: **A**) *Ex-vivo* NIR imaging of **Tc20** in the popliteal (1st LN) and inguinal lymph node (2nd LN).

The images revealed that little flow-through of **Tc20** to the second lymph nodes was observed in the NIR field. In fact, SPECT and NIR signals were confined to the popliteal node and injection site.

The excised lymph nodes were treated with optimal cutting temperature (OCT) compound and frozen sections (5 µm) were used for histological examination. Analysis of these sections for the popliteal node on a EVOS FI (digital fluorescence microscope) has shown no fluorescence when 1 nmol of **Tc20** was injected in Wistar rats. A fluorescence signal was detected when 10 nmol of the compound was used. As an example **Figure 5.20** shows the homogenous distribution of **Tc20** in a section of the 1st LN.

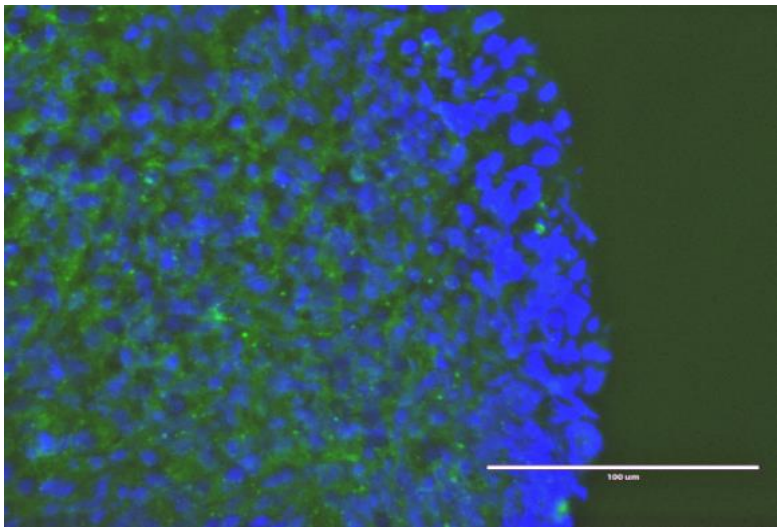

**Figure 5.20**: Histological verification of lymph node excision in the NIR field; cell nuclei were stained (blue color) with 4',6-diamidino-2-phenylindole (DAPI).

The difference found in the histological analysis of the popliteal nodes for Wistar rat injected with 1 nmol and 10 nmol of **Tc20** could be ascribed to the use of a digital microscope with no conventional charge-coupled (CCD) camera. Such detector (CCD), which enables accurate and precise quantitative fluorescence microscopy measurements,[161] would probably allow us to determine the cellular localization of **Tc20** in the lymph node when 1 nmol was injected in the animals.

## 5.8. Conclusions

Mannosylated dextran derivatives bearing pyrazolyl-diamine chelating units (**L18** and **L19**) as well as a NIR fluorophore (**L20**) were synthesized and characterized from the chemical and physical point of view. These conjugates allowed the preparation of (radio)metallated nanocompounds **Tc18** – **Tc20** as well as of the corresponding rhenium surrogates **Re18** – **Re20**.

Biological evaluation in Wistar rat model has shown that **Tc19** and **Tc20** presented the highest SLN extraction values. These data has also shown a persistent retention of the tracers in the lymph node, which we have demonstrated to be specific and mediated by mannose receptor binding. Moreover, we have shown that **Tc20** was a useful bimodal probe for SPECT/CT and NIR optical imaging of the popliteal lymph node. Indeed, the perfect coregistration between gamma radiation and NIR fluorescence signals of **Tc20** complement each other in detection and excision of the popliteal lymph. These studies also demonstrate that all compounds present similar accumlation in the injection site (> 80% IA/organ at 3 h p.i.) with minimal spread to non-target organs.

# 6

## Concluding Remarks and Outlook

# 6. Concluding Remarks and Outlook

The main goal of this thesis was to develop $^{99m}Tc(CO)_3$-based probes for targeting the melanocortin 1 receptor (MC1R), overexpressed in malignant melanoma, and the mannose receptor (MR) expressed on lymph node macrophages. Whereas in the former case, those specific tracers would allow early detection of a particularly aggressive type of skin cancer and associated metastasis by SPECT imaging, in the latter case they would allow the detection of the sentinel lymph node (SLN), which is a relevant procedure in medicine.

Within this context, tridentate bifunctional chelators containing a pyrazolyl-diamine chelating unit with a *N*,*N*,*N* donor atom set were selected to simultaneously stabilize the *fac*-$[^{99m}Tc(CO)_3]^+$ core and to be conjugated to targeting moieties or to nanocarriers.

Despite the considerable research efforts towards the design of radiotracers containing α-melanocyte-stimulating hormone (α-MSH) analogs for MC1R targeting, insufficient accumulation within the neoplastic cell and/or unfavorable pharmacokinetics, namely significant uptake in excretory organs have limited their translation into clinical practice.

Aiming to contribute to address these issues, we have envisaged three strategies. The first one comprised the design of new homobivalent conjugates (**L5** and **L6**) bearing two copies of the linear α-MSH analog **NAPamide** separated by linkers of different nature, and length. **L5** and **L6** presented a 19- and 4-fold higher affinity for MC1R, respectively, as compared to the monovalent construct **L4**. Metallation of these compounds yielded isostructural complexes of the type *fac*-$[M(CO)_3(\kappa^3\text{-}\mathbf{L})]$ (M = $^{99m}$Tc/Re; **Tc4**/**Re4,** L = **L4**; **Tc5**/**Re5**, L = **L5**; **Tc6**/**Re6**, L **= L6**) (**Scheme 6.1**). **Re5** and **Re6** displayed binding affinities in the sub- and nanomolar range, which were still better (**Re5**: $IC_{50}$ = 0.15 ± 0.08 nM) than or comparable (**Re6**: $IC_{50}$ = 1.14 ± 1.13 nM) to the binding affinity of **NAPamide** ($IC_{50}$ = 0.78 ± 0.03 nM). Cell internalization studies in B16F1 murine melanoma cells have shown that **Tc5** and **Tc6** internalize via an MC1R-mediated mechanism, with **Tc5** presenting the highest level of internalization.

Biodistribution studies in B16F1 melanoma-bearing mice have shown that the tumor uptakes of **Tc5** (2.96 ± 0.36 % IA/g) and **Tc6** (1.81 ± 0.44 % IA/g) were lower than that of **Tc4** (4.24 ± 0.94 % IA/g) at for 4 h p.i. Moreover, there was no positive

correlation between tumor uptake and valency, even in the case of **Tc5**, which had the highest cellular internalization level and better retention. One commom feature to both homobivalent radiopeptides was the high non-specific accumulation and retention in the kidney, which led to very low tumor to kidney ratios. Such behavior has been already reported for other radiolabeled bivalent α-MSH and multivalent RGD derivatives.

Brought together, the results have demonstrated that the high *in vitro* MC1R-binding affinity and the high level of cellular internalization/retention observed for $^{99m}Tc(CO)_3$-labeled bivalent **NAPamide** conjugates did not lead to increased tumor uptake and improved pharmacokinetic profile relative to the monovalent counterpart.

The second strategy focused on the synthesis of novel cyclic α-MSH derivatives containing a thioether (**SNBA-MSH$_{hex}$**) or an amino bridge (**NNBA-MSH$_{hex}$**) within the macrocycle ring. The Lys residue at the C-terminal in both peptides (not present in the cognate peptide **PG10N**) was used for conjugation to the bifunctional chelator. Metallation of the resulting conjugates **L7** and **L8** gave complexes of the type *fac*-$[M(CO)_3(\kappa^3\text{-}\mathbf{L})]^+$ (M = $^{99m}$Tc/Re; **Tc7**/**Re7**, L = **L7**; **Tc8**/**Re8**, L = **L8**) (**Scheme 6.1**).
*In vitro* MC1R-binding affinity assays indicated that the substitution of the thioether bridge (19-membered macrocyclic ring) by an amino bridge (22-membered macrocyclic ring) enhanced the receptor recognition properties (**SNBA-MSH$_{hex}$**: $IC_{50}$ = 1800 ± 500 nM, **NNBA-MSH$_{hex}$**: $IC_{50}$ = 51 ± 12 nM). However, both peptide were considerably less potent than the cognate peptide **PG10N** ($IC_{50}$ = 3.7± 0.5 nM). It is also worth mentioning that the conjugation of the bifunctional chelator to **SNBA-MSH$_{hex}$** and **NNBA-MSH$_{hex}$** gave conjugates with lower (**L7**: $IC_{50}$ = 430 ± 0.1 nM) and higher binding affinity (**L8**: $IC_{50}$ = 179 ± 39 nM), respectively. Metallation of the peptides did not lead to a significant decrease of binding affinity towards MC1R, as concluded by comparing the $IC_{50}$ values of **Re7** ($IC_{50}$ = 690 ± 250 nM) and **Re8** ($IC_{50}$ = 176 ± 5 nM) with those of **L7** and **L8**.

NMR structural characterization of the family containing the alkylthioaryl bridge (**SNBA-MSH$_{hex}$**, **L7** and **Re7**) and **NNBA-MSH$_{hex}$** were performed to identify structural factors that might affect the MC1R recognition ability of the peptide derivatives. Althougt the structural features of **PG10N** have not been reported, our NMR studies indicated that the low binding affinity of **SNBA-MSH$_{hex}$** could be ascribed to a pronounced anisotropic effect that arises from the interaction of the Arg side chain with the surrounding aromatic residues in the pharmacophore sequence (His-

DPhe-Arg-Trp). Such effect might hamper a favorable interaction of the amino acid with the MC1R.

More important, the NMR structural analysis demonstrated that the three-dimensional structural features of the peptide moiety were conserved upon conjugation of the chelator to the Lys side chain or upon incorporation of the organometallic fragment into the peptide conjugate. Nevertheless, further studies are needed to understand the molecular interactions that take place at the MC1R binding pocket for these (metallo)peptides.

In the third strategy, we tried to improve the pharmacokinetics of the $^{99m}Tc(CO)_3$-labeled lactam bridge-cyclized α-MSH analog **βAlaNleCycMSH$_{hex}$**. To achieve such goal, peptide conjugates **L9** (methyl groups at the 3,5 positions of the pyrazolyl ring), **L13** (no substituent groups in the azolyl-ring), **L14** (carboxylate at the 4-position of the azolyl-ring) and **L15** (carboxylate at the 4-position and methyl groups at the 3,5 positions of the pyrazolyl ring) were prepared by reaction of **βAlaNleCycMSH$_{hex}$** with the respective Boc-protected bifunctional chelators **L1-Boc**, **L10-Boc**, **L11-Boc** and **L12-Boc**.

Conjugation of the bifunctional chelators to **βAlaNleCycMSH$_{hex}$** did not affect the MC1R binding properties of the peptide conjugates that present sub-nanomolar $IC_{50}$ values (**L9**: $IC_{50}$ = 0.21 ± 0.05 nM, **L13**: $IC_{50}$ = 0.02 ± 0.01 nM, **L14**: $IC_{50}$ = 0.04±0.01 nM and **L15**: $IC_{50}$ = 0.16 ± 0.1nM).

Radiometallation of the peptide conjugates gave complexes of the type *fac*-[$^{99m}Tc(CO)_3(\kappa^3$-**L**)] (**Tc9**, L = **L9**; **Tc13**, L = **L13**; **Tc14**, L = **L14** and **Tc15**, L **= L15**) (**Scheme 6.1**). The log $P_{o/w}$ values determined experimentally indicated that the presence of an additional carboxylate in the azolyl-ring enhanced the hydrophilic nature of the radiometallated peptides, namely **Tc14** and **Tc15**. Internalization studies in murine B16F1 melanoma cells have shown that cellular uptake of the $^{99m}Tc(CO)_3$-labeled peptides **Tc9** and **Tc13** – **Tc15** was MC1R-mediated, confirming that the affinity of the radiopeptides was preserved upon radiometallation.

The *in vivo* MC1R-targeting properties of the radiopeptides were evaluated in B16F1 melanoma-bearing mice. High melanoma uptake (ca. 10 % IA/g) was observed for all radiopeptides at 1 h p.i. The presence of a carboxylate group in the pyrazolyl ring of the chelator had a profound effect in the pharmacokinetic profile of the radiopeptides. **Tc14** and **Tc15** presented a striking kidney and liver uptake reduction (> 90 %, at 4h p.i.) as compared to **Tc9**. Moreover, the overall radioactivity elimination of both

radiopeptides occurred mainly through the renal pathway, and the whole-body clearance was faster than observed for **Tc9** or **Tc13**.

The favourable biodistribution profile of **Tc14** and **Tc15** allowed a clear visualization of flank melanoma lesions in tumour-bearing mice by SPECT imaging at 1 h p.i. Moreover, both compounds generated high contrast between tumor and background due to their enhanced uptake ratios of tumor/kidney and tumor/liver.

Taken together, the results highlighted the possibility of tuning the pharmacokinetic properties of $^{99m}Tc(CO)_3$-labeled α-MSH derivatives through structural modifications in the bifunctional chelator, without compromising their *in vitro* and *in vivo* receptor-targeting properties. Indeed, this study demonstrated that the introduction of carboxylate groups shifted the excretion pathway of a radiopeptide from mainly hepatobiliar towards renal, improving notably tumor/non-target organs ratios. The potential usefulness of **Tc14** and **Tc15** should be furhter investigated for the visualization of melanoma (micro)metastases in B16F1 melanoma-bearing mice or human melanoma.

Although being widely used in the clinical setting for sentinel lymph node (SLND), $^{99m}$Tc-based nanoparticles present a set of properties that are far from ideal, namely, slow clearance rate from the injection sites or low residence times in the SLN. In addition, they are not universally approved by authorities for this specific application, and their chemical characterization is not well-defined. In this thesis, we have introduced the first class of fully characterized receptor-targeted mannosylated dextran derivatives for *in vivo* visualization of MR by SPECT or by SPECT combined with NIR optical imaging.

First, we prepared and characterized the mannosylated dextran derivatives **L18** and **L19**, which contain 4 and 8 chelating units per mol of dextran to stablize the *fac*-$[M(CO)_3]^+$ (M = Re, $^{99m}$Tc), respectively, as well as 13 mannose units per mol of dextran. In addtion, we have also synthesized a mannosylated dextran-based polymer that contains 3 NIR fluorophore units per mol of dextran (**L20**) by reaction of **L19** with heptamethine cyanine derivative. Metallation of **L18 – L20** gave metallated polymers of the type *fac*-$[M(CO)_3(\kappa^3\text{-}\mathbf{L})]^+$ (M = $^{99m}$Tc/Re; **Tc18**/**Re18**, L = **L18**; **Tc19**/**Re19**, L = **L19**; **Tc20**/**Re20**, L = **L20**) (**Scheme 6.1**). Physical characterization of the mannosylated dextran derivatives and their percursors by dynamic light scattering (DLS), atomic force microscopy (AFM) and laser Doppler velocimetry (LDV) has shown, as expected, that the hydrodynamic diameter and the zeta potencial of the

nanocompounds were affected by chemical modification. Indeed, **L18** – **L20** presented a hydrodynamic diameter within the range of 7.0 to 17.7 nm, whereas unmodified dextran has a diameter of ca. 4 nm. The conjugation of the NIR fluorophore to the dextran backbone increased 2.5-fold the size of the nanocompounds, as concluded by comparing the hydrodynamic diameter of **L20** (17.7 ± 2.0 nm) and **Re20** (22.5 ± 2.9 nm) with **L19** (7.0 ± 0.7 nm) and **Re19** (8.7 ± 0.3 nm), respectively. An higher hydrodynamic diameter was also found for the metallated polymers (**Re18**: 8.4 ± 0.5, **Re19**: 8.7 ± 0.3 nm, **Re20**: 22.5 ± 2.9 nm) as compared to the conjugates (**L18**: 7.0 ± 0.3 nm, **L19**: 7.0 ± 0.7 nm, **L20**: 17.7 ± 2.0 nm).

Biological evaluation of **Tc18** and **Tc19** in Wistar rats have shown good accumulation in the popliteal (sentinel) node (6.71 ± 2.35 % and 7.53 ± 0.69 %, respectively), at 1 h p.i. Both radioactive nanocompounds presented significant retention up to 3 h, which was mediated by mannose receptor binding. The higher SLN extraction values of **Tc19** (94.47 ± 2.45 %) as compared to **Tc18** (61.81 ± 2.42 %) at 1 h p.i. highlights the superior biological properties of **Tc19** to be further explored as SLN imaging agent. The NIR fluorescent $^{99m}Tc(CO)_3$-labeled mannosylated dextran derivative **Tc20**, which maintains the initial composition of **Tc19** in terms of bifunctional chelators and mannose units, has shown a great degree of specific retention and a clear delineation of the sentinel node, with minimal spread to other regions at 1 h. The SPECT result obtained for **Tc20** compared well with the SPECT/CT image obtained for **Tc19** at the same time point. At 3 h p.i., the radioactive probe **Tc19** and the bimodal probe **Tc20** presente similar SLN extraction values (87.81 ± 3.75 % and 89.66 ± 0.03 %, respectively), while the accumulation of radioactivity at the injection site was slightly higher in the case of the latter compound (**Tc19**: 81.13 ± 0.01 % IA/ organ, **Tc20**: 86.73 ± 0.92 % IA/ organ). It is noteworthy that the bimodal imaging features of **Tc20** ensured perfect coregistration of the two signals, allowing nuclear and NIR optical techniques to complement each other in the detection and excision of the popliteal lymph node.

The versatility of dextran-based nanoplataform not only enables the incorporation of other targeting moieties but also the conjugation of DOTA-based bifunctional chelators to stabilize radiometals such as $^{68}Ga$ and $^{67}Ga$. Such feature highlights the potential of this nanocompounds not only for SPECT/CT-NIR imaging but also for PET/CT-NIR.

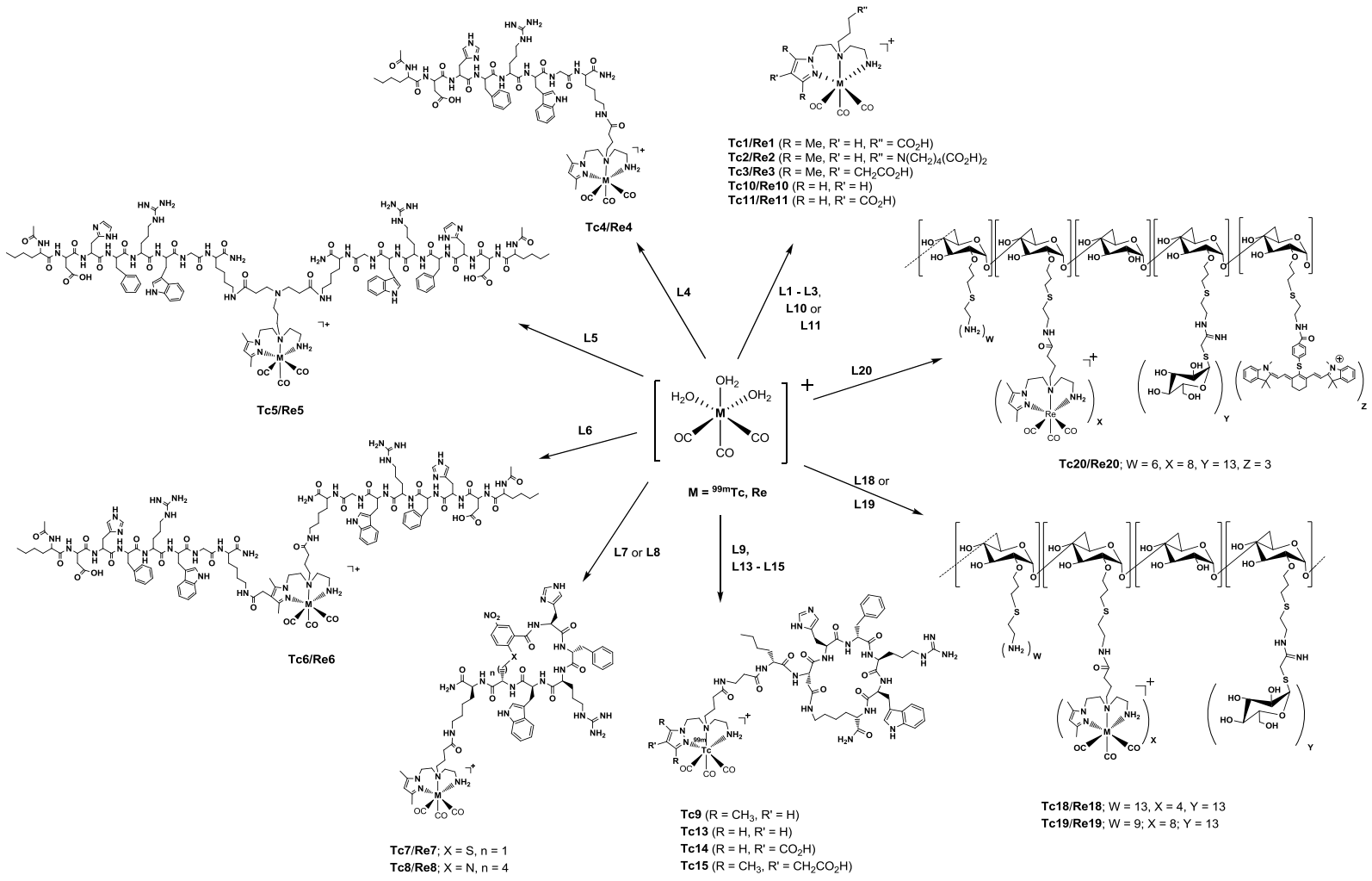


**Scheme 6.1**: Main compounds described in this thesis.

# 7

## Experimental Part

# 7. Experimental Part

## 7.1. Materials

All chemicals and solvents were of reagent grade and were used without purification, unless stated otherwise. The compounds tert-butyl 2-((3-aminopropyl)(2-(3,5-dimethyl-1H-pyrazol-1-yl)ethyl) amino)ethylcarbamate (**I**), ethyl 4-((2-(4-(2-(benzyloxy)-2-oxoethyl)-3,5-dimethyl-1H-pyrazol-1-yl)ethyl)(2-(tert-butoxycarbonyl amino)ethyl)amino)butanoate (**II**), tert-butyl 2-(2-(1H-pyrazol-1-yl)ethylamino) ethylcarbamate (**III**), ethyl 1-(2-(2-(tert-butoxy carbonylamino)ethylamino)ethyl)-1H-pyrazole-4-carboxylate (**IV**), tert-butyl 2-(1-(2-(2-(tert-butoxycarbonylamino)ethyl amino)ethyl)-3,5-dimethyl-1H-pyrazol-4-yl)acetate (**V**), ethyl 4-((2-(1H-pyrazol-1-yl)ethyl)(2-(tert-butoxycarbonylamino)ethyl)amino) butanoate (**VI**), 4-((2-(tert-butoxy carbonylamino)ethyl)(2-(3,5-dimethyl-1H-pyrazol-1-yl)ethyl)amino)butanoic acid (**L1-Boc**), **Re1** and IME-thiomannose were prepared according to described methods.[48d, 51b, 51e, 154, 162] The amino acids and **IR775-Cl** were purchased from Novabiochem and Sigma-Aldrich, respectively. The organometallic precursor *fac*-$[Re(CO)_3(H_2O)_3]Br$ was prepared according to a published method.[155] The radioactive precursor $[^{99m}Tc(CO)_3(H_2O)_3]^+$ was prepared according to the manufacturer's insert by adding $[^{99m}TcO_4]^-$ generator eluent to the IsoLink vial, heating for 30 min at 100 ºC, and adding 1M HCl (160 µL) to neutralize the solution, after cooling down. The IsoLink vials were obtained as a gift from Covidien.

## 7.2. Characterization and Purification Techniques

### Infrared Spectroscopy (IR)

Infrared spectra were recorded as KBr pellets in a Bruker Tensor 27 spectrometer.

## Nuclear Magnetic Resonance Spectrometry (NMR)

### Small Molecules

$^{1}H$ and $^{13}C$-NMR spectra were recorded in a Varian Unity 300 MHz spectrometer; $^{1}H$ and $^{13}C$ chemical shifts were referenced to the residual solvent resonances relative to tetramethylsilane (SiMe4).

Multiplicities are reported using the following abbreviations: s (singlet), d (doublet), t (triplet), q (quartet), quint (quintuplet), m (multiplet), br (broad) or a suitable combination of them.

### Peptide Derivatives

NMR spectra of **NAPamide**, **SNBA-MSH$_{hex}$**, **NNBA-MSH$_{hex}$**, **L4**, **Re4**, **L7**, **L8**, **Re7**, **Re8** and **L14** were acquired at 5 ºC and 25 ºC on a Bruker AV-600 spectrometer operating at a proton frequency of 600.13 MHz and equipped with a cryoprobe. The temperature of the NMR probe was calibrated using a methanol sample. 1D spectra were acquired using 32 K data points, which were zero-filled to 64 K data points before performing the Fourier transformation. As previously reported,[163] 2D spectra, i.e., phase-sensitive correlated spectroscopy (COSY), total correlated spectroscopy (TOCSY), nuclear Overhauser enhancement spectroscopy (NOESY), and rotating frame nuclear Overhauser spectroscopy (ROESY), were recorded by standard techniques using presaturation of the water signal and the time-proportional phase incrementation mode. NOESY and ROESY mixing times were 150 ms and 200 ms, respectively. TOCSY spectra were acquired using 60 ms DIPSI2 with z filter spin-lock sequence. $^{1}H$-$^{13}C$ and $^{1}H$-$^{15}N$ heteronuclear single quantum coherence spectra (HSQC) were recorded at natural heteronuclear abundance. Acquisition data matrices were defined by 2048 x 512 (128 in the case of the $^{1}H$-$^{15}N$ HSQC spectrum) points in $t_2$ and $t_1$, respectively. Data were processed using the standard TOPSPIN program. The 2D data matrix was multiplied by either a square-sine-bell or a sine-bell window function with the corresponding shift optimised for every spectrum and zero-filled to a 2K x 1K (256 points in the $^{1}H$-$^{15}N$ HSQC) complex matrix prior to Fourier transformation. Baseline correction was applied in both dimensions. The 0 ppm $^{13}C$ and $^{15}N$ δ-values were obtained indirectly by multiplying the spectrometer frequency that corresponds to

0 ppm in the $^{1}H$ spectrum, assigned to internal DSS reference, by 0.25144953 and 0.101329118, respectively.[139a]

The sample solutions (1 mM) were prepared by dissolving the lyophilized compounds (~0.5 mg) in 0.5 mL $H_2O/D_2O$ (9:1 v/v) before NMR spectra acquisition. The pH was adjusted to 2.5 by adding minimal amounts of NaOD or DCl, measured with a glass micro electrode and not corrected for isotope effects. Sodium 2,2-dimethyl-2-silapentane-5-sulfonate (DSS) was used as an internal reference.

**NMR assignment**

The chelator resonances in the corresponding peptide conjugates, metallopeptides and polymeric compounds were assigned by the combined analysis of 2D COSY, TOCSY, NOESY and $^{1}H,^{13}C$-HSQC spectra, and taking into account previous NMR assignments for the isolated chelator.

$^{1}H$-NMR signals of the peptide derivatives were assigned by standard sequential assignment methods.[136] Then, the $^{13}C$ and $^{15}N$ resonances were straightforwardly assigned from the cross-correlations observed in the corresponding HSQC spectra between the proton and the bound carbon or nitrogen, respectively.

**Column Chromatography**

Some compounds were purified by column chromatography, using silica gel 60 with 70 - 230 mesh granulometry (ASTM Merck) and glass columns with dimensions appropriate to the amount of compound to purify.

**Thin Layer Chromatography (TLC)**

Some chemical reactions were monitored by TLC, using silica-gel plates MERCK 60 - F254 with 0.25 mm of thickness, in an aluminium support; the plates were analysed with U.V. radiation or $I_2$.

### High Performance Liquid Chromatography (HPLC)

Reverse phase HPLC analyses were performed with a Perkin Elmer LC pump 200 coupled to an U.V. detector (Shimadzu SPD-10 AV or Perkin Helmer LC 290) or to a γ detector (Berthold-LB 507A or LB 509). The solvents were of HPLC grade and the water bidistilled from a quartz distillation unit. The solvents were filtered by Millipore 0.22 μm filters and purged with helium.

**Analytical Control of Compounds L2-Boc, L3-Boc, Re1, Re2, Re3, L10-Boc, L11-Boc** and **L12-Boc, Re10** and **Re11:**

**Column**: Analytical, EC250/3 Nucleosil 100-10 C18, Macherey Nagel; **Pre-column**: EP 30/8 Nucleosil 100-7 C18, Macherey Nagel; **Flow**: 1.0 mL/min; **γ detection**; **U.V. detection**: λ = 220 nm; **Eluents**: **A** - TFA 0.1 % in $H_2O$; **B** - $CH_3OH$.

**HPLC Method A**:

| Step | Time (min) | % B |
|---|---|---|
| 0 | 5 | 0 |
| 1 | 0 – 3 | 0 |
| 2 | 3 – 3.1 | 0 → 25 |
| 3 | 3.1 – 9 | 25 |
| 4 | 9 – 9.1 | 25 → 34 |
| 5 | 9.1 – 20 | 34 → 100 |
| 6 | 20 – 25 | 100 |
| 7 | 25 – 25.1 | 100 → 0 |
| 8 | 25.1 – 30 | 0 |

**Preparative Purification of Compounds Re1**, **Re2**, **Re3**, **Re10** and **Re11**

**Column**: Preparative, Waters μ Bondapak C18 (150/19 mm); **Pre-column**: Hypersil C18 (ODS), 4.6 × 25 mm, 10 μm; Flow: 5.0 mL/min; **U.V. detection**: λ = 254 or 220 nm; Eluents: A - TFA 0.1 % in $H_2O$; B - $CH_3OH$.

**HPLC Method B**:

| Step | Time (min) | % B |
|---|---|---|
| 0 | 5 | 0 |
| 1 | 0 – 3 | 0 |
| 2 | 3 – 3.1 | 0 → 25 |
| 3 | 3.1 – 9 | 25 |
| 4 | 9 – 9.1 | 25 → 34 |
| 5 | 9.1 – 18 | 34 → 100 |
| 6 | 20 – 25 | 100 |
| 7 | 25 – 25.1 | 100 → 0 |
| 8 | 25.1 – 30 | 0 |

**Analytical Control of Pp-NAPamide**

**Column**: Analytical, 5 µm (250 X 4.6 mm) C18, Discovery® BioWide Pore analytic; **Flow**: 1.0 mL/min; **γ detection**, **U.V. detection**: λ = 220 nm and 280 nm; **Eluents**: **A** - 0.1% TFA in $H_2O$; **B** - 0.1% TFA in $CH_3CN$.

**HPLC Method C**:

| Step | Time (min) | % B |
|---|---|---|
| 0 | 5 | 50 |
| 1 | 0 – 25 | 50 → 100 |
| 2 | 25 – 35 | 100 |
| 3 | 35 – 36 | 100 → 50 |
| 4 | 36 – 40 | 50 |

**Semi-Preparative Purification of Pp-NAPamide**

**Column**: Semi-Preparative, 5 µm (250 x 10 mm) C18, Discovery® BioWide Pore; **Flow**: 2.0 mL/min; **γ detection**, **U.V. detection**: λ = 220 nm and 280 nm; **Eluents**: **A** - 0.1 % TFA in $H_2O$; **B** - 0.1% TFA in $CH_3CN$.

**HPLC Method D**:

| Step | Time (min) | % B |
|---|---|---|
| 0 | 5 | 70 |
| 1 | 0 – 35 | 70 → 100 |
| 2 | 35 – 37 | 100 |
| 3 | 37 – 38 | 100 → 70 |
| 4 | 38 – 40 | 70 |

**Analytical Control of L4, L5, L6, Re4, Re5, Re6, Tc4, Tc5 and Tc6**

**Column**: Hypersil ODS column (250/4 mm, 10 μm); **Flow**: 1 mL/min; **γ detection**, **U.V. detection**: λ = 220 nm; **Eluents**: **A** - 0.5 % TFA in $H_2O$; B - 0.5% TFA in $CH_3CN$

**HPLC Method E**

| Step | Time (min) | % B |
|---|---|---|
| 0 | 5 | 0 |
| 1 | 0 – 3 | 0 |
| 2 | 3 – 3.1 | 0 → 25 |
| 3 | 3.1 – 9 | 25 |
| 4 | 9 – 9.1 | 25 → 34 |
| 5 | 9.1 – 14.1 | 34 → 100 |
| 6 | 14.1 – 19 | 100 |
| 7 | 19 – 21 | 100 → 0 |
| 8 | 21 – 30 | 0 |

**Semi-Preparative Purification of Tc4, Tc5 and Tc6**

**Column**: Semi-Preparative, Hypersil ODS column (250/8 mm, 10 μm); **Flow**: 3 mL/min; **γ detection**, **U.V. detection**: λ = 220 nm; **Eluents**: **A** - 0.5 % TFA in $H_2O$; **B** - 0.5% TFA in $CH_3CN$. **HPLC Method E.**

**Analytical Control and Purification of [$^{125}$I]-NDP-MSH**

**Column**: Analytical, EC250/4 Nucleosil 100-10 C18, Macherey Nagel; **Pre-column**: EP 30/8 Nucleosil 100-7 C18, Macherey Nagel; **Flow**: 1.0 mL/min; **γ detection**; **U.V.**

**detection**: λ = 254 nm; **Eluents**: **A** - TFA 0.1 % in $H_2O$; **B** - 140 mL $CH_3CN$/ 60 mL $H_2O$/ 200 µL concentrated TFA.

**HPLC Method F**

| Step | Time (min) | % B |
|---|---|---|
| 0 | 5 | 30 |
| 1 | 0 – 45 | 30 → 50 |
| 2 | 45 – 55 | 50 → 100 |
| 3 | 55 – 56 | 100 |
| 4 | 56 – 60 | 100 → 30 |

**Analytical Control and Semi-Preparative Purification of SNBA-$MSH_{hex}$, NNBA-$MSH_{hex}$, L7, L8, Re7 and Re8**

**Column**: Analytical, 5 µm (250 X 4.6 mm) C18, Discovery® BioWide Pore analytic; **Flow**: 1.0 mL/min; **γ detection**, **U.V. detection**: λ = 220 nm and 280 nm; **Eluents**: **A** - 0.1% TFA in $H_2O$; **B** - 0.1% TFA in $CH_3CN$.

**Column**: Semi-Preparative, Hypersil ODS column (250/8 mm, 10 µm); **Flow**: 3 mL/min; **γ detection**, **U.V. detection**: λ = 220 nm; **Eluents**: **A** - 0.5 % TFA in $H_2O$; **B** - 0.5% TFA in $CH_3CN$.

**HPLC Method G**

| Step | Time (min) | % B |
|---|---|---|
| 0 | 5 | 20 |
| 1 | 0 – 35 | 20 → 60 |
| 2 | 35 – 37 | 60 |
| 3 | 37 – 38 | 60 → 20 |
| 4 | 38 – 40 | 20 |

**Analytical Control of Tc7, Tc8, Re7, Re8, Tc13, Tc14 and Tc15**

**Column**: Hypersil ODS column (250/4 mm, 10 µm); **Flow**: 1 mL/min; **γ detection**, **U.V. detection**: λ = 220 nm; **Eluents**: **A** - 0.5 % TFA in $H_2O$; B - 0.5% TFA in $CH_3CN$

**HPLC Method H**

| Step | Time (min) | % B |
|---|---|---|
| 0 | 5 | 15 |
| 1 | 0 – 18 | 15 → 100 |
| 2 | 18 – 20 | 100 |
| 3 | 20 – 22 | 100 → 15 |
| 4 | 22 – 30 | 15 |

**Semi-Preparative Purification of Tc7** and **Tc8**

**Column**: Semi-Preparative, Hypersil ODS column (250/8 mm, 10 μm); **Flow**: 3 mL/min; **γ detection**, **U.V. detection**: λ = 220 nm; **Eluents**: **A** - 0.5 % TFA in $H_2O$; **B** - 0.5% TFA in $CH_3CN$.

**HPLC Method I**

| Step | Time (min) | % B |
|---|---|---|
| 0 | 5 | 15 |
| 1 | 0 – 15 | 15 → 30 |
| 2 | 15 – 30 | 30 |
| 3 | 30 – 45 | 30 → 60 |
| 4 | 45 – 55 | 60 →100 |
| 5 | 55 – 56 | 100 →15 |
| 6 | 56 – 60 | 100 |

**Analytical Control and Semi-Preparative Purification (Fmoc-)βAlaNleCycMSH$_{hex}$**

**Column**: Analytical, 5 μm (250 X 4.6 mm) C18, Discovery® BioWide Pore analytic; **Flow**: 1.0 mL/min; **γ detection**, **U.V. detection**: λ = 220 nm and 280 nm; **Eluents**: **A** - 0.1% TFA in $H_2O$; **B** - 0.1% TFA in $CH_3CN$.

**Column**: Semi-Preparative, 5 μm (250 x 10 mm) C18, Discovery® BioWide Pore; **Flow**: 2.0 mL/min; **γ detection**, **U.V. detection**: λ = 220 nm and 280 nm; **Eluents**: **A** - 0.1 % TFA in $H_2O$; **B** - 0.1% TFA in $CH_3CN$.

**HPLC Method J**

| Step | Time (min) | % B |
|---|---|---|
| 0 | 5 | 10 |
| 1 | 0 – 50 | 10 → 95 |
| 2 | 50 – 50.1 | 95 → 100 |
| 3 | 50.1 – 54 | 100 |
| 4 | 54 – 55 | 100 →10 |
| 5 | 55 – 60 | 10 |

**Semi-Preparative Purification of Tc13, Tc14 and Tc15**

**Column**: Semi-Preparative, Hypersil ODS column (250/8 mm, 10 μm); **Flow**: 3 mL/min; **γ detection**, **U.V. detection**: λ = 220 nm; **Eluents**: **A** - 0.5 % TFA in $H_2O$; **B** - 0.5% TFA in $CH_3CN$.

**HPLC Method K**

| Step | Time (min) | % B |
|---|---|---|
| 0 | 5 | 15 |
| 1 | 0 – 5 | 15 → 30 |
| 2 | 5 – 10 | 30 |
| 3 | 10 – 25 | 30 → 60 |
| 4 | 25 – 28 | 60 |
| 5 | 28 – 30 | 60 → 15 |

**Analytical Control of Dextran derivatives L16 – L20**, **Tc16 – Tc20**, **Re19 and Re20**

**Column**: Shodex OHpack SB-803 HQ analytical column; **Flow**: 0.5 mL/min; **γ detection**, **U.V. detection**: λ = 220 nm and 760 nm; **Eluents**: **A** - $H_2O$ (0.02 % $NaN_3$);.

**HPLC Method L** (Isocratic)

| Step | Time (min) | % A |
|---|---|---|
| 0 | 5 | 100 |
| 1 | 0 – 60 | 100 |

**Column**: Analytical, 5 μm (250 X 4.6 mm) C18, Discovery® BioWide Pore analytic; **Flow**: 1.0 mL/min; **γ detection**, **U.V. detection**: λ = 220 nm and 760 nm; **Eluents**: **A** - 0.1% TFA in $H_2O$; **B** - 0.1% TFA in $CH_3CN$.

**HPLC Method M**

| Step | Time (min) | % B |
|---|---|---|
| 0 | 5 | 0 |
| 1 | 0 – 9 | 0 → 80 |
| 2 | 9 – 14 | 80 |
| 3 | 14 – 15 | 80 → 0 |
| 4 | 15 – 20 | 0 |

**Mass Spectrometry**

ESI/QITMS analyses of compounds were performed with a Bruker HCT instrument, which was acquired with the support of the Programa Nacional de Reequipamento Científico of FCT and is part of Rede Nacional de Espectrometria de Massa - RNEM).

**Physical characterization of the polymeric nanoparticles**

The hydrodynamic diameter of dextran and its derivatives were determined in 0.01 M phosphate buffer, pH 7.4, by DLS using a ZetaSizer Nano ZS from Malvern. Particle size was measured at 25 ºC with a 173° scattering angle. The surface charge was determined by electrophoretic mobility using Laser Doppler Velocimetry and Zeta Potencial Cells. A Digital Instruments MultiMode Scanning Probe Microscope (SPM) with a Nanoscope IIIA controller in tapping mode was used for the Atomic Force Microscopy measurements.

**Spectrophotometry**

Absorption data of all α-MSH and dextran derivatives was collected in a Shimadzu UV-1800 Spectrophotometer (range: 200 – 1100 nm). Results from colorimetry assays were also collected in a Shimadzu UV-1800 Spectrophotometer at 490 nm. Emission spectra of **L20** and **Re20** was recorded with a USB2000+ Miniature Fiber Optic Spectrometer

from Ocean Optics, which is responsive from 200-1100 nm with resolution to 0.35 nm (FWHM). An optical fiber was used to collect the emission of the sample cell, in the right angle geometry. The excitation source was a femtosecond Ti:sapphire laser (TISSA-100, CDP), pumped by a solid state Millennia Xs laser (Spectra Physics). The laser system generates a 86 MHz pulse train in the tuning range: 750–850 nm (ca. 200 fs FWHM). Measurements were carried out exciting the sample at 790 nm (average power 400 mW.) with parallel polarized light. SpectraSuite Spectroscopy Operating Software was used to process the fluorescence spectra. The NIR emission of **L20** and **Tc20** was quantified in a Odyssey imager, Li-Cor BioSciences, Lincoln, NE, USA, by simultanoeus excitation at 700 nm and 800 nm while emission was collected in the 800 channel.

**Instant Thin-Layer Chromatography**

Instant thin-layer chromatography (ITLC) was performed using ITLC silica gel strips (SG-PALL) developed with a mobile phase of 5% HCl (6M)/ MeOH. Radioactive distribution on the ITLC strips was detected using a Berthold LB 505 detector, equipped with a NaI(Tl) scintillation crystal, coupled to a radiochromatogram scanner.

**Activity Measurements of Radioactive Solutions**

The radioactivity of the $^{99m}$Tc solutions was measured in an ionization chamber (Aloka, Curiemeter IGC-3). The samples with activity less than 2 μCi were measured in a Gamma Counter (Berthold LB 2111).

## 7.3. Synthesis and Characterization of the Compounds

### 7.3.1. 4-((2-(tert-butoxycarbonylamino)ethyl)(2-(3,5-dimethyl-1H-pyrazol-1-yl)ethyl)amino)butanoic acid (L1-Boc)

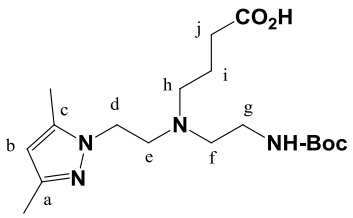


**L1-Boc** was synthesized and characterized as previously reported.[48d]

**$^{1}$H-RMN** (300 MHz, $CDCl_3$): $\delta_H$ (ppm) 5.82 (s, $CH^b$, 1H), 4.74 (br s, NH, 1H), 4.07 (t, $CH_2^d$, 2H), 3.01 (m, $CH_2^j$, 2H), 2.79 (t, $CH_2^g$, 2H), 2.52 (m, $CH_2^e$ + $CH_2^f$ + $CH_2^h$, 6H); 2.22 (s, $CH_3^a$, 3H), 2.20 (s, $CH_3^c$, 3H), 1.77 (t, $CH_2^i$, 2H), 1.40 (s, 9H, $CH_3$).

**$^{13}$C-NMR** (75.5 MHz, $CDCl_3$): $\delta_C$ (ppm) 182.1 (CO), 159.3 (CO), 148.2 ($C^c$), 147.2 ($C^a$), 105.3 ($C^b$), 79.3 ($C$($CH_3$), 59.6 ($C^h$), 56.7 ($C^e$), 53.9 ($C^f$), 49.2 ($C^d$), 38.8 ($C^g$), 36.2 ($C^j$), 28.2 (C($CH_3$)), 23.7 ($C^i$), 13.5 ($CH_3^c$), 11.8 ($CH_3^a$).

### 7.3.2. 4-((2-aminoethyl)(2-(3,5-dimethyl-1H-pyrazol-1-yl)ethyl)amino)butanoic acid (L1)

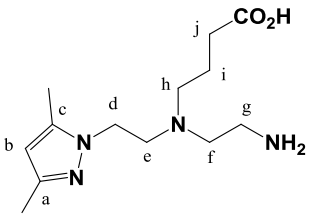


**L1** was synthesized and characterized as previously reported.[48d]

**$^{1}$H-RMN** (300 MHz, $D_2O$): $\delta_H$ (ppm) 6.11 (s, $CH_2^b$, 1H), 4.50 (t, $CH_2^d$, 2H), 3.53 (t, $CH_2^e$, 2H), 3.44 (m, $CH_2^{g/f}$, 2H), 3.35 (m, $CH_2^{g/f}$, 2H), 3.15 (m, $CH_2^j$, 2H), 2.29 (t, $CH_2^h$, 2H), 2.16 (s, $CH_3^a$, 3H), 2.10 (s,$CH_3^c$, 3H), 3.15 (m, $CH_2^i$, 2H).

**$^{13}$C-NMR** (75.5 MHz, $D_2O$): $\delta_C$ (ppm) 183.0 (CO), 165.3 (q, CF3$C$OO$^-$), 148.2 ($C^c$), 141.4 ($C^a$), 118.6 (q, $CF_3COO^-$), 106.0 ($C^b$), 54.2 ($C^h$), 54.0 ($C^e$), 52.0 ($C^f$), 47.0 ($C^d$), 38.4 ($C^g$), 36.0 ($C^j$), 24.7 ($C^i$), 13.3 ($CH_3^c$); 11.0 ($CH_3^a$).

### 7.3.3. tert-butyl 2-((3-aminopropyl)(2-(3,5-dimethyl-1H-pyrazol-1-yl)ethyl) amino) ethylcarbamate (I)

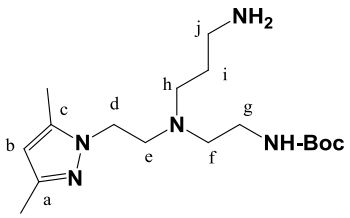


Intermediate **I** was synthesized and characterized as previously reported by our group.[51e]

**$^1$H-NMR** (300 MHz, $CDCl_3$): $\delta_H$ (ppm) 5.75 (s, $CH^b$,1H); 5.28 (br s, $NH_2$, 2H); 5.10 (br s, NHBoc, 1H); 3.96 (t, $CH_2^d$, 2H), 3.07 (m, $CH_2^e$, 2H), 2.76 (t, $CH_2^f$, 2H), 2.60 (t, $CH_2^g$, 2H), 2.48 (m, $CH_2^h$ /$CH_2^j$, 4H), 2.21 (s, $CH_3^a$, 3H), 2.19 (s, $CH_3^c$, 3H), 1.45 (m, $CH_2^i$, 2H), 1.42 (s, $CH_3$, 9H).

### 7.3.4. Methyl 8-(2-(3,5-dimethyl-1H-pyrazol-1-yl)ethyl)-12-(3-methoxy-3-oxopropyl)-2,2-dimethyl-4-oxo-3-oxa-5,8,12-triazapentadecan-15-oate (L2-Boc-Me$_2$)

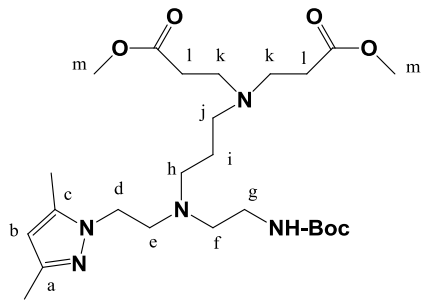


A solution of **I** (0.0600 g, 0.170 mmol) in dry methanol was added dropwise to a cold methanolic solution (0 ºC) of methyl acrylate (0.076 g, 0.88 mmol). After stirring overnight at room temperature, the solvent was evaporated, and the crude product was purified by column chromatography (silica gel, $CHCl_3$/MeOH 2.5-20%), giving **L2-Boc-Me$_2$** as a white solid. Yield: 71 % (0.0700 g, 0.130 mmol).

**$^1$H-NMR** (300 MHz, $CDCl_3$): $\delta_H$ (ppm) 5.75 (s, $CH^b$, 1H), 3.96 (t, $CH_2^d$, 2H), 3.64 (s,$CH_3^m$, 6H), 3.07 (d, $CH_2^g$, 2H), 2.76 (t, $CH_2^k$, 2H), 2.70 (t, $CH_2^e$, 2H), 2.49 (t, $CH_2^f$, 2H), 2.38 (t, $CH_2^{l,\,j}$, 4H), 2.29 (t, $CH_2^h$, 2H), 2.21, (s, $CH_3^a$, 3H), 2, 19 (s, $CH_3^c$, 3H), 1.48 (t, $CH_2^i$,2H), 1.42 (s, $CH_3$, 9H).

### 7.3.5. 12-(2-carboxyethyl)-8-(2-(3,5-dimethyl-1H-pyrazol-1-yl)ethyl)-2,2-dimethyl-4-oxo-3-oxa-5,8,12-triazapentadecan-15-oic acid (L2-Boc)

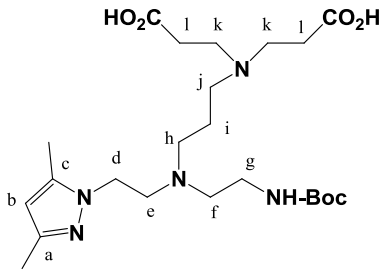


A solution of **L2-Boc-Me$_2$** (0.0700 g, 0.130 mmol) and NaOH (0.0550 g, 1.370 mmol) in $H_2O$/THF (1:1, 6 mL) was refluxed overnight. After neutralization of the reaction solution with 1M HCl at 0 ºC and evaporation of the solvent, the crude obtained was purified through Sep-Pack C-18 cartridge ($H_2O$/MeOH 0-100%), giving **L2-Boc** as a white solid. Yield: 75% (0.0500 g, 0.100 mmol).

**$^1$H-NMR** (300 MHz, $D_2O$): $\delta_H$ (ppm) 5.78 (s, $CH^b$, 1H), 3.88 (t, $CH_2^d$, 2H), 3.10 (t, $CH_2^k$, 4H), 2.96 (t, $CH_2^g$, 2H), 2.79 (t, $CH_2^e$, 2H), 2.70 (t, $CH_2^f$, 2H), 2.41 (t, $CH_2^{l, j, h}$, 8H), 2.10 (s, $CH_3^a$, 3H), 1.99 (s, $CH_3^c$, 3H), 1.61 (t, $CH_2^i$, 2H), 1.25 (s, $CH_3$, 9H).

**$^{13}$C-NMR** (75.3 MHz, $D_2O$): $\delta_C$ (ppm) 179.7 (CO), 179.6 (CO), 160.1 (CO), 150.5 ($C^c$), 143.5 ($C^a$), 107.3 ($C^b$), 81.9 ($C$($CH_3$)), 54.6 ($C^h$), 54.5 ($C^e$), 52.4 ($C^f$), 52.1 ($C^j$), 52.2 ($C^k$), 47.9 ($C^d$), 39.9 ($C^g$), 32.8 ($C^l$), 29.8 (C($CH_3$)), 22.9 ($C^i$), 14.3 ($CH_3^c$), 12.4 ($CH_3^a$).

**ESI-MS** (-) (m/z): 482.4 $[M-H]^-$, calcd. for $C_{23}H_{41}N_5O_6$ = 483.3.

**RP-HPLC** (Method A): 99% ($t_R$ = 17.4 min).

### 7.3.6. 3,3'-(3-((2-aminoethyl)(2-(3,5-dimethyl-1H-pyrazol-1-yl)ethyl)amino) propylazanediyl) dipropanoate (L2-Me$_2$)

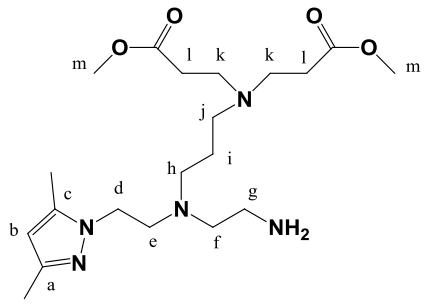


**L2-Boc-Me$_2$** (0.0700 g, 0.130 mmol) was suspended in a solution (5 mL) of TFA (5% TFA/$CH_2Cl_2$) and the reaction mixture allowed to stir at room temperature for 3 hours.

After evaporation of the solvent, **L2-Me$_2$** was obtained as colorless oil. Yield: 88% (0.0500 g, 0.120 mmol).

**$^1$H-NMR** (300 MHz, $D_2O$): $\delta_H$ (ppm) 5.58 (s, $CH^b$, 1H), 4.27 (t, $CH_2^d$, 2H), 3.2 (s, $CH_3^m$, 6H), 2.96 (t, $CH_2^{e+k}$, 6H), 2.59-2.51 (m, $CH_2^{g+j+h}$, 6H), 2.38 (t, $CH_2^l$, 4H), 2.29 (t, $CH_2^f$, 2H), 1.77 (s, $CH_3^a$, 3H), 1.69 (s, $CH_3^c$, 3H), 1.39 (t, $CH_2^i$, 2H).

### 7.3.7. ethyl 4-((2-(4-(2-(benzyloxy)-2-oxoethyl)-3,5-dimethyl-1H-pyrazol-1-yl)ethyl)(2-(tert-butoxycarbonylamino)ethyl)amino)butanoate (II)

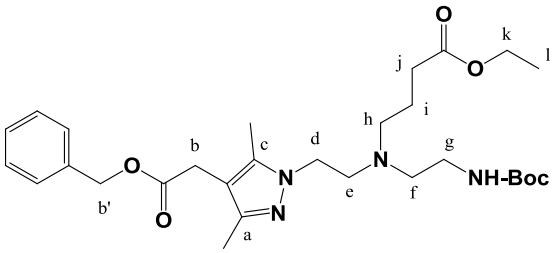


Intermediate **II** was synthesized and characterized as previously reported.[51b]

**$^1$H-NMR** (300 MHz, $CDCl_3$): $\delta_H$ (ppm) 7,26 (m, 5 CH-Ar, 5H,), 5.32 (s br, NH, 1H), 5.02 (s, $CH^{b'}$, 1H), 4.02 (m, $CH_2^{d+k}$, 4H), 3.91 (t, $CH_2^e$, 2H), 3.30 (s, $CH_2^b$, 2H), 2.98 (m, $CH_2^g$, 2H), 2.68 (t, $CH_2^f$, 2H), 2.42 (t, $CH_2^h$, 2H), 2.36 (t, $CH_2^j$, 2H), 2.10 (m, 2 $CH_3^{a+c}$, 6H), 1.55 (m, $CH_2^i$, 2H), 1.36 (s, $CH_3$, 9H); 1,16 (t, $CH_3^l$, 3H).

### 7.3.8. 4-((2-(tert-butoxycarbonylamino)ethyl)(2-(4-(carboxymethyl)-3,5-dimethyl-1H-pyrazol-1-yl)ethyl)amino)butanoic acid (L3-Boc)

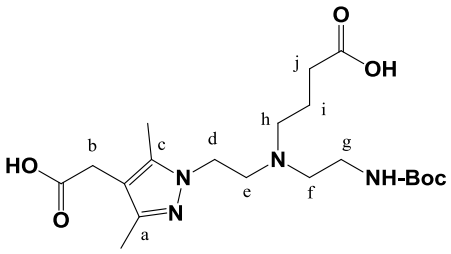


A solution of **II** (0.2000 g, 0.440 mmol) and excess NaOH (0.7500 g, 2.100 mmol) in $H_2O$/THF (1:1, 10mL) was refluxed overnight. After neutralization with 1M HCl at 0 $^oC$ and evaporation of the solvent, the crude product obtained was purified by solid phase extraction using Sep-Pack C-18 cartridge ($H_2O$/MeOH 0-100%), giving **L3-Boc** as a white solid after evaporationof the solvent. Yield: 68% (0.1400 g, 0.300 mmol).

**$^{1}$H-NMR** (300 MHz, $D_2O$): $\delta_H$ (ppm) 4.33 (t,$CH_2^{d}$, 2H), 3.57 (t, $CH_2^{e}$, 2H), 3.39 (s, $CH_2^{b}$, 2H), 3.30 (m, $CH_2^{f/h}$, 4H), 3.17 (t, $CH_2^{g}$, 2H), 2.34 (t, $CH_2^{j}$, 2H), 2.10 (s, $CH_3^{a}$, 3H), 2.03 (s, $CH_3^{c}$, 3H), 1.86 (t, $CH_2^{i}$, 2H), 1.24 (s, $CH_3$, 9H).

**$^{13}$C-NMR** (75.3 MHz, $D_2O$): $\delta_C$ (ppm) 189.8 (CO), 187.6 (CO), 165.1 (CO), 154.5 ($C^{c}$), 145.9 ($C^{a}$), 119.4 (Cpz), 88.8 (*C*($CH_3$)), 60.2 ($C^{h}$), 59.7 ($C^{e}$), 59.2 ($C^{f}$), 52.4 ($C^{d}$), 44.1 ($C^{g}$), 42.3 ($C^{j}$), 38.8 ($C^{b}$), 34.8 (C(*C*H3)), 29.5 ($C^{i}$), 17.7 ($CH_3^{c}$), 15.9 ($CH_3^{a}$).

**RP-HPLC** (Method A): 99% ($t_R$ = 16.7 min).

### 7.3.9. 4-((2-aminoethyl)(2-(4-(carboxymethyl)-3,5-dimethyl-1H-pyrazol-1-yl)ethyl) amino)butanoic acid (L3)

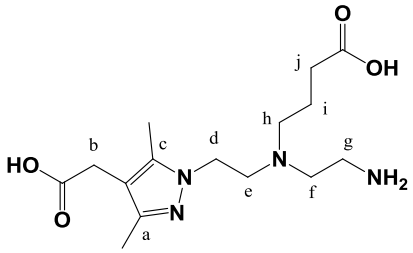


Boc deprotection of **L3-Boc** and **L12-Boc** (0.1000 g, 0.200 mmol) with $CH_2Cl_2$/TFA (1:3, 4mL) gave **L3** as a colorless oil after evaporation of the solvent. Yield: 92 % (0.0800 g, 0.190 mmol, calcd. for $C_{15}H_{26}N_4O_4$.TFA).

Boc deprotection of **L12-Boc** (0.1000 g, 0.207 mmol) with $CH_2Cl_2$/TFA (1:3, 4mL) gave **L3** as a colorless oil after evaporation of the solvent. Yield: 88 % (0.0800 g, 0.190 mmol, calcd. for $C_{15}H_{26}N_4O_4$.TFA).

**$^{1}$H-NMR** (300 MHz, $D_2O$): $\delta_H$ (ppm) 4.42 (t, $CH_2^{d}$, 2H), 3.51 (t, $CH_2^{e}$, 2H), 3.40 (m, $CH_2^{f}$, 2H), 3.32 (s, $CH_2^{b}$, 2H), 3.23 (m, $CH_2^{g}$, 2H), 3.09 (m, $CH_2^{j,}$ 2H), 2.72 (t, $CH_2^{h}$, 2H), 2.06 (s, $CH_3^{a}$, 3H), 1.99 (s, $CH_3^{c}$, 3H), 1.77 (m, $CH_2^{i}$, 2H).

**$^{13}$C-NMR** (75.3 MHz, $D_2O$): $\delta_C$ (ppm) 178.2 (CO), 176.9 (CO), 165.4 (q, $CF_3COO^-$), 149.4 ($C^{c}$), 145.5 ($C^{a}$), 118.4 (q, $CF_3COO^-$), 114.1 ($C^{b}$), 54.4 ($C^{h}$), 53.3 ($C^{e}$), 51.5 ($C^{f}$), 44.2 ($C^{d}$), 35.5 ($C^{g}$), 31.7 ($C^{j}$), 29.8 ($C^{b}$), 19.8 ($C^{i}$), 11.5 ($CH_3^{c}$), 10.6 ($CH_3^{a}$).

**ESI-MS** (+) (m/z): 327.1 $[M+H]^+$, calcd. for $C_{15}H_{26}N_4O_4$ = 326.2.

### 7.3.10. Pp-NAPamide (Partially Protected NAPamide)

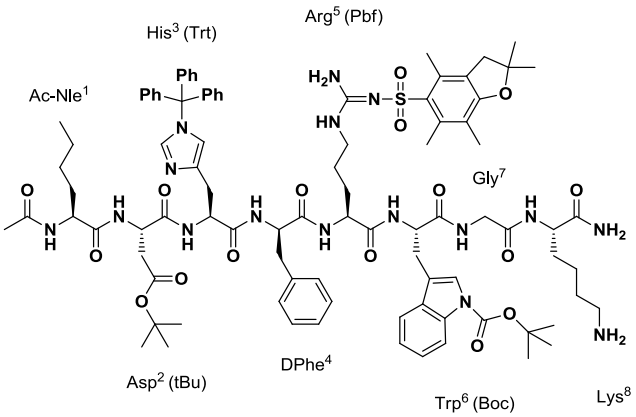


The fully protected α–MSH analog **NAPamide** ([Ac-Nle$^4$,Asp$^5$,*D*-Phe$^7$, Lys$^{11}$]α-MSH$_{4–11}$) was prepared by Fmoc-based Solid Phase Peptide Synthesis in a CEM 12-Channel Automated Peptide Synthesizer (scale 0.1 mM), using hyperacid sensitive Sieber Amide resin (0.177 g; substitution: 0.59 mmol/ g) and the following side chain protecting groups: Trt for His, Boc for Trp, *t*-Bu for Asp, Pbf for Arg, and Mtt for Lys.

After one-pot reaction under mild acidic conditions (1% TFA/$CH_2Cl_2$) for selective removal of the Mtt group and peptide cleavage from the resin (0.06 g), the solution was concentrated to 5% of the initial volume and a white solid was precipitated with water in an ice bath. The white solid was isolated by centrifugation and consecutively washed with water (3 times), 5% $NaHCO_3$ aqueous solution (2 times), water (3 times), 0.05 M $KHSO_4$ (2 times), water (6 times) and dried under vacuum. The crude peptide was dissolved in $CH_3CN$ and purified by semi-preparative HPLC (Method D, $t_R$ = 11.4 min). After evaporation of the solvent, the **Pp-NAPamide** was obtained as a white solid.

**RP-HPLC** (Method C): 99% ($t_R$ = 19.4 min).

**ESI-MS** (+) (m/z): 897 $[M+CH_3CN+2H]^{2+}$, calcd. for $C_{93}H_{120}N_{16}O_{16}S$ = 1748.9.

### 7.3.11. NAPamide

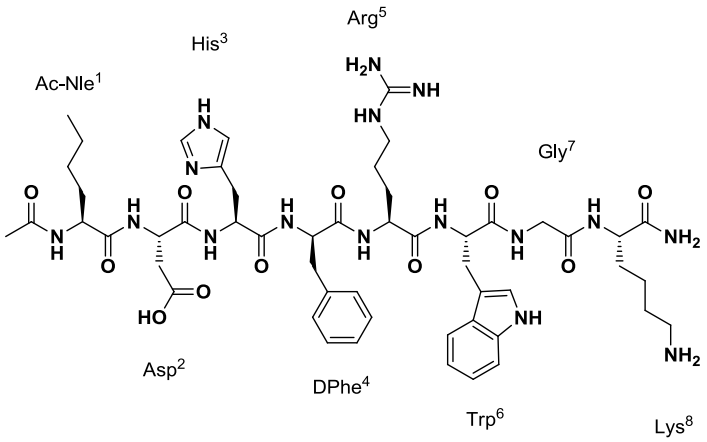


The fully protected α–MSH analog **NAPamide** ([Ac-Nle$^4$,Asp$^5$,*D*-Phe$^7$, Lys$^{11}$]α-MSH$_{4–11}$) was prepared as described in **7.3.10**. The peptide was cleaved from the resin (0.06 g; substitution: 0.59 mmol/g) by treatment with a mixture of 95% TFA, 2.5% TIS, and 2.5% $H_2O$ (5 mL) for 2 h. The cleavage solution was separated from the resin by filtration and concentrated under $N_2$. The crude peptide was precipitated and washed with ice-cold diethylether, vacuum-dried, and dissolved in water before lyophilization. After analytical purification and evaporation of solvents from the corresponding fractions, **NAPamide** was obtained as white solid.

**RP-HPLC** (Method E): 99% ($t_R$ = 9.4 min).

**ESI-MS** (+) (m/z): 1099.8 $[M+H]^+$, calcd. for $C_{52}H_{74}N_{16}O_{11}$ = 1098.6.

**Table 7.1**: $^{1}H$, $^{13}C$ and $^{15}N$ chemical shifts (ppm, from DSS) of **NAPamide** in $H_2O/D_2O$ 9:1 v/v at pH 2.5 and 5 ºC.

| Residue | $^{15}N$ | HN | $^{13}C_\alpha$ | $C_\alpha H$ | $^{13}C_\beta$ | $C_\beta H$ | Others |
|---|---|---|---|---|---|---|---|
| Ac | | | 24.3 | | | | |
| Nle[1] | 127.7 | 8.32 | 57.1 | 4.06 | 33.2 | 1.60 | $^{13}C_\gamma$ 29.8; $C_{\gamma\gamma'}H$ 1.18, 1.18; $^{13}C_\delta$ 24.4; $C_{\delta\delta'}H$ 1.23, 1.23; $^{13}C_\varepsilon$ 15.9; $C_\varepsilon H_3$ 0.82 |
| Asp[2] | 119.1 | 8.45 | 53.1 | 4.51 | 37.9 | 2.71, 2.78 | |
| His[3] | 118.7 | 8.41 | 55.3 | 4.60 | 29.0 | 3.01, 3.13 | $C_{\delta 2}H$ 7.06 $C_{\varepsilon 1}H$ 8.51 |
| DPhe[4] | 122.5 | 8.48 | 58.9 | 4.47 | 39.4 | 2.99 | $C_{\delta\delta'}H$ 7.23, 7.23 $C_{\varepsilon\varepsilon'}H$ 7.35, 7.35 |
| Arg[5] | 125.4 | 8.37 | 56.2 | 4.07 | 29.9 | 1.49, 1.31 | $^{13}C_\gamma$ 26.6; $C_{\gamma\gamma'}H$ 0.88, 0.96 $^{13}C_\delta$ 43.1; $C_{\delta\delta'}H$ 2.90, 2.90; $^{15}N_\varepsilon$ 84.7; $N_\varepsilon H$ 7.05 |
| Trp[6] | 121.7 | 8.24 | 57.5 | 4.65 | 29.4 | 3.25, 3.34 | $C_{\delta 1}H$ 7.24 $^{15}N_{\varepsilon 1}$ 129.4; $N_{\varepsilon 1}H$ 10.18; $C_{\varepsilon 3}H$ 7.61 $C_{\zeta 3}H$ 7.12 $C_{\eta 2}H$ 7.19 $C_{\zeta 2}H$ 7.44 |
| Gly[7] | 110.7 | 8.28 | 45.2 | 3.88, 3.81 | | | |
| Lys[8] | 121.4 | 8.20 | 56.0 | 4.24 | 33.1 | 1.70, 1.84 | $^{13}C_\gamma$ 24.8; $C_{\gamma\gamma'}H$ 1.37, 1.42; $^{13}C_\delta$ 29.1; $C_{\delta\delta'}H$ 1.65, 1.65; $^{13}C_\varepsilon$ 42.1; $C_{\varepsilon\varepsilon'}H$ 2.96, 2.96; $^{15}N_\zeta$ 69.3; $N_\zeta H$ 7.60 |

**Table 7.2**: $^{1}H$, $^{13}C$ and $^{15}N$ chemical shifts (ppm, from DSS) of **NAPamide** in $H_2O/D_2O$ 9:1 v/v at pH 2.5 and 25 ºC. "nd" stands for not determined.

| Residue | $^{15}N$ | HN | $^{13}C_\alpha$ | $C_\alpha H$ | $^{13}C_\beta$ | $C_\beta H$ | Others |
|---|---|---|---|---|---|---|---|
| Ac | | | 24.4 | 1.98 | | | |
| Nle[1] | 127.6 | 8.18 | 57.1 | 4.09 | 33.2 | 1.62 | $^{13}C_\gamma$ 29.8; $C_{\gamma\gamma'}H$ 1.20, 1.20; $^{13}C_\delta$ 24.3; $C_{\delta\delta'}H$ 1.23, 1.23; $^{13}C_\varepsilon$ 15.9; $C_\varepsilon H_3$ 0.82 |
| Asp[2] | 119.1 | 8.38 | 53.2 | 4.52 | 38.1 | 2.74, 2.76 | |
| His[3] | 118.6 | 8.30 | 55.3 | 4.60 | 29.0 | 3.05, 3.12 | $C_{\delta 2}H$ 7.06; $C_{\varepsilon 1}H$ 8.51; |
| DPhe[4] | 122.4 | 8.33 | 58.8 | 4.49 | 39.5 | 2.99 | $C_{\delta\delta'}H$ 7.22, 7.22; $C_{\varepsilon\varepsilon'}H$ 7.34, 7.34; $C_\zeta H$ 7.32; |
| Arg[5] | 124.8 | 8.18 | 56.2 | 4.10 | 30.1 | 1.50, 1.34 | $^{13}C_\gamma$ 26.6; $C_{\gamma\gamma'}H$ 0.96, 1.02 $^{13}C_\delta$ 43.2; $C_{\delta\delta'}H$ 2.92, 2.92; $^{15}N_\varepsilon$ 85.2; $N_\varepsilon H$ 6.99 |
| Trp[6] | 121.7 | 8.12 | nd | 4.67 | 29.5 | 3.24, 3.35 | $C_{\delta 1}H$ 7.25; $N_{\varepsilon 1}H$ 10.10; $C_{\varepsilon 3}H$ 7.62; $C_{\zeta 3}H$ 7.13; $C_{\eta 2}H$ 7.21; $C_{\zeta 2}H$ 7.45; |
| Gly[7] | 110.7 | 8.18 | 45.3 | 3.88, 3.83 | | | |
| Lys[8] | 121.4 | 8.07 | 56.0 | 4.25 | 33.1 | 1.69, 1.83 | $^{13}C_\gamma$ 24.7; $C_{\gamma\gamma'}H$ 1.38, 1.41; $^{13}C_\delta$ 29.0; $C_{\delta\delta'}H$ 1.66, 1.66; $^{13}C_\varepsilon$ 42.2 ; $C_{\varepsilon\varepsilon'}H$ 2.98, 2.98; $^{15}N_\zeta$ 69.3; |

### 7.3.12. L4

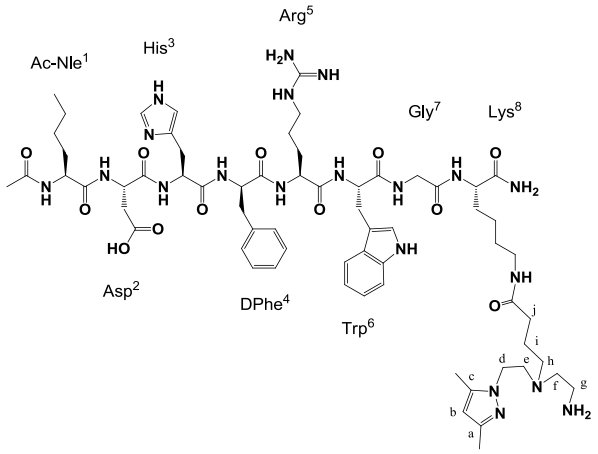


A solution of **Pp-NAPamide** (0.0060 g, 0.003 mmol) in DIPEA (20 μL)/DMF (250 μL) was added to the Boc-protected bifunctional chelator **L1-Boc** (0.0010 g, 0.003 mmol) preincubated for 30 min with HATU (0.0010 g, 0.003 mmol) in DMF. The pH was adjusted to 7-8 with DIPEA and the reaction mixture was left under stirring at room

temperature for 3 hours. The reaction mixture was purified by semi-preparative RP-HPLC (Method C). The HPLC fraction corresponding to the compound was collected and evaporated. The residue was deprotected with the standard cocktail mixture (95% TFA, 2.5% TIS, 2.5% $H_2O$) and the compound was precipitated with ice-cold diethylether. The precipitate was dried under nitrogen flow and dissolved in water before lyophilization. Yield: 42% (0.0150 g, 0.001 mmol; $\varepsilon_{Trp}$ (280 nm) = 5560 L $mol^{-1}$ $cm^{-1}$).

**RP-HPLC** (Method E): 99% ($t_R$ = 14.1 min).

**ESI-MS** (+) (m/z): 1349.8 $[M+H]^+$, calcd. for $C_{65}H_{96}N_{20}O_{12}$ = 1348.8.

**Table 7.3**: $^1H$, $^{13}C$ and $^{15}N$ chemical shifts (ppm, from DSS) of **L4** in $H_2O/D_2O$ 9:1 v/v at pH 2.5 and 5 ºC. "nd" stands for not determined.

| **Residue** | **$^{15}N$** | **HN** | **$^{13}C_\alpha$** | **$C_\alpha H$** | **$^{13}C_\beta$** | **$C_\beta H$** | **Others** |
|---|---|---|---|---|---|---|---|
| Ac | | | 24.4 | | | | |
| Nle[1] | 127.7 | 8.32 | 57.1 | 4.05 | 33.2 | 1.60 | $^{13}C_\gamma$ 29.9; $C_{\gamma\gamma'}H$ 1.18, 1.18; $^{13}C_\delta$ 24.4; $C_{\delta\delta'}H$ 1.23, 1.23; $^{13}C_\varepsilon$ 16.0; $C_\varepsilon H_3$ 0.82 |
| Asp[2] | 119.1 | 8.49 | 53.1 | 4.50 | 37.9 | 2.70, 2.77 | |
| His[3] | 118.7 | 8.39 | 55.3 | 4.59 | 29.0 | 2.99, 3.11 | $C_{\delta 2}H$ 7.05; $C_{\varepsilon 1}H$ 8.51; |
| DPhe[4] | 122.5 | 8.47 | 58.9 | 4.47 | 39.4 | 2.99 | $C_{\delta\delta'}H$ 7.22, 7.22; $C_{\varepsilon\varepsilon'}H$ 7.35, 7.35; $C_\zeta H$ 7.30; $^{13}C_\zeta$ 129.9 |
| Arg[5] | 125.3 | 8.38 | 56.2 | 4.05 | 29.9 | 1.32, 1.50 | $^{13}C_\gamma$ 26.7; $C_{\gamma\gamma'}H$ 0.87, 0.95 $^{13}C_\delta$ 43.1; $C_{\delta\delta'}H$ 2.90, 2.90; $^{15}N_\varepsilon$ 84.8; $N_\varepsilon H$ 7.05 |
| Trp[6] | 121.4 | 8.26 | 57.7 | 4.61 | 29.2 | 3.26, 3.35 | $C_{\delta 1}H$ 7.23; $^{15}N_{\varepsilon 1}$ 129.5; $N_{\varepsilon 1}H$ 10.18; $C_{\varepsilon 3}H$ 7.59; $C_{\zeta 3}H$ 7.10; $C_{\eta 2}H$ 7.17; $C_{\zeta 2}H$ 7.42; |
| Gly[7] | 110.3 | 8.29 | 45.3 | 3.88, 3.80 | | | |
| Lys[8] | 121.5 | 8.09 | 56.2 | 4.22 | 33.3 | 1.69, 1.82 | $^{13}C_\gamma$ 25.3; $C_{\gamma\gamma'}H$ 1.32, 1.37; $^{13}C_\delta$ 30.4; $C_{\delta\delta'}H$ 1.49, 1.49; $^{13}C_\varepsilon$ 42.1; $C_{\varepsilon\varepsilon'}H$ 3.14, 3.14; $^{15}N_\zeta$ 126.6; $N_\zeta H$ 8.15 |

| **BFC** | a | b | c | d | e | f | g | h | i | j |
|---|---|---|---|---|---|---|---|---|---|---|
| **$^1H$** | nd | 5.93 | nd | 4.27 | 3.49 | 3.41 | 3.35 | 3.07 | 1.85 | 2.29 |
| **$^{13}C$** | nd | nd | nd | 45.4 | 55.0 | 52.5 | 37.2 | 56.2 | 22.3 | 35.2 |

**Table 7.4**: $^{1}H$, $^{13}C$ and $^{15}N$ chemical shifts (ppm, from DSS) of **L4** in $H_2O/D_2O$ 9:1 v/v at pH 2.5 and 25 ºC). "nd" stands for not determined.

| **Residue** | **$^{15}N$** | **HN** | **$^{13}C_\alpha$** | **$C_\alpha H$** | **$^{13}C_\beta$** | **$C_\beta H$** | **Others** |
|---|---|---|---|---|---|---|---|
| Ac | | | 24.5 | | | | |
| Nle[1] | 127.6 | 8.18 | 57.1 | 4.09 | 33.2 | 1.62 | $^{13}C_\gamma$ 29.8; $C_{\gamma\gamma'}H$ 1.21, 1.21; $^{13}C_\delta$ 24.4; $C_{\delta\delta'}H$ 1.23, 1.23; $^{13}C_\varepsilon$ 15.9; $C_\varepsilon H_3$ 0.82 |
| Asp[2] | 119.0 | 8.38 | nd | 4.52 | 38.1 | 2.72, 2.78 | |
| His[3] | 118.5 | 8.29 | nd | 4.60 | 29.0 | 3.01, 3.14 | $C_{\delta 2}H$ 7.06; $C_{\varepsilon 1}H$ 8.51; |
| DPhe[4] | 122.4 | 8.32 | nd | 4.49 | 39.5 | 2.99 | $C_{\delta\delta'}H$ 7.22, 7.22; $C_{\varepsilon\varepsilon'}H$ 7.35, 7.35; $^{13}C_\varepsilon$ 131.6 $C_\zeta H$ 7.30; $^{13}C_\zeta$ 129.9 |
| Arg[5] | 124.7 | 8.19 | 56.2 | 4.09 | 30.1 | 1.35, 1.50 | $^{13}C_\gamma$ 26.7; $C_{\gamma\gamma'}H$ 0.97, 1.02 $^{13}C_\delta$ 43.2; $C_{\delta\delta'}H$ 2.90, 2.90; $^{15}N_\varepsilon$ 85.2; $N_\varepsilon H$ 7.00 |
| Trp[6] | 121.5 | 8.13 | nd | 4.64 | 29.4 | 3.25, 3.35 | $C_{\delta 1}H$ 7.24; $^{15}N_{\varepsilon 1}$ 129.5; $N_{\varepsilon 1}H$ 10.10; $C_{\varepsilon 3}H$ 7.60; $C_{\zeta 3}H$ 7.11; $C_{\eta 2}H$ 7.18; $C_{\zeta 2}H$ 7.44; |
| Gly[7] | 110.4 | 8.18 | 45.4 | 3.89, 3.84 | | | |
| Lys[8] | 121.6 | 7.98 | 56.2 | 4.23 | 33.3 | 1.66, 1.81 | $^{13}C_\gamma$ 25.3; $C_{\gamma\gamma'}H$ 1.32, 1.35; $^{13}C_\delta$ 30.5; $C_{\delta\delta'}H$ 1.48, 1.48; $^{13}C_\varepsilon$ 42.1; $C_{\varepsilon\varepsilon'}H$ 3.13, 3.13; $^{15}N_\zeta$ 126.5; $N_\zeta H$ 7.99 |

| **BFC** | a | b | c | d | e | f | g | h | i | j |
|---|---|---|---|---|---|---|---|---|---|---|
| **$^{1}H$** | nd | 5.94 | nd | 4.26 | 3.44 | 3.35 | 3.33 | 3.02 | 1.83 | 2.27 |
| **$^{13}C$** | nd | nd | nd | 45.9 | 55.4 | 52.9 | 37.8 | 56.5 | 22.9 | 35.5 |

### 7.3.13. L5

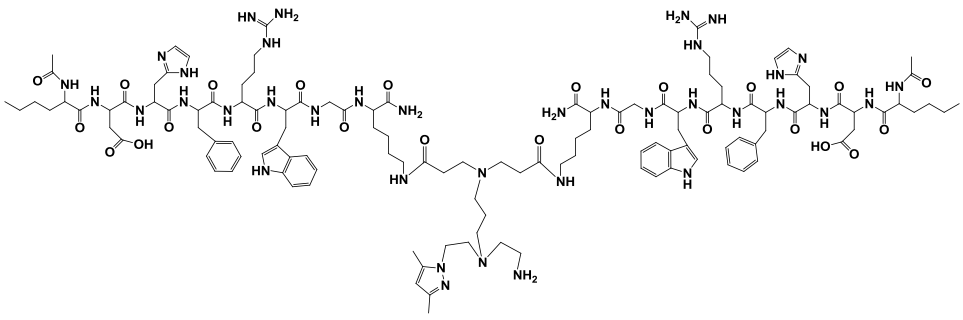

A solution of **Pp-NAPamide** (0.0090 g, 0.005 mmol) in DIPEA (20 μL)/DMF (250 μL) was added to the Boc-protected bifunctional chelator **L2-Boc** (0.0010 g, 0.002 mmol) preincubated for 30 min with HATU (0.0009 g, 0.0024 mmol) in DMF. The pH was adjusted to 7-8 with DIPEA and the reaction mixture was left under stirring at room

temperature for 3 hours. The reaction mixture was purified by semi-preparative RP-HPLC (Method C). The HPLC fraction corresponding to the compound was collected and evaporated. The residue was deprotected with the standard cocktail mixture (95% TFA, 2.5% TIS, 2.5% $H_2O$) and precipitated with ice-cold diethylether. The precipitate was dried under nitrogen flow and dissolved in water before lyophilization. Yield: 23% (0.0012 g, 0.001 mmol; $\varepsilon_{Trp}$ (280 nm) = 2 x 5560 L $mol^{-1}$ $cm^{-1}$).

**RP-HPLC** (Method E): 99% ($t_R$ = 15.3 min).

**ESI-MS** (+) (m/z): 849.5 $[M+3H]^{3+}$, calcd. for $C_{122}H_{177}N_{37}O_{24}$ = 2544.5.

### 7.3.14. L6

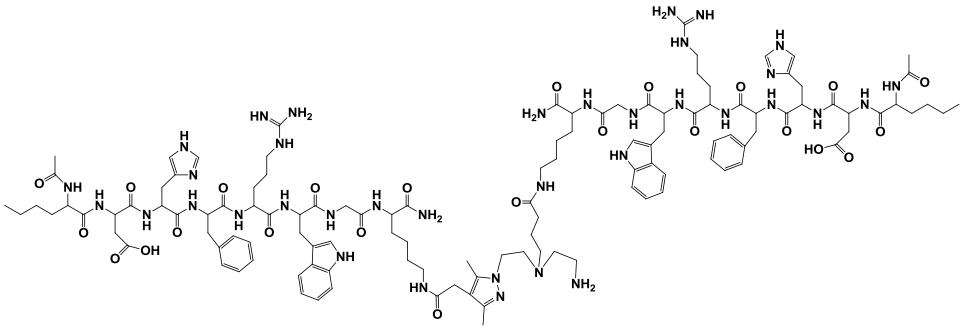

Following the methodology described in **7.3.13**, the conjugation of **Pp-NAPamide** to **L3-Boc** was achieved after three cycles of microwave irradiation (40W, 75 ºC, 5 min). The reaction mixture was purified by semi-preparative RP-HPLC (Method C). The HPLC fraction corresponding to the compound was collected and evaporated. The residue was deprotected with the standard cocktail mixture (95% TFA, 2.5% TIS, 2.5% $H_2O$) and precipitated with ice-cold diethylether. The precipitate was dried under nitrogen flow and dissolved in water before lyophilization. Yield: 14% (0.0008 g, 0.001 mmol; $\varepsilon_{Trp}$ (280 nm) = 2 x 5560 L $mol^{-1}$ $cm^{-1}$).

**RP-HPLC** (Method E): 99% ($t_R$ = 15.0 min).

**ESI-MS** (+) (m/z): 1244.6 $[M+2H]^{2+}$, calcd. for $C_{119}H_{170}N_{36}O_{24}$ = 2,487.3.

### 7.3.15. *fac*-[Re(CO)$_3$(κ$^3$-L1)]$^+$ (Re1)

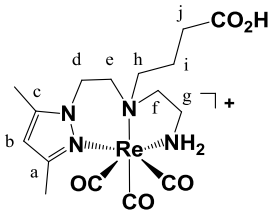


This compound was synthesized and characterized as previously reported.[162] Briefly, **L1** (0.0500 g, 0.130 mmol) reacted with the organometallic precursor [Re(CO)$_3$(H$_2$O)$_3$]Br (0.0500 g, 0.130 mmol) in refluxing water for 18 h. After evaporation of the solvent the resulting residue was purified by preparative RP-HPLC (Method B). Yield: 57% (0.0400 g, 0.070 mmol).

**IR** (KBr) (ν/cm$^{-1}$): 2033s and 1932s (C≡O) and 1684s (C=O).

**$^1$H-NMR** (300 MHz, D$_2$O): δ$_H$ (ppm) 6.01 (s, H$^b$, 1H), 5.07 (q br, NH, 1H), 4.33 (dd, CH$^d$, 1H), 4.07 (m, CH$^{d'}$, 1H), 3.62 (s br, NH, 1H), 3.50 (m, CH$^j$, 1H), 3.37 (m, CH$^{j'}$ + CH$^e$, 2H), 3.05 (s br, CH$^g$, 1H), 2.72 (d, CH$^f$ + CH$^{f'}$, 2H), 2.54 (t br, CH$^{e'}$, 1H), 2.37 (m br, CH$^{g'}$, 1H), 2.33 (t, CH$^h$ + CH$^{h'}$, 2H), 2.24 (s, CH$_3{}^a$, 3H), 2.14 (s, CH$_3{}^c$, 3H), 2.04 (m, CH$^i$, 1H), 1.88 (m, 1H, CH$^{i'}$).

**$^{13}$C-NMR** (75 MHz, D$_2$O): δ$_C$ (ppm) 196.6 (C≡O), 196.2 (C≡O), 196.1 (C≡O), 179.8 (C=O), 155.7 (C$^c$), 146.3 (C$^a$), 109.8 (C$^b$), 67.8 (C$^h$), 63.2 (C$^f$), 54.5 (C$^e$), 49.1 (C$^d$), 44.2 (C$^g$), 33.1 (C$^j$), 21.5 (C$^i$), 17.3 (CH$_3{}^c$), 12.9 (CH$_3{}^a$).

**RP-HPLC** (Method A): 99% (t$_R$ = 18.3 min).

**ESI-MS** (+) (m/z): 542.6 [M+H]$^+$, calcd. for C$_{16}$H$_{27}$N$_4$O$_5$Re = 541.6.

### 7.3.16. *fac*-[Re(CO)$_3$(κ$^3$-L2)]$^+$ (Re2)

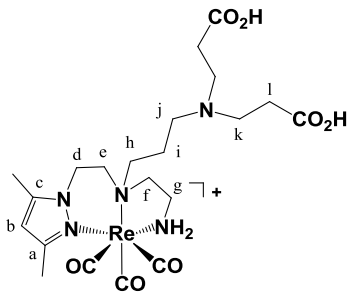


The complex was prepared according to the methodology described in **7.3.15**. Briefly, **L2-Me$_2$** (0.0500 g, 0.122 mmol) reacted with the organometallic precursor [Re(CO)$_3$(H$_2$O)$_3$]Br (0.0500 g, 0.130 mmol) in refluxing water for 18 h. After

evaporation of the solvent the resulting residue was purified by preparative RP-HPLC (Method B). The complex **Re2** was isolated as colorless clear oil. Yield: 50 % (0.0400 g, 0.06 mmol).

**IR** (KBr) ($\nu$/cm$^{-1}$): 2033s and 1932s (C≡O) and 1684s (C=O).

**$^{1}$H-NMR** (300 MHz, $D_2O$): $\delta_H$ (ppm) 6.07 (s, $H^b$, 1H), 5.12 (q br, NH, 1H), 4.39 (dd, $CH^d$, 1H), 4.17 (m, $CH^{d'}$, 1H), 3.70 (q br, NH, 1H), 3.59 (dd, $CH^h$, 1H), 3.47 (t, $CH^k$, 4H), 3.36 (m, $CH^{h'}$, 1H), 3.31 (dd, $CH^e$, 1H), 3.22 (t, $CH^j$, 2H), 3.08 (dd, $CH^g$, 1H), 2.85 (t, $CH^l$, 4H), 2.78 (s, $CH^f$, 2H) , 2.69 (m, $CH^{g'+e'}$, 2H), 2.48 (m, $CH^i$, 1H), 2.30 (s, $CH_3^{a+i'}$, 4H), 2.19 (s, $CH_3^c$, 3H).

**$^{13}$C-NMR** (75.3 MHz, $D_2O$): $\delta_C$ (ppm) 197.1 (C≡O), 196.6 (C≡O), 195.4 (C≡O), 176.9 (C=O), 156.5 ($C^c$), 147.1 ($C^a$), 110.5 ($C^b$), 65.3 ($C^h$), 63.8 ($C^f$), 55.4 ($C^e$), 53.7 ($C^h$), 52.2 ($C^k$), 49.6 ($C^j$), 44.9 ($C^g$), 30.9 ($C^l$), 21.9 ($C^i$), 17.9 ($CH_3^c$), 12.5 ($CH_3^a$).

**RP-HPLC** (220nm, Method A): 99% ($t_R$ = 15.9 min).

**ESI-MS** (+) (m/z): 658.3 $[M+H]^+$, calcd. for $C_{21}H_{36}N_5O_7Re$ = 657.2.

### 7.3.17. *fac*-[Re(CO)$_3$($\kappa^3$-L3)]$^+$ (Re3)

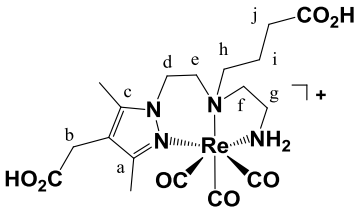


The complex was prepared according to the methodology described in **7.3.15**. Briefly, **L3** (0.0400 g, 0.122 mmol) reacted with the organometallic precursor $[Re(CO)_3(H_2O)_3]Br$ (0.0500 g, 0.130 mmol) in refluxing water for 18 h. After evaporation of the solvent the resulting residue was purified by preparative RP-HPLC (Method B). The complex **Re3** was isolated as colorless clear oil. Yield: 82 % (0.060 g, 0.101 mmol, calcd. for $C_{18}H_{29}N_4O_7Re$·TFA).

**IR** (KBr) ($\nu$/cm$^{-1}$): 2028s and 1927s (C≡O) and 1686s (C=O).

**$^{1}$H-NMR** (300 MHz, $D_2O$): $\delta_H$ (ppm) 5.03 (br m, NH, 1H), 4.33 (dd, $CH^d$, 1H), 4.07 (dd, $CH^{d'}$, 1H), 3.61 (m, NH, 1H), 3.46 (m, $CH^j$, 1H), 3.33 (s, $CH_2^b$, 2H), 3.33 (m, $CH^e$ + $CH^{j'}$, 2H), 3.03 (br dd, $CH^g$, 1H), 2.73 (br m, $CH_2^f$, 2H), 2.53 (m, $CH_2^{e'}$, 1H), 2.40 (m, $CH^{g'}$, 1H), 2.29 (t, $CH^h$, 2H), 2.18 (s, $CH_3^a$, 3H), 2.07 (s, $CH_3^c$, 3H), 1.96 (m, $CH^i$, 1H), 1.85 (m, $CH^{i'}$, 1H).

**$^{13}$C-NMR** (75.3 MHz, $D_2O$): $\delta_C$ (ppm) 196.3 (C≡O), 195.8 (C≡O), 194.8 (C≡O), 179.2 (C=O), 177.6 (C=O), 164.8 (q, $CF_3COO^-$), 154.4 ($C^c$), 144.7 ($C^a$), 118.2 (q, $CF_3COO^-$), 113.38 (pz), 67.4 ($C^h$), 62.9 ($C^f$), 54.2 ($C^e$), 49.1 ($C^d$), 44.0 ($C^g$), 32.6 ($C^j$), 30.5 ($C^b$), 21.1 ($C^i$), 15.4 ($CH_3{}^c$), 11,2 ($CH_3{}^a$).

**RP-HPLC** (Method A): 99% ($t_R$ = 17.5 min).

**ESI-MS** (+) (m/z): 601.5 $[M+H]^+$, calcd. for $C_{18}H_{29}N_4O_7Re$ = 599.6.

### 7.3.18. Re4

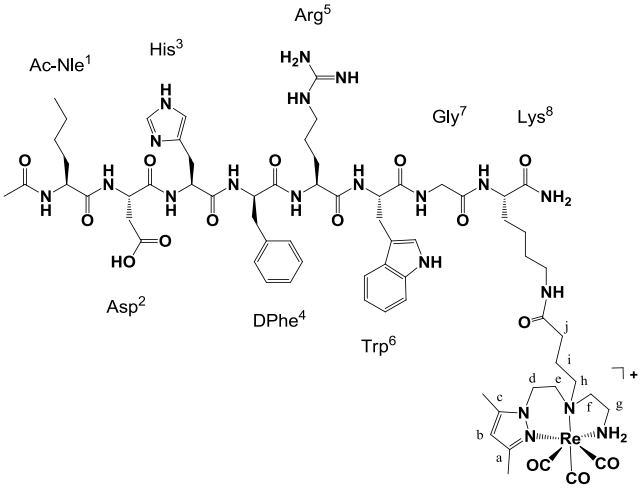


The precursors **Pp-NAPmide** and **Re1** were used to prepare the metallopeptide **Re4**, following the same conjugation strategy described for **L4**. The reaction mixture was purified by semi-preparative RP-HPLC (Method C). The HPLC fraction corresponding to the compound was collected and evaporated. The residue was deprotected with the standard cocktail mixture (95% TFA, 2.5% TIS, 2.5% $H_2O$) and the compound was precipitated with ice-cold diethylether. The precipitate was dried under nitrogen flow and dissolved in water before lyophilization. Yield: 55% (0.0015 g, 0.0009 mmol; $\varepsilon_{Trp}$ (280 nm) = 5560 L $mol^{-1}$ $cm^{-1}$).

**RP-HPLC** (Method E): 99% ($t_R$ = 15.3 min).

**ESI-MS** (+) (m/z): 810.4 $[M+2H]^{2+}$, calcd. for $C_{68}H_{96}N_{20}O_{15}Re$ = 1622.7.

**Table 7.5**: $^{1}H$, $^{13}C$ and $^{15}N$ chemical shifts (ppm, from DSS) for **Re4** in $H_2O/D_2O$ 9:1 v/v at pH 2.5 and 5 ºC. "nd" stands for not determined.

| **Residue** | **$^{15}N$** | **HN** | **$^{13}C_\alpha$** | **$C_\alpha H$** | **$^{13}C_\beta$** | **$C_\beta H$** | **Others** |
|---|---|---|---|---|---|---|---|
| Ac | | | 24.3 | | | | |
| Nle[1] | 127.7 | 8.32 | 57.1 | 4.05 | 33.2 | 1.60 | $^{13}C_\gamma$ 29.8; $C_{\gamma\gamma'}H$ 1.18, 1.18; $^{13}C_\delta$ 24.4; $C_{\delta\delta'}H$ 1.22, 1.22; $^{13}C_\varepsilon$ 15.9; $C_\varepsilon H_3$ 0.82 |
| Asp[2] | 119.0 | 8.49 | 53.0 | 4.50 | 37.8 | 2.71, 2.77 | |
| His[3] | 118.6 | 8.40 | 55.3 | 4.59 | 29.0 | 2.99, 3.11 | $C_{\delta 2}H$ 7.05; $C_{\varepsilon 1}H$ 8.51; |
| DPhe[4] | 122.5 | 8.44 | 58.9 | 4.46 | 39.4 | 2.99 | $C_{\delta\delta'}H$ 7.21, 7.21; $C_{\varepsilon\varepsilon'}H$ 7.33, 7.33; $C_\zeta H$ 7.30; |
| Arg[5] | 125.1 | 8.35 | 56.2 | 4.05 | 30.0 | 1.31, 1.50 | $^{13}C_\gamma$ 26.7; $C_{\gamma\gamma'}H$ 0.87, 0.95 $^{13}C_\delta$ 43.1; $C_{\delta\delta'}H$ 2.89, 2.89; $^{15}N_\varepsilon$ 84.7; $N_\varepsilon H$ 7.05 |
| Trp[6] | 121.2 | 8.22 | 57.6 | 4.60 | 29.2 | 3.25, 3.32 | $C_{\delta 1}H$ 7.22; $^{15}N_{\varepsilon 1}$ 129.4; $N_{\varepsilon 1}H$ 10.19; $C_{\varepsilon 3}H$ 7.59; $C_{\zeta 3}H$ 7.10; $C_{\eta 2}H$ 7.17; $C_{\zeta 2}H$ 7.43; |
| Gly[7] | 110.1 | 8.26 | 45.4 | 3.88, 3.81 | | | |
| Lys[8] | 121.4 | 8.07 | 56.2 | 4.23 | 33.3 | 1.70, 1.85 | $^{13}C_\gamma$ 25.4; $C_{\gamma\gamma'}H$ 1.36, 1.40; $^{13}C_\delta$ 30.4; $C_{\delta\delta'}H$ 1.53, 1.53; $^{13}C_\varepsilon$ 42.0; $C_{\varepsilon\varepsilon'}H$ 3.21, 3.21; $^{15}N_\zeta$ 127.8; $N_\zeta H$ 8.27 |

| **BFC** | a | b | c | d | e | f | g | h | i | j |
|---|---|---|---|---|---|---|---|---|---|---|
| **$^{1}H$** | nd | 5.99 | nd | 4.31/ 4.03 | 3.30/ 2.60 | 2.78 | 2.44/ 3.12 | 3.36/ 3.54 | 1.96/ 2.11 | 2.29 |
| **$^{13}C$** | nd | nd | nd | nd | 54.9 | 63.6 | 44.8 | 68.1 | 22.8 | 35.5 |

**Table 7.6**: $^{1}H$, $^{13}C$ and $^{15}N$ chemical shifts (ppm, from DSS) for **Re4** in $H_2O/D_2O$ 9:1 v/v at pH 2.5 and 25 ºC. "nd" stands for not determined.

| **Residue** | **$^{15}N$** | **HN** | **$^{13}C_\alpha$** | **$C_\alpha H$** | **$^{13}C_\beta$** | **$C_\beta H$** | **Others** |
|---|---|---|---|---|---|---|---|
| Ac | | | 24.7 | | | | |
| Nle[1] | 127.6 | 8.18 | 57.3 | 4.09 | 33.5 | 1.62 | $^{13}C_\gamma$ 30.0; $C_{\gamma\gamma}$,H 1.19, 1.19; $^{13}C_\delta$ 24.6; $C_{\delta\delta}$,H 1.22, 1.22; $^{13}C_\varepsilon$ 16.1; $C_\varepsilon H_3$ 0.82 |
| Asp[2] | 118.9 | 8.38 | 53.4 | 4.52 | 38.3 | 2.71, 2.78 | |
| His[3] | 118.5 | 8.29 | nd | 4.59 | 29.2 | 3.00, 3.13 | $C_{\delta 2}H$ 7.06; $C_{\varepsilon 1}H$ 8.51; |
| DPhe[4] | 122.3 | 8.29 | 58.9 | 4.48 | 39.8 | 2.98 | $C_{\delta\delta}$,H 7.21, 7.21; $C_{\varepsilon\varepsilon}$,H 7.34, 7.34; $C_\zeta H$ 7.30; |
| Arg[5] | 124.6 | 8.16 | 56.5 | 4.08 | 30.4 | 1.34, 1.50 | $^{13}C_\gamma$ 26.9; $C_{\gamma\gamma}$,H 0.96, 1.00 $^{13}C_\delta$ 43.4; $C_{\delta\delta}$,H 2.91, 2.91; $^{15}N_\varepsilon$ 85.1; $N_\varepsilon H$ 7.00 |
| Trp[6] | 121.4 | 8.10 | nd | 4.62 | 29.6 | 3.24, 3.32 | $C_{\delta 1}H$ 7.22; $^{15}N_{\varepsilon 1}$ 129.4; $C_{\varepsilon 3}H$ 7.59; $C_{\zeta 3}H$ 7.11; $C_{\eta 2}H$ 7.19; $C_{\zeta 2}H$ 7.44; |
| Gly[7] | 110.2 | 8.15 | 45.7 | 3.87, 3.84 | | | |
| Lys[8] | 121.5 | 7.95 | 56.5 | 4.24 | 33.6 | 1.68, 1.83 | $^{13}C_\gamma$ 25.6; $C_{\gamma\gamma}$,H 1.35, 1.39; $^{13}C_\delta$ 30.8; $C_{\delta\delta}$,H 1.53, 1.53; $^{13}C_\varepsilon$ 42.3; $C_{\varepsilon\varepsilon}$,H 3.20, 3.20; $^{15}N_\zeta$ 127.5; $N_\zeta H$ 8.10 |

| **BFC** | a | b | c | d | e | f | g | h | i | j |
|---|---|---|---|---|---|---|---|---|---|---|
| **$^{1}H$** | nd | 6.03 | nd | 4.33/ 4.03 | 3.31/ 2.60 | 2.79 | 2.45/ 3.14 | 3.36/ 3.52 | 1.97/ 2.12 | 2.29 |
| **$^{13}C$** | nd | nd | nd | 49.6 | 55.4 | 64.0 | 45.1 | 68.5 | 23.2 | 35.7 |

### 7.3.19. Re5

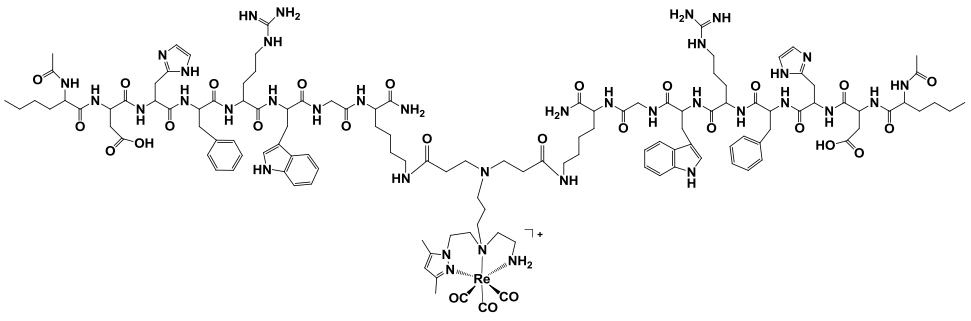

The precursors **Pp-NAPmide** and **Re2** were used to prepare the metallopeptide **Re5**, following the same conjugation strategy described for **L5**. The reaction mixture was purified by semi-preparative RP-HPLC (Method C). The HPLC fraction corresponding to the compound was collected and evaporated. The residue was deprotected with the standard cocktail mixture (95% TFA, 2.5% TIS, 2.5% $H_2O$) and the compound was precipitated with ice-cold diethylether. The precipitate was dried under nitrogen flow and dissolved in water before lyophilization. Yield: 18% (0.0007 g, 0.0002 mmol; $\varepsilon_{Trp}$ (280 nm) = 2 x 5560 L $mol^{-1}$ $cm^{-1}$).

**RP-HPLC** (Method E): 99% ($t_R$ = 15.6 min).

**ESI-MS** (+) (m/z): 705.0 $[M+3H]^{3+}$, calcd. for $C_{125}H_{177}N_{37}O_{27}Re$ = 2818.3.

### 7.3.20. Re6

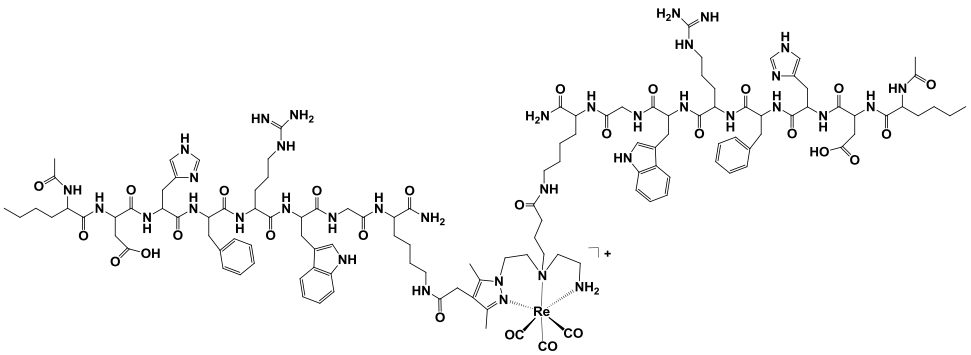

The precursors **Pp-NAPmide** and **Re3** were used to prepare the metallopeptide **Re6**, following the same conjugation strategy described for **L6**. The reaction mixture was purified by semi-preparative RP-HPLC (Method C). The HPLC fraction corresponding to the compound was collected and evaporated. The residue was deprotected with the

standard cocktail mixture (95% TFA, 2.5% TIS, 2.5% $H_2O$) and the compound was precipitated with ice-cold diethylether. The precipitate was dried under nitrogen flow and dissolved in water before lyophilization. Yield: 15% (0.0006 g, 0.0001 mmol; $\varepsilon_{Trp}$ (280 nm) = 2 x 5560 L $mol^{-1}$ $cm^{-1}$).

**RP-HPLC** (Method E): 99% ($t_R$ = 15.5 min).

**ESI-MS** (+) (m/z): 920.6 $[M+3H]^{3+}$, calcd. for $C_{122}H_{170}N_{36}O_{27}Re$ = 2761.3.

### 7.3.21. General method for the preparation of Tc4 – Tc6

In a capped nitrogen purged glass vial, 100 μL of a 5 x $10^{-4}$ M solution of the ligands **L4** – **L6** were added to a solution of *fac*-$[^{99m}Tc(CO)_3(H_2O)_3]^+$ (900 μL, 37 – 74 MBq) in 0.01 M PBS, pH 7.4. The vial was incubated at 90 °C for 30 min and the resulting complexes were analyzed by RP-HPLC (Method E) using the same method of the rhenium surrogates. Retention times: 16.0 min (**Tc4**), 15.6 min (**Tc5**) and 15.5 min (**Tc6**).

### 7.3.22. SNBA-$MSH_{hex}$

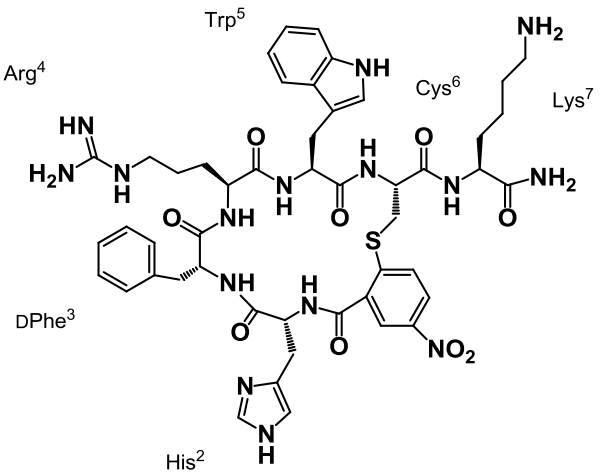


The peptide **SNBA-$MSH_{hex}$** was prepared following a modified procedure from the literature.[143] Briefly, the peptide linear sequence $NH_2$-His(Trt)-DPhe-Arg(Pbf)-Trp(Boc)-Cys(Trt)-Lys(Boc)-$NH_2$ was assembled to the MBHA rink Amide resin (0.18 g; substitution: 0.59 mmol/g) by Fmoc-based Solid Phase Peptide Synthesis in a CEM 12-Channel Automated Peptide Synthesizer (scale: 0.1 mM) using HOBT/HBTU as coupling agents. As previously reported, the linear sequence was capped with fluoronitrobenzoic acid and, before the cyclization step, the S-Trt group of the Cys

residue was removed with dilute TFA (5% in $CH_2Cl_2$) without cleavage of the peptide from the resin (0.1 g). The cyclization step was carried out by treating the supported peptides with 5 equiv. $K_2CO_3$ in DMF at 25 ºC with gentle shaking for 36 h. The peptide-resin was washed with DMF (2x), water (3x), DMF (3x), water (2x), $CH_3OH$ (3x), $CH_2Cl_2$ (3x), and then vacuum dried. The peptides were cleaved from the resin by treatment with a mixture of 95 % TFA, 2.5 % TIS and 2.5 % $H_2O$ (5 mL) for 2 h. The cleavage solution was separated from the resin by filtration and concentrated under $N_2$. The crude peptide was precipitated and washed with ice-cold diethylether, vacuum dried and dissolved in $H_2O$ before lyophilization. After semi-preparative purification (Method G) and evaporation of solvents from the corresponding fractions, **SNBA-MSH$_{hex}$** was obtained as yellow solid.

**RP-HPLC** (Method G): 99 % ($t_R$ = 9.1 min).

**ESI-MS** (+) (m/z): 1022.4 $[M+H]^+$, calcd. for $C_{48}H_{59}N_{15}O_9S$ = 1021.5.

**Table 7.7**: $^{1}H$, $^{13}C$ and $^{15}N$ chemical shifts (ppm, from DSS) for **SNBA-MSH$_{hex}$** in $H_2O/D_2O$ 9:1 v/v at pH 2.5 and 5 ºC.

| **Residue** | **$^{15}N$** | **NH** | **$^{13}C_\alpha$** | **$C_\alpha H$** | **$^{13}C_\beta$** | **$C_\beta H$** | **Others** |
|---|---|---|---|---|---|---|---|
| pNO2-BenzAcid[1] | ---- | ----- | ----- | ----- | ----- | ----- | $C_{\delta 1}H$ 8.16; $C_{\delta 2}H$ 7.75; $C_{\varepsilon 2}H$ 8.38; |
| His[2] | 126.9 | 9.30 | nd | 4.94 | 28.9 | 3.32, 3.38 | $C_{\delta 2}H$ 7.32; $C_{\varepsilon 1}H$ 8.59; |
| DPhe[3] | 125.7 | 8.88 | 59.3 | 4.44 | 39.4 | 3.04, 3.10 | $C_{\delta\delta'}H$ 7.24, 7.24; $C_{\varepsilon\varepsilon'}H$ 7.37, 7.37; $C_{\zeta}H$ 7.32; |
| Arg[4] | 124.3 | 8.26 | 56.2 | 4.04 | 29.7 | 1.11, 1.39 | $^{13}C_{\gamma}$ 26.2; $C_{\gamma\gamma'}H$ 0.49, 0.77; $^{13}C_{\delta}$ 43.1; $C_{\delta}H$ 2.76, 2.76; $^{15}N_{\varepsilon}$ 84.7; $N_{\varepsilon}H$ 6.95; $N_{\eta}H$ 6.54, 6.79; |
| Trp[5] | 119.5 | 8.10 | 57.6 | 4.58 | 28.5 | 3.27, 3.27 | $C_{\delta 1}H$ 7.22; $^{15}N_{\varepsilon 1}$ 129.3; $N_{\varepsilon 1}H$ 10.11; $C_{\varepsilon 3}H$ 7.54; $C_{\zeta 3}H$ 7.08; $C_{\eta 2}H$ 7.17; $C_{\zeta 2}H$ 7.37; |
| Cys[6] | 118.2 | 7.80 | 54.1 | 4.57 | 35.2 | 3.26, 3.58 | |
| Lys[7] | 123.5 | 8.44 | 56.2 | 4.24 | 33.1 | 1.76, 1.84 | $^{13}C_{\gamma}$24.8; $C_{\gamma\gamma'}H$ 1.42, 1.42; $^{13}C_{\delta}$ 29.1; $C_{\delta\delta'}H$ 1.67, 1.67; $^{13}C_{\varepsilon}$ 42.1; $C_{\varepsilon\varepsilon'}H$ 2.97, 2.97; $^{15}N_{\zeta}$ 69.3; $N_{\zeta}H_3$ 7.58; |
| $CONH_2$ | 109.1 | 7.26, 7.73 | | | | | |

**Table 7.8**: $^{1}H$, $^{13}C$ and $^{15}N$ chemical shifts (ppm, from DSS) for **SNBA-MSH$_{hex}$** in $H_2O/D_2O$ 9:1 v/v at pH 2.5 and 25 ºC. "nd" stands for not determined.

| Residue | $^{15}N$ | NH | $^{13}C_\alpha$ | $C_\alpha H$ | $^{13}C_\beta$ | $C_\beta H$ | Others |
|---|---|---|---|---|---|---|---|
| pNO2-BenzAcid 1 | ---- | ----- | ----- | ----- | ----- | ----- | $C_{\delta1}H$ 8.14; $C_{\delta2}H$ 7.73; $C_{\varepsilon2}H$ 8.38; |
| His[2] | 126.9 | 9.12 | nd | 4.96 | 28.9 | 3.32, 3.38 | $C_{\delta2}H$ 7.32; $C_{\varepsilon1}H$ 8.61; |
| DPhe[3] | 125.5 | 8.71 | nd | 4.47 | 39.8 | 3.04, 3.08 | $C_{\delta\delta'}H$ 7.25, 7.25; $C_{\varepsilon\varepsilon'}H$ 7.38, 7.38; $C_\zeta H$ 7.32; |
| Arg[4] | 124.3 | 8.11 | 56.6 | 4.02 | 30.0 | 1.12, 1.38 | $^{13}C_\gamma$ 26.5; $C_{\gamma\gamma'}H$ 0.56, 0.79; $^{13}C_\delta$ 43.4; $C_\delta H$ 2.78, 2.78; $^{15}N_\varepsilon$ 85.2; $N_\varepsilon H$ 6.90; $N_\eta H$ 6.54, 6.61; |
| Trp[5] | 119.4 | 7.98 | nd | 4.59 | 28.5 | 3.27, 3.27 | $C_{\delta1}H$ 7.22; $^{15}N_{\varepsilon1}$ 129.4; $N_{\varepsilon1}H$ 10.04; $C_{\varepsilon3}H$ 7.55; $C_{\zeta3}H$ 7.08; $C_{\eta2}H$ 7.17; $C_{\zeta2}H$ 7.37; |
| Cys[6] | 118.0 | 7.70 | 54.6 | 4.58 | 35.7 | 3.28, 3.53 | |
| Lys[7] | 123.2 | 8.27 | 56.4 | 4.26 | 33.4 | 1.74, 1.83 | $^{13}C_\gamma$ 25.0; $C_{\gamma\gamma'}H$ 1.40, 1.40; $^{13}C_\delta$ 29.3; $C_{\delta\delta'}H$ 1.66, 1.66; $^{13}C_\varepsilon$ 42.4; $C_{\varepsilon\varepsilon'}H$ 2.96, 2.96; $^{15}N_\zeta$ 69.6; $N_\zeta H_3$ 7.50; |
| $CONH_2$ | 108.8 | 7.14, 7.60 | | | | | |

### 7.3.23. NNBA-MSH$_{hex}$

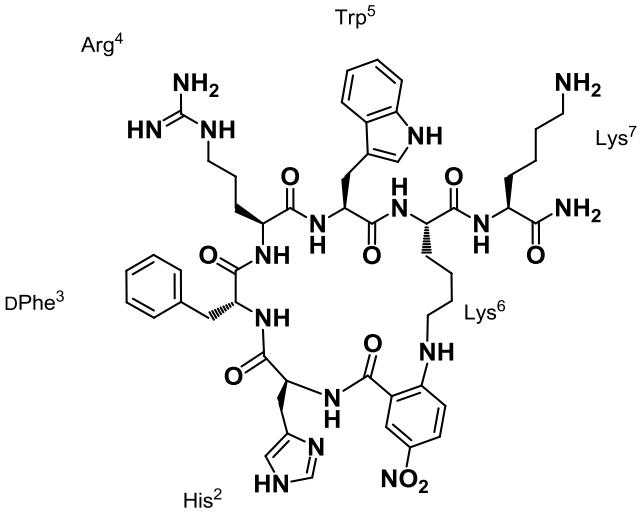


The cyclic peptide **NNBA-MSH$_{hex}$** was prepared according to the methodology described for **SNBA-MSH$_{hex}$**, replacing the residue Cys(Trt) by Lys(ivDde) in the linear sequence. Briefly, the N-terminus of the linear peptide was capped with fluoronitrobenzoic acid and the N-ivDde group of the Lys residue was selectively removed with 2% hidrazine in DMF without cleavage of the peptide from the resin (0.1 g). The cyclization step was carried out by treating the supported peptides with 5 equiv. $K_2CO_3$ in DMF at 25 ºC with gentle shaking for 36 h. The peptide-resin was washed with DMF (2x), $H_2O$ (3x), DMF (3x), $H_2O$ (2x), $CH_3OH$ (3x), $CH_2Cl_2$ (3x), and then vacuum dried. The peptides were cleaved from the resin by treatment with a mixture of 95% TFA, 2.5% TIS and 2.5% $H_2O$ (5 mL) for 2 h. The cleavage solution was separated from the resin by filtration and concentrated under $N_2$. The crude peptide was precipitated and washed with ice-cold diethylether, vacuum dried and dissolved in $H_2O$ before lyophilization. After semi-preparative purification (Method G) and evaporation of solvents from the corresponding fractions, **NNBA-MSH$_{hex}$** was obtained as a pale green solid.

**RP-HPLC** (Method G): 99% ($t_R$ = 9.3 min).

**ESI-MS** (+) (m/z): 1047.5 $[M+H]^+$, calcd. for $C_{51}H_{66}N_{16}O_9$ = 1046.5.

**Table 7.9**: $^{1}H$, $^{13}C$ and $^{15}N$ chemical shifts (ppm, from DSS) for **NNBA-MSH$_{hex}$** in $H_2O/D_2O$ 9:1 v/v at pH 2.5 and 25 ºC.

| Residue | $^{15}N$ | HN | $^{13}C_\alpha$ | $C_\alpha H$ | $^{13}C_\beta$ | $C_\beta H$ | Others |
|---|---|---|---|---|---|---|---|
| pNO2-BenzAcid[1] | ---- | ----- | ----- | ----- | ----- | ----- | $C_{\delta1}H$ 8.42; $C_{\delta2}H$ 6.85; $C_{\varepsilon2}H$ 8.12 |
| His[2] | 119.5 | 8.72 | nd | 4.68 | 28.8 | 3.23, 3.23 | $C_{\delta2}H$ 7.15; $C_{\varepsilon1}H$ 8.36 |
| DPhe[3] | 125.6 | 8.93 | 59.1 | 4.51 | 39.2 | 2.75, 3.08 | $C_{\delta\delta'}H$ 7.19, 7.19; $C_{\varepsilon\varepsilon'}H$ 7.36, 7.36; $C_\zeta H$ nd |
| Arg[4] | 121.2 | 8.20 | 55.5 | 4.42 | 31.3 | 1.48, 1.69 | $^{13}C_\gamma$ 27.0; $C_\gamma H$ 1.02, 1.22; $^{13}C_\delta$ 43.7; $C_\delta H$ 2.48, 2.82; $^{15}N_\varepsilon$ 84.6; $N_\varepsilon H$ 6.90 $N_\eta H$ 6.52 |
| Trp[5] | 123.0 | 8.37 | 59.0 | 4.38 | 29.1 | 3.03, 3.26 | $C_{\delta1}H$ 7.04; $^{15}N_{\varepsilon1}$ 129.4; $N_{\varepsilon1}H$ 10.00; $C_{\varepsilon3}H$ 7.52; $C_{\zeta3}H$ 7.11; $C_{\eta2}H$ 7.17; $C_{\zeta2}H$ 7.36 |
| Lys[6] | 122.2 | 8.01 | 56.7 | 4.21 | 34.1 | 1.66, 1.80 | $^{13}C_\gamma$ 26.4; $C_\gamma H$ 1.37, 1.45; $^{13}C_\delta$ 30.6; $C_{\delta\delta'}H$ 1.62, 1.67; $^{13}C_\varepsilon$ 45.9; $C_{\varepsilon\varepsilon'}H$ 3.30, 3.36; $^{15}N_\zeta$ nd; $N_\zeta H$ nd |
| Lys[7] | 121.3 | 7.91 | 56.5 | 4.06 | 33.2 | 1.68, 1.77 | $^{13}C_\gamma$ 25.0; $C_\gamma H$ 1.40, 1.40; $^{13}C_\delta$ 29.4; $C_{\delta\delta'}H$ 1.66, 1.66; $^{13}C_\varepsilon$ 42.4; $C_{\varepsilon\varepsilon'}H$ 2.99, 2.99; $^{15}N_\zeta$ 68.8; $N_\zeta H_3$ 7.54 |
| $CONH_2$ | 108.2 | 7.07, 7.48 | | | | | |

### 7.3.24. L7

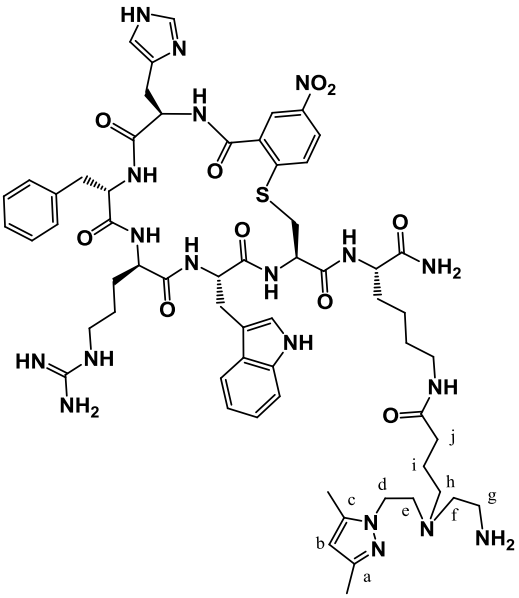


A solution of **NNBA-MSH$_{hex}$** (0.002 g, 0.002 mmol) in DIPEA (20 μL)/DMF (250 μL) was added to the Boc-protected bifunctional chelator **L1-Boc** (0.001g; 0.0027 mmol) preincubated for 30 min with HATU (0.0013 g, 0.0032 mmol) in DMF. The pH was adjusted to 7-8 with DIPEA and the reaction mixture was left under stirring at room temperature for 3 hours. The reaction mixture was purified by semi-preparative RP-HPLC (Method G). After evaporation of the solvent, the compound was deprotected with the standard cocktail mixture (95% TFA, 2.5% TIS, 2.5% $H_2O$) and precipitated with ice-cold diethylether. The precipitate was dried under nitrogen flow and dissolved in water before lyophilization. Yield: 24% (0.0006 g, 0.0005 mmol; $\varepsilon_{Trp}$ (280 nm) = 5560 L mol$^{-1}$ cm$^{-1}$).

**RP-HPLC** (Method G): 99% ($t_R$ = 10.2 min).

**ESI-MS** (+) (m/z): 1272.5 $[M+H]^+$, calcd. for $C_{61}H_{81}N_{19}O_{10}S$ = 1271.5.

**Table 7.10**: $^{1}H$, $^{13}C$ and $^{15}N$ chemical shifts (ppm, from DSS) for **L7** in $H_2O/D_2O$ 9:1 v/v at pH 2.5 and 5 ºC. "nd" stands for not determined.

| Residue | $^{15}N$ | NH | $^{13}C_\alpha$ | $C_\alpha H$ | $^{13}C_\beta$ | $C_\beta H$ | Others |
|---|---|---|---|---|---|---|---|
| pNO2-BenzAcid[1] | ---- | ----- | ----- | ----- | ----- | ----- | $C_{\delta1}H$ 8.16; $C_{\delta2}H$ 7.75; $C_{\varepsilon2}H$ 8.38; |
| His[2] | 126.8 | 9.30 | nd | 4.94 | 28.9 | 3.31, 3.36 | $C_{\delta2}H$ 7.32; $C_{\varepsilon1}H$ 8.60; |
| DPhe[3] | 125.8 | 8.88 | 59.3 | 4.44 | 39.4 | 3.03, 3.07 | $C_{\delta\delta'}H$ 7.23, 7.23; $C_{\varepsilon\varepsilon'}H$ 7.37, 7.37; $C_\zeta H$ 7.32; |
| Arg[4] | 124.3 | 8.30 | 56.2 | 4.00 | 29.8 | 1.09, 1.38 | $^{13}C_\gamma$ 26.2; $C_{\gamma\gamma'}H$ 0.50, 0.77; $^{13}C_\delta$ 43.1; $C_\delta H$ 2.75, 2.75; $^{15}N_\varepsilon$ 84.8; $N_\varepsilon H$ 6.96; $N_\eta H$ 6.54, 6.80; |
| Trp[5] | 119.5 | 8.11 | 57.5 | 4.54 | 28.4 | 3.23, 3.23 | $C_{\delta1}H$ 7.18; $^{15}N_{\varepsilon1}$ 129.3; $N_{\varepsilon1}H$ 10.11; $C_{\varepsilon3}H$ 7.49; $C_{\zeta3}H$ 7.06; $C_{\eta2}H$ 7.16; $C_{\zeta2}H$ 7.36; |
| Cys[6] | 118.1 | 7.82 | 54 | 4.61 | 35.3 | 3.26, 3.56 | |
| Lys[7] | 123.6 | 8.40 | 56.4 | 4.20 | 33.2 | 1.73, 1.81 | $^{13}C_\gamma$ 25.2; $C_{\gamma\gamma'}H$ 1.35, 1.35; $^{13}C_\delta$ 30.4; $C_{\delta\delta'}H$ 1.49, 1.49; $^{13}C_\varepsilon$ 42.1; $C_{\varepsilon\varepsilon'}H$ 3.11, 3.11; $^{15}N_\zeta$126.6; $N_\zeta H$ 8.13; |
| $CONH_2$ | 108.7 | 7.25, 7.70 | | | | | |

| **BFC** | a | b | c | d | e | f | g | H | i | j |
|---|---|---|---|---|---|---|---|---|---|---|
| **$^{1}H$** | nd | 5.93 | nd | 4.27 | 3.49 | 3.41 | 3.35 | 3.07 | 1.85 | 2.29 |
| **$^{13}C$** | nd | nd | nd | 45.4 | 55.0 | 52.5 | 37.2 | 56.2 | 22.3 | 35.2 |

**Table 7.11**: $^{1}H$, $^{13}C$ and $^{15}N$ chemical shifts (ppm, from DSS) for **L7** in $H_2O/D_2O$ 9:1 v/v at pH 2.5 and 25 ºC. "nd" stands for not determined.

| Residue | $^{15}N$ | NH | $^{13}C_\alpha$ | $C_\alpha H$ | $^{13}C_\beta$ | $C_\beta H$ | Others |
|---|---|---|---|---|---|---|---|
| pNO2-BenzAcid[1] | ---- | ----- | ----- | ----- | ----- | ----- | $C_{\delta1}H$ 8.13; $C_{\delta2}H$ 7.72; $C_{\varepsilon2}H$ 8.37; |
| His[2] | 126.8 | 9.12 | nd | 4.96 | 29.2 | 3.30, 3.36 | $C_{\delta2}H$ 7.32; $C_{\varepsilon1}H$ 8.61; |
| DPhe[3] | 125.5 | 8.70 | 59.3 | 4.47 | 39.9 | 3.03, 3.08 | $C_{\delta\delta'}H$ 7.23, 7.23; $C_{\varepsilon\varepsilon'}H$ 7.36, 7.36; $C_\zeta H$ 7.33; |
| Arg[4] | 124.3 | 8.15 | 56.7 | 3.99 | 30.1 | 1.13, 1.39 | $^{13}C_\gamma$ 26.6; $C_{\gamma\gamma'}H$ 0.60, 0.81; $^{13}C_\delta$ 43.3; $C_\delta H$ 2.77, 2.77; $^{15}N_\varepsilon$ 85.1; $N_\varepsilon H$ 6.91; $N_\eta H$ 6.54, 6.61; |
| Trp[5] | 119.3 | 7.99 | nd | 4.56 | 28.7 | 3.23, 3.23 | $C_{\delta1}H$ 7.18; $^{15}N_{\varepsilon1}$ 129.4; $N_{\varepsilon1}H$ 10.03; $C_{\varepsilon3}H$ 7.50; $C_{\zeta3}H$ 7.06; $C_{\eta2}H$ 7. 15; $C_{\zeta2}H$ 7.36; |
| Cys[6] | 117.9 | 7.72 | nd | 4.61 | 35.7 | 3.28, 3.51 | |
| Lys[7] | 123.3 | 8.20 | 56.7 | 4.22 | 33.5 | 1.71, 1.81 | $^{13}C_\gamma$ 25.5; $C_{\gamma\gamma'}H$ 1.35, 1.35; $^{13}C_\delta$ 30.7; $C_{\delta\delta'}H$ 1.49, 1.49; $^{13}C_\varepsilon$ 42.3; $C_{\varepsilon\varepsilon'}H$ 3.12, 3.12; $^{15}N_\zeta$126.4; $N_\zeta H$ 7.96; |
| $CONH_2$ | 108.4 | 7.12, 7.56 | | | | | |

| **BFC** | a | b | c | d | e | f | g | H | i | j |
|---|---|---|---|---|---|---|---|---|---|---|
| **$^{1}H$** | nd | 5.94 | nd | 4.26 | 3.44 | 3.35 | 3.33 | 3.02 | 1.83 | 2.27 |
| **$^{13}C$** | nd | nd | nd | 45.9 | 55.4 | 52.9 | 37.8 | 56.5 | 22.9 | 35.5 |

### 7.3.25. L8

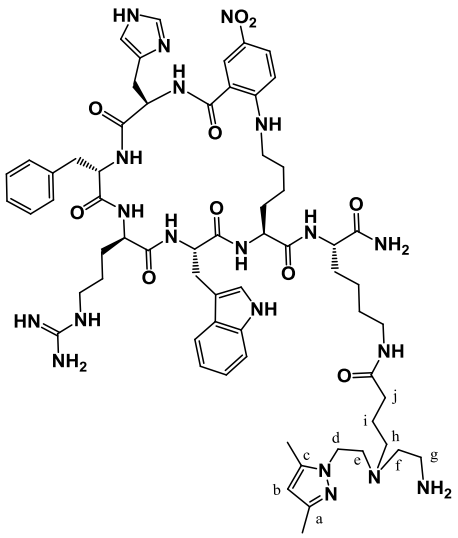

The peptide conjugate **L8** was prepared according to the methodology described for **L7**.

Yield: 25% (0.0006 g, 0.001 mmol; $\varepsilon_{Trp}$ (280 nm) = 5560 L mol$^{-1}$ cm$^{-1}$).

**RP-HPLC** (Method G): 99% ($t_R$ = 10.4 min).

**ESI-MS** (+) (m/z): 1297.7 $[M+H]^+$, calcd. for $C_{64}H_{88}N_{20}O_{10}$ = 1296.7.

### 7.3.26. Re7

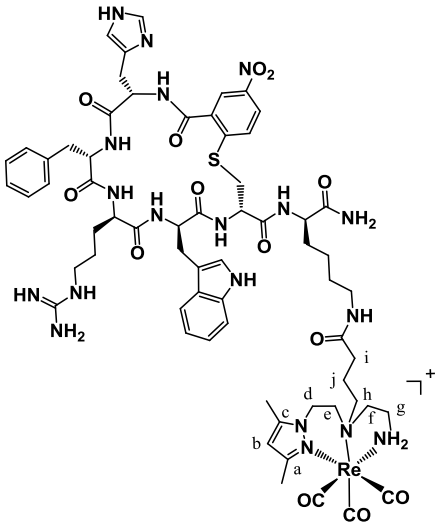

The peptide **SNBA-MSH$_{hex}$** and **Re1** were used to prepare the metallopeptide **Re7**, following the same conjugation strategy described for **L7**.

Yield: 25% (0.0008 g, 0.0005 mmol; $\varepsilon_{Trp}$ (280 nm) = 5560 L mol$^{-1}$ cm$^{-1}$).

**RP-HPLC** (Method G): 99% ($t_R$ = 11.9 min).

**ESI-MS** (+) (m/z): 772.4 $[M+2H]^{2+}$, calcd. for $C_{64}H_{84}N_{19}O_{13}ReS$ = 1544.6.

**Table 7.12**: $^{1}H$, $^{13}C$ and $^{15}N$ chemical shifts (ppm, from DSS) for **Re7** in $H_2O/D_2O$ 9:1 v/v at pH 2.5 and 5 ºC. Chemical shifts for one of the two observed species are in italics. "nd" stands for not determined.

| **Residue** | **$^{15}N$** | **NH** | **$^{13}C_\alpha$** | **$C_\alpha H$** | **$^{13}C_\beta$** | **$C_\beta H$** | **Others** |
|---|---|---|---|---|---|---|---|
| pNO2-BenzAcid[1] | ---- | ----- | ----- | ----- | ----- | ----- | $C_{\delta1}H$ 8.15/*8.14*; $C_{\delta2}H$ 7.73/*7.69*; $C_{\varepsilon2}H$ 8.37/*8.38*; |
| His[2] | 126.9 | 9.24/*9.24* | nd | nd | 28.8 | 3.30, 3.37 | $C_{\delta2}H$ 7.32; $C_{\varepsilon1}H$ 8.59; |
| DPhe[3] | 125.8/*125.5* | 8.82/*8.78* | 59.3 | 4.44/*4.45* | 39.4 | 3.00, 3.07/ *3.03, 3.06* | $C_{\delta\delta'}H$ 7.22, 7.22; $C_{\varepsilon\varepsilon'}H$ 7.36, 7.36; $C_\zeta H$ 7.31; |
| Arg[4] | 124.3/*124.1* | 8.31/*8.30* | 56.4 | 3.96 | 29.8 | 1.11, 1.41/ *1.14, 1.41* | $^{13}C_\gamma$ 26.3; $C_{\gamma\gamma'}H$ 0.55, 0.79/ *0.58, 0.82*; $^{13}C_\delta$ 43.1; $C_\delta H$ 2.75, 2.75/ *2.77, 2.77*; $^{15}N_\varepsilon$ 84.8; $N_\varepsilon H$ 6.96/*6.98* |
| Trp[5] | 119.5 | 8.07/*8.06* | 57.6 | 4.52/*4.55* | 28.3 | 3.23, 3.23 | $C_{\delta1}H$ 7.18/*7.18*; $^{15}N_{\varepsilon1}$ 129.3/*129.3*; $N_{\varepsilon1}H$ 10.12/*10.10*; $C_{\varepsilon3}H$ 7.51/*7.51*; $C_{\zeta3}H$ 7.06/*7.04*; $C_{\eta2}H$ 7.16/*7.14*; $C_{\zeta2}H$ 7.36/*7.33*; |
| Cys[6] | 118.0/*117.7* | 7.83/*7.74* | 54.1 | 4.60/*4.60* | 35.2 | 3.26, 3.57/ *3.24, 3.43* | |
| Lys[7] | 123.0/*122.8* | 8.30/*8.21* | 56.6 | 4.22/*4.21* | 33.2 | 1.74, 1.86/ *1.73, 1.86* | $^{13}C_\gamma$ 25.4; $C_{\gamma\gamma'}H$ 1.43, 1.43/ *1.41, 1.41*; $^{13}C_\delta$ 30.4 (30.7); $C_{\delta\delta'}H$ 1.55, 1.55/ *1.55, 1.55*; $^{13}C_\varepsilon$ 41.9 (42.1); $C_{\varepsilon\varepsilon'}H$ 3.22, 3.22/ *3.21, 3.21*; $^{15}N_\zeta$127.9/*127.8*; $N_\zeta H$ 8.28/*8.26*; |
| $CONH_2$ | 108.7 | 7.25, 7.70 | | | | | |

| **BFC** | a | b | c | d | e | f | G | h | i | j |
|---|---|---|---|---|---|---|---|---|---|---|
| **$^{1}H$** | nd | 6.03/ *5.99* | nd | 4.31, 4.03/ *4.21, 4.00* | 3.30, 2.60/ *3.25, 2.58* | 2.78 | 2.44/ 3.12 | 3.36/ 3.54 | 1.96/ 2.11 | 2.29 |
| **$^{13}C$** | nd | nd | nd | nd | 54.9 | 63.6 | 44.8 | 68.1 | 22.8 | 35.5 |

**Table 7.13**: $^{1}H$, $^{13}C$ and $^{15}N$ chemical shifts (ppm, from DSS) for **Re7** in $H_2O/D_2O$ 9:1 v/v at pH 2.5 and 25 ºC. Chemical shifts for one of the two observed species are in italics. "nd" stands for not determined.

| **Residue** | **$^{15}N$** | **NH** | **$^{13}C_\alpha$** | **$C_\alpha H$** | **$^{13}C_\beta$** | **$C_\beta H$** | **Others** |
|---|---|---|---|---|---|---|---|
| pNO2-BenzAcid1 | ---- | ----- | ----- | ----- | ----- | ----- | $C_{\delta1}H$ 8.12/*8.11*; $C_{\delta2}H$ 7.71/*7.67*; $C_{\varepsilon2}H$ 8.37/*8.37*; |
| His[2] | 126.8 | 9.04/*9.02* | nd | 4.95 | 29.1 | 3.30, 3.38 | $C_{\delta2}H$ 7.32; $C_{\varepsilon1}H$ 8.61 |
| DPhe[3] | 125.4/*125.2* | 8.63/*8.59* | 59.3 | 4.46/*4.49* | 39.9 | 3.01,3.07/ *3.04, 3.07* | $C_{\delta\delta'}H$ 7.22, 7.22; $C_{\varepsilon\varepsilon'}H$ 7.36, 7.36; $C_\zeta H$ 7.31; |
| Arg[4] | 124.3/*124.1* | 8.18/*8.16* | 56.8 | 3.94 | 30.1 | 1.16, 1.41 /*1.18, 1.42* | $^{13}C_\gamma$ 26.7; $C_{\gamma\gamma'}H$ 0.60, 0.81/ *0.67, 0.87*; $^{13}C_\delta$ 43.3; $C_\delta H$ 2.77, 2.77 / *2.80, 2.80*; $^{15}N_\varepsilon$ 85.1; $N_\varepsilon H$ 6.92/*6.93*; |
| Trp[5] | 119.3 | 7.95/*7.94* | nd | 4.53/*4.55* | 28.7 | 3.23, 3.23 | $C_{\delta1}H$ 7.18/*7.18*; $^{15}N_{\varepsilon1}$129.4/*129.4*; $N_{\varepsilon1}H$ 10.04/*10.02*; $C_{\varepsilon3}H$ 7.52/*7.51*; $C_{\zeta3}H$ 7.06/*7.04*; $C_{\eta2}H$ 7.14/*7.13*; $C_{\zeta2}H$ 7.35/*7.32*; |
| Cys[6] | 117.6/*117.5* | 7.74/*7.65* | nd | 4.61/*4.62* | 35.7 | 3.29, 3.52/ *3.27, 3.38* | |
| Lys[7] | 122.6/*122.5* | 8.10/*8.03* | 56.7 | 4.24/*4.24* | 33.5 | 1.71, 1.86/ *1.71, 1.86* | $^{13}C_\gamma$ 25.6; $C_{\gamma\gamma'}H$ 1.41, 1.41/ *1.39, 1.39*; $^{13}C_\delta$ 30.7; $C_{\delta\delta'}H$ 1.54, 1.54/ *1.54, 1.54*; $^{13}C_\varepsilon$ 42.1; $C_{\varepsilon\varepsilon'}H$ 3.21, 3.21; $^{15}N_\zeta$127.5/*127.8*; $N_\zeta H$ 8.11/*8.26*; |
| $CONH_2$ | 108.7 | 7.12, 7.56 | | | | | |

| **BFC** | a | b | c | d | e | f | G | h | i | j |
|---|---|---|---|---|---|---|---|---|---|---|
| **$^{1}H$** | nd | 6.06/ *6.03* | nd | 4.33, 4.03/ *4.29, 4.03* | 3.31, 2.60/ *3.30, 2.59* | 2.79 | 2.45/ 3.14 | 3.36/ 3.52 | 1.97/ 2.12 | 2.29 |
| **$^{13}C$** | nd | nd | nd | nd | 55.4 | 64.0 | 45.1 | 68.5 | 23.2 | 35.7 |

### 7.3.27. Re8

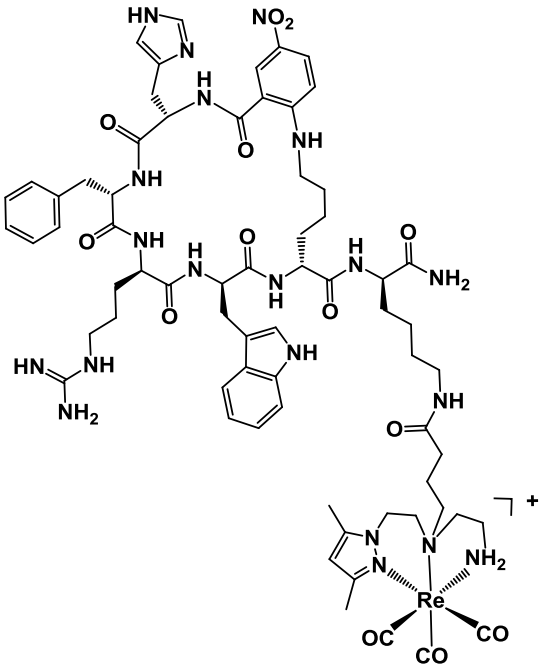

The peptide **NNBA-MSH$_{hex}$** and **Re1** were used to prepare the metallopeptide **Re8**, following the same conjugation strategy described for **L7**.

Yield: 22% (0.0007 g, 0.001 mmol; $\varepsilon_{Trp}$ (280 nm) = 5560 L mol$^{-1}$ cm$^{-1}$).

**RP-HPLC** (Method G): 99% ($t_R$ = 12.1 min).

**ESI-MS** (+) (m/z): 784.4 $[M+2H]^{2+}$, calcd. for $C_{67}H_{91}N_{20}O_{13}Re$ = 1569.7.

### 7.3.28. General method for the preparation of Tc7 and Tc8

In a capped nitrogen purged glass vial, 50 μL of a 5 – 8 x 10$^{-4}$ M solution of **L7** or **L8** was added to of a solution of *fac*-[$^{99m}$Tc(CO)$_3$(H$_2$O)$_3$]$^+$ (450 μL, 37 - 74 MBq) in 0.01 M PBS, pH 7.4. The vial was incubated at 75 °C for 30 min and the resulting complexes were analyzed by RP-HPLC (Method H) using the same method of the rhenium surrogates. Retention times: 12.2 min (**Tc7**) and 12.3 min (**Tc8**).

### 7.3.29. tert-butyl 2-(2-(1H-pyrazol-1-yl)ethylamino)ethylcarbamate (III)

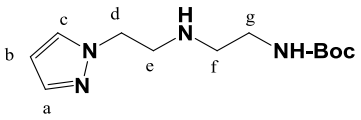


The precursor **III** was prepared as described elsewhere.[48d]

**$^1$H-NMR** (300 MHz, $CDCl_3$): $\delta_H$ (ppm) 7.87 (dd, $H^{a/c}$, 1H), 7.29 (dd, $H^{a/c}$, 1H), 6.29 (s, $H^b$, 1H), 5.06 (br s, NHBoc, 1H), 4.55 (t, $CH_2^d$, 2H), 4,23 (s br, 1H, NH), 3.32 (t, $CH_2^g$, 2H), 2.93 (t, $CH_2^e$, 2H), 2.66 (t, $CH_2^f$, 2H), 1.44 (s, CH3, 9H).

### 7.3.30. Ethyl 1-(2-(2-(tert-butoxycarbonylamino)ethylamino)ethyl)-1H-pyrazole -4-carboxylate (IV)

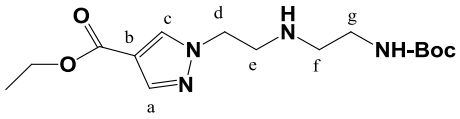


Compound **IV** was prepared as described elsewhere.[48d]

**$^1$H-NMR** (300 MHz, $CDCl_3$): $\delta_H$ (ppm) 8,09 (s, 1H, $H^{a/c}$); 7,80 (s, 1H, $H^{a/c}$); 5,80 (s br, 1H, NH); 4,56 (t, $CH_2^d$, 2H), 4,23 (s br, NH, 1H); 4,20 (q, C*H*$_2$CH3, 2H), 3,57 (t, $CH_2^g$ , 2H); 3,41 (t, $CH_2^e$, 2H); 3,19 (t, $CH_2^f$, 2H); 1,32 (s, 9H, $3CH_3$); 1,26 (t, $CH_2C$*H*$_3$, 3H).

### 7.3.31. tert-butyl 2-(1-(2-(2-(tert-butoxycarbonylamino)ethylamino)ethyl)-3,5-dimethyl-1H-pyrazol-4-yl)acetate (V)

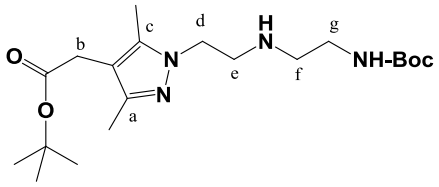


Compound **V** was prepared as described elsewhere, using diferent protecting group (*tert*-butyl).[51b]

**$^1$H-NMR** (300 MHz, $CDCl_3$) $\delta_H$ (ppm) 5.23 (br s, NHBoc, 1H), 4.01 (t, $CH_2^d$, 2H), 3.17 (s, $CH_2^b$, 2H), 3.14 (t, $CH_2^g$, 2H), 2.96 (t, $CH_2^e$, 2H) 2.68 (t, $CH_2^f$, 2H), 2.13 (s, $CH_3^a$, 3H), 2.12 (s, $CH_3^c$, 3H), 1.37(s, $CH_3$, 9H), 1.36 (s, $CH_3$, 9H).

### 7.3.32. ethyl 4-((2-(1H-pyrazol-1-yl)ethyl)(2-(tert-butoxycarbonylamino)ethyl) amino)butanoate (VI)

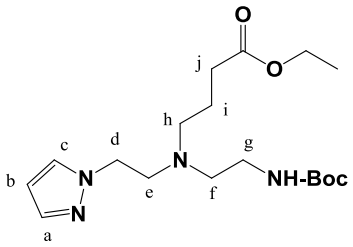


Compound **VI** was prepared as described elsewhere.[48d]

**$^1$H-RMN** (300 MHz, $CDCl_3$): $\delta_H$ (ppm) 7,46 (d, $H^{a/c}$, 1H,); 7,40 (d, $H^{a/c}$ , 1H); 6,19 (s, $H^b$, 1H); 5,15 (s br, NH, 1H), 4,08 (m, $OCH2CH_3$+$CH_2^d$, 4H); 3,00 (t, $CH_2^e$, 2H); 2,80 (t, $CH_2^g$, 2H); 2,46 (t, $CH_2^f$, 2H); 2,39 (t, $CH_2^h$, 2H); 2,08 (t, $CH_2^j$, 2H); 1,58 (m, $CH_2^i$, 2H); 1,40 (s, $CH_3$, 9H); 1,21 (t, $OCH_2CH_3$, 3H).

### 7.3.33. ethyl 1-(2-((2-(tert-butoxycarbonylamino)ethyl)(4-ethoxy-4-oxobutyl) amino)ethyl)-1H-pyrazole-4-carboxylate (VII)

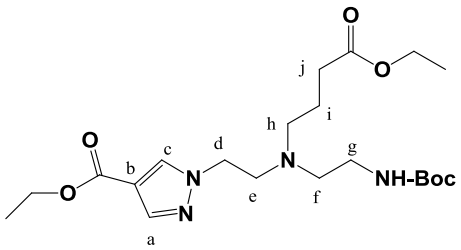


Precursor **IV** (0.5400 g, 1.70 mmol), ethyl 4-bromobutanoate (0.65 g, 2.4 mmol), $K_2CO_3$ (0.4200 g, 2.400 mmol) and a catalytic amount of KI were dissolved/ suspended in $CH_3CN$ (20 mL), and allowed to reflux for 18 h. The solution was filtered, vacuum dried, and the obtained residue was purified by flash chromatography (silica gel, $CH_2Cl_2$/MeOH 0-5%), giving **VII** as a yellowish oil, after removal of the solvent from the collected fractions. Yield: 69 % (0.5000 g, 1.100 mmol).

**IR** (KBr) ($\nu$/cm$^{-1}$): 3424 s, 1690 s, 1561s and 1414s.

**$^1$H-NMR** (300 MHz, $CDCl_3$): $\delta_H$ (ppm) 7.92 (s, $H^{a/c}$, 1H), 7.89 (s, $H^{a/c}$, 1H), 5.01 (br s, NHBoc, 1H), 4.21 (t, $CH_2^d$, 2H), 4.12 (q, $OCH_2CH_3$, 4H), 3.05 (q, $CH_2^e$, 2H), 2.51 (s, $CH_2^f$, 2H), 2.44 (q, $CH_2^h$, 2H), 2.13 (t, $CH_2^j$, 2H), 1.58 (t, $CH_2^i$, 2H), 1.42 (s, $CH_3$, 9H), 1.29 (q, $OCH_2CH_3$, 6H).

**$^{13}$C-NMR** (75.3 MHz, $CDCl_3$): $\delta_C$ (ppm) 173.1 (CO), 162.5 (CO), 155.9 (CO), 140.6 ($C^c$), 131.7 ($C^a$), 115.3 (pz), 80.5 ($C(CH_3)$), 62.1($CH_2CH_3$), 61.8 ($CH_2CH_3$), 59.6 ($C^h$), 56.4 ($C^e$), 53.9 ($C^f$), 51.4 ($C^d$), 38.8 ($C^g$), 31.6 ($C^j$), 28.6 ($C(CH_3)$), 24.4 ($C^i$), 14.2 ($CH_2CH_3$).

### 7.3.34. ethyl 4-((2-(4-(2-tert-butoxy-2-oxoethyl)-3,5-dimethyl-1H-pyrazol-1-yl) ethyl)(2-(tert-butoxycarbonylamino)ethyl)amino)butanoate (VIII)

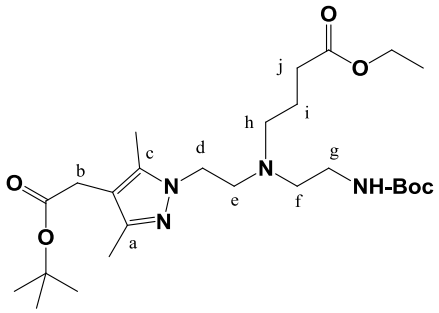


Precursor **V** (0.5400 g, 1.700 mmol), ethyl 4-bromobutanoate (0.3900 g, 2.000 mmol), $K_2CO_3$ (0.2800, 2.000 mmol) and a catalytic amount of KI were dissolved/ suspended in acetonitrile (10 mL) and the resulting mixture allowed to reflux for 18 h. The solution was filtered, vacuum dried, and the residue was purified by flash chromatography (silica gel, ethyl acetate/methanol, 0-15%), giving **VIII** as a yellowish oil. Yield: 45 % (0.2300 g, 0.450 mmol).

**$^{1}$H-NMR** (300 MHz, $CDCl_3$): $\delta_H$ (ppm) 5.34 (br s, NHBoc, 1H), 4.07 (q, $OCH_2CH_3$, 2H), 3.94 (t, $CH_2^d$, 2H), 3.18 (s, $CH_2^b$, 2H), 3.01 (t, $CH_2^e$, 2H), 2.71 (t, $CH_2^g$, 2H), 2.37 (m, $CH_2^f$/$CH_2^h$, 4H), 2.15 (s, $CH_3^a$, 3H), 2.14 (s, $CH_3^c$, 3H), 2.07 (t, $CH_2^j$, 2H), 1.76 - 1.66 (m, $CH_2^i$, 2H), 1.37(s, $CH_3$, 9H), 1.36 (s, $CH_3$, 9H), 1.15 (q, $OCH_2CH_3$, 2H).

**$^{13}$C-NMR** (75.3 MHz, $CDCl_3$): $\delta_C$ (ppm) 173.9 (CO), 171.2 (CO), 156.4 (CO), 146.6 ($C^c$), 137.1 ($C^a$), 109.9 ($C^{Pz}$), 80.8 ($C(CH_3)$), 79.1 ($C(CH_3)$), 60.5 ($OCH_2CH_3$), 53.9 ($C^h$), 53.8 ($C^e$); 53.5 ($C^f$), 49.9 ($C^d$), 47.5 ($C^g$), 38.7 ($C^j$), 31.7 ($C^b$), 28.7 ($C(CH_3)$), 28.2 ($C(CH_3)$), 22.6 ($C^i$), 14.5 ($OCH_2CH_3$), 12.0 ($CH_3^c$), 10.0 ($CH_3^a$).

### 7.3.35. 4-((2-(1H-pyrazol-1-yl)ethyl)(2-(tert-butoxycarbonylamino)ethyl)amino) butanoic acid (L10-Boc)

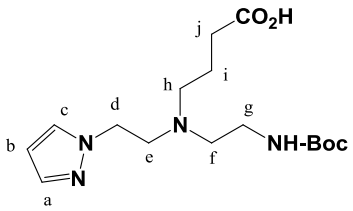


A solution of NaOH (0.1800 g, 0.450 mmol) in $H_2O$/THF (1:1, 5 mL) was added to **VI** (0.100 g, 0.270 mmol) in THF (1 mL), and the reaction mixture was stirred overnight at room temperature. After neutralization of the reaction mixture with 1M HCl at 0 $^oC$, the solvent was evaporated and the residue was purified by flash chromatography (methanol/$CHCl_3$, 5-100%), giving **L10-Boc** as a colorless oil. Yield: 50% (0.0460 g, 0.140 mmol).

**$^1$H-NMR** (300 MHz, $CDCl_3$): $\delta_H$ (ppm)7.47 (dd, $H^{a/c}$, 1H), 7.43 (dd, $H^{a/c}$, 1H), 6.19 (s, $H^b$, 1H), 5.06 (br s, NHBoc, 1H), 4.15 (t, $CH_2^d$, 2H), 3.02 (t, $CH_2^g$, 2H), 2.86 (t, $CH_2^e$, 2H), 2.46 (d, $CH_2^{f+h}$, 4H), 2.14 (br s, $CH_2^j$, 2H), 3.12), 1.61 (br s, $CH_2^i$, 2H), 1.40 (s, CH3, 9H).

**$^{13}$C-NMR** (75.3 MHz, $CDCl_3$): $\delta_C$ (ppm)184.7 (CO), 173.2 (CO), 142.9 ($C^c$), 135.6 ($C^a$), 122.4 ($C^b$), 83.1 ($C(CH_3)$) 55.2 ($C^h$), 54.6 ($C^e$), 52.3 ($C^f$), 50.1 ($C^d$), 39.1 ($C^g$), 37.1 ($C^j$), 29.7 ($C(CH_3)$), 24.3 ($C^i$).

**RP-HPLC** (Method A): 99% ($t_R$ = 16.3 min).

**ESI-MS** (+) (m/z): 341.1 $[M+H]^+$, calcd. for $C_{16}H_{28}N_4O_4$ = 340.2.

### 7.3.36. 1-(2-((2-(tert-butoxycarbonylamino)ethyl)(3-carboxypropyl)amino) ethyl)-1H-pyrazole-4-carboxylic acid (L11-Boc)

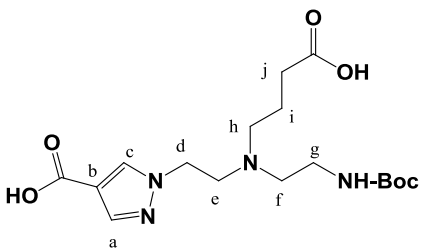


A solution of NaOH (0.1800 g, 0.450 mmol) in $H_2O$/THF (1:1, 5 mL) was added to **VII** (0.1000 g, 0.220 mmol) in THF (1 mL), and the reaction mixture was stirred overnight at room temperature. After neutralization with 1M HCl at 0 $^oC$, and solvent evaporation

under reduced pressure, the crude was purified through Sep-Pack C-18 cartridge ($H_2O$/MeOH, 0-100%), giving **L11-Boc** as a colorless oil. Yield: 29% (0.0300 g, 0.080 mmol).

**$^1$H-NMR** (300 MHz, $D_2O$): $\delta_H$ (ppm) 7.84 (s, $H^{a/c}$, 1H), 7.67 (s, $H^{a/c}$, 1H), 4.16 (t, $CH_2^d$, 2H), 2.99 (m, $CH_2$ $^{e/g}$, 4H), 2.55 (m, $CH_2$ $^{h/f}$, 4H), 2.01 (s, $CH_2^j$, 2H), 1.56 (m, $CH_2^i$, 2H), 1.25 (s, $CH_3$, 9H).

**$^{13}$C-NMR** (75.3 MHz, $D_2O$): $\delta_C$ (ppm) 184.7 (CO), 173.2 (CO), 160.1 (CO), 142.9 ($C^c$), 135.6 ($C^a$), 122.4 ($C^b$), 83.1 ($C$($CH_3$)) 55.2 ($C^h$), 54.6 ($C^e$), 52.3 ($C^f$), 50.1 ($C^d$), 39.1 ($C^g$), 37.1 ($C^j$), 29.7 (C($CH_3$)), 24.3 ($C^i$).

**RP-HPLC** (Method A): 99% ($t_R$ = 15.1 min).

**ESI-MS** (+) (m/z): 385.2 $[M+H]^+$, calcd. for $C_{17}H_{28}N_4O_6$ = 384.2.

### 7.3.37. 4-((2-(4-(2-tert-butoxy-2-oxoethyl)-3,5-dimethyl-1H-pyrazol-1-yl)ethyl) (2-(tert-butoxycarbonylamino)ethyl)amino)butanoic acid (L12-Boc)

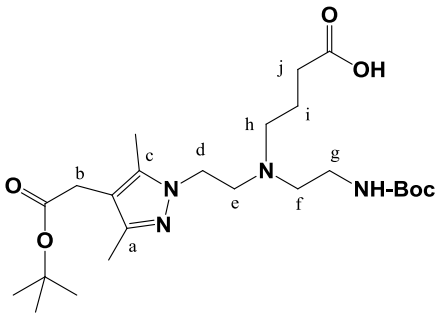


A solution of NaOH (0.7500 g, 2.100 mmol) in $H_2O$/THF (1:1, 6 mL) was added to **VIII** (0.2300 g, 0.450 mmol) in THF (2 mL), and the reaction mixture was stirred overnight at room temperature. After neutralization with 1M HCl at 0 $^oC$ and solvent evaporation under reduced pressure, the residue was purified by flash chromatography (silica gel, $CH_2Cl_2$/ MeOH, 0-20%), giving **L12-Boc** as a white solid. Yield: 67% (0.1400 g, 0.290 mmol).

**$^1$H-NMR** (300 MHz, $CDCl_3$): $\delta_H$ (ppm) 4.08 (t,$CH_2^d$, 2H), 3.21 (s, $CH_2^b$, 2H), 3.04 (q, $CH_2^e$, 2H), 2.83 (t, $CH_2^g$, 2H), 2.57 (t, $CH_2^f$, 2H), 2.49 (t, $CH_2^h$, 2H), 2.36 (t, $CH_2^j$, 2H), 2.1 (s, $CH_3^a$, 3H), 2.03 (s, $CH_3^c$, 3H), 1.86 (t, $CH_2^i$, 2H), 1.24 (s, $CH_3$, 18H).

**$^{13}$C-NMR** (75.3 MHz, $CDCl_3$): ): $\delta_C$ (ppm) 189.8 (CO), 187.6 (CO), 165.1 (CO), 154.5 ($C^c$), 145.9 ($C^a$), 119.4 ($C^{Pz}$), 81.0 ($C$($CH_3$)$_3$), 79.1 ($C$($CH_3$)$_3$), 60.2 ($C^h$), 59.7 ($C^e$), 59.2 ($C^f$), 52.4 ($C^d$), 44.1 ($C^g$), 42.3 ($C^j$), 38.8 ($C^b$), 34.8 (C($CH_3$)), 29.5 ($C^i$), 17.7 ($CH_3^c$), 15.9 ($CH_3^a$).

**RP-HPLC** (Method A): 99% ($t_R$ = 19.9 min).

**ESI-MS** (+) (m/z): 483.7 $[M+H]^+$, calcd. for $C_{24}H_{42}N_4O_6$ = 482.6.

### 7.3.38. 4-((2-(1H-pyrazol-1-yl)ethyl)(2-aminoethyl)amino)butanoic acid (L10)

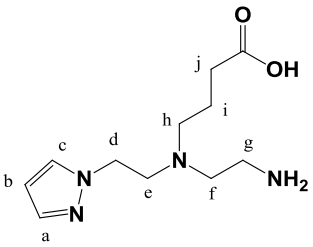


Deprotection of **L10-Boc** (0.1000 g, 0.290 mmol) with $CH_2Cl_2$/TFA (1 mL/3 mL) gave **L10** as a colorless oil after evaporation of the solvent. Yield: 77 % (0.0800 g, 0.220 mmol, calcd. for $C_{11}H_{20}N_4O_2$.TFA).

**$^1$H-NMR** (300 MHz, $D_2O$): $\delta_H$ (ppm) 7.58 (d, $H^c$, 1H); 7.48 (d, $H^a$, 1H); 6.25 (m, $H^b$, 1H); 4.49 (t, $CH_2^d$, 2H); 3.64 (t, $CH_2^e$, 2H); 3.42 (t, $CH_2^f$, 2H); 3.25 (t, $CH_2^h$, 2H); 3.12 (t, $CH_2^g$,2H); 2.30 (t, $CH_2^j$, 2H); 1.79 (m, $CH_2^i$, 2H).

**$^{13}$C-NMR** (75.3 MHz, $D_2O$): $\delta_C$ (ppm) 179.9 (CO), 140.1 ($C^c$), 131.8 ($C^a$); 106.7 ($C^b$); 54.9 ($C^f$); 54.1 ($C^h$); 52,0 ($C^e$); 50.7 ($C^d$); 38.6 ($C^g$); 33.9 ($C^j$); 23.9 ($C^i$).

### 7.3.39. 1-(2-((2-aminoethyl)(3-carboxypropyl)amino)ethyl)-1H-pyrazole-4-carboxylic acid (L11)

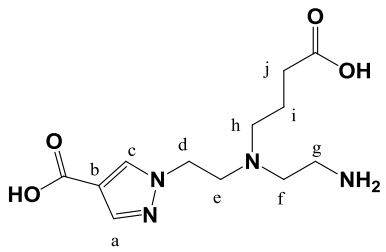


**L11** was prepared as described for **L10**. Deprotection of **L11-Boc** (0.1000 g, 0.260 mmol) with dichloromethane/TFA (1 mL/3 mL) gave **L11** a colorless oil. Yield: 77 % (0.0800 g, 0.2000 mmol, calcd. for $C_{12}H_{20}N_4O_4$.TFA).

**$^1$H-NMR** (300 MHz, $D_2O$): $\delta_H$ (ppm) 8.29 (s, $H^c$, 1H), 8.05 (s, $H^a$, 1H), 4.67 (t, $CH_2^d$, 2H), 3.77 (t, $CH_2^e$, 2H), 3.52-3.42 (m, $CH_2^{f/g}$, 4H), 3.24 (t, $CH_2^h$, 2H), 2.47 (t, $CH_2^j$, 2H), 2.01 (s, $CH_2^j$, 2H), 1.95 (m, $CH_2^i$, 2H).

**$^{13}$C-NMR** (75.3 MHz, $D_2O$): $\delta_C$ (ppm) 180.1 (CO), 165.5 (CO), 145,1 ($C^c$); 138,1 ($C^a$); 109,2 ($C^b$); 54,9 ($C^h$); 54,1 ($C^e$); 52,0 ($C^f$); 50,7 ($C^d$); 38,6 ($C^g$); 33,9 ($C^j$); 23,9 ($C^i$).

**Table 7.14**: $^1$H, $^{13}$C and chemical shifts (ppm, from DSS) of **L11** in $H_2O/D_2O$ 9:1 v/v at pH 2.5 and 25 ºC. "nd" stands for not determined.

| BFC | a | b | c | d | e | F | g | h | i | j |
|---|---|---|---|---|---|---|---|---|---|---|
| $^1$H | 8.05 | nd | 8.29 | 4.67 | 3.77 | 3.52 | 3.42 | 3.24 | 1.95 | 2.47 |
| $^{13}$C | 145.1 | nd | 138.1 | 49.3 | 55.5 | 52.6 | 37.0 | 55.8 | 21.4 | 33.2 |

### 7.3.40. *fac*-[Re(CO)$_3$(κ$^3$-L10)]$^+$ (Re10)

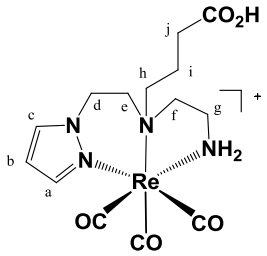


The complex **Re10** was prepared according to the methodology described for **Re1**. Briefly, **L10** (0.0500 g, 0.150 mmol) reacted with the organometallic precursor $[Re(CO)_3(H_2O)_3]Br$ (0.0610 g, 0.190 mmol) in refluxing water for 18 h (pH 7). After evaporation of the solvent the resulting residue was purified by preparative RP-HPLC (Method B). **Re10** was obtained as a colorless oil. Yield: 65 % (0.0600 g, 0.090 mmol, calcd. for $C_{14}H_{22}N_4O_5Re$.TFA).

**IR** (KBr) (ν/cm$^{-1}$): 3441s, 2033s (C≡O), 1920s (C≡O) and 1687s (C=O).

**$^1$H-NMR** (300 MHz, $D_2O$): $\delta_H$ (ppm) 7.84 (d, $CH^c$, 1H), 7.78 (d, $CH^a$, 1H), 6.41 (t, $CH^b$, 1H), 5.07 (br s, NH, 1H), 4.52 (m, $CH^d$, 1H), 4.37 (m, $CH^{d'}$, 1H), 4.10 (br s, NH, 1H), 3.59 (m, $CH^h$, 1H), 3.42 (m, $CH^{h'}$+$CH^e$, 2H), 3.14 (m, $CH^g$, 1H) 2.89 (m, $CH^{f+f'}$, 2H), 2.70 (m, $CH^{e'}$, 1H), 2.40 (t, $CH^j$, 2H), 2.36 (m, $CH^{g'}$, 1H) 2.13 (m, $CH^i$, 1H), 1.97 (m, $CH^{i'}$, 1H).

**$^{13}$C-NMR** (75.3 MHz, $D_2O$): $\delta_C$ (ppm) 195.1 (C≡O), 194.6 (C≡O), 193.1 (C≡O), 177.6 (C=O), 145.4 ($C^c$), 134.7 ($C^a$), 107.8 ($C^b$), 66.4 ($C^h$), 61.7 ($C^f$), 53.2 ($C^e$), 50.8 ($C^d$), 41.9 ($C^j$), 30.8 ($C^h$), 19.7 ($C^i$).

**RP-HPLC** (Method A): 99% ($t_R$ = 16.7 min).

**ESI-MS** (+) (m/z): 511.2 $[M]^+$, calcd. for $C_{14}H_{20}N_4O_5Re$ = 510.5.

### 7.3.41. *fac*-[Re(CO)$_3$($\kappa^3$-L11)]$^+$ (Re11)

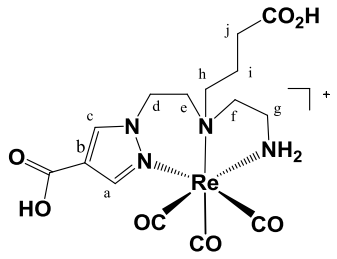


The complex **Re11** was prepared according to the methodology described for **Re1**.

Yield: 71 % (0.0600 g, 0.090 mmol, calcd. for $C_{15}H_{22}N_4O_7Re$.TFA).

**IR** (KBr) ($\nu$/cm$^{-1}$): 3441s, 2035s (C≡O), 1921s (C≡O) and 1687s (C=O).

**$^1$H-NMR** (300 MHz, $D_2O$): $\delta_H$ (ppm) 8.27 (s, $CH^a$+$CH^c$, 2H), 5.11 (br m, NH, 1H), 4.53 (dd, $CH^d$, 1H), 4.46 (dd, $CH^{d'}$, 1H), 4.22 (br dd, NH, 1H), 3.56 (m, $CH^e$, 1H), 3.32 (m, $CH^{h'}$+$CH^h$, 2H), 3.08 (br d, $CH^g$, 1H), 2.85-2.69 (m, $CH^f$+$CH^{f'}$+$CH^{e'}$, 3H), 2.36 (br t, $CH^{g'}$+$CH_2^j$, 3H), 2.06 (m, $CH^i$, 1H), 1.94 (m, $CH^{i'}$, 1H).

**$^{13}$C-NMR** (75.3 MHz, $D_2O$): $\delta_C$ (ppm) 194.6 (C≡O), 194.1 (C≡O), 192.3 (C≡O), 177.5 (C=O), 165.1 (C=O), 147.3 ($C^c$), 137.3 ($C^a$), 116.4 ($C^b$), 66.3 ($C^h$), 61.6 ($C^f$), 52.5 ($C^e$), 51.5 ($C^d$), 41.9 ($C^g$), 30.8 ($C^j$), 19.6 ($C^i$).

**RP-HPLC** (Method A): 99 % ($t_R$ = 16.4 min).

**ESI-MS** (+) (m/z): 555.0 $[M]^+$, calcd. for $C_{15}H_{22}N_4O_7Re$ = 557.1.

### 7.3.42. General method for the preparation of Tc3 – Tc11

In a capped nitrogen purged glass vial, 100 μL of a $10^{-4}$ M solution of the ligands **L3**, **L10** and **L11** were added to a solution of *fac*-[$^{99m}$Tc(CO)$_3$($H_2O$)$_3$]$^+$ (900 μL, 37 - 74 MBq) in 0.01 M PBS, pH 7.4. The vial was incubated at 100 °C for 30 min and the resulting complexes were analyzed by RP-HPLC (Method A) using the same method of the rhenium surrogates. Retention times: 17.2 min (**Tc3**),16.5 min (**Tc10**) and 16.2 min (**Tc11**).

### 7.3.43. βAlaNleCycMSH$_{hex}$

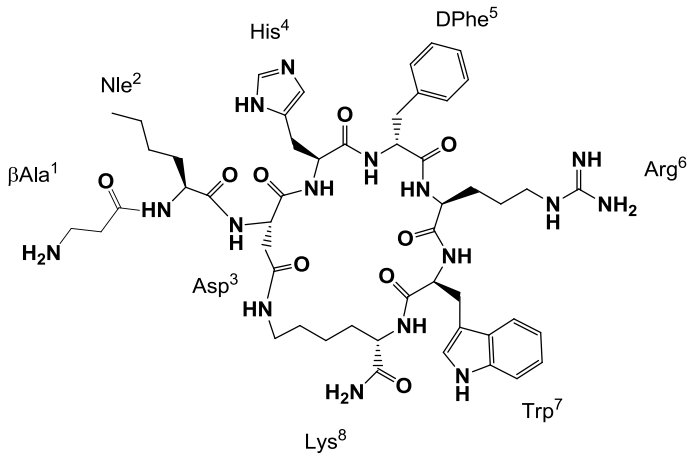


The linear sequence Fmoc-Asp(Dmab)-His(Trt)-DPhe-Arg(Pbf)-Trp(Boc)-Lys(ivDde)-$NH_2$ was assembled to MBHA Rink Amide resin (0.18 g; substitution 0.59 mmol/ g) by SPPS in a CEM 12-Channel Automated Peptide (scale 0.1 mM) using HBTU as coupling agent.

The peptidyl resin was treated with a freshly prepared mixture of hydroxylamine hydrochloride and imidazole in N-methylpyrrolidone to accomplish selective and simultaneous removal of the ODmab and ivDde side chain protecting groups. Condensation of the Asp and Lys side chains to form the intramolecular lactam bridge was carried out using PyBop (6 equiv), DIPEA (12 equiv), and HOBt (6 equiv) during 36 h (negative Kaiser test). After lactamization had reached completion, normal assembly of the remaining peptide chain was resumed up to the quantitative incorporation of the residues Nle and βAla. Cleavage of the proteted Fmoc-peptide from the solid support was performed by treatment of the peptidyl resin with TFA containing 2.5 % $H_2O$ and 2.5 % triisopropylsilane. The crude product was purified by RP-HPLC and **Fmoc-βAlaNleCycMSH$_{hex}$** was obtained as a white solid that was characterized by ESI-MS (calculated m/z for $[M+H]^+$: 1275.6 calcd. for $C_{66}H_{82}N_{16}O_{11}$ = 1274.6). RP-HPLC (Method J): 99 % ($t_R$ = 25.8 min).

Deprotection of the Fmoc group in **Fmoc-βAlaNleCycMSH$_{hex}$** with piperidine/DMF (1 mL/4 mL) gave **βAlaNleCycMSH$_{hex}$** as a white solid after removal of the solvent and washing with ice-cold diethylether. The peptide was dried under nitrogen flow, suspended in water and lyophilized.

**RP-HPLC** (Method J): 99 % ($t_R$ = 16.5 min).

**ESI-MS** (+) (m/z): 1053.6 $[M+H]^+$, calcd. for $C_{51}H_{72}N_{16}O_9$ = 1052.6.

### 7.3.44. L13

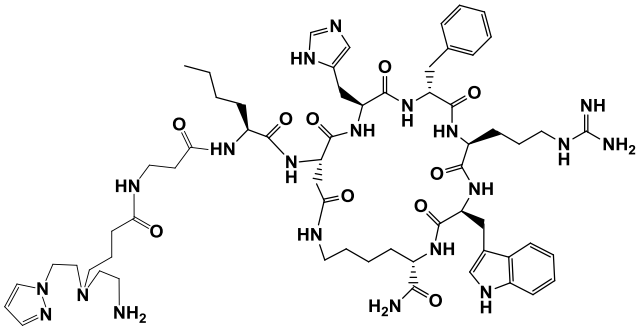

A solution of **βAlaNleCycMSH$_{hex}$** (0.0020 g, 0.002 mmol) in DIPEA (20 μL)/DMF (250 μL) was added to **L10-Boc** (0.0020g, 0.005 mmol) preincubated for 30 min with HATU (0.003 g, 0.006 mmol) in DMF. The pH was adjusted to 7-8 with DIPEA and the reaction mixture was left under stirring at room temperature for 3 hours. The reaction mixture was purified by semi-preparative RP-HPLC (Method J). After evaporation of the solvent, the compound was deprotected with the standard cocktail mixture (95% TFA, 2.5% TIS, 2.5% $H_2O$) and precipitated with ice-cold diethylether. The precipitate was dried under nitrogen flow and dissolved in water before lyophilization. Yield: 25 % (0.0006 g; 0.001 mmol; $\varepsilon_{Trp}$ (280 nm) = 5560 L mol$^{-1}$ cm$^{-1}$).

**RP-HPLC** (Method K): 99 % ($t_R$ = 13.3 min).

**ESI-MS** (+) (m/z): 639.2 $[M+2H]^{2+}$, calcd. for $C_{62}H_{90}N_{20}O_{10}$ = 1274.7.

### 7.3.45. L14

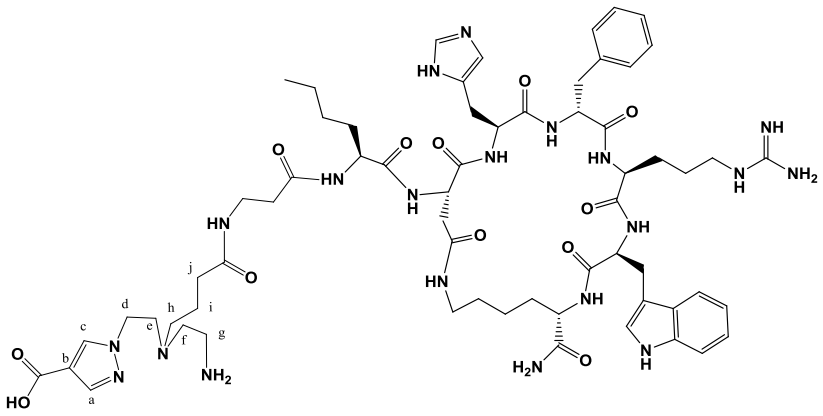

A solution of **βAlaNleCycMSH$_{hex}$** (0.0020 g, 0.002 mmol) in DIPEA (20 μL)/DMF (250 μL) was added to **L11-Boc** (0.0040 g, 0.010 mmol) preincubated for 30 min with HATU (0.0050 g, 0.012 mmol) in DMF. The pH was adjusted to 7-8 with DIPEA and

the reaction mixture was left under stirring at room temperature for 3 hours. The reaction mixture was purified by semi-preparative RP-HPLC (Method J). After evaporation of the solvent, the compound was deprotected with the standard cocktail mixture (95% TFA, 2.5% TIS, 2.5% $H_2O$) and precipitated with ice-cold diethylether. The precipitate was dried under nitrogen flow and dissolved in water before lyophilization. Yield: 28 % (0.0007 g, 0.001 mmol; $\varepsilon_{Trp}$ (280 nm) = 5560 L $mol^{-1}$ $cm^{-1}$).

**RP-HPLC** (Method K): 99% ($t_R$ = 12.7 min).

**ESI-MS** (+) (m/z): 442.56 $[M+3H]^{3+}$, calcd. for $C_{63}H_{90}N_{20}O_{12}$ = 1318.7.

**Table 7.15**: $^{1}H$, $^{13}C$ and $^{15}N$ chemical shifts (ppm, from DSS) of **L14** in $H_2O/D_2O$ 9:1 v/v at pH 2.5 and 25 ºC. "nd" stands for not determined.

| Residue | $^{15}N$ | HN | $^{13}C_\alpha$ | $C_\alpha H$ | $^{13}C_\beta$ | $C_\beta H$ | Others |
|---|---|---|---|---|---|---|---|
| βAla[1] | 122.8 | 8.02 | 38.6 | 3.35, 3.35 | 37.5 | 2.42, 2.48 | |
| Nle[2] | 126.9 | 8.22 | 56.7 | 4.26 | 33.7 | 1.54, 1.61 | $^{13}C_\gamma$ 29.9; $C_{\gamma\gamma'}H$ 1.15, 1.15; $^{13}C_\delta$ 24.4; $C_{\delta\delta'}H$ 1.20, 1.20; $^{13}C_\varepsilon$ 15.9; $C_\varepsilon H_3$ 0.79; |
| Asp[3] | 119.4 | 8.53 | nd | 4.62 | 40.1 | 2.67, 2.83 | |
| His[4] | 118.2 | 8.59 | nd | 4.41 | 28.3 | 3.04, 3.22 | $C_{\delta 2}H$ 7.10; $^{13}C_{\delta 2}$ 119.9; $C_{\varepsilon 1}H$ 8.51; $^{13}C_{\varepsilon 2}$ 136.3 |
| DPhe[5] | 120.9 | 8.41 | nd | 4.59 | 39.7 | 2.87, 3.12 | $C_{\delta\delta'}H$ 7.20, 7.20; $^{13}C_\delta$ 131.6 $C_{\varepsilon\varepsilon'}H$ 7.33, 7.33; $^{13}C_\varepsilon$ 131.6 $C_\zeta H$ 7.29; $^{13}C_\zeta$ 129.9 |
| Arg[6] | 121.6 | 7.92 | 55.9 | 4.25 | 31.3 | 1.55, 1.59 | $^{13}C_\gamma$ 26.9; $C_{\gamma\gamma'}H$ 1.28, 1.28 $^{13}C_\delta$ 43.3; $C_{\delta\delta'}H$ 3.04, 3.04; $^{15}N_\varepsilon$ 84.9; $N_\varepsilon H$ 7.06 |
| Trp[7] | 122.5 | 8.43 | nd | 4.63 | 29.1 | 3.29, 3.39 | $C_{\delta 1}H$ 7.26; $^{13}C_{\delta 1}$ 127.4 $^{15}N_{\varepsilon 1}$ 129.4; $N_{\varepsilon 1}H$ 10.14; $C_{\varepsilon 3}H$ 7.65; $^{13}C_{\varepsilon 3}$ 121.1 $C_{\zeta 3}H$ 7.14; $^{13}C_{\zeta 3}$ 122.1 $C_{\eta 2}H$ 7.23; $^{13}C_{\eta 2}$ 124.8 $C_{\zeta 2}H$ 7.48; $^{13}C_{\zeta 2}$ 114.8 |
| Lys[8] | 124.8 | 8.07 | 55.8 | 4.23 | 33.2 | 1.59, 1.72 | $^{13}C_\gamma$ 24.6; $C_{\gamma\gamma'}H$ 1.20, 1.30; $^{13}C_\delta$ 29.7; $C_{\delta\delta'}H$ 1.39, 1.50; $^{13}C_\varepsilon$ 41.6 ; $C_{\varepsilon\varepsilon'}H$ 3.17, 3.17; $^{15}N_\zeta$ 126.5; $N_\zeta H$ 7.93 |
| $CONH_2$ | 106.3 | 6.69, 6.84 | | | | | |

| **BFC** | a | B | c | d | e | f | g | h | i | j |
|---|---|---|---|---|---|---|---|---|---|---|
| **$^{1}H$** | 7.99 | Nd | 8.22 | 4.56 | 3.60 | 3.39 | 3.34 | 3.07 | 1.85 | 2.29 |
| **$^{13}C$** | 144.9 | Nd | 137.9 | 49.7 | 55.5 | 52.7 | 37.4 | 56.3 | 22.5 | 35.2 |

### 7.3.46. L15

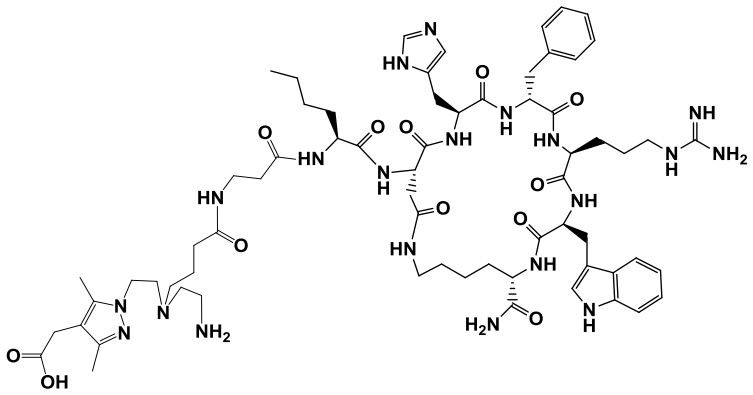

**L15** was prepared according to the methodology described for **L13**. A solution of **βAlaNleCycMSH$_{hex}$** (0.0020 g, 0.002 mmol) in DIPEA (20 μL)/DMF (250 μL) was added to **L12-Boc** (0.0020 g, 0.005 mmol) preincubated for 30 min with HATU (0.0030 g, 0.006 mmol) in DMF. The pH was adjusted to 7-8 with DIPEA and the reaction

mixture was left under stirring at room temperature for 3 hours. The reaction mixture was purified by semi-preparative RP-HPLC (Method J). After evaporation of the solvent, the compound was deprotected with the standard cocktail mixture (9 5% TFA, 2.5 % TIS, 2.5 % $H_2O$) and precipitated with ice-cold diethylether. The precipitate was dried under nitrogen flow and dissolved in water before lyophilization.Yield: 20 % (0.0005 g; 0.0004 mmol; $\varepsilon_{Trp}$ (280 nm) = 5560 L $mol^{-1}$ $cm^{-1}$).

**RP-HPLC** (Method K): 99% ($t_R$ = 11.2 min).

**ESI-MS** (+) (m/z): 682.3 $[M+2H]^{2+}$, calcd. for $C_{66}H_{96}N_{20}O_{12}$ = 1360.7.

### 7.3.47. General method for the preparation of Tc13 – Tc15

In a capped nitrogen purged glass vial, 50 μL of a $10^{-4}$ M solution of the ligands **L13** – **L15** were added to a solution of *fac*-[$^{99m}$Tc(CO)$_3$(H$_2$O)$_3$]$^+$ (450 μL, 37 - 74 MBq) in 0.01 M PBS, pH 7.4. The vial was incubated at 90 °C for 20 min and the resulting complexes were analyzed by RP-HPLC (Method H) using the same method of the rhenium surrogates. Retention times: 11.9 min (**Tc13**), 10.6 min (**Tc14**) and 11.2 min (**Tc15**).

### 7.3.48. L16 and L17

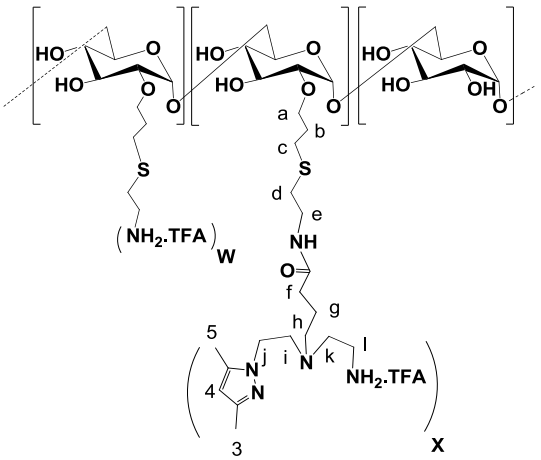


**L16**; W = 26, X = 4

**L17**; W = 22; X = 8

These compounds were synthesized and characterized as previously reported.[154] The $^1$H-NMR spectra of **L16** and **L17** present similar patterns, being the main differences

the intensity ratio of some $^{1}$H-NMR peaks. As an example, $^{1}$H-NMR data for **L16** is presented:

**$^{1}$H-NMR** (300 MHz, $D_2O$): $\delta_H$ (ppm) 5.92 (s, $H^{Pz\text{-}4}$), 4.96 (s, broad, $H_{subst.\ anom.}$), 4.85 (s, broad, $H_{anom.}$), 3.88-3.35 (m, dextran), 3.10 (t, $H^{d}$), 2.74 (t, $H^{e}$), 2.56 (s, broad), 2.27 (t, $H^{h}$), 2.21 (s, $CH_3(3)^{Pz}$), 2.14 (s, $CH_3(5)^{Pz}$), 1.85 (s, broad), 1.74 (s, $H^{b}$).

**L16**: M.W. calculated = 17650 g/mol

**L17**: M. W. calculated = 18650 g/mol

### 7.3.49. L18-Boc and L19-Boc

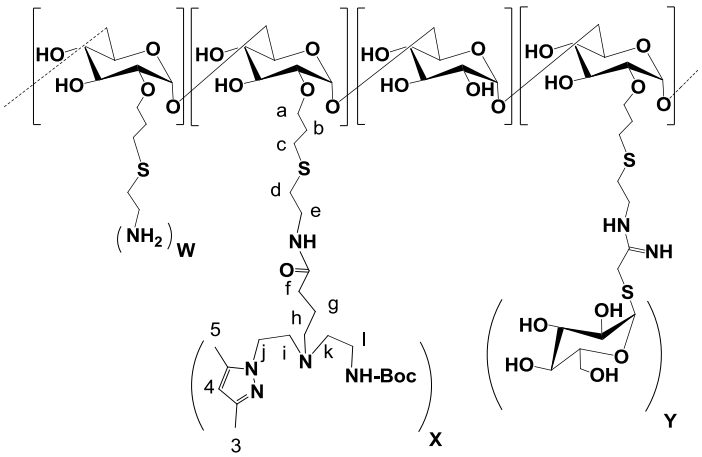


**L18**; W = 13, X = 4, Y = 13

**L19**; W = 9; X = 8; Y = 13

These compounds were synthesized and characterized as previously reported.[154] The $^{1}$H-NMR spectra of **L18-Boc** and **L19-Boc** present similar patterns, being the main differences the intensity ratio of some $^{1}$H-NMR peaks. As an example, $^{1}$H-NMR for **L19-Boc** is presented:

**$^{1}$H-NMR** (300 MHz, $D_2O$): $\delta_H$ (ppm) 5.85 (s, $H^{Pz\text{-}4}$), 5.27 (d, $H_{anom.\ manose}$), 5.01 (s, broad, $H_{anom.\ subst.}$), 4.82 (s, broad, $H_{anom.}$), 3.99 (s, broad), 3.78-3.35 (m, dextran), 2.99-2.76 (m), 2.59 (s, broad), 2.17 (s, $CH_3(3)^{Pz}$), 2.07 (s, $CH_3(5)^{Pz}$), 1.8 (s, broad), 1.31 (s, 9H, $CH_3$).

**L18-Boc**: M.W. calculated = 17693 g/mol

**L19-Boc**: M. W. calculated = 19093 g/mol

### 7.3.50. L18 and L19

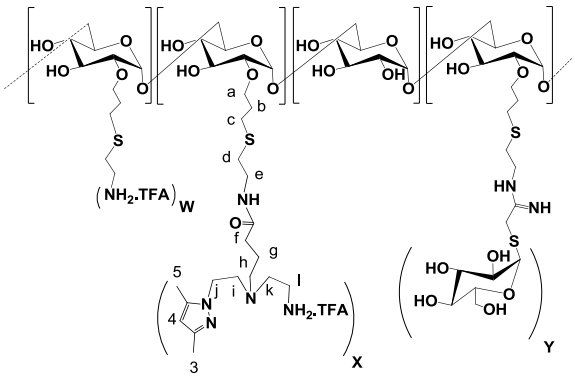

**L18**; W = 13, X = 4, Y = 13

**L19**; W = 9; X = 8; Y = 13

These compounds were synthesized and characterized as previously reported.[154] The $^{1}$H and $^{13}$C-NMR spectra of **L18** and **L19** present similar patterns, being the main differences the intensity ratio of some $^{1}$H-NMR peaks. As an example, NMR and IR data for **L19** is presented:

**IR** (KBr) (ν/cm-1): ν (O-H, br) 3418, ν (C=O, s) 1678, ν (C=O, s, dextran) 1643, 1384, 1261.

**$^{1}$H-NMR** (300 MHz, $D_2O$): $\delta_H$ (ppm) 5.80 (s, $H^{Pz\text{-}4}$), 5.22 (s,broad $H_{mannose\ anom.}$), 4.99 (s, broad, $H_{subst.\ anom.}$), 4.82 (s, broad, $H_{anom.}$), 4.39 (t, $CH_2^{j}$), 3.99 (s, broad), 3.74-3.35 (m, dextran), 3.10 (t, $H^{d}$), 2.74 ( t, $H^{e}$), 2.52 (s, broad), 2.24 (t, $H^{h}$), 2.07 (s, $CH_3^{Pz\text{-}3}$), 1.98 (s, $CH_3^{Pz\text{-}5}$), 1.74 (s, broad, $H^{b}$), 1.46 (t, $H^{g}$);

**$^{13}$C-NMR** (75.3 MHz, $D_2O$): $\delta_C$ (ppm) 176.4 (C=O), 165.9 (C=N), 162.8 (q, $CF_3COO^-$), 150.5 ($C^{Pz\text{-}3}$), 143.7 ($C^{Pz\text{-}5}$), 116.5 (q, $CF_3COO^-$), 107.4 ($C(4)^{Pz}$), 99.9 ($C_{anom.}$), 97.8 ($C_{subst.\ anom.}$), 86.9, 86.7, 82.4, 81.5 ($C^{a}$), 75.8-68.9 (m, 11C $_{dextran/mannose}$), 68.5, 67.4, 63.1, 62.8 ($C^{k}$), 54.5 ($C^{i}$), 52.3, 47.9 ($C^{j}$), 43.9 ($C^{l}$), 40.6 ($C^{e}$), 39.3, 35.2, 31.0, 30.8 ($C^{d}$), 30.3 ($C^{c}$), 29.6, 29.1 ($C^{b}$), 24.4 ($C^{g}$), 14.3 ($CH_3^{Pz\text{-}5}$), 12,3 ($CH_3^{Pz\text{-}3}$).

**L18**; M.W. calculated = 19231 g/mol;

**L19**; M. W. calculated = 20231 g/mol

**SEC-HPLC** (method L): 99% (**L18**: $t_R$ = 14.4 min); 99% (**L19**: $t_R$ = 14.6 min).

**RP-HPLC** (method M): 99% (**L18**: $t_R$ = 11.5 min); 99% (**L19**: $t_R$ = 11.6 min).

### 7.3.51. General method for the preparation of Re18 and Re19

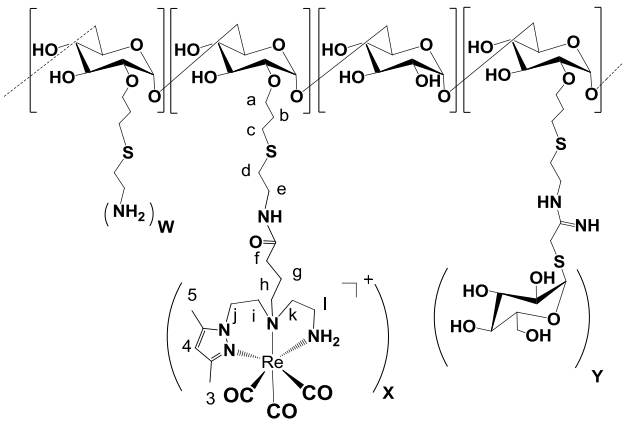

**Re18**; W = 13, X = 4, Y = 13

**Re19**; W = 9; X = 8; Y = 13

Reaction of *fac*-[Re(CO)$_3$(H$_2$O)$_3$]Br with **L18** (0.0500 g, 0.003 mmol) and **L19** (0.0500 g, 0.003 mmol) in water using a rhenium precursor/chelating unit molar ratio of 4:1. After stirring at 50 ºC for 16 h, the reaction mixtures were concentrated, dialyzed against water and the retentate concentrated and lyophilized. The resulting pale yellow powder was washed with $CH_2Cl_2$ and methanol. The progress of these reactions was monitored by taking aliquots of the reaction mixture at several time points. The aliquots were dried under reduced pressure, washed with chloroform and methanol, yielding a yellow solid that was analyzed by RP-HPLC and $^1$H-NMR spectroscopy. When complete, the reaction mixture was treated as referred above and the solids obtained were formulated as **Re18** and **Re19**.

**Re18**: M[$(C_6H_{10}O_5)_{30}$ $(C_{11}H_{21}NO_5S.C_2HF_3O_2)_{13}$$(C_{27}H_{43}N_5O_9SRe)_4$ $(C_{19}H_{34}N_2O_{10}S_2)_{13}$] = 19850 g/mol. Yield: 80 % (0.0400 g, 0.002 mmol).

**Re19**: M[$(C_6H_{10}O_5)_{30}$ $(C_{11}H_{21}NO_5S.C_2HF_3O_2)_9$ $(C_{27}H_{43}N_5O_9SRe)_8$ $(C_{19}H_{34}N_2O_{10}S_2)_{13}$] = 21479 g/mol. Yield: 80 % (0.0400 g, 0.002 mmol).

**IR** (KBr) (ν/cm$^{-1}$): ν (O-H, br) 3397, ν (C-H, m) 2950, ν (C≡O, s) 2027, ν (C≡O, w) 1999, ν (C≡O, s) 1899, ν (C=O, s) 1678, ν (C=O, s, dextran) 1643, 1556, 1384.

The $^1$H- and $^{13}$C-NMR spectra of **Re18** and **Re19** present similar patterns. As an example, NMR data for **Re19** is presented:

**$^1$H-NMR** (300 MHz, $D_2O$): $\delta_H$ (ppm) 6.1 (s, H(4)$^{Pz}$), 5.23 (d, $H_{mannose\ anom.}$), 4.98 (s, broad, $H_{subst.\ anom.\ dextran}$), 4.80 (s, broad, $H_{anom.}$), 4.39 (t, $CH_2^j$), 3.99 (s, broad), 3.74-3.35 (m, dextran), 3.10 (t, H$^d$), 2.71 (t, H$^e$), 2.52 (s, broad), 2.21 (s, $CH_3^{Pz-3}$), 2.12 (s, $CH_3^{Pz-5}$), 1.91 (t, H$^g$), 1.73 (s, broad, H$^b$).

**$^{13}$C-NMR** (75.3 MHz, $D_2O$): $\delta_C$ (ppm) 195.2 (ReCO), 194.7 (ReCO), 193.1 (ReCO), 176.2 (C=O), 165.4 (C=N), 168.2 (q, $CF_3COO^-$), 153.7 ($C^{Pz\text{-}3}$), 144.3 ($C^{Pz\text{-}5}$), 118.5 (q, $CF_3COO^-$), 114.6 ($C^{Pz\text{-}4}$), 108.1 (CH), 97.9 ($C_{\text{dextran anom.}}$), 96.1 ($C_{\text{dextran subst. anom.}}$), 85.1, 79.5-65.7 (11C), 60.9 (CH), 42.0 (CH), 38.7, 33.8, 32.9, 30.7 ($C^h$), 30.9, 30.0, 27.3, 20.3, 15.5 ($CH_3^{Pz\text{-}5}$), 11.1 ($CH_3^{Pz\text{-}3}$).

**SEC-HPLC** (method L): 99% (**Re18**: $t_R$ = 14.4 min); 99% (**Re19**: $t_R$ = 14.6 min).

**RP-HPLC** (method M): 99% (**Re18**: $t_R$ = 12.2 min); 99% (**Re19**: $t_R$ = 12.2 min).

### 7.3.52. 2-((E)-2-((E)-2-(4-carboxyphenylthio)-3-((Z)-2-(1,3,3-trimethylindolin-2-ylidene)ethylidene)cyclohex-1-enyl)vinyl)-1,3,3-trimethyl-3H-indolium (IX)

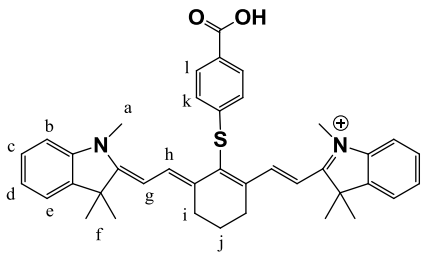


To a solution of **IR775-Cl** (0.1000 g, 0.200 mmol) in anhydrous DMF (4 mL) was added 4-mercaptobenzoic acid (0.0360 g, 0.200 mmol) and the resulting green reaction mixture was allowed to stir in the dark. After 15 h, the reaction was complete as monitored by TLC (15% $CH_2Cl_2$/ MeOH) and the solvent was evaporated. The solid residue was washed with a solution of acetic acid 5% (3x) and **IX** was sufficently pure to be used in the next step. Yield: 85% (0.0990 g; 0.160 mmol). $R_f$ = 0.63.

When impurites were found in the TLC, the crude was purified by flash chromatography ($CHCl_3$/ methanol, 1-15%), giving **IX** as a green solid. Yield: 35% (0.0400 g; 0. 0714 mmol).

**$^1$H-NMR** (300 MHz, $CDCl_3$): $\delta_H$ (ppm) 8.69 (d, $CH^e$, 2H), 8.04 (d, $CH^c$, 2H), 7.28 (t, $CH^d$, 2H), 7.22 (t, $CH^b$, 2H), 7.06 (dd, $CH^{l/k}$, 4H), 6.07 (d, $CH^{g/h}$, 2H), 3.55 (s, $CH_3^a$, 3H), 2.67 (t, $CH^i$, 2H), 1.98 (t, $CH^j$, 1H), 1.39 (s, $CH_3^f$, 6H).

**$^{13}$C-NMR** (75.3 MHz, $CDCl_3$): $\delta_C$ (ppm) 172.8 (CH), 150.2 (CH), 145.8 (CH), 142.5 (CH), 140.8 (CH), 133.9 (CH), 130.8 (CH), 128.6 (CH), 125.3 (CH), 122.0 (CH), 110.6, 101.6 (CH), 49.0 (CH), 45.8 (CH), 31.6 (CH), 27.6 (CH), 26.3 (CH), 20.6 (CH), 8.6 (CH).

**$\lambda_{max, abs}$** ($H_2O$/20% DMSO): 795 nm; $\varepsilon$ = 125 052 L mol$^{-1}$ cm$^{-1}$;

$\lambda_{max, abs}$ (EtOH): 778 nm; ε = 103560 L $mol^{-1}$ $cm^{-1}$;

**RP-HPLC** (Method M): 99% ($t_R$ = 19.2 min);

**SEC-HPLC** (Method L): 99% ($t_R$ = 29.1 min);

**ESI-MS** (+) (m/z): 601.4 $[M+H]^+$, calcd. for $C_{39}H_{41}N_2O_2S$ = 601.9.

*Determination of the molar extinction coefficient of **IX***

The molar extinction coefficient of **IX** was determined by using a standardized curve prepared from known quantities of the fluorophore (0.5 – 2.5 μg). Briefly, different amounts of **IX** were dissolved in 0.5 mL of 20% DMSO aqueous solution and absorbance reading was taken at 795 nm. The calibration curve obtained for **IX** was: y = 125052.8 x; $R^2$ = 1.00

### 7.3.53. 2-((E)-2-((E)-2-(4-((2,5-dioxopyrrolidin-1-yloxy)carbonyl)phenylthio)-3-((Z)-2-(1,3,3-trimethylindolin-2-ylidene)ethylidene)cyclohex-1-enyl) vinyl)-1,3,3-trimethyl-3H-indolium (X)

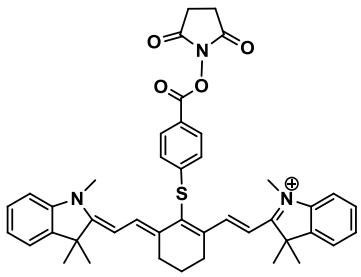

To a solution of **IX** (0.0200 g, 0.030 mmol) in anhydrous $CH_2Cl_2$ (5 mL) was added 1-ethyl-3-(3-dimethylaminopropyl)carbodiimide) (EDC: 0.0050 g, 0.050 mmol) and N-hydroxysuccinimide (NHS: 0.0040 g, 0.040 mmol). After 12 h, the reaction was complete as monitored by TLC (15% $CH_2Cl_2$/ MeOH) and the solvent was evaporated. The solid residue was washed with water and **X** was immediatly used in the next step. $R_f$ = 0.75.

### 7.3.54. L20-Boc

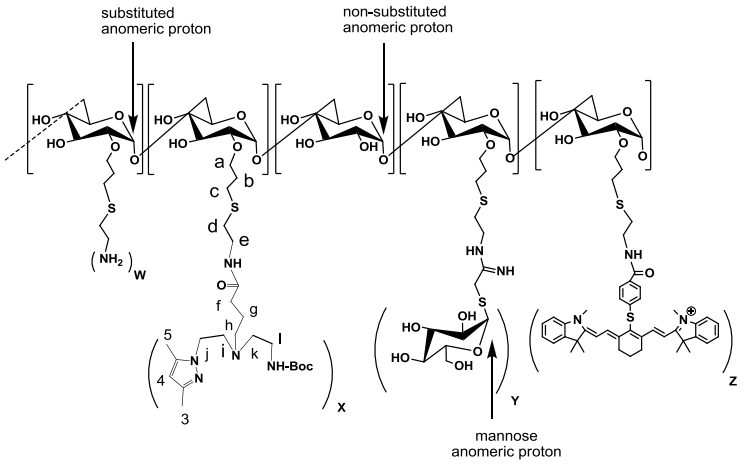


**W** = 6, **X** = 8, **Y** = 13, **Z** = 3

To a solution of **L19-Boc** (0.0500 g, 0.002 mmol) in DMSO/0.1 M borate buffer, pH 9 (1:1, 5mL) was added the precursor **X** (0.0600 g, 0.100 mmol) dissolved in acetonitrile. After overnight reaction at room temperature, the mixture was filtered and dialyzed against water. The solvent was removed under reduced pressure and the green solid was washed with $CH_2Cl_2$ (3x) and cold EtOH (3x) before lyophilization.

**L20-Boc**: $M[(C_6H_{10}O_5)_{30}(C_{11}H_{21}NO_5S)_5(C_{29}H_{51}N_5O_8S)_8(C_{19}H_{34}N_2O_{10}S_2)_{13}(C_{50}H_{60}N_3O_6S_2)_4]$ = 21434 g/mol.

Yield: 53 % (0.0300 g, 0.001 mmol)

**$^1$H-NMR** (300 MHz, $D_2O$): $\delta_H$ (ppm) 5.74 (s, $H^{Pz\text{-}4}$), 5.19 (d, $H_{mannose\ anom.}$), 4.99 (s, broad, $H_{subst.\ anom.\ dextran}$), 4.77 (s, broad, $H_{anom.}$), 3.88-3.35 (m, dextran; mannose), 3.08 (t, $H^d$), 2.67 (t, $H^e$), 2.49 (s, broad), 2.07 (s, $CH_3^{Pz\text{-}3}$), 1.97 (s, $CH_3^{Pz\text{-}5}$), 1.71 (s, broad, $H^b$), 1.52 (s, $H^g$), 1.22 (s, $(CH_3)_3$).

### 7.3.55. L20

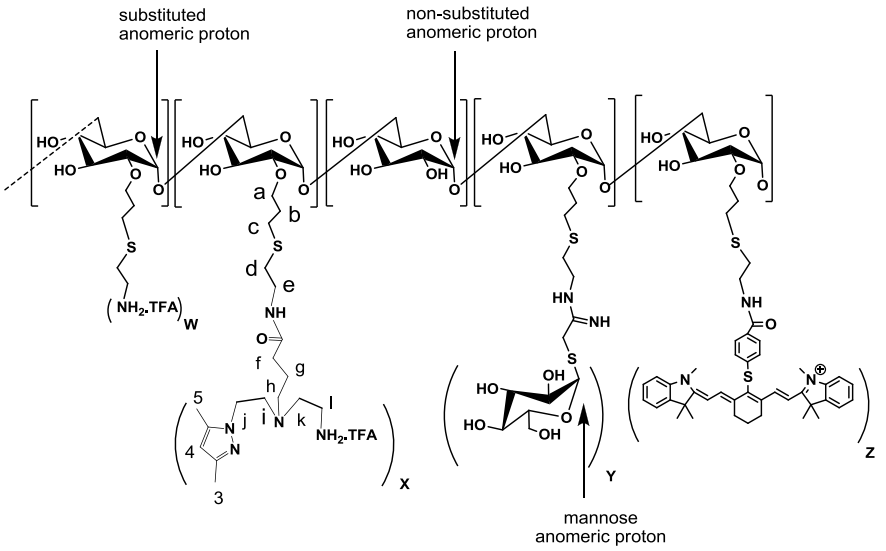


**W** = 6, **X** = 8, **Y** = 13, **Z** = 3

Deprotection of **L20-Boc** (0.0300 g, 0.001 mmol) with TFA (5 mL) gave a green mixture that was washed with $CH_2Cl_2$ (3x), cold EtOH (3x) and purified by sephadex G-25 gel filtration (eluent: NaCl 0.9%). Dyalisis and liofilization of the eluted gave **L20** as green solid.

**L20**: $M[(C_6H_{10}O_5)_{30}\ (C_{11}H_{21}NO_5S.C_2HF_3O_2)_5\ (C_{24}H_{43}N_5O_6S.\ C_2HF_3O_2)_8\ (C_{19}H_{34}N_2O_{10}S_2)_{13}\ (C_{50}H_{60}N_3O_6S_2)_4] = 22116$ g/mol.

Yield: 66 % (0.0200 g, 0.001 mmol)

**$^1$H-NMR** (300 MHz, $D_2O$): $\delta_H$ (ppm) 5.79 (s, $H^{Pz\text{-}4}$), 5.30 (d, $H_{mannose\ anom.}$), 5.06 (s, broad, $H_{subst.\ anom.\ dextran}$), 4.80 (s, broad, $H_{anom.}$), 4.32 (t, $H^j$) 3.90-3.17 (m, dextran and mannose), 2.80 (t, $H^d$), 2.70 (t, $H^e$), 2.51 (s, broad), 2.34 (t, $H^h$), 2.10 (s, $CH_3^{Pz\text{-}3}$), 2.00 (s, $CH_3^{Pz\text{-}5}$), 1.71 (s, broad, $H^b$), 1.48 (s, $H^g$).

**$\lambda_{max,\ abs}$** ($H_2O$/20% DMSO): 802 nm; **$\lambda_{max,\ em}$** = 826 nm

**SEC-HPLC** (method L): 99% ($t_R$ = 11.2 min);

**RP-HPLC** (method M): 99% ($t_R$ = 15.6 min)

*Quantification of glucose content in* **L20**

The glucose content of **L20** was determined from interpolation through a standardized curve prepared from glucose assays on samples with known quantities of that sugar (8 –

55 µg). Briefly, to a 10 mL test tube containing aqueous solution of **2** (0.5 mL) and 5% phenol solution (0.5 mL) was added 2.5 mL of 18 M $H_2SO_4$. The exothermic reaction was vortexed for one minute and allowed to cool to room temperature for 20 minutes, after which an absorbance reading at 490 nm was taken. The calibration curve obtained for glucose was: y = 12359 x + 0.028; $R^2$ = 0.9973

Absorbance data for 20 µg of **L20** was 0.291 ± 0.11 (λ = 490 nm), based on three determinations. The glucose concentration found for **L20** was 21.0 ± 0.03 µM.

*Quantification of fluorophore content in* **L20**

Compound **L20** (0.001 g) was dissolved in 20% DMSO aqueous solution (0.5 mL). Absorbance data for 20 µg of **L20** was 0.159 ± 0.02 (λ = 802 nm), based on three determinations. The fluorophore concentration found for **L20** was 1.3 ± 0.02 µM.

### 7.3.56. Re20

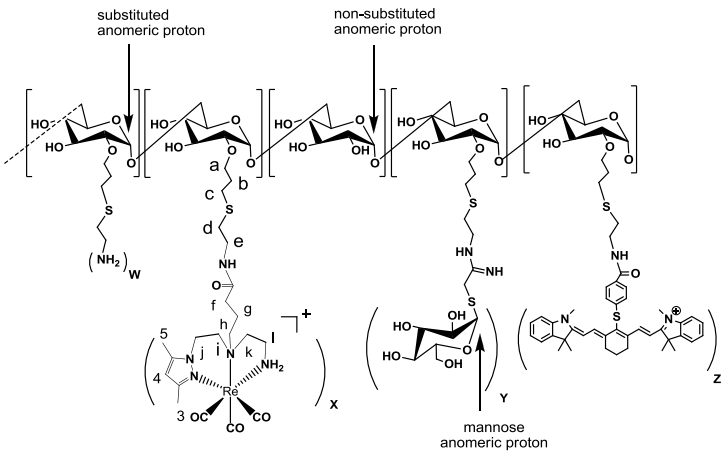


**W** = 6, **X** = 8, **Y** = 13, **Z** = 3

To a solution of **Re19** (0.0400 g, 0.002 mmol) in 5 mL of DMSO/0.1 M borate buffer, pH 9 (1:1) was added the precursor **X** (0.006 g, 0.01 mmol) dissolved in acetonitrile. After 8 h under stirring at room temperature, the mixture was filtered, and dialyzed against water. The solvent of the retentate was evaporated under reduced pressure and the green solid was washed with $CH_2Cl_2$ (3x) and cold EtOH (3x) before purification by sephadex G-25 gel filtration. Dyalisis and liofilization of the eluted gave **Re20** as green solid.

**Re20**: $M[(C_6H_{10}O_5)_{30}(C_{11}H_{21}NO_5S.C_2HF_3O_2)_5(C_{27}H_{43}N_5O_9SRe)_8(C_{19}H_{34}N_2O_{10}S_2)_{13}(C_{50}H_{60}N_3O_6S_2)_4]$ = 23364 g/mol.

Yield: 50 % (0.0200 g, 0.001 mmol)

**IR** (KBr) ($\nu/cm^{-1}$): ν (O-H, br) 3423, ν (C-H, m) 2924, ν (C≡O, s) 2027, ν (C≡O, w) 1914, ν (C≡O, s) 1679, ν (C=O, s) 1650, ν (C=O, s, dextran) 1543, 1434, 1385.

**$^1$H-NMR** (300 MHz, $D_2O$): $\delta_H$ (ppm) 6.12 (s, $H^{Pz\text{-}4}$), 5.21 (d, $H_{mannose\ anom.}$), 4.97 (s, broad, $H_{subst.\ anom.\ dextran}$), 4.82 (s, broad, $H_{anom.\ dextran}$), 4.32 (d, $CH_2^j$), 3.99 (s, broad), 3.74-3.35 (m, dextran and mannose), 3.10 (t, $H^d$), 2.71 (t, $H^e$), 2.52 (s, broad), 2.21 (s, $CH_3^{Pz\text{-}3}$), 2.12 (s, $CH_3^{Pz\text{-}5}$), 1.91 (t, $H^g$), 1.73 (s, broad, $H^b$).

**$\lambda_{max,\ abs}$** ($H_2O$/20% DMSO): 805 nm.

**SEC-HPLC** (method L): 99% ($t_R$ = 11.3 min).

**RP-HPLC** (method M): 99% ($t_R$ = 15.2 min).

*Quantification of glucose content in* **Re20**

Following the same methodology described for **L20**, the absorbance data for 20 μg of **Re20** was 0.301 ± 0.08 (λ = 490nm), based on three determinations. The glucose concentration found for **Re20** was 22.1 ± 0.08 μM.

*Quantification of fluorophore content in* **Re20**

Following the same methodology described for **L20**, the absorbance data for 20 μg of **Re20** was 0.157 ± 0.03 (λ = 802 nm), based on three determinations. The fluorophore concentration found for **Re20** was 1.3 ± 0.03 μM.

### 7.3.57. General method for the preparation of Tc18 – Tc20

In a capped nitrogen purged glass vial, 100 μg of solution of the ligands **L18** – **L20** were added to a solution of *fac*-$[^{99m}Tc(CO)_3(H_2O)_3]^+$ (1 mL, 74 - 222 MBq) in 0.01 M PBS, pH 7.4. The vial was incubated at 90 °C for 10 min and the resulting compounds were analyzed by RP-HPLC (Method M) using the same method of the rhenium surrogates. Retention times: 12.2 min (**Tc18**), 12.2 min (**Tc19**) and 15.6 min (**Tc20**).

### 7.3.58. Quantification of the NIR emission for L20 and Tc20

The NIR emission of equimolar (1.8 nM) solutions of **L20** and **Tc20** was quantified in an Odyssey Infrared Imaging system (LI-COR Biosciences, Lincoln, NE, USA) with both 700- and 800-nm channels by scanning the application of both compounds in ITLC SG-PALL strips.

## 7.4. Partition coefficient

The partition coefficient was evaluated by the ‘‘shakeflask’’ method.[151] The radioconjugate was added to a mixture of octanol (1 mL) and 0.1 M PBS, pH 7.4 (1 mL) which had been previously saturated with each other by stirring. This mixture was vortexed and centrifuged (3,000 rpm, 10 min) to allow phase separation. Aliquots of both octanol and PBS were counted in a γ-counter. The partition coefficient in octanol/ water (log $P_{o/w}$) was calculated by dividing the counts in the octanol phase by those in the buffer, and the results were expressed as log P(o/w) ± the standard deviation.

## 7.5. *In vitro* stability studies

The *in vitro* stability of the $^{99m}$Tc(I) complexes was evaluated by RP-HPLC analysis of cysteine, histidine and human serum aliquots.

**Cysteine and histidine challenge**: Aliquots of the $^{99m}$Tc(I) complexes (100 μL) were added to 5 x $10^{-3}$ M cysteine or histidine solutions in PBS, pH 7.4 (400 μL). The resulting solutions were incubated at 37 ºC for 24 h and analyzed by analytical RP-HPLC.

**Human serum**: The *in vitro* stability of the radioactive compounds was determined in aliquots of fresh human serum obtained from a healthy volunteer. The volunteer was recruited and asked to provide informed consent. The $^{99m}$Tc complex (100 μL, approximately 18 MBq) was added to fresh human serum (1 mL), and the mixture was incubated at 37 ºC. At appropriate time points (2, 4, and 6 h), 100 μL aliquots (in duplicate) were sampled and treated with 200 μL of EtOH to precipitate the proteins. Samples were centrifuged at 3,000 rpm for 15 min at 4 ºC, and the supernatant was

analyzed by HPLC. The stability of the radiolabeled conjugate in the solutions containing 0.2% BSA was checked by RP-HPLC using the chromatographic methods previously described and by instant thin-layer chromatography (5% 6 M HCl in MeOH).

## 7.6. Cell Culture

B16F1 murine melanoma cells (ECACC, Porton Down, UK) were grown in DMEM containing GlutaMax I supplemented with 10% heat-inactivated fetal bovine serum and 1% penicillin/streptomycin antibiotic solution (all from Gibco-Invitrogen). Cells were cultured in a humidified atmosphere of 95% air and 5% CO2 at 37 ºC (Heraeus, Germany), with the medium changed every other day. The cells were adherent in monolayers and, when confluent, were harvested from the cell culture flasks with trypsin–EDTA (Gibco-Invitrogen) and seeded further apart.

### 7.6.1. Competitive binding assay

#### 7.6.1.1. [$^{125}$I]-NDP-α-MSH

Radioiodination of NDP-α-MSH with $^{125}$I was performed by the chloramine-T method with small modifications.[140] Briefly, NDP-α-MSH (5 μg; 3. 03 nmol) in 0.3 M PBS (50 μL) was mixed with Na$^{125}$I (10 μL, 83 MBq) and then 10 μL of a chloramine-T (8.1 nmol) solution in 0.3 M PBS (2 mg/mL) was added. After incubation for 5 min at room temperature, the reaction was stopped with 500 μL of dithiothreitol (20 mg/mL) and 100 μL of BSA (10 mg/mL) were added before purification. The mixture was loaded into a small reversed-phase cartridge (Sep-Pak C18, Waters) which was eluted in a first step with TFA aqueous solution (0.1% TFA, 5 mL), followed by methanol (100%). The iodinated peptide was eluted with methanol and collected in fractions of 500 μL, which were stored at –20°C. Preceding each binding experiment, an additional purification was performed by RP-HPLC. Analytical purification of [$^{125}$I]-NDP-MSH was achieved by analytical RP-HPLC (Method F) with simultaneous radioactivity and UV detection (258 nm).

#### 7.6.1.2. Determination of $IC_{50}$

The inhibitory concentration of 50% ($IC_{50}$) values for the α-MSH analogs were determined by competitive binding assays with [$^{125}$I]-NDP-MSH in B16F1 melanoma cells. Cells were harvested, seeded into a 24-well cell culture plates (2 x $10^5$ cells per well), and allowed to attach overnight. After they had been washed once with the binding medium [0.3 mL, DMEM with 25 mM N-(2- hydroxyethyl)piperazine-N0-ethanesulfonic acid and 0.2 % BSA], the cells were incubated at room temperature (25 ºC) for 2 h with [$^{125}$I]-NDP-MSH (50,000 Cpm in 0.2 mL) and the competitor peptide solution (0.1 mL), yielding a final concentration ranging from 1 x $10^{-5}$ to 1 x $10^{-12}$ M. The reaction medium was then removed, and the cells were washed twice with cold 0.01 M PBS pH 7.2 with 0.2% BSA (0.5 mL) and lysed with 1 M NaOH (0.5 mL) for 5 min. The radioactivity of the lysate was measured with a γ-counter. The competitive binding curves were obtained by plotting the percentage of [$^{125}$I]-NDP-MSH bound to the cells *versus* the concentrations of displacing peptides. $IC_{50}$ values for the peptides were calculated by using GraphPad Prism. All cell binding experiments were conducted in triplicate.

### 7.6.2. Internalization and cellular retention studies

Internalization assays of the radiopeptides were performed in B16F1 murine melanoma cells seeded at a density of 0.2 million per well in plates and allowed to attach overnight. The cells were incubated at room temperature or 37 ºC for a period of 5 min to 4 h with about 200,000 Cpm of the conjugate in 0.5 mL of assay medium [DMEM with 25 mM N-(2-hydroxyethyl)piperazine-N-ethanesulfonic acid and 0.2% BSA]. Incubation was terminated by washing the cells with ice-cold assay medium. Cell-surface-bound radioligand was removed by two steps of acid wash (50 mM glycine, HCl/100 mM NaCl, pH 2.8) at room temperature for 5 min. The pH was neutralized with cold PBS with 0.2% BSA, and subsequently the cells were lysed by 10 min incubation with 1 M NaOH at 37 ºC to determine internalized radioligand. For assessing the specific MC1R-mediated uptake and internalization, a parallel study was performed using NDP–MSH (3.5 μg per well) to block the MC1Rs. To determine the retention properties of the internalized radioconjugates, B16F1 cells were first incubated with the radioligands for 3 h at 37 °C to allow internalization. The cells were washed with cold

assay medium (to stop the internalization) and with acid buffer (to remove the membrane-bound radioactivity). Finally, the cells were incubated with culture medium (0.5 mL) during 4 h at 37 °C. At different time points (10 min, 30 min, 1, 2, 3, and 4 h), the radioactivity released in the medium (externalized radioactivity) as well as the radioactivity retained in the cells (lysed with NaOH, 1M) was collected and counted.

### 7.7. Biodistribution studies

**Evaluation of $^{99m}$Tc(I)-labeled peptides**

All animal experiments were performed in compliance with national and European regulations for animal treatment. The animals were housed in a temperature- and humidity-controlled room with a 12 h light/12 h dark schedule. Biodistribution of the radiopeptides was performed in melanoma-bearing C57BL/6 female mice (8–10 weeks old). The mice had previously been implanted subcutaneously with 1 x $10^6$ B16F1 cells to generate a primary skin melanoma. 10 to 12 days after the inoculation, tumors reached a weight of 0.2–1 g. Radiolabeled peptides (26 – 37 MBq) diluted in 100 μL of PBS, pH 7.2 was intravenously injected into the retroorbital sinus of the mice. The mice (n = 3–5 per time point) were killed by cervical dislocation at 1 and 4 h p.i. Administered radioactivity and the radioactivity in the killed animals were measured using a dose calibrator (Curiemeter IGC-3, Aloka, Tokyo, Japan or Carpintec CRC-15W, Ramsey, USA). The difference between the radioactivity in the injected and that in the killed animals was assumed to be due to excretion. Tumors and normal tissues of interest were dissected, rinsed to remove excess blood, weighed, and their radioactivity was measured using a γ-counter (LB2111, Berthold, Germany). The uptake in the tumor and healthy tissues of interest was calculated and expressed as a percentage of the injected radioactivity dose per gram of tissue. For blood, bone, muscle, and skin, total activity was estimated assuming that these organs constitute 6, 10, 40, and 15% of the total body weight, respectively. Urine was also collected and pooled together at the time the mice were killed.

## Evaluation of the $^{99m}$Tc(I)-model Complexes

The biodistribution of the 99mTc complexes Tc3, Tc10 and Tc11 was evaluated in groups of 3 - 4 CD-1 female mice (Charles River outbred strain, from IFFA CREDO, Barcelona, Spain). Mice were intravenously injected with 100 μl of each complex (3 - 10 MBq) via the tail vein and the animals were kept in normal diet *ad libitum*. Animals were sacrificed by cervical dislocation at 1 and 4 h after injection. The administered dose and the radioactivity in the sacrificed animals were measured with a dose calibrator (Curiemeter IGC-3, Aloka, Tokyo, Japan or Carpintec CRC-15W, Ramsey, USA). The difference in radioactivity between the injected animal and the sacrificed animal was assumed to be due to excretion. Tissues and organs of interest were dissected, rinsed to remove excess blood, weighted, and their radioactivity was measured using the dose calibrator or a γ-counter. The uptake in the tissues or organs was calculated and expressed as percent injected dose per gram of tissue or organ (% IA/g). For blood, bone, muscle, and skin, total activity was estimated assuming that they represent 6, 10, 40, and 15 % of the total body weight, respectively.

## Evaluation of $^{99m}$Tc(I)-labeled Mannosylated Dextran Derivatives

Biodistribution of mannosylated dextran derivatives **Tc18** – **Tc20** was performed in female Wistar rats weighing 200-250 g were used in the experiment. The animals were first anesthetized by intraperitoneal injection of a mixture of xylazine (70 mg/kg) and ketamine (7 mg/kg) or Nembutal (0.1mL/ 100 mg). Boosters if subsequently required were given using ketamine alone. Then ~50 μL of the $^{99m}$Tc-labeled preparation (37 MBq, containing ≈ 20 μg of the polymer) was injected subcutaneously in the footpad region. The area of injection was massaged gently with a strip of gauze pad for about 2 min to facilitate movement of the radiolabeled preparation from the injection site. The rejection criterion followed was observation of any bleeding at the site of injection or measurement of more than 0.5% of administered dose on the gauze pad. The animals were kept in separate sets (n = 4 per set) p.i. for incubation periods of 15 min, 30 min, 60 min and 180 min under normal conditions, water provided *ad libitum*. In the case of **Tc18** and **Tc19**, ten minutes prior to the end of each incubation period, the animals injected under anesthetized condition were given a subcutaneous administration of ~50 μL of Patent Blue Dye (1% w/v in saline) in the same region as the labeled preparation.

At the end of the incubation, the animals were sacrificed and the relevant organs and tissues, including the popliteal (which serves as the sentinel lymph node in this protocol) and secondary nodes, were excised for the determination of in vivo distribution of $^{99m}$Tc activity. Radioactivity measurement was done on Integral Line flat-bed NaI(Tl) scintillation detector (Harshaw, USA). Activity retained in each organ/tissue was expressed as a percentage of the total injected activity (% IA).
In the case of **Tc20**, the fluorescent component enabled the excision of the popliteal and secondary node, after the animals were sacrificed. The relevant organs and tissues were excised for the determination of *in vivo* distribution of $^{99m}$Tc activity.

### 7.7.1. *In vivo* Stability

The *in vivo* stability of the $^{99m}$Tc(I) complexes was evaluated by RP-HPLC analysis of urine and blood.

**Urine:** The urine collected at the sacrifice time was centrifuged at 3000 rpm for 15 min and the supernatant was analyzed by RP-HPLC.

**Blood:** The blood was collected at the sacrifice time, centrifuged at 3000 rpm for 15 min at 4 °C, and the serum was separated. 100 μl aliquots of serum were sampled and treated with 200 μl of EtOH to precipitate the proteins. Samples were then centrifuged at 3000 rpm for 15 min at 4 °C. The supernatant was analyzed by RP-HPLC.

**Homogenates**: Liver, kidney and tumor were homogenized with a glass-homogenizer (Potter) in 50 mM Tris buffer with 0.2M sucrose, pH 7.4. The homogenate was then centrifuged at 4°C (20000 × g for 10 minutes). The supernatant was treated with ethanol in a 1:1 (v/v) ratio to precipitate the proteins, centrifuged again and the resulting supernatant injected into the HPLC.

## 7.8. Imaging Studies

For scintigraphic imaging, the animals were anesthetized using a mixture of ketamine and xylazine (80 and 20 mg/ml, respectively), injected with the radiopeptides (21 MBq) and placed over a γ camera (GE 400AC; Maxicamera, Milwaukie, USA) coupled with a

high-resolution parallel collimator and controlled with GENIE Acquisition computer. A set of dynamic images (60 images of 128×128 matrix, Zoom 2, with individual duration of 30 s), followed by static images (256×256 matrix, Zoom 2, 2 min), each lasting for 30 min until 2 h, was acquired.

Scintigraphic imaging of **Tc18** and **Tc19** were performed on the Millennium MPS medical imaging system (Wipro-GE Healthcare, India). Scintigraphic imaging studies for 13 and 14 were also performed in Wistar rat model. ~ 37 MBq of the radiolabeled preparation (in 50 μL volume) was used for each imaging study (n = 3). The technique employed for anesthesia of animals and administration of 13 and 14 preparations was the same as for the above-referred biodistribution studies, excepting that blue dye was not injected in the imaging protocol. For the acquisition, the animals were placed with their dorsal side facing the camera. Planar static images were acquired at 10 min, 30 min, 60 min and 180 min p.i. using the Genie Acq Image Acquisition software (release 3.0). Acquisition parameters were as follows: matrix 256 x 256, zoom 1.33, 5 min acquisition time. The site of injection was masked with lead shielding during acquisition. Subsequent image processing was achieved with the Xeleris image processing software (version 1.0272).

SPECT-CT imaging of **Tc19** was performed in Wistar rat. A 50 μL solution of **Tc19** (0.5−2 MBq containing $1 \times 10^{-9}$ mol) was injected subcutaneously in the rear footpad. Three animals were used for each imaging study. After anesthetizing with Isofluran, SPECT images were taken with SPECT/CT (FX-3000, Gamma Medica Ideas Inc., Northridge, CA, USA) at 60 min p.i.

SPECT/micro-CT was performed after an intravenous injection of 3.7 MBq (20 μg, 1 x $10^{-9}$ mol) of **Tc20**. Images were taken 1 h p.i. Micro-CT imaging was performed prior to single pinhole SPECT at 1 h p.i. The CT-scan was obtained with a dual-source CT-scanner (Skyscan 1178; Skyscan) at 60 kV and 615mA, with a resolution of 83 mm. Images were reconstructed by performing filtered back projection (NRecon; Skyscan). Total body SPECT was performed with a dual-head g-camera (e.cam180; Siemens Medical Solutions), constructed with two single pinhole collimators (1.5mm; 25.7cm radius of rotation). Images were acquired in 64 projections with 20 s per step over 360.

Images were reconstructed with an iterative reconstruction algorithm and reoriented for fusion with micro-CT images.

NIR image acquisition of **L20** and **Tc20** was performed in a FLuoBeam800 (FluOptics, Grenoble, France), exciting the near-infrared fluorophore at 780 nm and a charge-coupled-device (CCD) camera that detects fluorescence emission above 800 nm. Data were collected over a 150-750 milliseconds (ms) exposure. Image processing was performed with Photoshop. The FLuoBeam800 was used for real time fluorescence-guided node excision.

### 7.9. Histology

Immediately following excision, lymph nodes were weighed and then coated in optimal cutting temperature (OCT) compound (Sakura Tissue-Tec # 4585) cryogenic embedding medium to prevent lymph nodes from becoming dehydrated during overnight scintillation counting. Lymph nodes were frozen at -80 °C for extended periods of time in this preservative. Frozen sections (5 $\mu$m) of the lymph nodes were imaged under NIR conditions on an EVOS Fl (Digital Fluorescence Microscope), AMG (Advanced Microscopy Group), Bothell, WA, USA. To allow imaging at 800 nm, Cy7 light cube from AMG was used. The 4',6-diamidino-2-phenylindole (DAPI) light cube was used for imaging DAPI stained tissue samples (objective: 40x).

# References

## References


1. de Hevesy, G. Nobel lecture: Some applications of isotopic indicators [online] http://www.nobelprize.org/nobel_prizes/chemistry/laureates/1943/hevesy-lecture.pdf 1943.
2. Weissleder, R.; Pittet, M. J., Imaging in the era of molecular oncology. *Nature* **2008,** *452* (7187), 580-589.
3. Fass, L., Imaging and cancer: A review. *Mol Oncol* **2008,** *2* (2), 115-152.
4. (a) Histed, S. N.; Lindenberg, M. L.; Mena, E.; Turkbey, B.; Choyke, P. L.; Kurdziel, K. A., Review of functional/anatomical imaging in oncology. *Nucl Med Commun* **2012,** *33* (4), 349-361; (b) Pysz, M. A.; Gambhir, S. S.; Willmann, J. K., Molecular imaging: current status and emerging strategies. *Clin Radiol* **2010,** *65* (7), 500-516; (c) Blow, N., In vivo molecular imaging: the inside job. *Nat Methods* **2009,** *6* (6), 465-469; (d) Jaffer, F. A.; Weissleder, R., Molecular imaging in the clinical arena. *Jama-J Am Med Assoc* **2005,** *293* (7), 855-862.
5. (a) Massoud, T. F.; Gambhir, S. S., Molecular imaging in living subjects: seeing fundamental biological processes in a new light. *Gene Dev* **2003,** *17* (5), 545-580; (b) Sharma, R.; Wendt, J. A.; Rasmussen, J. C.; Adams, K. E.; Marshall, M. V.; Sevick-Muraca, E. M., New horizons for imaging lymphatic function. *Ann Ny Acad Sci* **2008,** *1131*, 13-36; (c) Kobayashi, H.; Longmire, M. R.; Ogawa, M.; Choyke, P. L., Rational chemical design of the next generation of molecular imaging probes based on physics and biology: mixing modalities, colors and signals. *Chem Soc Rev* **2011,** *40* (9), 4626-4648.
6. Kircher, M. F.; Hricak, H.; Larson, S. M., Molecular imaging for personalized cancer care. *Mol Oncol* **2012,** *6* (2), 182-195.
7. Cutler, C. S.; Hennkens, H. M.; Sisay, N.; Huclier-Markai, S.; Jurisson, S. S., Radiometals for Combined Imaging and Therapy. *Chem Rev* **2013,** *113* (2), 858-883.
8. (a) Kowalsky, R. J.; Falen, S., *Radiopharmaceuticals in Nuclear Pharmacy and Nuclear Medicine.* 2004; (b) Liu, S., Bifunctional coupling agents for radiolabeling of biornolecules and target-specific delivery of metallic radionuclides. *Adv Drug Deliver Rev* **2008,** *60* (12), 1347-1370.

9. (IAEA), I. A. E. A. *Technetium-99m Radiopharmaceuticals: Status and Trends*; 2009.
10. Saha, G. B., *Fundamentals of nuclear pharmacy*. 5th ed.; Springer-Verlag: New York, 2004.
11. Wester, H. J., Nuclear imaging probes: From bench to bedside. *Clin Cancer Res* **2007,** *13* (12), 3470-3481.
12. Pimlott, S. L.; Sutherland, A., Molecular tracers for the PET and SPECT imaging of disease. *Chem Soc Rev* **2011,** *40* (1), 149-162.
13. (a) Mariani, G.; Bruselli, L.; Kuwert, T.; Kim, E. E.; Flotats, A.; Israel, O.; Dondi, M.; Watanabe, N., A review on the clinical uses of SPECT/CT. *Eur J Nucl Med Mol I* **2010,** *37* (10), 1959-1985; (b) Buck, A. K.; Nekolla, S.; Ziegler, S.; Beer, A.; Krause, B. J.; Herrmann, K.; Scheidhauer, K.; Wester, H. J.; Rummeny, E. J.; Schwaiger, M.; Drzezga, A., Spect/Ct. *J Nucl Med* **2008,** *49* (8), 1305-1319; (c) Cherry, S. R., Multimodality Imaging: Beyond PET/CT and SPECT/CT. *Semin Nucl Med* **2009,** *39* (5), 348-353; (d) Wadas, T. J.; Wong, E. H.; Weisman, G. R.; Anderson, C. J., Coordinating Radiometals of Copper, Gallium, Indium, Yttrium, and Zirconium for PET and SPECT Imaging of Disease. *Chem Rev* **2010,** *110* (5), 2858-2902.
14. Hicks, R. J.; Hofman, M. S., Is there still a role for SPECT–CT in oncology in the PET–CT era? *Nat Rev Clin Oncol* **2012**.
15. Bartholoma, M. D.; Louie, A. S.; Valliant, J. F.; Zubieta, J., Technetium and Gallium Derived Radiopharmaceuticals: Comparing and Contrasting the Chemistry of Two Important Radiometals for the Molecular Imaging Era. *Chem Rev* **2010,** *110* (5), 2903-2920.
16. (a) Ametamey, S. M.; Honer, M.; Schubiger, P. A., Molecular imaging with PET. *Chem Rev* **2008,** *108* (5), 1501-1516; (b) Ido, T.; Wan, C. N.; Casella, V.; Fowler, J. S.; Wolf, A. P.; Reivich, M.; Kuhl, D. E., Labeled 2-Deoxy-D-Glucose Analogs - F-18-Labeled 2-Deoxy-2-Fluoro-D-Glucose, 2-Deoxy-2-Fluoro-D-Mannose and C-14-2-Deoxy-2-Fluoro-D-Glucose. *J Labelled Compd Rad* **1978,** *14* (2), 175-183.
17. (a) Blower, P., Towards molecular imaging and treatment of disease with radionuclides: the role of inorganic chemistry. *Dalton T* **2006,** (14), 1705-1711; (b) Schwaiger, M.; Wester, H. J., How Many PET Tracers Do We Need? *J Nucl Med* **2011,** *52*, 36s-41s.

18. (a) Buchegger, F.; Perillo-Adamer, F.; Dupertuis, Y. M.; Delaloye, A. B., Auger radiation targeted into DNA: a therapy perspective. *Eur J Nucl Med Mol I* **2006,** *33* (11), 1352-1363; (b) Volkert, W. A.; Hoffman, T. J., Therapeutic radiopharmaceuticals. *Chem Rev* **1999,** *99* (9), 2269-2292.

19. (a) Kassis, A. I.; Adelstein, S. J., Radiobiologic principles in radionuclide therapy. *J Nucl Med* **2005,** *46*, 4S-12S; (b) Kwekkeboom, D. J.; de Herder, W. W.; Kam, B. L.; van Eijck, C. H.; van Essen, M.; Kooij, P. P.; Feelders, R. A.; van Aken, M. O.; Krenning, E. P., Treatment with the radiolabeled somatostatin analog [Lu-177-DOTA(0), Tyr(3)] octreotate: Toxicity, efficacy, and survival. *J Clin Oncol* **2008,** *26* (13), 2124-2130; (c) Kam, B. L. R.; Teunissen, J. J. M.; Krenning, E. P.; de Herder, W. W.; Khan, S.; van Vliet, E. I.; Kwekkeboom, D. J., Lutetium-labelled peptides for therapy of neuroendocrine tumours. *Eur J Nucl Med Mol I* **2012,** *39*, 103-112.

20. (a) Nilsson, S.; Larsen, R. H.; Fossa, S. D.; Balteskard, L.; Borch, K. W.; Westlin, J. E.; Salberg, G.; Bruland, O. S., First clinical experience with alpha-emitting radium-223 in the treatment of skeletal metastases. *Clin Cancer Res* **2005,** *11* (12), 4451-4459; (b) Nilsson, S.; Franzen, L.; Parker, C.; Tyrrell, C.; Blom, R.; Tennvall, J.; Lennernas, B.; Petersson, U.; Johannessen, D. C.; Sokal, M.; Pigott, K.; Yachnin, J.; Garkavij, M.; Strang, P.; Harmenberg, J.; Bolstad, B.; Bruland, O. S., Bone-targeted radium-223 in symptomatic, hormone-refractory prostate cancer: a randomised, multicentre, placebo-controlled phase II study. *Lancet Oncol* **2007,** *8* (7), 587-594.

21. A Phase III Study of Radium-223 Dichloride in Patients With Symptomatic Hormone Refractory Prostate Cancer With Skeletal Metastases (ALSYMPCA). http://clinicaltrials.gov/show/NCT00699751.

22. (a) Stepanek, J.; Ilvonen, S. A.; Kuronen, A. A.; Lampinen, J. S.; Savolainen, S. E.; Valimaki, P. J., Radiation spectra of In-111, In-113m and In-114m. *Acta Oncol* **2000,** *39* (6), 667-671; (b) Kassis, A. I.; Walicka, M. A.; Adelstein, S. J., Double-strand break yield following I-125 decay - Effects of DNA conformation. *Acta Oncol* **2000,** *39* (6), 721-726; (c) Tavares, A. A. S.; Tavares, J. M. R. S., Tc-99m Auger electrons - Analysis on the effects of low absorbed doses by computational methods. *Appl Radiat Isotopes* **2011,** *69* (3), 607-608; (d) Reilly, R. M., *Monoclonal Antibody and Peptide-targeted Radiotherapy of Cancer*. John Wiley & Sons, Inc ed.; 2010.

23. Alberto, R., The Chemistry of Technetium-Water Complexes within, the Manganese Triad: Challenges and Perspectives. *Eur J Inorg Chem* **2009,** (1), 21-31.

24. Dilworth, J. R.; Parrott, S. J., The biomedical chemistry of technetium and rhenium. *Chem Soc Rev* **1998,** *27* (1), 43-55.

25. (a) Richards, P.; Tucker, W. D.; Srivastava, S. C., Technetium-99m - an Historical-Perspective - Introduction. *Int J Appl Radiat Is* **1982,** *33* (10), 793-799; (b) Eckelman, W. C., Unparalleled Contribution of Technetium-99m to Medicine Over 5 Decades. *Jacc-Cardiovasc Imag* **2009,** *2* (3), 364-368; (c) Knapp, F. F.; Mirzadeh, S., The Continuing Important Role of Radionuclide Generator Systems for Nuclear-Medicine. *Eur J Nucl Med* **1994,** *21* (10), 1151-1165.

26. Saha, G. B., Production of Radionuclides. *Fundamentals of Nuclear Pharmacy, Sixth Edition* **2010**, 49-66.

27. Abram, U.; Alberto, R., Technetium and rhenium - Coordination chemistry and nuclear medical applications. *J Brazil Chem Soc* **2006,** *17* (8), 1486-1500.

28. Lee, J. S.; Lee, J. S.; Park, U. J.; Son, K. J.; Han, H. S., Development of a high performance W-188/Re-188 generator by using a synthetic alumina. *Appl Radiat Isotopes* **2009,** *67* (7-8), 1162-1166.

29. Morais, G. R.; Paulo, A.; Santos, I., Organometallic Complexes for SPECT Imaging and/or Radionuclide Therapy. *Organometallics* **2012,** *31* (16), 5693-5714.

30. (a) Mendes, F.; Gano, L.; Fernandes, C.; Paulo, A.; Santos, I., Studies of the myocardial uptake and excretion mechanisms of a novel Tc-99m heart perfusion agent. *Nucl Med Biol* **2012,** *39* (2), 207-213; (b) Mendes, F.; Paulo, A.; Santos, I., Metalloprobes for functional monitoring of tumour multidrug resistance by nuclear imaging. *Dalton T* **2011,** *40* (20), 5377-5393.

31. Palma, E.; Correia, J. D. G.; Campello, M. P. C.; Santos, I., Bisphosphonates as radionuclide carriers for imaging or systemic therapy. *Mol Biosyst* **2011,** *7* (11), 2950-2966.

32. Palma, E.; Correia, J. D. G.; Oliveira, B. L.; Gano, L.; Santos, I. C.; Santos, I., Tc-99m(CO)(3)-labeled pamidronate and alendronate for bone imaging. *Dalton T* **2011,** *40* (12), 2787-2796.

33. Fritzberg, A. R.; Kasina, S.; Eshima, D.; Johnson, D. L., Synthesis and Biological Evaluation of Tc-99m Mag3 as a Hippuran Replacement. *J Nucl Med* **1986,** *27* (1), 111-116.

34. Schwaiger, M.; Beer, A.; Ziegler, S.; Wester, H. J., Functional Imaging. *European Journal of Cancer* **2012,** *48*, S13-S14.

35. Baath, M.; Kolbeck, K. G.; Danielsson, R., Somatostatin receptor scintigraphy with Tc-99m-depreotide (NeoSpect) in discriminating between malignant and benign lesions in the diagnosis of lung cancer: A pilot study. *Acta Radiol* **2004,** *45* (8), 833-839.

36. Banerjee, S. R.; Maresca, K. P.; Francesconi, L.; Valliant, J.; Babich, J. W.; Zubieta, J., New directions in the coordination chemistry of Tc-99m: a reflection on technetium core structures and a strategy for new chelate design. *Nucl Med Biol* **2005,** *32* (1), 1-20.

37. Liu, S., The role of coordination chemistry in the development of target-specific radiopharmaceuticals. *Chem Soc Rev* **2004,** *33* (7), 445-461.

38. Alberto, R.; Ortner, K.; Wheatley, N.; Schibli, R.; Schubiger, A. P., Synthesis and properties of boranocarbonate: a convenient in situ CO source for the aqueous preparation of [(99m)Tc(OH(2))3(CO)3]+. *J Am Chem Soc* **2001,** *123* (13), 3135-6.

39. Schibli, R.; Schubiger, P. A., Current use and future potential of organometallic radiopharmaceuticals. *Eur J Nucl Med Mol I* **2002,** *29* (11), 1529-1542.

40. Oliveira, B. L.; Morais, M.; Figueira, F.; Palma, E.; Gano, L.; Santos, I. C.; Santos, I.; Correia, J. D. G., **Unpublished results**.

41. Mundwiler, S.; Kundig, M.; Ortner, K.; Alberto, R., A new [2+1] mixed ligand concept based on [Tc-99(m)(OH2)(3)(CO)(3)](+): a basic study. *Dalton T* **2004,** (9), 1320-1328.

42. van Staveren, D. R.; Benny, P. D.; Waibel, R.; Kurz, P.; Pak, J. K.; Alberto, R., S-functionalized cysteine: Powerful ligands for the labelling of bioactive molecules with triaquatricarbonyltechnetium-99m(1+) ([Tc-99m(OH2)(3)(CO)(3)](+)). *Helv Chim Acta* **2005,** *88* (3), 447-460.

43. Oliveira, B. L.; Morais, M.; Moreira, I. S.; Fernandes, P. A.; Ramos, M. J.; Alberto, R.; Santos, I.; Correia, J. D. G., Unpublished results.

44. (a) Schibli, R.; La Bella, R.; Alberto, R.; Garcia-Garayoa, E.; Ortner, K.; Abram, U.; Schubiger, P. A., Influence of the denticity of ligand systems on the in vitro

and in vivo behavior of Tc-99m(I)-tricarbonyl complexes: A hint for the future functionalization of biomolecules. *Bioconjugate Chem* **2000,** *11* (3), 345-351; (b) van Staveren, D. R.; Mundwiler, S.; Hoffmanns, U.; Pak, J. K.; Spingler, B.; Metzler-Nolte, N.; Alberto, R., Conjugation of a novel histidine derivative to biomolecules and labelling with [Tc-99m(OH2)(3)(CO)(3)](+). *Org Biomol Chem* **2004,** *2* (18), 2593-2603.

45. Zobi, F.; Spingler, B.; Alberto, R., Syntheses, Structures and Reactivities of [CpTc(CO)(3)X](+) and [CpRe(CO)(3)X](+). *Eur J Inorg Chem* **2008,** (27), 4205-4214.

46. (a) James, S.; Maresca, K. P.; Allis, D. G.; Valliant, J. F.; Eckelman, W.; Babich, J. W.; Zubieta, J., Extension of the single amino acid chelate concept (SAAC) to bifunctional biotin analogues for complexation of the M(CO)(3)(+1) core (M = Tc and Re): Syntheses, characterization, biotinidase stability, and avidin binding. *Bioconjugate Chem* **2006,** *17* (3), 579-589; (b) Jiang, H.; Kasten, B. B.; Liu, H.; Qi, S.; Liu, Y.; Tian, M.; Barnes, C. L.; Zhang, H.; Cheng, Z.; Benny, P. D., Novel, Cysteine-Modified Chelation Strategy for the Incorporation of [MI(CO)3]+ (M = Re, 99mTc) in an α-MSH Peptide. *Bioconjugate Chem.* **2012**.

47. Suzuki, K.; Shimmura, N.; Thipyapong, K.; Uehara, T.; Akizawa, H.; Arano, Y., Assessment of macrocyclic triamine ligands as synthons for organometallic Tc-99m radiopharmaceuticals. *Inorg Chem* **2008,** *47* (7), 2593-2600.

48. (a) Correia, J. D.; Paulo, A.; Santos, I., Re and Tc Complexes with Pyrazolyl-Containing Chelators: from Coordination Chemistry to Target-Specific Delivery of Radioactivity. *Current Radiopharmaceuticals* **2009,** *2* (4), 277-94; (b) Alves, S.; Paulo, A.; Correia, J. D. G.; Domingos, A.; Santos, I., Coordination capabilities of pyrazolyl containing ligands towards the fac-[Re(CO)(3)](+) moiety. *J Chem Soc Dalton* **2002,** (24), 4714-4719; (c) Vitor, R. F.; Alves, S.; Correia, J. D. G.; Paulo, A.; Santos, I., Rhenium(I)- and technetium(I) tricarbonyl complexes anchored by bifunctional pyrazole-diamine and pyrazole-dithioether chelators. *J Organomet Chem* **2004,** *689* (25), 4764-4774; (d) Alves, S.; Paulo, A.; Correia, J. D. G.; Gano, L.; Smith, C. J.; Hoffman, T. J.; Santos, I., Pyrazolyl derivatives as bifunctional chelators for labeling tumor-seeking peptides with the fac-[M(CO)(3)](+) moiety (M=Tc-99m, Re): Synthesis, characterization, and biological behavior. *Bioconjugate Chem.* **2005,** *16* (2),

438-449; (e) Alves, S.; Correia, J. D. G.; Santos, I.; Veerendra, B.; Sieckman, G. L.; Hoffman, T. J.; Rold, T. L.; Figueroa, S. D.; Retzloff, L.; McCrate, J.; Prasanphanich, A.; Smith, C. J., Pyrazolyl conjugates of bombesin: a new tridentate ligand framework for the stabilization of fac-[M(CO)(3)](+) moiety. *Nucl Med Biol* **2006,** *33* (5), 625-634.

49. Garcia, R.; Paulo, A.; Domingos, A.; Santos, I.; Ortner, K.; Alberto, R., Re and Tc complexes containing B-H center dot center dot center dot M agostic interactions as building blocks for the design of radiopharmaceuticals. *J Am Chem Soc* **2000,** *122* (45), 11240-11241.

50. (a) Correia, J. D.; Paulo, A.; Raposinho, P. D.; Santos, I., Radiometallated peptides for molecular imaging and targeted therapy. *Dalton Trans* **2011,** *40* (23), 6144-6167; (b) Raposinho, P. D.; Correia, J. D. G.; Oliveira, M. C.; Santos, I., Melanocortin-1 Receptor-Targeting With Radiolabeled Cyclic alpha-Melanocyte-Stimulating Hormone Analogs for Melanoma Imaging. *Biopolymers* **2010,** *94* (6), 820-829.

51. (a) Esteves, T.; Marques, F.; Paulo, A.; Rino, J.; Nanda, P.; Smith, C. J.; Santos, I., Nuclear targeting with cell-specific multifunctional tricarbonyl M(I) (M is Re, Tc-99m) complexes: synthesis, characterization, and cell studies. *J Biol Inorg Chem* **2011,** *16* (8), 1141-1153; (b) Esteves, T.; Xavier, C.; Gama, S.; Mendes, F.; Raposinho, P. D.; Marques, F.; Paulo, A.; Pessoa, J. C.; Rino, J.; Viola, G.; Santos, I., Tricarbonyl M(I) (M = Re, (99m)Tc) complexes bearing acridine fluorophores: synthesis, characterization, DNA interaction studies and nuclear targeting. *Org Biomol Chem* **2010,** *8* (18), 4104-16; (c) Moura, C.; Esteves, T.; Gano, L.; Raposinho, P. D.; Paulo, A.; Santos, I., Synthesis, characterization and biological evaluation of tricarbonyl M(I) (M = Re, Tc-99m) complexes functionalized with melanin-binding pharmacophores. *New J Chem* **2010,** *34* (11), 2564-2578; (d) Oliveira, B. L.; Raposinho, P. D.; Mendes, F.; Santos, I. C.; Santos, I.; Ferreira, A.; Cordeiro, C.; Freire, A. P.; Correia, J. D. G., Targeting nitric oxide synthase with (99m)Tc/Re-tricarbonyl complexes containing pendant guanidino or isothiourea moieties. *J. Organomet. Chem.* **2011,** *696* (5), 1057-1065; (e) Oliveira, B. L.; Raposinho, P. D.; Mendes, F.; Figueira, F.; Santos, I.; Ferreira, A.; Cordeiro, C.; Freire, A. P.; Correia, J. D. G., Re and Tc Tricarbonyl Complexes: From the Suppression of NO Biosynthesis in

Macrophages to in Vivo Targeting of Inducible Nitric Oxide Synthase. *Bioconjugate Chem.* **2010,** *21* (12), 2168-2172.

52. (a) Foundation, M. R. Melanoma Research Foundation. http://www.melanoma.org/learn-more/melanoma-101/melanoma-statistics-facts (accessed 21 November); (b) Gray-Schopfer, V.; Wellbrock, C.; Marais, R., Melanoma biology and new targeted therapy. *Nature* **2007,** *445* (7130), 851-7; (c) Ren, G.; Pan, Y.; Cheng, Z., Molecular Probes for Malignant Melanoma Imaging. *Curr Pharm Biotechno* **2010,** *11* (6), 590-602; (d) Miao, Y.; Quinn, T. P., Peptide-targeted radionuclide therapy for melanoma. *Crit Rev Oncol Hematol* **2008,** *67* (3), 213-28.
53. Dancey, A. L.; Mahon, B. S.; Rayatt, S. S., A review of diagnostic imaging in melanoma. *J Plast Reconstr Aes* **2008,** *61* (11), 1275-1283.
54. Gershenwald, J. E.; Ross, M. I., Sentinel-Lymph-Node Biopsy for Cutaneous Melanoma. *New Engl J Med* **2011,** *364* (18), 1738-1745.
55. Alitalo, A.; Detmar, M., Interaction of tumor cells and lymphatic vessels in cancer progression. *Oncogene* **2012,** *31* (42), 4499-508.
56. Carlson, J. A.; Slominski, A.; Linette, G. P.; Mihm, M. C., Jr.; Ross, J. S., Biomarkers in melanoma: staging, prognosis and detection of early metastases. *Expert Rev Mol Diagn* **2003,** *3* (3), 303-30.
57. Ings, R. M. J., The Melanin Binding of Drugs and Its Implications. *Drug Metab Rev* **1984,** *15* (5-6), 1183-1212.
58. (a) Garbe, C.; Buttner, P.; Bertz, J.; Burg, G.; Dhoedt, B.; Drepper, H.; Guggenmoosholzmann, I.; Lechner, W.; Lippold, A.; Orfanos, C. E.; Peters, A.; Rassner, G.; Stadler, R.; Stroebel, W., Primary Cutaneous Melanoma - Identification of Prognostic Groups and Estimation of Individual Prognosis for 5093 Patients. *Cancer* **1995,** *75* (10), 2484-2491; (b) Kasper, B.; D'Hondt, V.; Vereecken, P.; Awada, A., Novel treatment strategies for malignant melanoma: A new beginning? *Crit Rev Oncol Hemat* **2007,** *62* (1), 16-22.
59. (a) Sala, E.; Mologni, L.; Truffa, S.; Gaetano, C.; Bollag, G. E.; Gambacorti-Passerini, C., BRAF silencing by short hairpin RNA or chemical blockade by PLX4032 leads to different responses in melanoma and thyroid carcinoma cells. *Mol Cancer Res* **2008,** *6* (5), 751-759; (b) Nazarian, R.; Shi, H.; Wang, Q.; Kong, X.; Koya, R. C.; Lee, H.; Chen, Z.; Lee, M. K.; Attar, N.; Sazegar, H.; Chodon, T.; Nelson, S. F.; McArthur, G.; Sosman, J. A.; Ribas, A.; Lo, R. S.,

Melanomas acquire resistance to B-RAF(V600E) inhibition by RTK or N-RAS upregulation. *Nature* **2010,** *468* (7326), 973-7.

60. Belhocine, T. Z.; Scott, A. M.; Even-Sapir, E.; Urbain, J. L.; Essner, R., Role of nuclear medicine in the management of cutaneous malignant melanoma. *J Nucl Med* **2006,** *47* (6), 957-967.
61. Cobben, D. C.; Jager, P. L.; Elsinga, P. H.; Maas, B.; Suurmeijer, A. J.; Hoekstra, H. J., 3'-18F-fluoro-3'-deoxy-L-thymidine: a new tracer for staging metastatic melanoma? *J Nucl Med* **2003,** *44* (12), 1927-32.
62. Ren, G.; Miao, Z.; Liu, H.; Jiang, L.; Limpa-Amara, N.; Mahmood, A.; Gambhir, S. S.; Cheng, Z., Melanin-targeted preclinical PET imaging of melanoma metastasis. *J Nucl Med* **2009,** *50* (10), 1692-9.
63. Michelot, J. M.; Moreau, M. F. C.; Labarre, P. G.; Madelmont, J. C.; Veyre, A. J.; Papon, J. M.; Parry, D. F.; Bonafous, J. F.; Boire, J. Y. P.; Desplanches, G. G.; Bertrand, S. J.; Meyniel, G., Synthesis and Evaluation of New I-125 Radiopharmaceuticals as Potential Tracers for Malignant-Melanoma. *J Nucl Med* **1991,** *32* (8), 1573-1580.
64. (a) Friebe, M.; Mahmood, A.; Bolzati, C.; Drews, A.; Johannsen, B.; Eisenhut, M.; Kraemer, D.; Davison, A.; Jones, A. G., [Tc-99m]oxotechnetium(V) complexes of amine-amide-dithiol chelates with dialkylaminoalkyl substituents as potential diagnostic probes for malignant melanoma. *J Med Chem* **2001,** *44* (19), 3132-3140; (b) Friebe, M.; Mahmood, A.; Spies, H.; Berger, R.; Johannsen, B.; Mohammed, A.; Eisenhut, M.; Bolzati, C.; Davison, A.; Jones, A. G., '3+1' mixed-ligand oxotechnetium(V) complexes with affinity for melanoma: Synthesis and evaluation in vitro and in vivo. *J Med Chem* **2000,** *43* (14), 2745-2752.
65. (a) N'Dongo, H. W. P.; Raposinho, P. D.; Fernandes, C.; Santos, I.; Can, D.; Schmutz, P.; Spingler, B.; Alberto, R., Preparation and biological evaluation of cyclopentadienyl-based Tc-99m-complexes [(Cp-R)Tc-99m(CO)(3)] mimicking benzamides for malignant melanoma targeting. *Nucl Med Biol* **2010,** *37* (3), 255-264; (b) Moura, C.; Gano, L.; Mendes, F.; Raposinho, P. D.; Abrantes, A. M.; Botelho, M. F.; Santos, I.; Paulo, A., Tc-99m(I)/Re(I) tricarbonyl complexes for in vivo targeting of melanotic melanoma: Synthesis and biological evaluation. *Eur J Med Chem* **2012,** *50*, 350-360.

66. (a) Kang, N.; Hamilton, S.; Odili, J.; Wilson, G.; Kupsch, J., In vivo targeting of malignant melanoma by (125)iodine- and (99m)technetium-labeled single-chain Fv fragments against high molecular weight melanoma-associated antigen. *Clin Cancer Res* **2000,** *6* (12), 4921-4931; (b) Kang, N. V.; Hamilton, S.; Sanders, R.; Wilson, G. D.; Kupsch, J. M., Efficient in vivo targeting of malignant melanoma by single-chain Fv antibody fragments. *Melanoma Res* **1999,** *9* (6), 545-556.

67. (a) Donatien, P. D.; Hunt, G.; Pieron, C.; Lunec, J.; Taieb, A.; Thody, A. J., The Expression of Functional Msh Receptors on Cultured Human Melanocytes. *Arch Dermatol Res* **1992,** *284* (7), 424-426; (b) Ghanem, G. E.; Comunale, G.; Libert, A.; Vercammengrandjean, A.; Lejeune, F. J., Evidence for Alpha-Melanocyte-Stimulating Hormone (Alpha-Msh) Receptors on Human-Malignant Melanoma-Cells. *Int J Cancer* **1988,** *41* (2), 248-255; (c) Siegrist, W.; Solca, F.; Stutz, S.; Giuffre, L.; Carrel, S.; Girard, J.; Eberle, A. N., Characterization of Receptors for Alpha-Melanocyte-Stimulating Hormone on Human-Melanoma Cells. *Cancer Res* **1989,** *49* (22), 6352-6358.

68. (a) Chen, J.; Cheng, Z.; Hoffman, T. J.; Jurisson, S. S.; Quinn, T. P., Melanoma-targeting properties of (99m)technetium-labeled cyclic alpha-melanocyte-stimulating hormone peptide analogues. *Cancer Res* **2000,** *60* (20), 5649-5658; (b) Salazar-Onfray, F.; Lopez, M.; Lundqvist, A.; Aguirre, A.; Escobar, A.; Serrano, A.; Korenblit, C.; Petersson, M.; Chhajlani, V.; Larsson, O.; Kiessling, R., Tissue distribution and differential expression of melanocortin I receptor, a malignant melanoma marker. *Brit J Cancer* **2002,** *87* (4), 414-422; (c) Lopez, M. N.; Pereda, C.; Ramirez, M.; Mendoza-Naranjo, A.; Serrano, A.; Ferreira, A.; Poblete, R.; Katergis, A. M.; Kiessling, R.; Salazar-Onfray, F., Melanocortin 1 receptor is expressed by uveal malignant melanoma and can be considered a new target for diagnosis and immunotherapy. *Invest Ophth Vis Sci* **2007,** *48* (3), 1219-1227; (d) Cheng, Z.; Xiong, Z.; Subbarayan, M.; Chen, X.; Gambhir, S. S., 64Cu-labeled alpha-melanocyte-stimulating hormone analog for microPET imaging of melanocortin 1 receptor expression. *Bioconjugate Chem.* **2007,** *18* (3), 765-72.

69. Lee, S.; Xie, J.; Chen, X., Peptide-based probes for targeted molecular imaging. *Biochemistry-Us* **2010,** *49* (7), 1364-1376.

70. (a) Chhajlani, V.; Wikberg, J. E. S., Molecular-Cloning and Expression of the Human Melanocyte Stimulating Hormone Receptor Cdna. *Febs Lett* **1992,** *309*

(3), 417-420; (b) Mountjoy, K. G.; Robbins, L. S.; Mortrud, M. T.; Cone, R. D., The Cloning of a Family of Genes That Encode the Melanocortin Receptors. *Science* **1992,** *257* (5074), 1248-1251.

71. (a) Holder, J. R.; Haskell-Luevano, C., Melanocortin ligands: 30 years of structure-activity relationship (SAR) studies. *Med Res Rev* **2004,** *24* (3), 325-56; (b) Yang, Y. K., Structure, function and regulation of the melanocortin receptors. *Eur J Pharmacol* **2011,** *660* (1), 125-130.

72. (a) van der Velden, P. A.; Sandkuijl, L. A.; Bergman, W.; Pavel, S.; van Mourik, L.; Frants, R. R.; Gruis, N. A., Melanocortin-1 receptor variant R151C modifies melanoma risk in Dutch families with melanoma. *Am J Hum Genet* **2001,** *69* (4), 774-779; (b) Scott, M. C.; Wakamatsu, K.; Ito, S.; Kadekaro, A. L.; Kobayashi, N.; Groden, J.; Kavanagh, R.; Takakuwa, T.; Virador, V.; Hearing, V. J.; Abdel-Malek, Z. A., Human melanocortin 1 receptor variants, receptor function and melanocyte response to UV radiation. *J Cell Sci* **2002,** *115* (11), 2349-2355.

73. (a) Gerst, J. E.; Sole, J.; Hazum, E.; Salomon, Y., Identification and Characterization of Melanotropin Binding-Proteins from M2r Melanoma-Cells by Covalent Photoaffinity-Labeling. *Endocrinology* **1988,** *123* (4), 1792-1797; (b) Muceniece, R.; Mutule, I.; Mutulis, F.; Prusis, P.; Szardenings, M.; Wikberg, J. E. S., Detection of regions in the MC1 receptor of importance for the selectivity of the MC1 receptor super-selective MS04/MS05 peptides. *Bba-Protein Struct M* **2001,** *1544* (1-2), 278-282; (c) Solca, F.; Siegrist, W.; Drozdz, R.; Girard, J.; Eberle, A. N., The Receptor for Alpha-Melanotropin of Mouse and Human-Melanoma Cells - Application of a Potent Alpha-Melanotropin Photoaffinity Label. *J Biol Chem* **1989,** *264* (24), 14277-14281.

74. Hruby, V. J.; Cai, M. Y.; Cain, J.; Nyberg, J.; Trivedi, D., Design of novel melanocortin receptor ligands: Multiple receptors, complex pharmacology, the challenge. *Eur J Pharmacol* **2011,** *660* (1), 88-93.

75. (a) Palczewski, K.; Kumasaka, T.; Hori, T.; Behnke, C. A.; Motoshima, H.; Fox, B. A.; Le Trong, I.; Teller, D. C.; Okada, T.; Stenkamp, R. E.; Yamamoto, M.; Miyano, M., Crystal structure of rhodopsin: A G protein-coupled receptor. *Science* **2000,** *289* (5480), 739-745; (b) Wu, B. L.; Chien, E. Y. T.; Mol, C. D.; Fenalti, G.; Liu, W.; Katritch, V.; Abagyan, R.; Brooun, A.; Wells, P.; Bi, F. C.; Hamel, D. J.; Kuhn, P.; Handel, T. M.; Cherezov, V.; Stevens, R. C., Structures of the CXCR4 Chemokine GPCR with Small-Molecule and Cyclic Peptide

Antagonists. *Science* **2010,** *330* (6007), 1066-1071; (c) Carlsson, J.; Coleman, R. G.; Setola, V.; Irwin, J. J.; Fan, H.; Schlessinger, A.; Sali, A.; Roth, B. L.; Shoichet, B. K., Ligand discovery from a dopamine D-3 receptor homology model and crystal structure. *Nat Chem Biol* **2011,** *7* (11), 769-778.

76. (a) Garcia-Borron, J. C.; Sanchez-Laorden, B. L.; Jimenez-Cervantes, C., Melanocortin-1 receptor structure and functional regulation. *Pigment Cell Research* **2005,** *18* (6), 393-410; (b) Ringholm, A.; Klovins, J.; Rudzish, R.; Phillips, S.; Rees, J. L.; Schioth, H. B., Pharmacological characterization of loss of function mutations of the human melanocortin 1 receptor that are associated with red hair. *J Invest Dermatol* **2004,** *123* (5), 917-923.

77. (a) Li, Z. B.; Cai, W.; Cao, Q.; Chen, K.; Wu, Z.; He, L.; Chen, X., (64)Cu-labeled tetrameric and octameric RGD peptides for small-animal PET of tumor alpha(v)beta(3) integrin expression. *J Nucl Med* **2007,** *48* (7), 1162-71; (b) Barkey, N. M.; Tafreshi, N. K.; Josan, J. S.; De Silva, C. R.; Sill, K. N.; Hruby, V. J.; Gillies, R. J.; Morse, D. L.; Vagner, J., Development of Melanoma-Targeted Polymer Micelles by Conjugation of a Melanocortin 1 Receptor (MC1R) Specific Ligand. *J Med Chem* **2011,** *54* (23), 8078-8084.

78. (a) Guo, H.; Yang, J.; Gallazzi, F.; Prossnitz, E. R.; Sklar, L. A.; Miao, Y., Effect of DOTA Position on Melanoma Targeting and Pharmacokinetic Properties of 111In-labeled Lactam Bridge-Cyclized Alpha-Melanocyte Stimulating Hormone Peptide. *Bioconjugate Chem.* **2009,** *20* (11), 2162–2168; (b) Iyengar, R.; Hildebrandt, J. D., *Methods Enzymology: G Protein Pathways*. Academic Press: 2001; Vol. Vol. 343.

79. Haskell-Luevano, C.; Todorovic, A.; Gridley, K.; Sorenson, N.; Irani, B.; Xiang, Z., The melanocortin pathway: effects of voluntary exercise on the melanocortin-4 receptor knockout mice and ACTH(1-24) ligand structure activity relationships at the melanocortin-2 receptor. *Endocr Res* **2004,** *30* (4), 591-7.

80. Doedens, L.; Opperer, F.; Cai, M. Y.; Beck, J. G.; Dedek, M.; Palmer, E.; Hruby, V. J.; Kessler, H., Multiple N-Methylation of MT-II Backbone Amide Bonds Leads to Melanocortin Receptor Subtype hMC1R Selectivity: Pharmacological and Conformational Studies. *J Am Chem Soc* **2010,** *132* (23), 8115-8128.

81. (a) Froidevaux, S.; Calame-Christe, M.; Tanner, H.; Sumanovski, L.; Eberle, A. N., A novel DOTA-alpha-melanocyte-stimulating hormone analog for metastatic melanoma diagnosis. *J Nucl Med* **2002,** *43* (12), 1699-1706; (b) Raposinho, P. D.; Xavier, C.; Correia, J. D. G.; Falcao, S.; Gomes, P.; Santos, I., Melanoma targeting with alpha-melanocyte stimulating hormone analogs labeled with fac-[Tc-99m(CO)(3)](+): effect of cyclization on tumor-seeking properties. *J Biol Inorg Chem* **2008,** *13* (3), 449-459.

82. (a) Froidevaux, S.; Calame-Christe, M.; Schuhmacher, J.; Tanner, H.; Saffrich, R.; Henze, M.; Eberle, A. N., A gallium-labeled DOTA-alpha-melanocyte-stimulating hormone analog for PET imaging of melanoma metastases. *J Nucl Med* **2004,** *45* (1), 116-123; (b) Raposinho, P. D.; Correia, J. D. G.; Alves, S.; Botelho, M. F.; Santos, A. C.; Santos, I., A Tc-99m(CO)(3)-labeled pyrazolyl-alpha-melanocyte-stimulating hormone analog conjugate for melanoma targeting. *Nucl Med Biol* **2008,** *35* (1), 91-99.

83. Giblin, M. F.; Wang, N.; Hoffman, T. J.; Jurisson, S. S.; Quinn, T. P., Design and characterization of alpha-melanotropin peptide analogs cyclized through rhenium and technetium metal coordination. *Proc Natl Acad Sci U S A* **1998,** *95* (22), 12814-12818.

84. Chen, J. Q.; Cheng, Z.; Owen, N. K.; Hoffman, T. J.; Miao, Y. B.; Jurisson, S. S.; Quinn, T. P., Evaluation of an In-111-DOTA-rhenium cyclized alpha-MSH analog: A novel cyclic-peptide analog with improved tumor-targeting properties. *J Nucl Med* **2001,** *42* (12), 1847-1855.

85. Chen, J. Q.; Cheng, Z.; Miao, Y. B.; Jurisson, S. S.; Quinn, T. P., alpha-melanocyte-stimulating hormone peptide analogs labeled with technetium-99m and indium-111 for malignant melanoma targeting. *Cancer* **2002,** *94* (4), 1196-1201.

86. Miao, Y. B.; Benwell, K.; Quinn, T. P., (99)mTc and In-111-labeled alpha-melanocyte-stimulating hormone peptides as imaging probes for primary and pulmonary metastatic melanoma detection. *J Nucl Med* **2007,** *48* (1), 73-80.

87. McQuade, P.; Miao, Y. B.; Yoo, J.; Quinn, T. P.; Welch, M. J.; Lewis, J. S., Imaging of melanoma using Cu-64- and Y-86-DOTA-ReCCMSH(Arg(11)), a cyclized peptide analogue of alpha-MSH. *J Med Chem* **2005,** *48* (8), 2985-2992.

88. Wei, L.; Butcher, C.; Miao, Y.; Gallazzi, F.; Quinn, T. P.; Welch, M. J.; Lewis, J. S., Synthesis and biologic evaluation of 64Cu-labeled rhenium-cyclized alpha-

MSH peptide analog using a cross-bridged cyclam chelator. *J Nucl Med* **2007,** *48* (1), 64-72.

89. (a) Wei, L.; Miao, Y.; Gallazzi, F.; Quinn, T. P.; Welch, M. J.; Vavere, A. L.; Lewis, J. S., Gallium-68-labeled DOTA-rhenium-cyclized alpha-melanocyte-stimulating hormone analog for imaging of malignant melanoma. *Nucl Med Biol* **2007,** *34* (8), 945-953; (b) Cantorias, M. V.; Figueroa, S. D.; Quinn, T. P.; Lever, J. R.; Hoffman, T. J.; Watkinson, L. D.; Carmack, T. L.; Cutler, C. S., Development of high-specific-activity (68)Ga-labeled DOTA-rhenium-cyclized alpha-MSH peptide analog to target MC1 receptors overexpressed by melanoma tumors. *Nucl Med Biol* **2009,** *36* (5), 505-13.
90. Yang, J.; Guo, H.; Gallazzi, F.; Berwick, M.; Padilla, R. S.; Miao, Y., Evaluation of a novel Arg-Gly-Asp-conjugated alpha-melanocyte stimulating hormone hybrid peptide for potential melanoma therapy. *Bioconjugate Chem* **2009,** *20* (8), 1634-42.
91. Miao, Y.; Gallazzi, F.; Guo, H.; Quinn, T. P., In-111-labeled lactam bridge-cyclized alpha-melanocyte stimulating hormone peptide analogues for melanoma imaging. *Bioconjugate Chem* **2008,** *19* (2), 539-547.
92. Guo, H.; Yang, J.; Shenoy, N.; Miao, Y., Gallium-67-labeled lactam bridge-cyclized alpha-melanocyte stimulating hormone peptide for primary and metastatic melanoma imaging. *Bioconjugate Chem.* **2009,** *20* (12), 2356-2363.
93. Valldosera, M.; Monso, M.; Xavier, C.; Raposinho, P.; Correia, J. D. G.; Santos, I.; Gomes, P., Comparative study of chemical approaches to the solid-phase synthesis of a tumor-seeking alpha-MSH analogue. *Int J Pept Res Ther* **2008,** *14* (3), 273-281.
94. Guo, H.; Yang, J.; Gallazzi, F.; Miao, Y., Reduction of the ring size of radiolabeled lactam bridge-cyclized alpha-MSH peptide, resulting in enhanced melanoma uptake. *J Nucl Med* **2010,** *51* (3), 418-426.
95. Guo, H. X.; Yang, J. Q.; Gallazzi, F.; Miao, Y. B., Effects of the Amino Acid Linkers on the Melanoma-Targeting and Pharmacokinetic Properties of (111)In-Labeled Lactam Bridge-Cyclized alpha-MSH Peptides. *J Nucl Med* **2011,** *52* (4), 608-616.
96. Guo, H.; Gallazzi, F.; Miao, Y., Gallium-67-Labeled Lactam Bridge-Cyclized Alpha-MSH Peptides with Enhanced Melanoma Uptake and Reduced Renal Uptake. *Bioconjug Chem* **2012**.

97. Guo, H. X.; Miao, Y. B., Cu-64-Labeled Lactam Bridge-Cyclized alpha-MSH Peptides for PET Imaging of Melanoma. *Mol. Pharmaceutics* **2012,** *9* (8), 2322-2330.

98. Morton, D. L.; Chan, A. D., The concept of sentinel lymph node localization: How it started. *Semin Nucl Med* **2000,** *30* (1), 4-10.

99. Leong, S. P.; Nakakura, E. K.; Pollock, R.; Choti, M. A.; Morton, D. L.; Henner, W. D.; Lal, A.; Pillai, R.; Clark, O. H.; Cady, B., Unique patterns of metastases in common and rare types of malignancy. *J Surg Oncol* **2011,** *103* (6), 607-14.

100. (a) Shayan, R.; Achen, M. G.; Stacker, S. A., Lymphatic vessels in cancer metastasis: bridging the gaps. *Carcinogenesis* **2006,** *27* (9), 1729-1738; (b) Veronesi, U.; Galimberti, V.; Zurrida, S.; Pigatto, F.; Veronesi, P.; Robertson, C.; Paganelli, G.; Sciascia, V.; Viale, G., Sentinel lymph node biopsy as an indicator for axillary dissection in early breast cancer. *European Journal of Cancer* **2001,** *37* (4), 454-458; (c) Alex, J. C., The application of sentinel node radiolocalization to solid tumors of the head and neck: A 10-year experience. *Laryngoscope* **2004,** *114* (1), 2-19; (d) Torne, A.; Puig-Tintore, L. M., The use of sentinel lymph nodes in gynaecological malignancies. *Curr Opin Obstet Gyn* **2004,** *16* (1), 57-64.

101. (a) Hoshida, T.; Isaka, N.; Hagendoorn, J.; di Tomaso, E.; Chen, Y. L.; Pytowski, B.; Fukumura, D.; Padera, T. P.; Jain, R. K., Imaging steps of lymphatic metastasis reveals that vascular endothelial growth factor-C increases metastasis by increasing delivery of cancer cells to lymph nodes: Therapeutic implications. *Cancer Res* **2006,** *66* (16), 8065-8075; (b) Catalano, O.; Caraco, C.; Mozzillo, N.; Siani, A., Locoregional Spread of Cutaneous Melanoma: Sonography Findings. *Am J Roentgenol* **2010,** *194* (3), 735-745.

102. (a) Scoyer, R. A.; Murali, R.; Satzger, I.; Thompson, J. F., The detection and significance of melanoma micrometastases in sentinel nodes. *Surg Oncol* **2008,** *17* (3), 165-174; (b) Scolyer, R. A.; Murali, R.; Gershenwald, J. E.; Cochran, A. J.; Thompson, J. F., Clinical relevance of melanoma micrometastases in sentinel nodes: too early to tell. *Ann Oncol* **2007,** *18* (4), 806-U14; (c) van Akkooi, A. C. J.; de Wilt, J. H. W.; Verhoef, C.; Schmitz, P. I. M.; van Geel, A. N.; Eggermont, A. M. M.; Kliffen, M., Clinical relevance of melanoma micrometastases (< 0.1 mm) in sentinel nodes: are these nodes to be considered negative? *Ann Oncol* **2006,** *17* (10), 1578-1585.

103. Nune, S. K.; Gunda, P.; Majeti, B. K.; Thallapally, P. K.; Forrest, M. L., Advances in lymphatic imaging and drug delivery. *Adv Drug Deliver Rev* **2011,** *63* (10-11), 876-885.

104. Yi, M.; Giordano, S. H.; Meric-Bernstam, F.; Mittendorf, E. A.; Kuerer, H. M.; Hwang, R. F.; Bedrosian, I.; Rourke, L.; Hunt, K. K., Trends in and Outcomes from Sentinel Lymph Node Biopsy (SLNB) Alone vs. SLNB with Axillary Lymph Node Dissection for Node-Positive Breast Cancer Patients: Experience from the SEER Database. *Ann Surg Oncol* **2010,** *17*, S343-S351.

105. Keshtgar, M.; Zaknun, J. J.; Sabih, D.; Lago, G.; Cox, C. E.; Leong, S. P. L.; Mariani, G., Implementing Sentinel Lymph Node Biopsy Programs in Developing Countries: Challenges and Opportunities. *World J Surg* **2011,** *35* (6), 1159-1168.

106. (a) Vera, D. R.; Wisner, E. R.; Stadalnik, R. C., Sentinel node imaging via a nonparticulate receptor-binding radiotracer. *J Nucl Med* **1997,** *38* (4), 530-5; (b) East, L.; Isacke, C. M., The mannose receptor family. *Bba-Gen Subjects* **2002,** *1572* (2-3), 364-386.

107. Achord, D. T.; Brot, F. E.; Sly, W. S., Inhibition of the rat clearance system for agalacto-orosomucoid by yeast mannans and by mannose. *Biochem Biophys Res Commun* **1977,** *77* (1), 409-15.

108. Lindhorst, T. K., *Essentials of Carbohydrate Chemistry and Biochemistry*. 2nd ed.; Wiley-VCH: 2004.

109. Liu, Y.; Misulovin, Z.; Bjorkman, P. J., The molecular mechanism of sulfated carbohydrate recognition by the cysteine-rich domain of mannose receptor. *J Mol Biol* **2001,** *305* (3), 481-90.

110. (a) Marttila-Ichihara, F.; Turia, R.; Miiluniemi, M.; Karikoski, M.; Maksimow, M.; Niemela, J.; Martinez-Pomares, L.; Salmi, M.; Jalkanen, S., Macrophage mannose receptor on lymphatics controls cell trafficking. *Blood* **2008,** *112* (1), 64-72; (b) Movahedi, K.; Schoonooghe, S.; Laoui, D.; Houbracken, I.; Waelput, W.; Breckpot, K.; Bouwens, L.; Lahoutte, T.; De Baetselier, P.; Raes, G.; Devoogdt, N.; Van Ginderachter, J. A., Nanobody-Based Targeting of the Macrophage Mannose Receptor for Effective In Vivo Imaging of Tumor-Associated Macrophages. *Cancer Res* **2012,** *72* (16), 4165-4177.

111. Petrova, T. V.; Makinen, T.; Makela, T. P.; Saarela, J.; Virtanen, I.; Ferrell, R. E.; Finegold, D. N.; Kerjaschki, D.; Yla-Herttuala, S.; Alitalo, K., Lymphatic

endothelial reprogramming of vascular endothelial cells by the Prox-1 homeobox transcription factor. *Embo J* **2002,** *21* (17), 4593-4599.

112. Irjala, H.; Alanen, K.; Grenman, R.; Heikkila, P.; Joensuu, H.; Jalkanen, S., Mannose receptor (MR) and common lymphatic endothelial and vascular endothelial receptor (CLEVER)-1 direct the binding of cancer cells to the lymph vessel endothelium. *Cancer Res* **2003,** *63* (15), 4671-4676.
113. Wilhelm, A. J.; Mijnhout, G. S.; Franssen, E. J. F., Radiopharmaceuticals in sentinel lymph-node detection - an overview. *Eur J Nucl Med* **1999,** *26* (4), S36-S42.
114. Zhang, F.; Niu, G.; Lu, G. M.; Chen, X. Y., Preclinical Lymphatic Imaging. *Mol Imaging Biol* **2011,** *13* (4), 599-612.
115. (a) Henze, E.; Schelbert, H. R.; Collins, J. D.; Najafi, A.; Barrio, J. R.; Bennett, L. R., Lymphoscintigraphy with Tc-99m-Labeled Dextran. *J Nucl Med* **1982,** *23* (10), 923-929; (b) Matsunaga, K.; Hara, K.; Imamura, T.; Fujioka, T.; Takata, J.; Karube, Y., Technetium labeling of dextran incorporating cysteamine as a ligand. *Nucl Med Biol* **2005,** *32* (3), 279-285.
116. (a) Takagi, K.; Uehara, T.; Kaneko, E.; Nakayama, M.; Koizumi, M.; Endo, K.; Arano, Y., Tc-99m-labeled mannosyl-neoglycoalbumin for sentinel lymph node identification. *Nucl Med Biol* **2004,** *31* (7), 893-900; (b) Jeong, J. M.; Hong, M. K.; Kim, Y. J.; Lee, J.; Kang, J. H.; Lee, D. S.; Chung, J. K.; Lee, M. C., Development of Tc-99m-neomannosyl human serum albumin (Tc-99m-MSA) as a novel receptor binding agent for sentinel lymph node imaging. *Nucl Med Commun* **2004,** *25* (12), 1211-1217; (c) Vera, D. R.; Wallace, A. M.; Hoh, C. K.; Mattrey, R. F., A synthetic macromolecule for sentinel node detection: (99m)Tc-DTPA-mannosyl-dextran. *J Nucl Med* **2001,** *42* (6), 951-9; (d) Vera, D. R.; Wallace, A. M.; Hoh, C. K., [(99m)Tc]MAG(3)-mannosyl-dextran: a receptor-binding radiopharmaceutical for sentinel node detection. *Nucl Med Biol* **2001,** *28* (5), 493-8.
117. (a) Wallace, A. M.; Hoh, C. K.; Limmer, K. K.; Darrah, D. D.; Schulteis, G.; Vera, D. R., Sentinel lymph node accumulation of Lymphoseek and Tc-99m-sulfur colloid using a "2-day" protocol. *Nucl Med Biol* **2009,** *36* (6), 687-692; (b) Leong, S. P.; Kim, J.; Ross, M.; Faries, M.; Scoggins, C. R.; Metz, W. L.; Cope, F. O.; Orahood, R. C., A phase 2 study of (99m)Tc-tilmanocept in the detection

of sentinel lymph nodes in melanoma and breast cancer. *Ann Surg Oncol* **2011,** *18* (4), 961-9.

118. Pirmettis, I.; Arano, Y.; Tsotakos, T.; Okada, K.; Yamaguchi, A.; Uehara, T.; Morais, M.; Correia, J. D. G.; Santos, I.; Martins, M.; Pereira, S.; Triantis, C.; Kyprianidou, P.; Pelecanou, M.; Papadopoulos, M., New Tc-99m(CO)(3) Mannosylated Dextran Bearing S-Derivatized Cysteine Chelator for Sentinel Lymph Node Detection. *Mol Pharmaceut* **2012,** *9* (6), 1681-1692.
119. Subramanian, S.; Pandey, U.; Papadopoulos, M.; Pirmettis, I.; Venkatesh, M.; Samuel, G., Studies Toward the Biological Efficacy of Tc-99m-Labeled Dextran-Cysteine-Mannose ([Tc-99m(CO)(3)]DCM20) for Sentinel Lymph Node Detection. *Cancer Biother Radio* **2012,** *27* (6), 365-370.
120. Ocampo-Garcia, B. E.; Ramirez, F. D.; Ferro-Flores, G.; De Leon-Rodriguez, L. M.; Santos-Cuevas, C. L.; Morales-Avila, E.; de Murphy, C. A.; Pedraza-Lopez, M.; Medina, L. A.; Camacho-Lopez, M. A., Tc-99m-labelled gold nanoparticles capped with HYNIC-peptide/mannose for sentinel lymph node detection. *Nucl Med Biol* **2011,** *38* (1), 1-11.
121. Choi, J. Y.; Jeong, J. M.; Yoo, B. C.; Kim, K.; Kim, Y.; Yang, B. Y.; Lee, Y. S.; Lee, D. S.; Chung, J. K.; Lee, M. C., Development of Ga-68-labeled mannosylated human serum albumin (MSA) as a lymph node imaging agent for positron emission tomography. *Nucl Med Biol* **2011,** *38* (3), 371-379.
122. (a) Culver, J.; Akers, W.; Achilefu, S., Multimodality molecular imaging with combined optical and SPECT/PET modalities. *J Nucl Med* **2008,** *49* (2), 169-172; (b) van den Berg, N. S.; Valdes-Olmos, R. A.; van der Poel, H. G.; van Leeuwen, F. W., Sentinel lymph node biopsy for prostate cancer: a hybrid approach. *J Nucl Med* **2013,** *54* (4), 493-6; (c) Thorp-Greenwood, F. L.; Coogan, M. P., Multimodal radio-(PET/SPECT) and fluorescence imaging agents based on metallo-radioisotopes: current applications and prospects for development of new agents. *Dalton T* **2011,** *40* (23), 6129-6143; (d) Melendez-Alafort, L.; Muzzio, P. C.; Rosato, A., Optical and Multimodal Peptide-Based Probes for In Vivo Molecular Imaging. *Anti-Cancer Agent Me* **2012,** *12* (5), 476-499.
123. (a) Luo, S. L.; Zhang, E. L.; Su, Y. P.; Cheng, T. M.; Shi, C. M., A review of NIR dyes in cancer targeting and imaging. *Biomaterials* **2011,** *32* (29), 7127-7138; (b) Ting, R.; Aguilera, T. A.; Crisp, J. L.; Hall, D. J.; Eckelman, W. C.; Vera, D. R.; Tsien, R. Y., Fast F-18 Labeling of a Near-Infrared Fluorophore

Enables Positron Emission Tomography and Optical Imaging of Sentinel Lymph Nodes. *Bioconjugate Chem* **2010,** *21* (10), 1811-1819.

124. Buckle, T.; van Leeuwen, A. C.; Chin, P. T. K.; Janssen, H.; Muller, S. H.; Jonkers, J.; van Leeuwen, F. W. B., A self-assembled multimodal complex for combined pre- and intraoperative imaging of the sentinel lymph node. *Nanotechnology* **2010,** *21* (35).
125. Emerson, D. K.; Limmer, K. K.; Hall, D. J.; Han, S. H.; Eckelman, W. C.; Kane, C. J.; Wallace, A. M.; Vera, D. R., A Receptor-targeted Fluorescent Radiopharmaceutical for Multireporter Sentinel Lymph Node Imaging. *Radiology* **2012,** *265* (1), 186-193.
126. (a) Kramer, R. H.; Karpen, J. W., Spanning binding sites on allosteric proteins with polymer-linked ligand dimers. *Nature* **1998,** *395* (6703), 710-713; (b) Handl, H. L.; Vagner, J.; Yamamura, H. I.; Hruby, V. J.; Gillies, R. J., Lanthanide-based time-resolved fluorescence of in cyto ligand-receptor interactions. *Anal Biochem* **2004,** *330* (2), 242-250; (c) Vance, D.; Shah, M.; Joshi, A.; Kane, R. S., Polyvalency: A promising strategy for drug design. *Biotechnol Bioeng* **2008,** *101* (3), 429-434.
127. Kiessling, L. L.; Gestwicki, J. E.; Strong, L. E., Synthetic multivalent ligands as probes of signal transduction. *Angew Chem Int Ed Engl* **2006,** *45* (15), 2348-68.
128. Abiraj, K.; Jaccard, H.; Kretzschmar, M.; Helm, L.; Maecke, H. R., Novel DOTA-based prochelator for divalent peptide vectorization: synthesis of dimeric bombesin analogues for multimodality tumor imaging and therapy. *Chem Commun (Camb)* **2008,** (28), 3248-50.
129. (a) Liu, S., Radiolabeled multimeric cyclic RGD peptides as integrin alphavbeta3 targeted radiotracers for tumor imaging. *Mol Pharm* **2006,** *3* (5), 472-87; (b) Singh, A. N.; Liu, W.; Hao, G.; Kumar, A.; Gupta, A.; Oz, O. K.; Hsieh, J. T.; Sun, X., Multivalent Bifunctional Chelator Scaffolds for Gallium-68 Based Positron Emission Tomography Imaging Probe Design: Signal Amplification via Multivalency. *Bioconjugate Chem.* **2011,** *22* (8), 1650-1662; (c) Dijkgraaf, I.; Kruijtzer, J. A.; Liu, S.; Soede, A. C.; Oyen, W. J.; Corstens, F. H.; Liskamp, R. M.; Boerman, O. C., Improved targeting of the alpha(v)beta (3) integrin by multimerisation of RGD peptides. *Eur J Nucl Med Mol Imaging* **2007,** *34* (2), 267-73.

130. (a) Eberle, A.; Kriwaczek, V. M.; Schwyzer, R., Hormone--receptor interactions: melanotropic activities of the covalent serum albumin complexes with alpha-melanotropin, alpha-melanotropin fragments, and enkephalin. *Febs Lett* **1977,** *80* (2), 246-50; (b) Kriwaczek, V. M.; Eberle, A. N.; Muller, M.; Schwyzer, R., Tobacco Mosaic-Virus as a Carrier for Small Molecules .1. Preparation and Characterization of a Tmv-Alpha-Melanotropin Conjugate. *Helv Chim Acta* **1978,** *61* (4), 1232-1240.

131. (a) Vagner, J.; Handl, H. L.; Monguchi, Y.; Jana, U.; Begay, L. J.; Mash, E. A.; Hruby, V. J.; Gillies, R. J., Rigid linkers for bioactive peptides. *Bioconjugate Chem.* **2006,** *17* (6), 1545-1550; (b) Handl, H. L.; Sankaranarayanan, R.; Josan, J. S.; Vagner, J.; Mash, E. A.; Gillies, R. J.; Hruby, V. J., Synthesis and evaluation of bivalent NDP-alpha-MSH(7) peptide ligands for binding to the human melanocortin receptor 4 (hMC4R). *Bioconjugate Chem.* **2007,** *18* (4), 1101-1109.

132. Bagutti, C.; Stolz, B.; Albert, R.; Bruns, C.; Pless, J.; Eberle, A. N., [111In]-DTPA-labeled analogues of alpha-melanocyte-stimulating hormone for melanoma targeting: receptor binding in vitro and in vivo. *Int J Cancer* **1994,** *58* (5), 749-55.

133. Bapst, J. P.; Froidevaux, S.; Calame, M.; Tanner, H.; Eberle, A. N., Dimeric DOTA-alpha-melanocyte-stimulating hormone analogs: synthesis and in vivo characteristics of radiopeptides with high in vitro activity. *J Recept Signal Transduct Res* **2007,** *27* (5-6), 383-409.

134. (a) Merrifield, R. B., Solid Phase Peptide Synthesis .1. Synthesis of a Tetrapeptide. *J Am Chem Soc* **1963,** *85* (14), 2149-&; (b) Pedersen, S. L.; Tofteng, A. P.; Malik, L.; Jensen, K. J., Microwave heating in solid-phase peptide synthesis. *Chem Soc Rev* **2012,** *41* (5), 1826-1844.

135. Chan, W. C.; White, P. D., *Fmoc Solid Phase Peptide Synthesis: A Practical Approach*. 1st Edition ed.; Oxford University Press: Oxford, 2004.

136. Wüthrich, K., *NMR of Proteins and Nucleic Acids*. Wiley: New York, 1986.

137. (a) Wishart, D. S.; Bigam, C. G.; Holm, A.; Hodges, R. S.; Sykes, B. D., H-1, C-13 and N-15 Random Coil Nmr Chemical-Shifts of the Common Amino-Acids .1. Investigations of Nearest-Neighbor Effects. *Journal of Biomolecular Nmr* **1995,** *5* (1), 67-81; (b) Wishart, D. S.; Sykes, B. D., Chemical-Shifts as a Tool for Structure Determination. *Method Enzymol* **1994,** *239*, 363-392; (c) Wishart,

D. S.; Sykes, B. D., The C-13 Chemical-Shift Index - a Simple Method for the Identification of Protein Secondary Structure Using C-13 Chemical-Shift Data. *Journal of Biomolecular Nmr* **1994,** *4* (2), 171-180; (d) Wishart, D. S.; Sykes, B. D.; Richards, F. M., Relationship between Nuclear-Magnetic-Resonance Chemical-Shift and Protein Secondary Structure. *Journal of Molecular Biology* **1991,** *222* (2), 311-333.

138. Teng, Q., *Structural Biology: Practical NMR Applications*. Springer: New York, 2005.

139. (a) Wishart, D. S.; Bigam, C. G.; Yao, J.; Abildgaard, F.; Dyson, H. J.; Oldfield, E.; Markley, J. L.; Sykes, B. D., 1H, 13C and 15N chemical shift referencing in biomolecular NMR. *J Biomol NMR* **1995,** *6* (2), 135-140; (b) Wang, Y. J.; Jardetzky, O., Probability-based protein secondary structure identification using combined NMR chemical-shift data. *Protein Sci* **2002,** *11* (4), 852-861.

140. Froidevaux, S.; Calame-Christe, M.; Tanner, H.; Eberle, A. N., Melanoma targeting with DOTA-alpha-melanocyte-stimulating hormone analogs: Structural parameters affecting tumor uptake and kidney uptake. *J Nucl Med* **2005,** *46* (5), 887-895.

141. (a) Bapst, J. P.; Calame, M.; Tanner, H.; Eberle, A. N., Glycosylated DOTA-alpha-Melanocyte-Stimulating Hormone Analogues for Melanoma Targeting: Influence of the Site of Glycosylation on in Vivo Biodistribution. *Bioconjugate Chem.* **2009,** *20* (5), 984-993; (b) de Jong, M.; Barone, R.; Krenning, E.; Bernard, B.; Melis, M.; Visser, T.; Gekle, M.; Willnow, T. E.; Walrand, S.; Jamar, F.; Pauwels, S., Megalin is essential for renal proximal tubule reabsorption of (111)In-DTPA-octreotide. *J Nucl Med* **2005,** *46* (10), 1696-1700; (c) Vegt, E.; de Jong, M.; Wetzels, J. F. M.; Masereeuw, R.; Melis, M.; Oyen, W. J. G.; Gotthardt, M.; Boerman, O. C., Renal Toxicity of Radiolabeled Peptides and Antibody Fragments: Mechanisms, Impact on Radionuclide Therapy, and Strategies for Prevention. *J Nucl Med* **2010,** *51* (7), 1049-1058; (d) Verroust, P. J.; Christensen, E. I., Megalin and cubilin--the story of two multipurpose receptors unfolds. *Nephrol Dial Transplant* **2002,** *17* (11), 1867-71.

142. (a) Behr, T. M.; Goldenberg, D. M.; Becker, W., Reducing the renal uptake of radiolabeled antibody fragments and peptides for diagnosis and therapy: present status, future prospects and limitations. *Eur J Nucl Med* **1998,** *25* (2), 201-212;

(b) Rolleman, E. J.; Valkema, R.; de Jong, M.; Kooij, P. P. M.; Krenning, E. R., Safe and effective inhibition of renal uptake of radiolabelled octreotide by a combination of lysine and arginine. *Eur J Nucl Med Mol I* **2003,** *30* (1), 9-15; (c) Akizawa, H.; Uehara, T.; Arano, Y., Renal uptake and metabolism of radiopharmaceuticals derived from peptides and proteins. *Adv Drug Deliver Rev* **2008,** *60* (12), 1319-1328; (d) Gotthardt, M.; van Eerd-Vismale, J.; Oyen, W. J. G.; de Jong, M.; Zhang, H.; Rolleman, E.; Maecke, H. R.; Behe, M.; Boerman, O., Indication for different mechanisms of kidney uptake of radiolabeled peptides. *J Nucl Med* **2007,** *48* (4), 596-601; (e) Miao, Y.; Fisher, D. R.; Quinn, T. P., Reducing renal uptake of 90Y- and 177Lu-labeled alpha-melanocyte stimulating hormone peptide analogues. *Nucl Med Biol* **2006,** *33* (6), 723-733.

143. Grieco, P.; Cai, M.; Liu, L.; Mayorov, A.; Chandler, K.; Trivedi, D.; Lin, G.; Campiglia, P.; Novellino, E.; Hruby, V. J., Design and microwave-assisted synthesis of novel macrocyclic peptides active at melanocortin receptors: discovery of potent and selective hMC5R receptor antagonists. *J Med Chem* **2008,** *51* (9), 2701-7.

144. Nijenhuis, W. A. J.; Wanders, N.; Kruijtzer, J. A. W.; Liskamp, R. M.; Gispen, W. H.; Adan, R. A. H., Accelerating sensory recovery after sciatic nerve crush: non-selective versus melanocortin MC4 receptor-selective peptides. *Eur J Pharmacol* **2004,** *495* (2-3), 145-152.

145. Grieco, P.; Campiglia, P.; Gomez-Monterrey, I.; Lama, T.; Novellino, E., Rapid and efficient methodology to perform macrocyclization reactions in solid-phase peptide chemistry. *Synlett* **2003,** (14), 2216-2218.

146. (a) Slutsky, M. M.; Marsh, E. N. G., Cation-pi interactions studied in a model coiled-coil peptide. *Protein Sci* **2004,** *13* (8), 2244-2251; (b) Tsou, L. K.; Tatko, C. D.; Waters, M. L., Simple cation-pi interaction between a phenyl ring and a protonated amine stabilizes an alpha-helix in water. *J Am Chem Soc* **2002,** *124* (50), 14917-14921.

147. (a) Ying, J.; Kover, K. E.; Gu, X.; Han, G.; Trivedi, D. B.; Kavarana, M. J.; Hruby, V. J., Solution structures of cyclic melanocortin agonists and antagonists by NMR. *Biopolymers* **2003,** *71* (6), 696-716; (b) Elipe, M. V. S.; Mosley, R. T.; Bednarek, M. A.; Arison, B. H., H-1-NMR studies on a potent and selective antagonist at human melanocortin receptor 4 (hMC-4R). *Biopolymers* **2003,** *68* (4), 512-527.

148. Singh, A.; Wilczynski, A.; Holder, J. R.; Witek, R. M.; Dirain, M. L.; Xiang, Z. M.; Edison, A. S.; Haskell-Luevano, C., Incorporation of a Bioactive Reverse-Turn Heterocycle into a Peptide Template Using Solid-Phase Synthesis To Probe Melanocortin Receptor Selectivity and Ligand Conformations by 2D H-1 NMR. *J Med Chem* **2011,** *54* (5), 1379-1390.

149. (a) Oliveira, B. L.; Correia, J. D.; Raposinho, P. D.; Santos, I.; Ferreira, A.; Cordeiro, C.; Freire, A. P., Re and (99m)Tc organometallic complexes containing pendant l-arginine derivatives as potential probes of inducible nitric oxide synthase. *Dalton Trans* **2009,** (1), 152-62; (b) Simpson, E. J.; Hickey, J. L.; Breadner, D.; Luyt, L. G., Investigation of isomer formation upon coordination of bifunctional histidine analogues with (99m)Tc/Re(CO)(3). *Dalton Trans* **2012,** *41* (10), 2950-8; (c) Perera, T.; Marzilli, P. A.; Fronczek, F. R.; Marzilli, L. G., Several novel N-donor tridentate ligands formed in chemical studies of new fac-Re(CO)3 complexes relevant to fac-99mTc(CO)3 radiopharmaceuticals: attack of a terminal amine on coordinated acetonitrile. *Inorg Chem* **2010,** *49* (5), 2123-31.

150. Morais, M.; Raposinho, P. D.; Oliveira, M. C.; Correia, J. D. G.; Santos, I., Evaluation of novel Tc-99m(I)-labeled homobivalent alpha-melanocyte-stimulating hormone analogs for melanocortin-1 receptor targeting. *J Biol Inorg Chem* **2012,** *17* (4), 491-505.

151. Troutner, D. E.; Volkert, W. A.; Hoffman, T. J.; Holmes, R. A., A Neutral Lipophilic Complex of Tc-99m with a Multidentate Amine Oxime. *Int J Appl Radiat Is* **1984,** *35* (6), 467-470.

152. Wallace, A. M.; Han, L. K.; Povoski, S. P.; Deck, K.; Schneebaum, S.; Hall, N. C.; Hoh, C. K.; Limmer, K. K.; Krontiras, H.; Frazier, T. G.; Cox, C.; Avisar, E.; Faries, M.; King, D. W.; Christman, L.; Vera, D. R., Comparative Evaluation of [Tc]Tilmanocept for Sentinel Lymph Node Mapping in Breast Cancer Patients: Results of Two Phase 3 Trials. *Ann Surg Oncol* **2013**.

153. (a) Liu, G. Z.; Hnatowich, D. J., Labeling biomolecules with radiorhenium - A review of the bifunctional chelators. *Anti-Cancer Agent Me* **2007,** *7* (3), 367-377; (b) Liu, S.; Edwards, D. S., Synthesis and characterization of two In-111-labeled DTPA-peptide conjugates. *Bioconjugate Chem* **2001,** *12* (4), 630-634.

154. Morais, M. Compostos de 99mTc(I) contendo conjugados dextrano-manose. Compostos de 99mTc(I) contendo conjugados dextrano-manose, Universidade de Lisboa, Lisbon, 2008.

155. Zubieta, J.; Lazarova, N.; James, S.; Babich, J., A convenient synthesis, chemical characterization and reactivity of [Re(CO)(3)(H2O)(3)]Br: the crystal and molecular structure of [Re(CO)(3)(CH3CN)(2)Br]. *Inorganic Chemistry Communications* **2004,** *7* (9), 1023-1026.

156. (a) Amiot, C. L.; Xu, S. P.; Liang, S.; Pan, L. Y.; Zhao, J. X. J., Near-infrared fluorescent materials for sensing of biological targets. *Sensors-Basel* **2008,** *8* (5), 3082-3105; (b) Kobayashi, H.; Ogawa, M.; Alford, R.; Choyke, P. L.; Urano, Y., New Strategies for Fluorescent Probe Design in Medical Diagnostic Imaging. *Chem Rev* **2010,** *110* (5), 2620-2640.

157. (a) Harrison, W. J.; Mateer, D. L.; Tiddy, G. J. T., Liquid-crystalline J-aggregates formed by aqueous ionic cyanine dyes. *J Phys Chem-Us* **1996,** *100* (6), 2310-2321; (b) Xiang, J. F.; Yang, X. R.; Chen, C. P.; Tang, Y. L.; Yan, W. P.; Xu, G. Z., Effects of NaCl on the J-aggregation of two thiacarbocyanine dyes in aqueous solutions. *J Colloid Interf Sci* **2003,** *258* (1), 198-205; (c) Kang, J.; Kaczmarek, O.; Liebscher, J.; Dahne, L., Prevention of H-Aggregates Formation in Cy5 Labeled Macromolecules. *Int J Polym Sci* **2010**; (d) Licha, K.; Welker, P.; Weinhart, M.; Wegner, N.; Kern, S.; Reichert, S.; Gemeinhardt, I.; Weissbach, C.; Ebert, B.; Haag, R.; Schirner, M., Fluorescence Imaging with Multifunctional Polyglycerol Sulfates: Novel Polymeric near-IR Probes Targeting Inflammation. *Bioconjugate Chem* **2011,** *22* (12), 2453-2460.

158. Hilderbrand, S. A.; Kelly, K. A.; Weissleder, R.; Tung, C. H., Monofunctional near-infrared fluorochromes for imaging applications. *Bioconjugate Chem* **2005,** *16* (5), 1275-1281.

159. (a) Philip, R.; Penzkofer, A.; Baumler, W.; Szeimies, R. M.; Abels, C., Absorption and fluorescence spectroscopic investigation of indocyanine green. *J Photoch Photobio A* **1996,** *96* (1-3), 137-148; (b) Villaraza, A. J. L.; Milenic, D. E.; Brechbiel, M. W., Improved Speciation Characteristics of PEGylated Indocyanine Green-Labeled Panitumumab: Revisiting the Solution and Spectroscopic Properties of a Near-Infrared Emitting anti-HER1 Antibody for Optical Imaging of Cancer. *Bioconjugate Chem* **2010,** *21* (12), 2305-2312; (c) Pauli, J.; Vag, T.; Haag, R.; Spieles, M.; Wenzel, M.; Kaiser, W. A.; Resch-

Genger, U.; Hilger, I., An in vitro characterization study of new near infrared dyes for molecular imaging. *Eur J Med Chem* **2009,** *44* (9), 3496-503.

160. Rao, P.; Pattabiraman, T. N., Reevaluation of the Phenol Sulfuric-Acid Reaction for the Estimation of Hexoses and Pentoses. *Anal Biochem* **1989,** *181* (1), 18-22.
161. Waters, J. C., Accuracy and precision in quantitative fluorescence microscopy. *J Cell Biol* **2009,** *185* (7), 1135-1148.
162. Palma, E.; Oliveira, B. L.; Correia, J. D. G.; Gano, L.; Maria, L.; Santos, I. C.; Santos, I., A new bisphosphonate-containing Tc-99m(I) tricarbonyl complex potentially useful as bone-seeking agent: synthesis and biological evaluation. *J Biol Inorg Chem* **2007,** *12* (5), 667-679.
163. Mirassou, Y.; Santiveri, C. M.; de Vega, M. J. P.; Gonzalez-Muniz, R.; Jimenez, M. A., Disulfide Bonds versus Trp center dot center dot center dot Trp Pairs in Irregular beta-Hairpins: NMR Structure of Vammin Loop 3-Derived Peptides as a Case Study. *Chembiochem* **2009,** *10* (5), 902-910.